2011

Seismic Hazard Mitigation of Building Structures Using Magneto-Rheological Dampers

Yunbyeong Chae
Lehigh University

Seismic Hazard Mitigation of Building Structures Using Magneto-Rheological Dampers

by

Yunbyeong Chae

Presented to the Graduate Research Committee
of Lehigh University
in Candidacy for the Degree of
Doctor of Philosophy

in
Structural Engineering

Lehigh University

May 2011

Approved and recommended for acceptance as a dissertation in partial fulfillment of the requirements for the degree of Doctor of Philosophy.

Date

Dr. James M. Ricles
Dissertation Co-advisor

Dr. Richard Sause
Dissertation Co-advisor

Accepted Date

Committee Members:

Dr. Shamim N. Pakzad
Committee Chair

Dr. John L. Wilson
Member

Dr. Bill F. Spencer, Jr.
External Member

Acknowledgements

The research presented in this dissertation was conducted at the Engineering Research Center for Advanced Technology for Large Structural Systems (ATLSS), Department of Civil and Environmental Engineering, Lehigh University, Bethlehem, Pennsylvania. During the study, the chairmanship of the department was held by Dr. Stephen P. Pessiki.

The author deeply appreciates Dr. James M. Ricles and Dr. Richard Sause, the research advisors, for their vision, guidance, direction, and advice. Their persistent enthusiasm and continual encouragement have been most valuable to him. The author would like to thank his other committee members, Dr. Shamim Pakzad, Dr. John L. Wilson, and Dr. Bill F. Spencer, Jr. for their help and advice. The author also would like to express his gratitude to Dr. Yunfeng Zhang for the advice and financial support during his first year of Ph.D study.

Financial support from National Science Foundation (NSF) and Pennsylvania Infrastructure Technology Alliance (PITA) is greatly appreciated. The MR dampers of this research, manufactured by Lord Corporation, were made available by Professor Richard Christenson from the University of Connecticut. The author appreciates his generous support.

The author would like to thank Gary Novak, Tommy Marullo, John Hoffner, Edward Tomlinson and Peter Bryan. Their excellent work is gratefully recognized. A special thank you is extended to Dr. Choung-Yeol Seo for his advice and assistance

with the OpenSees work. The author's appreciation also goes to his friends and fellow students, Kihyon Kwon, Sunyong Kim, Yeun-Chul Park, Minwoo Chang, and Baiping Dong.

The author would like to extend his deepest gratitude to his mother, brothers and sister for their steadfast support and loyal encouragement. The author extends special thanks to his wonderful son Heeseo for his smiles and laughs. Most of all, the author is extremely thankful for the faithful love, help, support and patience of his dear wife Nayoung. Without her, this dissertation would not exist.

Table of Contents

List of Tables

List of Figures

Abstract

A magneto-rheological (MR) damper is a cylindrical device that consists of a two chamber system filled with MR fluid, where the chambers are separated by a piston head. The movement of the piston rod of the damper results in the MR fluid passing from one chamber to the other, past a small orifice between the piston head and the inner wall of the cylinder of the damper. Coils are located in the piston head. When a current is input into the coil a magnetic field develops near the orifice. The shear strength and viscosity of the MR fluid, which consists of carbonate iron particles suspended in a fluid, is sensitive to the strength of the magnetic field. An MR damper can have its force capacity altered by changing the amount of current input into the damper. A number of semi-active control laws for MR dampers have consequently been developed, which alter the current input of the damper in order to reduce the dynamic response of a structure.

During the last couple of decades a number of researchers have investigated the behavior of MR dampers and semi-active control laws associated with using these devices for vibration reduction of civil engineering structural systems. A majority of this research, however, has involved small-scale MR dampers, while only a few studies have been conducted with large-scale MR dampers. No performance-based practical design procedures have been developed for structural systems with MR dampers that enable the determination of damper capacity and the deployment of dampers to be done in conjunction with achieving building performance objectives in the design. In

addition, existing MR damper models have not been validated for large-scale dampers subject to realistic seismic demand.

This dissertation focuses on the seismic hazard mitigation of buildings with magneto-rheological dampers. Existing MR damper models for the prediction of the behavior of large-scale dampers under earthquake demand are investigated. The advantages and disadvantages of the existing MR damper models are discussed and a new MR damper model, called Maxwell Nonlinear Slider (MNS) model, is introduced. The MNS model can accurately account for the highly nonlinear behavior of MR dampers under the demand induced from a large earthquake. The robust MNS model makes it possible to predict the seismic behavior of structures with MR dampers more accurately and to validate the design procedure of these structures.

A simplified static analysis method to predict the response of a structure with MR dampers is developed based on a quasi-static MR damper model. This method is then integrated into a design procedure to develop the simplified design procedure (SDP) for the performance-based design procedure of structures with MR dampers. The design procedure is applied to a 3-story building structure with MR dampers, where three performance objectives are specified that are associated with two different seismic hazard levels. A series of 44 nonlinear time history analyses of the 3-story building is conducted using the MNS model to validate the proposed design procedure. The results of the analyses show that the SDP enables the 3-story building to achieve its performance objectives, with the design predictions from the SDP in close agreement with the median response of the structure acquired from the time history analysis. The

SDP was also validated using real-time hybrid simulations with the DBE level ground motions. The conclusions derived from the experimental results are in close agreement with those from the comparison of the SDP and numerical simulations involving nonlinear time history analyses.

Various structural control strategies are evaluated by conducting numerical and experimental studies of the 3-story building structure. The experimental studies involved performing real-time hybrid simulations with large-scale MR dampers. The control strategies in the study include semi-active control where the current is changed in accordance with a control law, and passive control where the current is held constant. The semi-active controllers studied in this dissertation include: (1) linear quadratic regulator control; (2) sliding mode control; (3) decentralized bang-bang control; and (4) a newly developed controller called the *Phase Angle Control*. Statistical results for the 3-story building structure show that the performance of the structure achieved with passive control is similar to that achieved with the semi-active controllers under the design basis earthquake (DBE) and the maximum consider earthquake (MCE), where the former and latter have an average return period of 475 years and 2475 years, respectively. The numerical and experimental results are in close agreement with each other, validating the use of real-time hybrid simulation as a means of investigating the seismic performance of structures with semi-active MR dampers subject to DBE and MCE level ground motions.

Numerical and experimental studies are conducted to evaluate the collapse resistance of structures with MR dampers under extreme ground motions. Incremental

dynamic analyses (IDAs) are performed using OpenSees to obtain the statistical response and the collapse margin ratio (CMR) of the 3-story building structure with various control strategies. The results of the study show that dampers can improve the collapse resistance of the building, however, there is only a marginal difference in the collapse resistance of the building with passive control compared to semi-active control. Real-time hybrid simulations are performed to experimentally validate the numerical results. The real-time hybrid simulation results are in close agreement with the numerical results, validating the time history analysis results, the real-time hybrid simulation method, and the MNS damper model for demands associated with extreme ground motions that lead to structural collapse.

Chapter 1

Introduction

1.1. General

Civil infrastructure such as buildings, highways and bridges are susceptible to damage over their life time due to extreme loads. Among extreme loads, earthquake loading is one major concerns for structural engineers. During the Northridge earthquake that occurred on January 17th, 1994, fifty-seven people died, more than 9,000 were injured, and over 20,000 were displaced from their homes by the effects of the earthquake. The estimated losses caused by the earthquake were $20 billion. The Northridge earthquake is considered one of the costliest natural disasters in United States history and reminds structural engineers again of the importance of seismic resistant design of structures.

The occurrence of damaging earthquakes has led to many revisions to seismic design methods. Earthquakes in the early part of the 20th century led to the development of regulations to provide for minimum levels of lateral strength. In the latter part of the 20th century earthquakes such as the 1971 San Fernando earthquake led to the realization that, in addition to strength, buildings needed to have the ability to deform without catastrophic failure, e.g., a characteristic known as ductility (FEMA 2006). The design paradigm has been changed once more after the 1994 Northridge and 1995 Kobe earthquakes. Before these earthquakes, building owners and insurers generally believed that code-compliant structures would not suffer any severe damage during an

earthquake. However, these earthquakes led to losses that were unexpected and subsequently huge financial loss, pushing researchers and practitioners toward the development of a new design methodology, i.e., performance-based seismic design, which considers seismic hazards, vulnerabilities, and consequences of damage.

Traditional prescriptive design focuses mainly on achieving an acceptable demand-to-capacity ratio; the objective of performance-based design is to achieve a specified level of performance (see Table 1.1), given the hazards that exist. Prescriptive design criteria can provide certain levels of structural performance, but more rigorous evaluations of structural performance are not assessed. Thus, the performance of some buildings designed to these prescriptive criteria can be better than the minimum performance anticipated by the code, while the performance of others could be worse.

Figure 1.1 shows the general procedure for performance-based design. The process begins with the selection of design criteria stated in the form of one or more performance objectives, followed by the development of an appropriate preliminary design concept. Then, the structural performance is assessed considering hazard level, determination of probable damage to structural or non-structural components, computation of the expected future losses, etc. The design is revised until the desired performance level is achieved. If the performance objectives cannot be met then an alternative structural system may be selected.

Energy dissipation devices can be effective tools in performance-based seismic design because they can efficiently reduce the response of structures subjected to earthquake ground motions, subsequently, enhancing the performance of the structure.

Energy dissipation systems can be classified into three distinctive categories: i) passive controlled systems; ii) active controlled systems; and iii) semi-active controlled systems.

A passive energy dissipation system can include a range of materials and devices for enhancing the damping, stiffness and strength of the system. The performance of the structural system is improved by passive movement of the energy dissipation devices from the excitation of the structure. Passive devices generally operate on principles such as frictional sliding, yielding of metals, phase transformation in metals, deformation of visco-elastic (VE) solids or fluids, fluid orificing, etc. (Soong and Spencer 2002). The inherent stability of a structural system with passive energy dissipation devices is one of the great advantages of this type of system. Although passive energy dissipation systems do not have the ability to adjust their energy dissipation properties to adapt to changes in usage patterns or environmental loadings, they are widely accepted in the structural engineering design community due to their simplicity (Spencer and Nagarajaiah 2003).

Active controlled structural systems employ force delivery devices integrated with real-time processing controllers and sensors within the structure. Active controlled structural systems are comprised of three main components: i) sensors that measure external excitations, or structural response, or both; ii) devices to process the measured information and to compute necessary control forces based on a selected control algorithm; and iii) actuators to produce the required force from the control device (Soong and Constantinou 1994). Active controlled structural systems have more versatility than passive controlled structural systems. Through the use of control devices

and the actuators generating the optimal control forces based on measured information and user-defined control algorithms, structural control objectives are more easily attainable by active controlled systems than by passive controlled systems. The uncertainty however associated with structural properties and a limited number of sensors can lead to a control signal to the actuators that can cause the structural system to become unstable. Moreover, in an active controlled structural system the actuators are typically large and require significant power sources, as well as control hardware and sensors. Consequently, active controlled structural systems are more expensive than passive controlled structural systems. One of the alternatives to active controlled structural systems is the use of a *hybrid controlled system*, generally referred to a combined passive and active controlled system. Since a portion of the control objective is accomplished by the passive system, less active control effort is required and fewer stability issues arise than that of the active controlled structural system. This is considered as one of the reasons why hybrid controlled systems rather than active controlled structural systems are more readily used in civil engineering structures (Housner et al 1997, Soong and Spencer 2002, Spencer and Nagarajaiah 2003).

Semi-active controlled structural systems combine the features of passive and active controlled structural systems. Semi-active controlled structural systems do not add energy into the structural system; hence, they do not have the potential to destabilize the system. In particular, they have the ability to adjust the energy dissipation capacity or system stiffness by adaptively changing the properties associated with either stiffness, damping, or friction, while the power consumption is considerably

lower than that of an active controlled structural system. These unique features of semi-active controlled structural systems have attracted the attention of many researchers and engineers during the last couple of decades. Semi-active controlled structural systems employ devices such as variable-orifice fluid dampers, controllable friction devices, variable-stiffness devices, smart tuned mass or liquid dampers, and controllable fluid dampers (Spencer and Nagarajaiah 2003).

The magneto-rheological (MR) damper is one popular semi-active controlled device. Figure 1.2 shows a schematic of a large-scale MR damper. The MR damper force depends on the yield stress of the MR fluid inside the damper, which is generally a function of the magnetic flux in the damper. When the MR fluid is subjected to a magnetic field by the electromagnetic coil, the iron particles in the fluid are aligned and form linear chains parallel to the line of magnetic flux, changing the state of the fluid to a semi-solid which restricts the fluid movement through the orifices of the MR damper. Owing to this feature, devices using MR fluids have been used in various applications in mechanical vibration such as vibration absorbers in vehicles (Han et al. 2002, Stelzer et. al. 2003) and disk brakes or clutches (Carlson et al. 1995).

In this dissertation, the dynamic behavior of structures with MR dampers is studied for the purpose of seismic hazard mitigation. Large-scale MR dampers are installed in the structure based on a simplified design procedure developed in this dissertation. The procedure includes considering selected performance levels of the structural system exposed to selected hazard levels. The performance of various control strategies for MR dampers are compared, and numerically and experimentally studied,

the latter by conducting real-time hybrid simulations. Collapse simulations of structures with MR dampers are conducted to assess the collapse potential of structures with MR dampers using the incremental dynamic analysis (IDA) procedure. The following section describes the objectives of this dissertation.

1.2 Research Objectives

The objectives of this dissertation are as follows:

- Develop a new MR damper model that can accurately predict the response of large-scale MR dampers in structural systems subject to earthquake ground motions;
- Develop a simplified seismic design procedure for structures with MR dampers satisfying selected performance objectives for earthquake conditions;
- Evaluate the performance of various control strategies for MR dampers, including passive and semi-active controllers to reduce structural response to seismic loading conditions;
- Assess the collapse potential of structures with MR dampers under earthquake motions using the incremental dynamic analysis procedure;
- Conduct real-time hybrid simulations to experimentally study the seismic behavior of structures with MR dampers and to validate the results of numerical simulations.

1.3 Organization of Dissertation

This dissertation consists of 12 chapters, with the remaining chapters organized as follows:

- **Chapter 2** reviews background information on the modeling and control of MR dampers developed in prior research studies.
- **Chapter 3** describes a new MR damper model, called the Maxwell Nonlinear Slider (MNS) model. Chapter 3 is mainly dedicated to describe the behavior of an MR damper under constant current input, i.e., in passive mode. Characterization tests of a large-scale MR damper are presented. The basic mechanical theory for this MNS damper model is based on separating the pre-yield and post-yield behavior of an MR damper. The procedure for identification of model parameters from characterization test data is presented using the particle swarm optimization algorithm (PSO). The predictions of damper behavior by the MNS model are compared to the experimental results from the characterization tests, damper displacement histories based on Gaussian white noise and earthquake loading.
- **Chapter 4** presents the behavior of MR dampers under variable current, which is for associated with semi-active controlled dampers. The dynamics of an MR damper is described using electromagnetic theory, considering the eddy current effect and magnetization behavior of damper materials. A nonlinear equation correlating the current in the damper coil with the equivalent static current for the prediction of damper force is proposed. The prediction of MR damper behavior under variable current via the nonlinear equation is compared to

experimental results from real-time hybrid simulations of a 3-story building structure with MR dampers.

- **Chapter 5** develops a systematic procedure for the dynamic response prediction of a SDOF structure with a diagonal brace and an MR damper. The prediction is based on a quasi-static MR damper model, from which the amplitude dependent loss factor and equivalent stiffness are calculated. Examples of this procedure are demonstrated and compared to the results of nonlinear time history analysis with the MNS model.
- **Chapter 6** provides a simplified design procedure (SDP) for the performance-based seismic design of structures with MR dampers. The procedure in Chapter 5 is extended to MDOF structures and is incorporated into the simplified design procedure. This simplified design procedure is demonstrated through a design example for a 3-story building structure satisfying three different performance objectives involving two levels of seismic hazard.
- **Chapter 7** validates the simplified design procedure proposed in Chapter 6 through a series of nonlinear time history analysis using OpenSees. The predicted responses from the simplified design procedure are compared to the results of the nonlinear time history analysis and the accuracy of the simplified design procedure is discussed.
- **Chapter 8** provides a newly developed semi-active controller called the phase angle control (PAC). The PAC is based on impulse response function theory and the phase angle of a structure. The PAC is first explained for an SDOF system

and extended to MDOF systems based on modal analysis theory. Unlike the linear quadratic regulator (LQR) and the sliding mode control (SMC), the PAC does not require any user-defined model parameters.

- **Chapter 9** evaluates the performance of various control strategies for MR dampers. Four different semi-active controllers are selected for the comparison: i) linear quadratic regulator (LQR); ii) sliding mode control (SMC); iii) decentralized bang-bang control (DBB); and, iv) phase angle control (PAC). The structural responses resulting from the use of the semi-active controllers are compared to that using a passive controller. In addition, the issues of uncertainty related to incorrect structural properties, noise in the feedback data, and the effect of response time of MR damper associated with variable current input are studied.
- **Chapter 10** investigates the collapse potential of a 3-story building structure with MR dampers by performing incremental dynamic analyses (IDAs). The building structure designed in Chapter 6 is used and the IDAs are conducted using OpenSees. A phenomenological based deterioration model for member plastic flexural hinges that is calibrated from experimental data is implemented into OpenSees, and five different controllers including the four semi-active controllers from Chapter 9 and a passive controller for the MR damper are used in the IDAs. Collapse fragility curves for these cases are obtained and compared to each other.

- **Chapter 11** describes the real-time hybrid simulations conducted for the experimental investigation of the seismic behavior of structural systems with MR dampers. The evaluation of the control strategies studied in Chapter 9 are experimentally assessed through the real-time hybrid simulations, using a group of selected ground motions. Moreover, the collapse simulation conducted in Chapter 10 is performed for a selected ground motion, and compared to the results of the numerical simulations.
- **Chapter 12** summarizes the findings and conclusions from this study, and makes recommendations for future research.

Table 1.1 Damage control and building performance levels (FEMA 2000b)

	Target Building Performance Levels			
	Collapse Prevention Level	Life Safety Level	Immediate Occupancy Level	Operational Level
Overall Damage	Severe	Moderate	Light	Very Light
General	Little residual stiffness and strength, but load bearing columns and walls function. Large permanent drifts. Some exits blocked. Infills and unbraced parapets failed or at incipient failure. Building is near collapse	Some residual strength and stiffness left in all stories. Gravity-load-bearing elements function. No out-of-plane failure of walls or tipping of parapets. Some permanent drift. Damage to partitions. Building may be beyond economical repair.	No permanent drift. Structure substantially retains original strength and stiffness. Minor cracking of facades, partitions, and ceilings as well as structural elements. Elevators can be restarted. Fire protection operable.	No permanent drift. Structure substantially retains original strength and stiffness. Minor cracking of facades, partitions, and ceilings as well as structural elements. All systems important to normal operation are functional.
Nonstructural components	Extensive damage	Falling hazards mitigated but many architectural, mechanical, and electrical systems are damaged.	Equipment and contents are generally secure, but may not operate due to mechanical failure or lack of utilities.	Negligible damage occurs. Power and other utilities are available, possibly from standby sources.

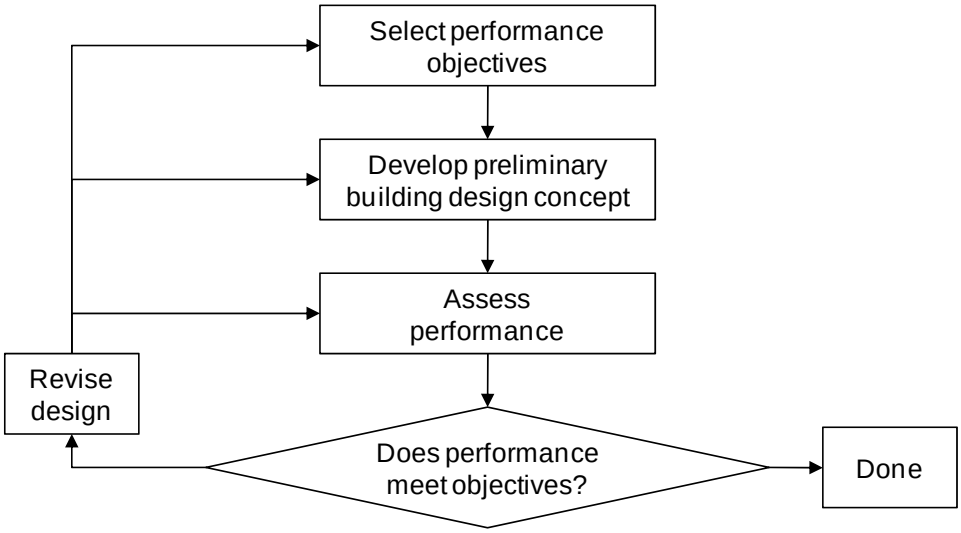

Figure 1.1 Performance-based design flow

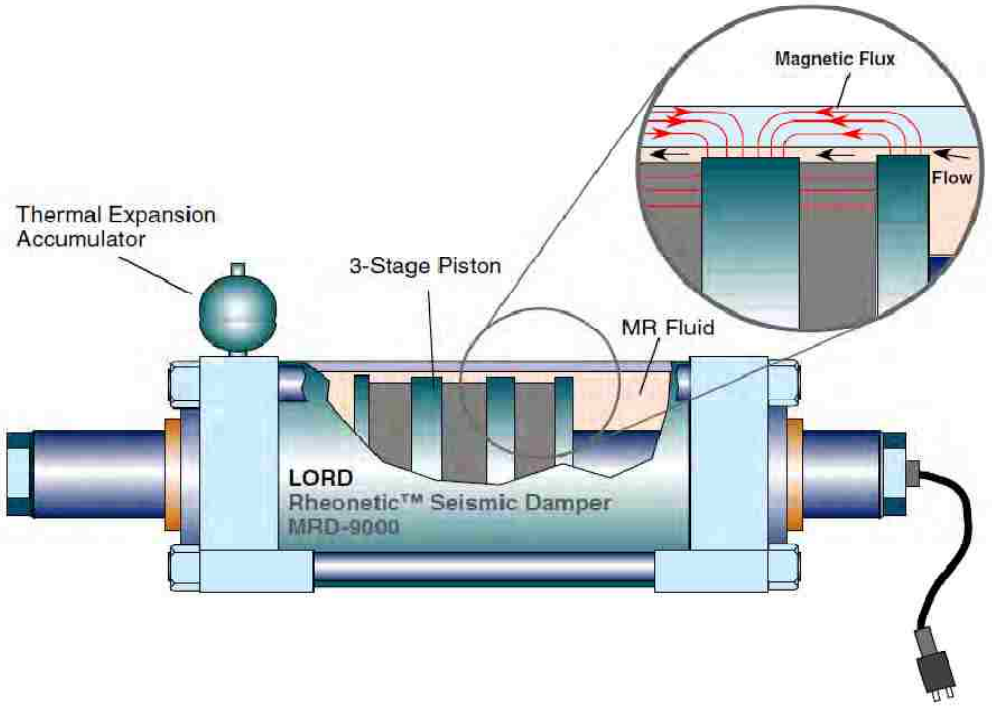

Figure 1.2 Schematic of the 1st generation large-scale MR damper manufactured by Lord Corporation (after Yang 2001)

Chapter 2

Background: MR Damper Models and Semi-Active Control Laws

2.1. General

In this chapter, previous relevant research related to the modeling of MR dampers and semi-active control strategies for MR dampers is summarized. This is followed by a description of the basic theory for semi-active controllers.

2.2 Modeling of MR Dampers

2.2.1 Bingham Model

The Bingham model, due to its simplicity, is frequently used to describe the behavior of small-scale MR dampers. The model consists of a dashpot and a friction element connected in parallel as shown in Figure 2.1. In Figure 2.1, x is the damper displacement. The damper force f in the Bingham model is

$$f = c_1\dot{x} + f_0\text{sgn}(\dot{x}) \tag{2.1}$$

where c_1 and f_0 are equal to the damping coefficient and the slider friction force, respectively. In Equation (2.1) sgn() is the signum function. The damping force is linearly dependent on the damper velocity $\dot{x}$, whereas the friction force is dependent on the sign of the velocity. The Bingham model generally provides a good prediction of the force-displacement relationship for MR dampers. However, it cannot adequately

describe the frequency dependent behavior of an MR damper (see the experimental force-displacement and force-velocity relationships with various frequencies shown in Figures 3.7 and 3.8, respectively) because it has only one path in the force-velocity curve (see Figure 5.2(a)). Moreover, this model assumes that the MR fluid remains rigid in the pre-yield region; thus it cannot accurately account for the pre-yield behavior of an MR damper.

2.2.2 Gamota and Filisko Model

Figure 2.2 shows a schematic of the model proposed by Gamota and Filisko (1991). This model was originally developed to model an electro-rheological (ER) damper, but it has been applied to the modeling of an MR damper by Spencer et al. (1997). This model consists of Bingham model in series with a standard model of a linear solid. The governing equations for this model are

$$\left.\begin{aligned} f &= k_1(x_2 - x_1) + c_1(\dot{x}_2 - \dot{x}_1) + f_0 \\ &= c_0\dot{x}_1 + f_c\mathrm{sgn}(\dot{x}_1) + f_0 \\ &= k_2(x_3 - x_2) + f_0 \end{aligned}\right\} \quad \text{if } |f| > f_c \tag{2.2}$$

$$\left.\begin{aligned} f &= k_1(x_2 - x_1) + c_1\dot{x}_2 + f_0 \\ &= k_2(x_3 - x_2) + f_0 \end{aligned}\right\} \quad \text{if } |f| \le f_c \tag{2.3}$$

where c_0 = damping coefficient for Bingham model; and k_1, k_2, and c_1 are stiffness and viscous damping coefficients, respectively, associated with a linear solid material. Although this model can describe the behavior of an MR damper better than the Bingham model, it has the shortcoming that a very small time step on the order of 10^{-6}

is required in the response determination using numerical integration. This is because Equations (2.2) and (2.3) are extremely stiff differential equations (Spencer et al. 1997).

2.2.3 BingMax Model

Makris et al. (1996) formulated a phenomenological model for an MR damper, called the *BingMax* model. The model is based on the Maxwell element and Bingham model as shown in Figure 2.3. The constitutive law of the BingMax model is expressed as

$$f(t) = k\int_0^t \exp\left(-\frac{t-\tau}{\lambda}\right)\dot{x}(\tau)d\tau + f_y \mathrm{sgn}(\dot{x}(t)) \tag{2.4}$$

where $\lambda = c/k$ is the quotient of the dashpot c and the spring k, and f_y is the frictional force in the slider. Equation (2.4) can be conveniently expressed in differential equation form (Butz and Von Stryk 2002) as

$$f + \lambda \dot{f}_d f = c\dot{x} + f_y \mathrm{sgn}(\dot{x}) \tag{2.5}$$

Makris et al. (1996) showed that the BingMax model captures both hysteretic and frequency-dependent behavior of an MR damper. Makris et al. also showed that the BingMax model achieves a better prediction of experimental response compared to the Bingham model. However, it is difficult for the BingMax model to account for non-

Newtonian MR fluid behavior (i.e., shear thinning and thickening behavior of the MR fluid) due to the linear dashpot that is present in the model.

2.2.4 Bouc-Wen Model

In order to capture the force roll-off phenomenon that occurs in an MR damper near the zero velocity region, Spencer et al. (1997) developed a more sophisticated model based on the combination of dashpots and springs with the Bouc-Wen element as shown in Figure 2.4. The damper force of this model is obtained by solving the following equations:

$$f = c_1\dot{y} + k_1(x - x_0) \tag{2.6}$$

$$c_1\dot{y} = \alpha z + k_0(x - y) + c_0(\dot{x} - \dot{y}) \tag{2.7}$$

$$\dot{z} = -\gamma|\dot{x} - \dot{y}|z|z|^{n-1} - \beta(\dot{x} - \dot{y})|z|^n + A(\dot{x} - \dot{y}) \tag{2.8}$$

In this model, k_1 represent the damper accumulator stiffness and c_0 is the dashpot coefficient associated with viscous damping at larger velocities. A dashpot c_1 is included in model to produce roll-off that was observed in experimental data at low velocities, k_0 is present to control the stiffness at larger velocities, and x_0 is an initial displacement of spring k_1 associated with nominal damper force due to the accumulator. Since the Bouc-Wen model can predict the behavior of MR dampers well, many researchers have used this model for the numerical simulation of structures with MR dampers. It was also used to model the first generation large-scale MR damper

manufactured by Lord Corporation (Yang et al. 2002). However, the initial guess of model parameters in algorithms to identify the model parameters needs to be done by trial and error, and it is difficult for this model to account for the non-Newtonian MR fluid behavior because the post-yield behavior is governed by the linear dashpot c_0.

2.2.5. Hyperbolic Tangent Model

Gavin (2001) developed the hyperbolic tangent model for the description of the dynamic behavior of an electro-rheological (ER) damper. The model consists of a series of Voigt visco-elastic elements combined with a lumped mass element and a nonlinear friction element as in Figure 2.5. The damper force of this model is represented as

$$f = c_1(\dot{x} - \dot{x}_0) + k_1(x - x_0) \tag{2.9}$$

$$m_0\ddot{x}_0 + (c_0 + c_1)\dot{x}_0 + f_0 \tanh\left(\dot{x}_0/V_{ref}\right) = c_1\dot{x} + k_1 x \tag{2.10}$$

A dashpot c_1 and a spring k_1 describe the pre-yield behavior of the MR damper; and the post-yield behavior is described by a dashpot c_0, a spring k_0 and a nonlinear slider based on the hyperbolic tangent function, $\tanh()$. In Equation (2.10), V_{ref} is a reference velocity normalizing $\dot{x}_0$. f_0 is a coefficient associated with the nonlinear friction element. The inertia of the MR damper is associated with the lumped mass m_0. Bass and Christenson (2007) used the hyperbolic tangent model to predict the behavior of the second generation large-scale MR dampers manufactured by Lord Corporation. The hyperbolic tangent model has shown a good performance to describe the nonlinear MR

damper response. However, the initial guess of model parameters needs to be done by trial and error, like the Bouc-Wen model, and it is also difficult for this model to account for non-Newtonian MR fluid behavior because the post-yield behavior is governed by the linear dashpot c_0.

2.2.6 Models Based on Intelligent Systems

In addition to mechanical MR damper models, intelligent prediction systems such as neural networks and fuzzy inference systems have also been developed to model MR dampers. A neural network system consists of multi-layer perceptrons (MLP), where nodes are arranged in multiple layers to provide connections from one layer to the next. The connection between the nodes is described by weights whose values are determined through training. Data is fed forward through the network to produce output. An error is determined from the output and propagated backwards through the layers. A back-propagation algorithm allows for movement to a minimal error over the course of the training process. Each time the weights are changed, the direction and magnitude of the change is determined so as to make a move towards the minimal error. An activation function is assigned to each node and used to increase the modeling flexibility.

Chang and Roschke (1998) developed a neural network based MR damper model. They used a feedforward neural network (FNN). The input of the FNN consists of a time series of displacements and voltages as well as delayed damper forces. Output is the damper force for the current time step. To optimize the network, an optimal brain

surgeon (OBS) strategy was applied to prune the superfluous weights from the network. They utilized the Bouc-Wen model shown in Figure 2.4 to train and validate their neural network system. Although they provided an alternative methodology for modeling MR dampers using the FNN, the model is not able to stand alone because it requires measured damper force as an input, which is not applicable to pure numerical simulations. To resolve this problem, Wang and Liao (2005) applied a recurrent neural network (RNN) to the modeling of MR dampers. Instead of measured damper forces, a series of predicted damper forces are fed into the input layers along with the time series of displacements and voltages. The architecture of this system is illustrated in Figure 2.6.

Schurter and Roschke (2000) presented an alternative for modeling of MR damper by using an adaptive neuro-fuzzy inference system (ANFIS). ANFIS uses a hybrid learning algorithm that combines the back-propagation gradient descent and least squares method to create a fuzzy inference system whose membership functions are iteratively adjusted according to a given set of input and output data. To cover the spectrum of operation in which the damper will function, they selected a set of displacement training data from Gaussian white noise with an amplitude of 4cm and frequency range approximately 0-3Hz. The voltage training data is selected to cover 0-4 volts and 0-3Hz frequency ranges. To train and validate the system, Schurter and Roschke used the Bouc-Wen model shown in Figure 2.4. The prediction by the ANFIS showed good agreement with target damper forces, although it did not capture the low frequency damper dynamic characteristics very well. The performance of both neural

networks and the ANFIS rely on the quality of training data. Therefore, the training set for these systems needs to be selected carefully, and the performance should be verified further through experimental work.

2.3 Semi-Active Controllers for MR Dampers

MR dampers can be used either in passive or semi-active mode for the control of structures. In a passive controlled system, shown in the block diagram in Figure 2.7, a constant current is supplied to the MR damper. No feedback data are required in the controller and the damper force is generated passively for the given current. In this system, passive-on or passive-off control is usually referred as to the case when the maximum current or minimum current is applied to the damper.

The semi-active controlled system shown in Figure 2.8 uses feedback data, requiring the use of sensors and a controller. The commonly accepted definition of a semi-active control device is the one that has properties which does not input energy into the system that is being controlled. In MR dampers the current going into the damper controls the damper force. This current can change the magnitude of damper force by changing the intensity of the magnetic flux from the electromagnetic coil, but it cannot change the direction of the damper force in a given state, like an active controller. To determine the appropriate control force, a semi-active controller involves the use of optimal control theory along with feedback data collected from sensors, such as accelerometers, load cells, displacement transducers, etc.

Since the force in an MR damper can be controlled by adjusting the input current into the damper, many researchers have studied the performance of an MR damper controlled by a semi-active controller. The command current to the damper from a semi-active control law can be a continuous form or a simple on-off type command, i.e., either the maximum current or minimum current. The latter type of command current is widely used. In this section, various semi-active controllers applied to the control of MR dampers and associated prior research are briefly introduced.

2.3.1 Controllers Based on LQR and LQG

Linear quadratic regulator (LQR) control is frequently used to control structures. LQR involves using is a feedback controller to minimize a quadratic cost function, subsequently resulting in stable motions. Dyke et al. (1996) developed a clipped-optimal controller based on the H2/LQG (linear quadratic Gaussian) method to suppress the vibration of a scaled 3-story shear building structure subjected to the El Centro earthquake ground motion. Jansen and Dyke (2000) investigated the response of a 6-story small scale shear building with two MR dampers mounted in the 1st and 2nd stories and employed various semi-active control algorithms, including the clipped-optimal controller to control the response of the structure to ground motions. Yi et al. (2001) applied the clipped-optimal controller to a small scale 6-story shear building and compared the experimental response obtained using a Lyapnov controller. Xu et al. (2000) proposed optimal displacement control strategies for MR and ER dampers based on LQR control theory, and drew the conclusion that the performance of their semi-

active controllers is better than that of a passive device. Tsang et al. (2006) developed a simplified inverse dynamic (SID) model for determining the command current to produce the desired damper force. The SID was based on a mechanical MR damper model such as the Bingham model and the Bouc-Wen model. Tsang et al. selected a 3-story shear building and applied the LQR controller to a MR damper installed in the 1st story to verify their SID model for determining the command current into the damper. Guo et al. (2009) performed shaking table tests on a base-isolated bridge to investigate the pounding effect between adjacent superstructures under earthquake ground motions. MR dampers were installed under the superstructure along with rubber bearings to control the relative structural movement between the foundation and the superstructure. The LQR was selected as a semi-active controller and the results were compared with those of passive controllers.

2.3.2 Sliding Mode Control (SMC)

The basic theory of sliding mode control (SMC) is to design the controller to drive the response trajectory along a sliding surface, where the motion on the sliding surface is stable (Yang et al. 1995). Moon et al. (2002) applied SMC based on Yang's work to control the response of a cable-stayed bridge to earthquake excitations. They showed the robustness of SMC by investigating the performance of SMC associated with uncertainties in stiffness. Hiemenz et al. (2003) compared the performance of three different semi-active controllers for a 3-story shear building, which included a skyhook controller, LQR controller, and continuous sliding mode (CSM) control. Both steady-

state frequency responses and transient seismic response were simulated. It was found that CSM outperformed the LQR and skyhook controllers in their results. Fan et al. (2008) performed a shaking table test on a 3-story steel frame equipped with a pendulum isolator system on the 1st floor. The isolator system was composed of a single MR damper with 6kN force capacity, a friction pendulum-type isolator, and a piece of mechanical equipment with known mass (mass equipment) on the friction isolator. They used a set of two decentralized sliding mode controls (DSMCs), where the command signal was determined only using the local feedback signals, as well as the LQR controller. The maximum acceleration of the mass equipment and the maximum displacement of the isolator were measured during the tests, and Fan et al. reported trade-offs between the acceleration and the displacement. Lu et al. (2008) conducted an experimental study of a 1/4 scale 6-story steel frame structure. 3kN MR dampers manufactured by Lord Corporation were installed in the building structure with four different damper deployment profiles. Several DSMCs were designed and applied to the structure along with the LQR controllers. The results from shaking table tests with these controllers showed the benefit of the DSMC over the LQR controllers.

2.3.3 Controllers Based on Lyapunov Stability Theory

Lyapunov stability theory provides a powerful tool for dealing with stability problems in both linear and nonlinear systems (Ogata 1997). This stability theory has been frequently applied to the design of controllers; the linear quadratic regulator and the sliding mode controller are based on Lyapunov stability theory..

Jansen and Dyke (2000) investigated the response of a 6-story small scale shear building with a controller based on Lyapunov theory. They showed that the Lyapunov controller worked comparably well to the clipped-optimal controller. Albarez and Jimenez (2003) studied the behavior of a 3-story shear building with an MR damper in the 1st story. They used a Lyapnov controller and conducted numerical simulations using the MR damper model based on a dynamic friction model. Their semi-active controller resulted in a significant reduction in structural response compared to the uncontrolled case. Sahasrabudhe and Nagarajaiah (2005) performed both experimental and numerical studies on a 1:20 scaled bridge model, where the MR damper was installed between the bridge deck and the pier. The Lyapunov function for their controller consisted of the total strain energy, the total dissipated energy, and the total kinetic energy. They showed that the semi-actively controlled MR damper reduces bearing displacements further than the passive low- and high-damping cases, while maintaining isolation level forces less than the passive high-damping case. Soneji and Jangid (2006) investigated the behavior of the Quincy Bay-view Bridge at Illinois, where the bridge is assumed to have isolators consisting of high damping rubber bearings (HDRB) and MR dampers. The controller based on Lyapunov stability theory showed better performance than that of the passive controlled case.

2.3.4 Neural Network Controllers

Intelligent controllers such as neural networks and fuzzy inference systems can be thought of as adaptive or self-organizing systems that learn through interaction with

their environment with little a priori knowledge (Housner et al 1997). A structural system with semi-actively controlled MR dampers could be a highly nonlinear system, considering the nonlinear characteristics of the MR dampers as well as the nonlinearity of the structure itself. Neural networks can be effectively applied to this kind of complex system. The main advantage of the neural network approach is that identification of an unknown system and evaluation of response can be performed without building a mathematical model of the system (Gallent 1993).

Xu et al. (2003) proposed an on-line real-time control method for semi-active control of structures with MR dampers using neural networks. The neural networks predict the displacement and velocity of the structure. If the predicted displacement is less than the desired value, then, the command current into the MR damper is zero. Otherwise, the current is gradually increased until it reaches the maximum current input. The predicted responses are compared with the measured (or calculated) structural responses with MR dampers, and the neural network is trained in such a manner that the errors between predicted and measured responses are minimized. Bani-Hani and Sheban (2006) applied a neural network system to control a 6-story building structure mounted on a semi-active base isolation system combined with MR dampers. An inverse neural network model (INV-MR) was constructed to replicate the inverse dynamics of the MR damper. Next, an LQG controller was designed to produce the optimal control force. The coupled LQG and INV-MR system was used to train a semi-active neuro-controller, designated as SA-NC, which produces the necessary control voltage into the MR damper. The effectiveness of the SA-NC was illustrated and compared to other passive

systems. Karmodin and Kazemi (2010) used a similar procedure to the one proposed by Bani-Hani and Sheban (2006) to control the 3-story ASCE benchmark structure (Ohtori et al. 2004) with MR dampers. According to their conclusions, the semi-active neuro-controller performed better than the clipped-optimal controller to reduce the story drift in the structure.

2.3.5 Fuzzy Controllers

Fuzzy control uses expert knowledge instead of a sophisticated mathematical model to describe a system. It is a process that uses fuzzy information to determine desirable control actions and is utilized in complex systems for which there are no simple mathematical model (Wilson 2005).

Zhou et al. (2003) provided an adaptive fuzzy control algorithm for the control of linear and nonlinear SDOF and MDOF structures with an MR damper. The algorithm involves the design of a fuzzy controller and an adaptation law for the combined structure-MR damper system. Numerical simulation conducted on a 3-story shear building structure with an MR damper in the 1st story showed the effectiveness of their semi-active controller. Choi et al. (2004) developed a fuzzy controller and applied it to the control of 3-story shear building structure used by Dyke et al. (1996). Based on their membership functions and fuzzy inference rule, Choi et al. (2004) generated a continuous command voltage into the MR damper between 0V and the maximum voltage. By comparing their results with those of passive controllers and the clipped-optimal controller, they illustrated the effectiveness of the fuzzy semi-active controller.

Lin et al. (2007) conducted experimental studies involving 21,772kg mass and a hybrid isolation system with four high damping rubber bearings (HDRBs) and a 300kN MR damper. Three different fuzzy logics were utilized to generate appropriate command voltages for the MR damper. The results with semi-active fuzzy controllers were compared with those of passive control cases, showing that the semi-active fuzzy controller exhibits good performance in reducing both the displacement and the acceleration of the isolated structure. Gu and Oyandiji (2008) utilized an adaptive neuro-fuzzy inference system (ANFIS) method to control structures with MR dampers. The LQG controller was used to generate a training data set and a force-feedback control scheme was employed in their controller. No significant difference in reducing the displacement of a 3-story shear building was reported between the ANFIS and the LQR controllers.

2.4 Basic Theory for Semi-Active Controllers

In this section, the basic theory for three different semi-active controllers is introduced, including: i) linear quadratic regulator; ii) sliding mode control; iii) decentralized bang-bang control. These controllers will be used in Chapter 9 for the evaluation of the performance of semi-active controllers in reducing structural response under seismic loading.

2.4.1 Equilibrium Equations

The motion of a linear-elastic structure subjected to a single component of horizontal ground motion is governed by the following set of equilibrium equations:

$$\mathbf{M}_s\ddot{\mathbf{x}} + \mathbf{C}_s\dot{\mathbf{x}} + \mathbf{K}_s\mathbf{x} = \mathbf{\Lambda f} - \mathbf{M}_s\mathbf{\Gamma}\ddot{x}_g \tag{2.11}$$

where $\mathbf{M}_s$ = mass matrix $(N \times N)$; $\mathbf{C}_s$ = damping matrix $(N \times N)$; $\mathbf{K}_s$ = stiffness matrix $(N \times N)$; $\mathbf{\Lambda}$ = MR damper location matrix $(N \times L)$; $\mathbf{f}$ = damper force vector $(L \times 1)$; $\mathbf{\Gamma}$ = unit vector of which all the row are 1 $(N \times 1)$; $\mathbf{x}$ = vector of displacements $(N \times 1)$; $\dot{\mathbf{x}}$ = vector of velocities $(N \times 1)$; $\ddot{\mathbf{x}}$ = vector of accelerations $(N \times 1)$; and $\ddot{x}_g$= input ground acceleration. N is the number of degrees-of-freedom(DOFs) of the structure and L is the number of MR dampers placed in the structure. The state-space form of Equation (2.11) can be written as

$$\dot{\mathbf{z}} = \mathbf{Az} + \mathbf{Bf} + \mathbf{E}\ddot{x}_g \tag{2.12}$$

$$\mathbf{y} = \mathbf{Cz} + \mathbf{Df} \tag{2.13}$$

where, $\mathbf{z}$ is the state vector consisting of $\mathbf{z} = [\mathbf{x}^T \ \dot{\mathbf{x}}^T]^T$ and $\mathbf{y}$ is an output vector. Matrices **A**, **B**, and **E** are defined as

$$\mathbf{A} = \begin{bmatrix} \mathbf{0} & \mathbf{I} \\ -\mathbf{M}_s^{-1}\mathbf{K}_s & -\mathbf{M}_s^{-1}\mathbf{C}_s \end{bmatrix}, \mathbf{B} = \begin{bmatrix} \mathbf{0} \\ \mathbf{M}_s^{-1}\mathbf{\Lambda} \end{bmatrix}, \mathbf{E} = \begin{bmatrix} \mathbf{0} \\ -\mathbf{\Gamma} \end{bmatrix} \tag{2.14}$$

2.4.2 Linear Quadratic Regulator (LQR)

2.4.2.1 Basic Theory

In the LQR control theory, the optimal damper forces are obtained by minimizing the scalar performance index defined as (Ogata 1997)

$$J = \int_0^\infty \mathbf{z}^{\mathrm{T}}\mathbf{Q}\mathbf{z} + \mathbf{f}^{\mathrm{T}}\mathbf{R}\mathbf{f}\, dt \tag{2.15}$$

where, **Q** and **R** are positive-definite symmetric matrices. These are user-defined weighting matrices of which dimensions are $(2N \times 2N)$ and $(L \times L)$, respectively. The optimal control force is determined by using the LQR gain matrix **K**

$$\mathbf{f} = -\mathbf{K}\mathbf{z} \tag{2.16}$$

The objective of the LQR controller is to find an optimal gain matrix **K** $(L \times 2N)$ that minimizes the performance index of Equation (2.15). The term containing the ground motion in Equation (2.12) is considered as a disturbance in the optimization procedure for determining **K** and ignored. Substituting Equation (2.16) into Equation (2.12), and ignoring the ground acceleration term, the following equation is obtained

$$\dot{\mathbf{z}} = (\mathbf{A} - \mathbf{B}\mathbf{K})\mathbf{z} \tag{2.17}$$

In the following derivations, the matrix $\mathbf{A} - \mathbf{B}\mathbf{K}$ is assumed to be stable. Substituting Equation (2.16) into Equation (2.15) yields

$$J = \int_0^\infty \mathbf{z}^{\mathrm{T}}(\mathbf{Q} + \mathbf{K}^{\mathrm{T}}\mathbf{R}\mathbf{K})\mathbf{z}\, dt \tag{2.18}$$

Assuming

$$\mathbf{z}^{\mathrm{T}}(\mathbf{Q} + \mathbf{K}^{\mathrm{T}}\mathbf{R}\mathbf{K})\mathbf{z} = -\frac{d}{dt}\mathbf{z}^{\mathrm{T}}\mathbf{P}\mathbf{z} \tag{2.19}$$

where **P** is a positive-definite symmetric matrix, then

$$\begin{aligned}\mathbf{z}^{\mathrm{T}}(\mathbf{Q} + \mathbf{K}^{\mathrm{T}}\mathbf{R}\mathbf{K})\mathbf{z} &= -\dot{\mathbf{z}}^{\mathrm{T}}\mathbf{P}\mathbf{z} - \mathbf{z}^{\mathrm{T}}\mathbf{P}\dot{\mathbf{z}} \\ &= -\mathbf{z}^{\mathrm{T}}[(\mathbf{A} - \mathbf{B}\mathbf{K})^{\mathrm{T}}\mathbf{P} + \mathbf{P}(\mathbf{A} - \mathbf{B}\mathbf{K})]\mathbf{z}\end{aligned} \tag{2.20}$$

Comparing both sides of Equation (2.20) and noting that this equation must hold true for any **z**, it is required that

$$(\mathbf{A} - \mathbf{B}\mathbf{K})^{\mathrm{T}}\mathbf{P} + \mathbf{P}(\mathbf{A} - \mathbf{B}\mathbf{K}) = -(\mathbf{Q} + \mathbf{K}^{\mathrm{T}}\mathbf{R}\mathbf{K}) \tag{2.21}$$

According to Lyapunov's stability theory, if the system is stable, there exists a positive-definite matrix **P**. Using Equation (2.19), the performance index J can be evaluated as

$$J = \int_0^\infty \mathbf{z}^{\mathrm{T}}(\mathbf{Q} + \mathbf{K}^{\mathrm{T}}\mathbf{B}\mathbf{K})\mathbf{z}\, dt = -\mathbf{z}^{\mathrm{T}}\mathbf{P}\mathbf{z}\Big|_0^\infty$$
$$= -\mathbf{z}^{\mathrm{T}}(\infty)\mathbf{P}\mathbf{z}(\infty) + \mathbf{z}^{\mathrm{T}}(0)\mathbf{P}\mathbf{z}(0) \tag{2.22}$$

Since the system is assumed to be stable, then $\mathbf{z}(\infty) \to \mathbf{0}$. Thus,

$$J = \mathbf{z}^{\mathrm{T}}(0)\mathbf{P}\mathbf{z}(0) \tag{2.23}$$

which means the performance index is obtained in terms of the initial conditions $\mathbf{z}(0)$ and $\mathbf{P}$. The optimization problem becomes one that involves finding $\mathbf{P}$ that minimizes Equation (2.23) for given initial values.

Since $\mathbf{R}$ has been assumed to be a positive-definite symmetric matrix, it can be written as

$$\mathbf{R} = \mathbf{T}^{\mathrm{T}}\mathbf{T} \tag{2.24}$$

where $\mathbf{T}$ is a nonsingular matrix. Then, Equation (2.21) can be written as

$$(\mathbf{A}^{\mathrm{T}} - \mathbf{K}^{\mathrm{T}}\mathbf{B}^{\mathrm{T}})\mathbf{P} + \mathbf{P}(\mathbf{A} - \mathbf{B}\mathbf{K}) + \mathbf{Q} + \mathbf{K}^{\mathrm{T}}\mathbf{T}^{\mathrm{T}}\mathbf{T}\mathbf{K} = \mathbf{0} \tag{2.25}$$

which can be rearranged as

$$\mathbf{A}^{\mathrm{T}}\mathbf{P} + \mathbf{P}\mathbf{A} + [\mathbf{T}\mathbf{K} - (\mathbf{T}^{\mathrm{T}})^{-1}\mathbf{B}^{\mathrm{T}}\mathbf{P}]^{\mathrm{T}}[\mathbf{T}\mathbf{K} - (\mathbf{T}^{\mathrm{T}})^{-1}\mathbf{B}^{\mathrm{T}}\mathbf{P}] - \mathbf{P}\mathbf{B}\mathbf{R}^{-1}\mathbf{B}^{\mathrm{T}}\mathbf{P} + \mathbf{Q} = \mathbf{0} \tag{2.26}$$

The minimization of J with respect to **K** requires the minimization of

$$\mathbf{z}^{\mathrm{T}}[\mathbf{T}\mathbf{K} - (\mathbf{T}^{\mathrm{T}})^{-1}\mathbf{B}^{\mathrm{T}}\mathbf{P}]^{\mathrm{T}}[\mathbf{T}\mathbf{K} - (\mathbf{T}^{\mathrm{T}})^{-1}\mathbf{B}^{\mathrm{T}}\mathbf{P}]\mathbf{z} \tag{2.27}$$

with respect to **K** (Ogata 1997). Since Equation (2.27) is quadratic in terms of **K** and nonnegative, the minimum occurs when it is zero, that is when

$$\mathbf{T}\mathbf{K} = (\mathbf{T}^{\mathrm{T}})^{-1}\mathbf{B}^{\mathrm{T}}\mathbf{P} \tag{2.28}$$

Hence, the optimal LQR gain **K** is obtained as

$$\mathbf{K} = \mathbf{T}^{-1}(\mathbf{T}^{\mathrm{T}})^{-1}\mathbf{B}^{\mathrm{T}}\mathbf{P} = \mathbf{R}^{-1}\mathbf{B}^{\mathrm{T}}\mathbf{P} \tag{2.29}$$

Consequently, the optimal damper force calculated from the minimization of the performance index J is given as

$$\mathbf{f}_{\mathrm{opt}} = -\mathbf{K}\mathbf{z} = -\mathbf{R}^{-1}\mathbf{B}^{\mathrm{T}}\mathbf{P}\mathbf{z} \tag{2.30}$$

where the matrix **P** is obtained by solving Equation (2.21) or the following reduced form of Equation (2.21)

$$\mathbf{A}^{\mathrm{T}}\mathbf{P} + \mathbf{P}\mathbf{A} - \mathbf{P}\mathbf{B}\mathbf{R}^{-1}\mathbf{B}^{\mathrm{T}}\mathbf{P} + \mathbf{Q} = \mathbf{0} \tag{2.31}$$

Equation (2.31) is called the reduced-matrix Riccati equation.

2.4.2.2 Control Law

Since an MR damper is a semi-active device, it cannot always produce the optimal damper force obtained from Equation (2.30). The command current for an MR damper is therefore obtained using the following criteria, which is known as the *clipped optimum control law*:

$$I_c^i = \begin{cases} I_{max} & \text{if } f_{opt}^i \cdot f_m^i > 0 \text{ and } \left|f_{opt}^i\right| - \left|f_m^i\right| > 0 \\ 0 & \text{otherwise} \end{cases} \tag{2.32}$$

where, I_c^i, I_{max}, f_{opt}^i and f_m^i are the command current, maximum current, optimal force and measured force of the i^{th} MR damper in a structure, respectively.

2.4.3 Sliding Mode Control (SMC)

The basic theory of sliding mode control (SMC) is to design the controller to drive the response trajectory along a sliding surface, where the motion on the sliding surface is stable (Yang et al. 1995). This sliding surface defines the rule for switching of the controller gain. When the response trajectory is above the surface, the feedback path

has one gain, and if the trajectory drops below the surface then a different gain. The sliding surface, **s**, is a set of hyper planes consisting of linear combinations of a state vector **z**, which is expressed as

$$\mathbf{s} = \mathbf{S}\mathbf{z} \tag{2.33}$$

where $\mathbf{S} \in \mathfrak{R}^{L\times 2N}$ is a gradient matrix for the sliding surface. There are several different methods to determine $\mathbf{S}$, including the poll placement method, optimal quadratic minimization method and eigenstructure assignment method (Utkin 1992, Edwards and Spurgeon 1998). The optimal quadratic minimization method is used with the procedure for the design of the sliding surface that is described in the following section.

2.4.3.1 Design of Sliding Surface

From Equation (2.12), the equation of the system in state-space form without a ground motion term is given as

$$\dot{\mathbf{z}} = \mathbf{A}\mathbf{z} + \mathbf{B}\mathbf{f} \tag{2.34}$$

In the sliding mode control, Equation (2.34) is converted to a particular canonical form, the so-called *regular form*, in order to get a convenient interpretation of the reduced-order sliding mode dynamics. Equation (2.34) is transformed to a regular form using an orthogonal transformation matrix, $\mathbf{T_r} \in \mathfrak{R}^{2N\times 2N}$, as follows

$$\begin{bmatrix}\dot{\mathbf{z}}_1\\ \dot{\mathbf{z}}_2\end{bmatrix} = \begin{bmatrix}\mathbf{A_{11}} & \mathbf{A_{12}}\\ \mathbf{A_{21}} & \mathbf{A_{22}}\end{bmatrix}\begin{bmatrix}\mathbf{z}_1\\ \mathbf{z}_2\end{bmatrix} + \begin{bmatrix}\mathbf{0}\\ \mathbf{B_2}\end{bmatrix}\mathbf{f} \tag{2.35}$$

where,

$$\mathbf{T_r z} = \begin{bmatrix}\mathbf{z}_1\\ \mathbf{z}_2\end{bmatrix} \qquad \mathbf{T_r A T_r^T} = \begin{bmatrix}\mathbf{A_{11}} & \mathbf{A_{12}}\\ \mathbf{A_{21}} & \mathbf{A_{22}}\end{bmatrix} \qquad \mathbf{T_r B} = \begin{bmatrix}\mathbf{0}\\ \mathbf{B_2}\end{bmatrix} \tag{2.36}$$

In Equation (2.36), $\mathbf{z_1} \in \mathfrak{R}^{2N-L}$ and $\mathbf{z_2} \in \mathfrak{R}^{L}$. $\mathbf{T_r}$ can be any orthogonal matrix that makes $\mathbf{B_2}$ nonsingular. In this study, $\mathbf{T_r}$ is obtained from a unitary matrix after performing the QR decomposition of **B**, and the upper triangular matrix becomes $\mathbf{B_2}$. The sliding surface is now represented I n terms of $\mathbf{z_1}$ and $\mathbf{z_2}$.

$$\mathbf{s} = \mathbf{S_1 z_1} + \mathbf{S_2 z_2} \tag{2.37}$$

where, $\mathbf{S_1} \in \mathfrak{R}^{L\times 2N-L}$ and $\mathbf{S_2} \in \mathfrak{R}^{L\times L}$ have the following relationship with **S**

$$\mathbf{S T_r^T} = [\mathbf{S_1}\ \ \mathbf{S_2}] \tag{2.38}$$

During the sliding motion, the sliding surface will be identically zero

$$\mathbf{S_1 z_1} + \mathbf{S_2 z_2} = \mathbf{0} \tag{2.39}$$

which can be rewritten as

$$\mathbf{z_2} = -\mathbf{S_2^{-1}S_1 z_1} = -\mathbf{M z_1} \tag{2.40}$$

where $\mathbf{M} \in \mathfrak{R}^{L\times 2N-L}$ from Equation (2.40) is equal to

$$\mathbf{M} = \mathbf{S_2^{-1}S_1} \tag{2.41}$$

As can be seen in Equation (2.40) that $\mathbf{z_2}$ is linearly related to $\mathbf{z_1}$, and therefore by using Equations (2.40) and (2.35) the equations of sliding mode are rewritten as

$$\dot{\mathbf{z}}_\mathbf{1} = \mathbf{A_{11}z_1} + \mathbf{A_{12}z_2} \tag{2.42}$$

$$\mathbf{z_2} = -\mathbf{M z_1} \tag{2.43}$$

This is an $(2N\text{-}L)^{\text{th}}$ order system where $\mathbf{z_2}$ has the role of a linear full-state feedback control signal. By closing the loop with feedback from Equation (2.43)**,** Equation (2.42) yields the following combined equations

$$\dot{\mathbf{z}}_\mathbf{1} = (\mathbf{A_{11}} - \mathbf{A_{12}M})\mathbf{z_1} \tag{2.44}$$

It should be noted that fixing $\mathbf{M}$ does not uniquely determine $\mathbf{S}$. The matrix $\mathbf{S_2}$ has no direct effect on the dynamics of the sliding motion and acts only as a scaling factor for

the sliding surface (Edwards and Spurgeon 1998). One convenient approach to determine $\mathbf{S_2}$ is letting it be equal to the identity matrix $\mathbf{I} \in \mathfrak{R}^{L\times L}$, from which the sliding surface is determined from Equations (2.38) and (2.41)

$$\mathbf{S} = [\mathbf{M}\ \ \mathbf{I}]\mathbf{T_r} \tag{2.45}$$

M can be determined by using several methods such as the poll placement method, optimal quadratic minimization method and eigenstructure assignment method. In the following section, the quadratic minimization procedure is demonstrated for determining an optimal **M**.

2.4.3.2 Quadratic Minimization

The performance index, which is quadratic in terms of the state vector, is considered as an objective function to be minimized during the sliding mode, where

$$J = \frac{1}{2}\int_{t_s}^{\infty} \mathbf{z}^{\mathrm{T}}\mathbf{Q_s}\mathbf{z}\, dt \tag{2.46}$$

In Equation (2.46), $\mathbf{Q_S}$ is a user-defined matrix and is both symmetric and positive definite. t_s is the time at which the sliding motion commences. The aim is to minimize Equation (2.46) subject to the system Equation (2.34). As the first step, the matrix $\mathbf{Q_s}$ is transformed and partitioned considering the compatibly with $\mathbf{z_1}$ and $\mathbf{z_2}$ by using the transformation matrix $\mathbf{T_r}$:

$$\mathbf{T_r Q_s T_r^T} = \begin{bmatrix} \mathbf{Q_{11}} & \mathbf{Q_{12}} \\ \mathbf{Q_{21}} & \mathbf{Q_{22}} \end{bmatrix} \tag{2.47}$$

where, $\mathbf{Q_{21}} = \mathbf{Q_{12}^T}$. Equation (2.46) can be expressed in terms of $\mathbf{z_1}$ and $\mathbf{z_2}$, along with Equation (2.47)

$$J = \frac{1}{2}\int_{t_s}^{\infty} \mathbf{z_1^T Q_{11} z_1} + 2\mathbf{z_1^T Q_{12} z_2} + \mathbf{z_2^T Q_{22} z_2}\, dt \tag{2.48}$$

In order to get the standard LQR form, the following equations are used to eliminate the $2\mathbf{z_1^T Q_{12} z_2}$ term in Equation (2.48), where

$$\begin{aligned} 2\mathbf{z_1^T Q_{12} z_2} + \mathbf{z_2^T Q_{22} z_2} = -\mathbf{z_1^T Q_{21}^T Q_{22}^{-1} Q_{21} z_1} + \\ (\mathbf{z_2} + \mathbf{Q_{22}^{-1} Q_{21} z_1})^{\mathrm{T}} \mathbf{Q_{22}} (\mathbf{z_2} + \mathbf{Q_{22}^{-1} Q_{21} z_1})^{\mathrm{T}} \end{aligned} \tag{2.49}$$

Substituting Equation (2.49) into Equation (2.48) yields

$$J = \frac{1}{2}\int_{t_s}^{\infty} \mathbf{z_1^T \hat{Q} z_1} + \mathbf{v^T Q_{22} v}\, dt \tag{2.50}$$

where,

$$\mathbf{\hat{Q}} = \mathbf{Q_{11}} - \mathbf{Q_{12} Q_{22}^{-1} Q_{21}} \tag{2.51}$$

$$\mathbf{v} = \mathbf{z_2} + \mathbf{Q_{22}^{-1}Q_{21}z_1} \tag{2.52}$$

Solving for $\mathbf{z_2}$ in Equations (2.52) and then substituting the result into Equation (2.42) yields the following modified constraint equations:

$$\dot{\mathbf{z}}_\mathbf{1} = \widehat{\mathbf{A}}\mathbf{z_1} + \mathbf{A_{12}v} \tag{2.53}$$

where,

$$\widehat{\mathbf{A}} = \mathbf{A_{11}} - \mathbf{A_{12}Q_{22}^{-1}Q_{21}} \tag{2.54}$$

Now the problem becomes one in standard LQR form (i.e., Equation (2.15)) with the objective function of Equation (2.50) that is constrained by Equation (2.53). Proceeding as before in the LQR the optimal **v** minimizing Equation (2.50) is therefore obtained by using Equations (2.30) and (2.31)

$$\mathbf{v} = -\mathbf{Q_{22}^{-1}A_{12}^{T}P_1z_1} \tag{2.55}$$

where, $\mathbf{P_1}$ is given by solving the following algebraic matrix Ricatti equation

$$\widehat{\mathbf{A}}^{\mathrm{T}}\mathbf{P_1} + \mathbf{P_1}\widehat{\mathbf{A}} - \mathbf{P_1A_{12}Q_{22}^{-1}A_{12}^{T}P_1} + \widehat{\mathbf{Q}} = \mathbf{0} \tag{2.56}$$

Substituting Equation (2.55) into Equation (2.52) results in

$$\mathbf{z_2} = -\mathbf{Q_{22}^{-1}}\left(\mathbf{A_{12}^{T}P_1} + \mathbf{Q_{21}}\right)\mathbf{z_1} \tag{2.57}$$

Comparing this with Equation (2.40) yields

$$\mathbf{M} = -\mathbf{Q_{22}^{-1}}\left(\mathbf{A_{12}^{T}P_1} + \mathbf{Q_{21}}\right) \tag{2.58}$$

Finally, **S** for the sliding surface is determined by substituting Equation (2.58) into Equation (2.45).

2.4.3.3 Control Law

Once **S** is determined the semi-active control law for the MR dampers can be established using the Lyapunov stability criterion, where the Lyapunov function is decided by using the sliding surface:

$$V = \frac{1}{2}\mathbf{s}^{\mathrm{T}}\mathbf{s} = \frac{1}{2}\mathbf{z}^{\mathrm{T}}\mathbf{S}^{\mathrm{T}}\mathbf{S}\mathbf{z} \tag{2.59}$$

The time derivative of V is obtained by differentiating Equation (2.59) and using the state form of Equation (2.12), whereby

$$\dot{V} = \mathbf{s}^{\mathrm{T}}\dot{\mathbf{s}} = \mathbf{z}^{\mathrm{T}}\mathbf{S}^{\mathrm{T}}\mathbf{S}\left(\mathbf{A}\mathbf{z} + \mathbf{E}\ddot{x}_g\right) + \mathbf{z}^{\mathrm{T}}\mathbf{S}^{\mathrm{T}}\mathbf{S}\mathbf{B}\mathbf{f} \tag{2.60}$$

Since V is positive-definite, the condition of $\dot{V} \leq 0$ assures the stability of the system. To make $\dot{V}$ as large and negative as possible, the last term containing the control force **f** in Equation (2.60) is used in the control law. Letting $\mathbf{r}^{\mathbf{T}} = \mathbf{z}^{\mathrm{T}}\mathbf{S}^{\mathrm{T}}\mathbf{S}\mathbf{B}$; the control law which minimizes $\dot{V}$ is given as

$$I_c^i = \begin{cases} I_{max} & \text{if } r^i \cdot f_m^i < 0 \\ 0 & \text{otherwise} \end{cases} \tag{2.61}$$

where i is associated with the i^{th} damper, and therefore r^i is the component of i^{th} row in **r** and f_m^i is the measured force in the i^{th} damper.

2.4.4 Decentralized Bang-Bang Control (DBB)

2.4.4.1 Basic Theory

In decentralized bang-bang control (DBB), the Lyapunov function is used to represent the total vibratory energy in the structure (Jenson and Dyke 2000). The total vibratory energy is the sum of the kinetic and potential energy, where

$$V = \frac{1}{2}\mathbf{x}^{\mathrm{T}}\mathbf{K}_{\mathbf{s}}\mathbf{x} + \frac{\mathbf{1}}{\mathbf{2}}\left(\dot{\mathbf{x}} + \mathbf{\Gamma}\dot{x}_g\right)^{\mathrm{T}}\mathbf{M}_{\mathbf{s}}\left(\dot{\mathbf{x}} + \mathbf{\Gamma}\dot{x}_g\right) \tag{2.62}$$

The time derivative of V is given by

$$\dot{V} = \mathbf{x}^{\mathrm{T}}\mathbf{K_s}\dot{\mathbf{x}} + \left(\dot{\mathbf{x}} + \mathbf{\Gamma}\dot{x}_g\right)^{\mathrm{T}}(-\mathbf{C_s}\dot{\mathbf{x}} - \mathbf{K_s}\mathbf{x} + \mathbf{\Lambda f}) \tag{2.63}$$

2.4.4.2 Control Law

Similar to the method used in sliding mode control, the control law is chosen in such a manner that makes the term containing the damper force a minimum for $\dot{V}$, whereby:

$$I_c^i = \begin{cases} I_{max} & \text{if } \left(\dot{\mathbf{x}} + \mathbf{\Gamma}\dot{x}_g\right)^{\mathrm{T}}\Lambda^i f_m^i < 0 \\ 0 & \text{otherwise} \end{cases} \tag{2.64}$$

where, Λ^i is the *i*-th column of the $\mathbf{\Lambda}$ matrix. It should be noted that this method does not require the need to define values for control law parameters.

2.5 Summary

In this chapter, various MR damper models and semi-active control strategies have been reviewed. Accurate MR damper models are essential to take advantage of MR dampers, by enabling numerical simulations of structural systems with dampers to be conducted to assess control law designs and structural performance under earthquake ground motions. Although various kinds of semi-active control algorithms have been developed, most of the research has focused on the effectiveness of the algorithm itself, and not a rigorous comparison with the performance of a passive controller and the

consideration of costs compared to a passive control system. Some research has shown a better performance of a system with semi-active controllers for selected structures and ground motions, while the others showed similar or poor structural performance of systems with semi-active control.

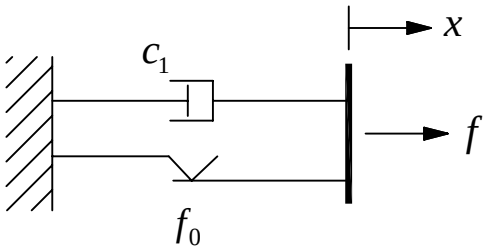

Figure 2.1 Bingham MR damper model

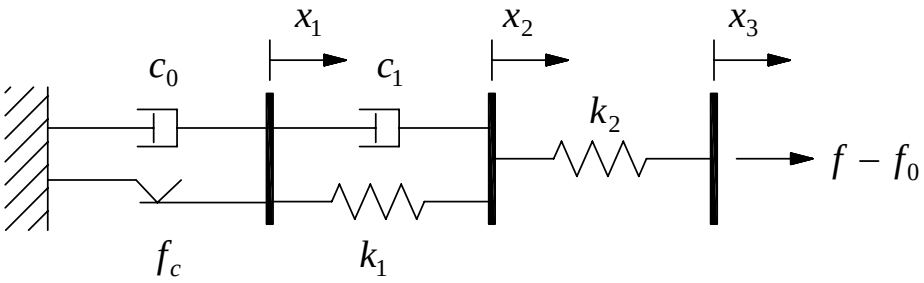

Figure 2.2 Model proposed by Gamota and Filisko (1991)

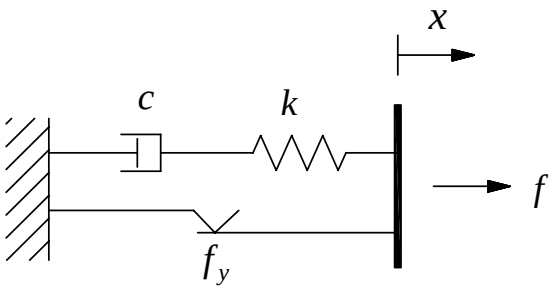

Figure 2.3 BingMax model

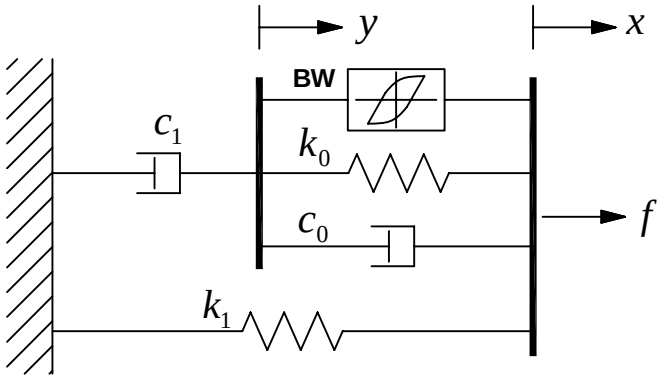

Figure 2.4 Phenomenological Bouc-Wen MR damper model

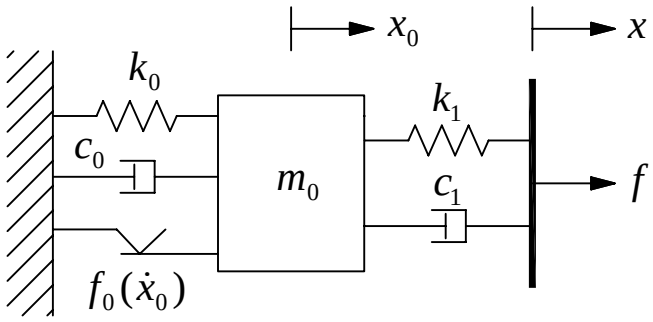

Figure 2.5 Hyperbolic tangent MR damper model

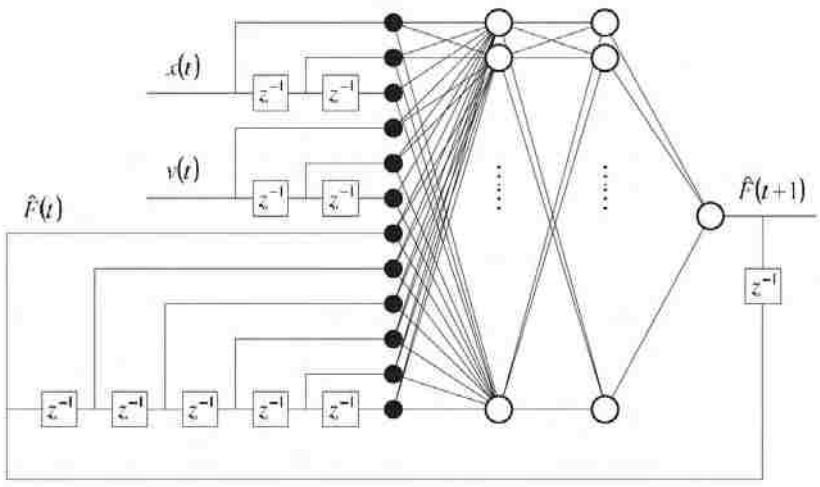

Figure 2.6 Three layer recurrent neural network (RNN) with 18-18-1 neurons (Wang and Liao 2005)

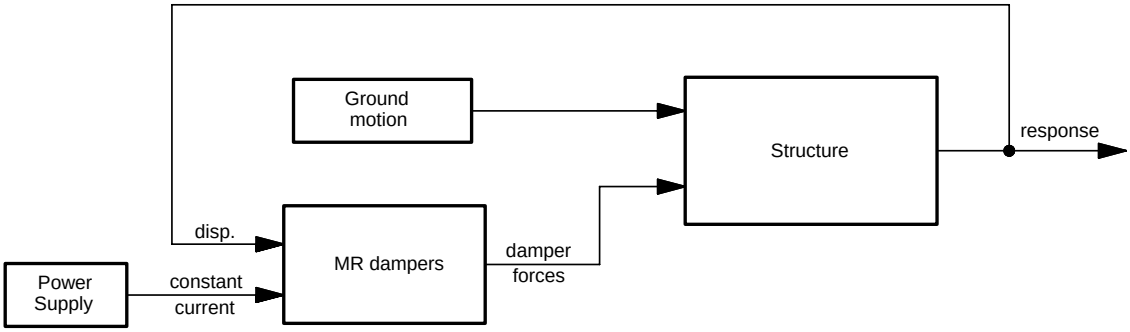

Figure 2.7 Block diagram for a passive controlled system with MR dampers

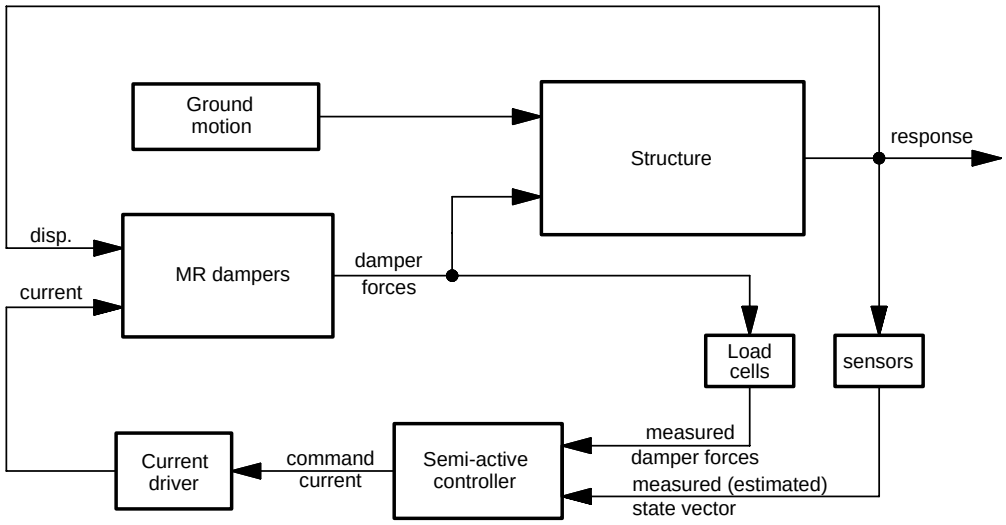

Figure 2.8 Block diagram for a semi-active controlled system with MR dampers

Chapter 3

Modeling of a Large-Scale Magneto-Rheological Damper for Seismic Hazard Mitigation: Passive Mode

3.1 General

The feasibility of using an MR damper as a device for the vibration reduction of a structure has been studied by numerous researchers (Dyke et al. 1996, Jenson and Dyke 2000, Xu et al 2000, Schurter and Roschke 2001, Ribakov and Gluck 2002, Moon et al 2002, Bani-Hani and Sheban 2006, Fan et al 2008). Most of those studies involved the use of small-scale MR dampers, which would not be applicable to full-scale structures. Lord Corporation developed its first generation large-scale MR damper (Carlson and Spencer 1996). Yang (2001) rigorously investigated the dynamic behavior of the damper, where he performed a series of characterization tests for obtaining data to model the MR damper. The maximum velocity in the characterization tests was restricted to 72.6mm/sec due to the limited capacity of the driving actuator. This maximum velocity is not adequate to describe the response of dampers under the design basis earthquake (DBE) or the maximum considered earthquake (MCE) level of ground motions, since the damper can exceed this velocity during these seismic hazard levels, as will be presented in Chapter 7. The MCE ground motion is represented by a ground shaking response spectra that has a 2% probability of exceedance in 50 years, and the DBE ground motion has a severity $2/3^{rd}$ that of MCE ground motion (FEMA 2000a). In 2005, Lord Corporation developed its second generation large-scale MR damper. Bass

and Christenson (2007) performed system identification of this damper using the hyperbolic tangent MR damper model.

The study reported herein describes a new MR damper model called the *Maxwell Nonlinear Slider* (MNS) model. This model is used to model large-scale MR dampers subject to realistic earthquake deformation and velocity demands. The MNS MR damper model can independently describe the pre-yield and post-yield behavior of an MR damper, which makes it easier to identify the parameters for the model. The Hershel-Bulkely visco-plastic element is incorporated into the MNS model for the description of the post-yield mode of the damper, so that the non-Newtonian MR fluid property can be effectively accounted for.

Characterization tests were performed, and the data was used to assign values to the parameters of the MNS model. The response from various experimental data and that predicted using the MNS model are compared and discussed for constant current input (i.e., with the damper in passive mode).

3.2 Experimental Setup for Characterization Test

The characterization tests were performed at the Lehigh NEES equipment site on a large-scale MR damper. The damper was manufactured by Lord Corporation and is their second generation large-scale MR damper. A schematic of the damper is shown in Figure 3.1. The length and available stroke of the damper are 1.5m and ±279mm, respectively. The electromagnetic coil consists of 368 turns of 18 AWG magnet wire with an annular gap of 1.0 mm between the piston head and the inside diameter of the

cylinder. The damper is filled with approximately 19 liters of MRF-132DG type MR fluid manufactured by Lord Corporation.

The experimental setup for the characterization test consists of two primary parts: i) a hydraulic actuator to control the movement of the MR damper; and ii) electrical hardware to supply an appropriate current to the damper for the control of the damper force. Figures 3.2 and 3.3 show the test setup for the characterization tests of the MR damper. The MR damper is connected to the hydraulic actuator through a stiff horizontal steel section. This is done in order to extend the arm of the actuator piston to accommodate the spacing of anchor locations for threaded rods that secure the damper and actuator to the laboratory strong floor. The maximum force capacity of the actuator is 1,700kN; with the actuator having the ability to generate approximately 500kN of force at a piston velocity of 1.0m/sec. A 534kN load cell is installed between the horizontal steel section and the damper piston to directly measure the force developed in the damper.

The current going into the damper is controlled by a pulse width modulation (PWM) type current driver manufactured by Advanced Motion Controls (30A8). Figure 3.4 shows an electrical hardware setup for the control of the current into the MR damper. The PWM servo-amplifier can supply current to the electrical circuit up to 30A by driving the DC motor at a high rate of switching frequency (22kHz). To reduce the noise from the electrical power source, a Schaffner line filter is deployed in front of the DC power supply that provides 72 DC voltage to the PWM servo-amplifier. The command current is transferred to the PWM servo-amplifier through voltage signals

from -10V to +10V to produce the desired current utilizing pulse width modulation. The current going into the MR damper is monitored by a current probe (CR Magnetics current transformer).

To monitor the temperature of the damper, four thermocouples are installed on the surface of the damper cylinder housing along the circumference at mid-length of the damper. Dyke et al (1996) stated that the property of MR fluid is not sensitive to a change of temperature. However, Yang (2001) reported that 15~25% force drop was observed when the damper temperature increased from room temperature to 180ºF, while the damper was subjected to cyclic triangular displacement excitations. Thus, it is important to maintain the damper near ambient temperature in order to minimize the effect of temperature on the damper characterization tests. Each characterization test was performed with an initial temperature of 72ºF to 75ºF.

3.3 Test Matrix for Characterization Test

To identify the frequency and velocity dependent behavior of the MR damper, characterization tests consisting of sinusoidal displacement at the selected amplitudes and frequencies listed in Table 3.1 were performed on the large-scale MR damper. The test matrix in Table 3.1 covers a velocity range from 8 mm/sec to 479mm/sec. These sinusoidal tests were conducted with six different constant current levels, including 0.0, 0.5, 1.0, 1.5, 2.0 and 2.5Amps.

3.4 Characterization Test Results

Figure 3.5 shows a set of sinusoidal test results for various current input with 25.4mm displacement amplitude and 1.0Hz frequency. The results illustrate the response of the damper displacement and damper force subjected to this displacement history for a different current input. Figure 3.6 show the associated force-displacement and the force-velocity relationships of the MR damper. As can be observed in Figures 3.5 and 3.6, the damper force is dependent on the current input; i.e., a larger damper force can be observed with a higher current input. Figures 3.7 and 3.8 show the response of the MR damper under sinusoidal displacement inputs with various frequencies when the current inputs are I=0.0Amp and I=2.5Amp, respectively.

Tests were also performed that included random displacement histories. Five random displacement inputs are considered based on Gaussian white noise with a frequency bandwidth ranging from 2 to 50 Hz, as indicated in Table 3.2. Three different current inputs were considered for each case: 0.0, 1.0 and 2.5Amps. In addition to the MNS model, the parameters for the Bouc-Wen and the hyperbolic tangent models were both identified. These test results will be used to assess and compare the predictions by three MR damper models being considered with experimental response.

In addition, a test was performed using a pre-defined input displacement based on the simulated response of an MR damper model in a structure subject to earthquake ground motion.

3.5 Maxwell Nonlinear Slider (MNS) MR Damper Model

The Bouc-Wen model and the hyperbolic tangent model are among the more commonly-used MR damper models. However, due to the complexity of these models, which includes nonlinear components, the estimation of the model parameters for these damper models is not easy. In particular, the initial guess for the model parameters used in the process to identify the final parameters needs to be done by trial and error. Since the post-yield behavior is dominantly described by the dashpot c_0 (see Figures 2.4 and 2.5) in both the Bouc-Wen model and the hyperbolic tangent model, the post-yield behavior of these two models have the characteristics of a Newtonian fluid where the damper force is proportional to velocity. It is difficult for these models to therefore describe the shear thinning or thickening behavior (see Figure 3.9) that occurs in an MR fluid (Yang 2001), especially in the post yield response at high velocities. Consequently, an inaccurate prediction of damper force at large amplitudes and high velocities can occur in these models.

A schematic of the MNS model is shown in Figure 3.10. The model has two modes: pre-yield and post-yield. In Figure 3.10, x is the degree of freedom of the model that is associated with the displacement of the MR damper piston relative to its initial position, while y and z are variables associated with the pre-yield mode of the model. In this study, x and $\dot{x}$ are referred to as the *damper displacement* and the *damper velocity*, respectively, for simplicity. The variables x and y are related through the velocities $\dot{x}$ and $\dot{y}$ as well as the force f in the damper. The variables y and z are related through equilibrium with the damper force f applied to the model.

One of the advantages of the MNS model is that the pre- and post-yield modes of response can be separated from each other, enabling the model parameters that describe these two modes of behavior to be independently identified. This makes it easier to identify the parameters for the model compared to other existing MR damper models. The following sections provide a detailed explanation of the MNS model and the estimation of its parameters.

3.5.1 Pre-yield Mode

In the pre-yield mode, the behavior of the damper is described by a Maxwell element consisting of a dashpot with coefficient c and stiffness k (see Figure 3.10) where the damper force f is determined by solving the following differential equation

$$f = k(y - z) = c\dot{z} \tag{3.1}$$

When the damper is in pre-yield mode, $\dot{y}$ is equal to the damper velocity $\dot{x}$. The initial value of y is set to be equal to x; thus Equation (3.1) can be solved in terms of z for a given x, enabling the damper force f to be determined. The parameters for the Maxwell element can be easily estimated from the visco-elastic behavior of the MR damper, especially when the damper is subjected to small displacement amplitudes and low velocities. The values of c and k of the Maxwell element are obtained from the force-velocity relationship by selecting two appropriate points on the hysteretic force-velocity curve and then applying visco-elasticity theory. Assuming the Maxwell element is

subjected to a harmonic motion with an amplitude of u_0 and circular excitation frequency of ω, the coefficients c and k are calculated as follows

$$c = \frac{1}{u_0 \omega} \frac{f_0^2 + f_m^2}{f_m}, \qquad k = \frac{1}{u_0} \frac{f_0^2 + f_m^2}{f_0} \tag{3.2}$$

where f_0 and f_m are damper forces when the velocities are zero and a maximum, respectively. The derivation for the relationships for c and k is given in Appendix 1. Figure 3.11 illustrates the steady-state force-velocity relationship of a Maxwell element under a harmonic excitation and the definition of f_0 and f_m. Figure 3.12 shows the comparison of damper forces when the damper is subjected to two different sinusoidal displacement histories with frequencies of f=0.5Hz and f=1.0Hz. The amplitude and the current input are 1.5mm and 2.5A, respectively, for both tests. The parameters for the Maxwell element are calculated as c=11,804 kN-sec/m and k=115,000 kN/m based on Equation (3.2) for the sinusoidal test result with f=1.0Hz, where f_0=50 kN and f_m=80 kN, respectively. As can be observed from Figure 3.12, the MNS model shows good agreement with experimental data for both cases with f=0.5Hz and f=1.0Hz. The values for parameter c and k can be refined using the optimization algorithm discussed later in this chapter.

3.5.2 Post-yield Mode

The post yield behavior of an MR damper is closely related to the velocity $\dot{x}$. A damper model based on Hershel-Bulkley visco-plasticity theory can describe the non-

Newtonian fluid behavior that occurs in the MR fluid, i.e., the shear thinning and shear thickening behavior of the fluid, by using a power law model (Wang and Gordaninejad 2000, Lee and Wereley 2000). Yang (2001) used the Hershel-Bulkley model to describe the quasi-static behavior of MR dampers and found that the Hershel-Bulkley model has good agreement with the experimental behavior of the 20-ton large-scale MR damper. Yang used the Hershel-Bulkley model to only describe the quasi-static behavior of the MR damper. For the dynamic modeling of the MR damper involving the hysteretic response, the Bouc-Wen hysteresis model was used in his study.

In the MNS model, only the nonlinear slider is used to describe the post-yield response of the MR damper, where the post-yield behavior is assumed to be described by a post-yield curve that is a pre-defined trajectory of damper force in the force-velocity plane. Figure 3.13 shows the post-yield curves for the MNS model. The post-yield curve consists of a curve based on the Hershel-Bulkley model and a linear line which is tangential to the curve at the velocity of $\dot{x}_t^+$ or $\dot{x}_t^-$. Mathematical representation of the positive force post-yield curve for the MNS model is given as

$$f_{py}^+(\dot{x}) = \begin{cases} a + b|\dot{x}|^n & \text{if } \dot{x} \geq \dot{x}_t^+ \\ a_t(\dot{x} - \dot{x}_t^+) + f_t^+ & \text{if } \dot{x} < \dot{x}_t^+ \end{cases} \tag{3.3}$$

where a, b, n, and $\dot{x}_t^+$ are parameters to be identified, and $a_t = bn|\dot{x}_t^+|^{n-1}$, $f_t^+ = a + b|\dot{x}_t^+|^n$. The negative force post-yield curve, $f_{py}^-(\dot{x})$, can be defined in a similar manner as $f_{py}^+(\dot{x})$, using the appropriate values for the negative force post-yield curve parameters. Most MR dampers are manufactured with imperfections whereby their

force-velocity hysteretic response does not show a perfect symmetry. Thus, defining the post-yield curves separately for the positive and negative force curves can improve the accuracy of the damper model by fitting the curves to the experimental data.

The experimental post-yield curve in quadrant I and III in Figure 3.13 can be obtained from a constant velocity or sinusoidal test. The parameters a, b, and n in Equation (3.3) can be identified from the experimental data using optimization theory. Due to the simplicity of the Hershel-Bulkley model, the initial guess of the parameters is attainable with minimum effort and this procedure is completely independent of the identification of the value for c and k that describe the pre-yield mode of the MNS model. As noted above, the tangential line is added to define the post yield curve in quadrant II and IV. A small positive value for $\dot{x}_t^+$ and negative value for $\dot{x}_t^-$ can be initially used and then, their values are adjusted using an optimization algorithm so that the model matches the available experimental data.

Identifying the post-yield curves in quadrant II and IV may be quite a challenging task because it is difficult to obtain the experimental post-yield data from the constant velocity test in these quadrants. In this study, the tangential lines in quadrants II and IV are used to make it easy to describe the change of mode from post-yield to pre-yield. In the MNS model, the change of mode from post-yield to pre-yield usually occurs near zero velocity. For example, suppose the damper is in the post-yield mode and the damper force decreases along the path of the positive force post-yield curve. In general, the mode change occurs when the positive velocity approaches zero velocity. If the acceleration is large, however, the damper force tends to keep moving

down along the path of the positive force post-yield curve; hence, the post-yield curve in quadrant II needs to be defined appropriately by the use of the tangential line to replace the post-yield curve in quadrant II. In this case, the mode change occurs at a negative velocity, but not far from zero velocity. A small positive value for $\dot{x}_t^+$ is usually used to minimize the distortion of the Hershel-Bulkley curve in quadrant I, but not too small because the tangential line needs to have an appropriate slope to match the experimental data observed in quadrant II. The same phenomenon exists along the path of the negative force post-yield curve in quadrants III and IV.

The post-yield curve is composed of two phases in the MNS model, namely, a *increasing phase* and *decreasing phase*. If the magnitude of the damper force is increasing during the post-yield mode, the damper is in the increasing phase. On the contrary, the damper is in the decreasing phase if the magnitude of the damper force is decreasing. Since the post yield curve shows a monotonic increase or decrease in damper force with respect to the velocity $\dot{x}$, the damper is in the increasing phase when $\ddot{x} > 0$ in the positive force post-yield mode where $\ddot{x}$ is the damper acceleration, while it is in the decreasing phase when $\ddot{x} < 0$. Experimental data from the characterization tests show the trajectory of damper forces can be slightly different during the increasing and decreasing phase as can be observed in Figure 3.14. The arrows in the figure show the path of cyclic damper force in the force-velocity plot for the case involving a frequency of f=3.0Hz. For the other cases involving other frequencies, a similar trend was found. The solid and dashed arrows represent the paths of the pre-yield mode and post-yield mode, respectively. When the mode changes from the pre-yield to the post-

yield, the slope of the damper force abruptly changes, enabling the mode change to be identified in the experimental data by examining the slope of the damper force in the force-velocity plot. After the mode change occurs, the damper force generally increases with increasing velocity (i.e., increasing phase). When the velocity begins to decrease after passing the maximum velocity, the damper force also decreases (i.e., decreasing phase). The difference between the paths for the increasing and decreasing phases can be distinctly observed in Figure 3.14 (a) where the current is I=1.0A. For the case of I=2.5A, the discrepancy between the force paths in quadrant I is not as significant as that in quadrant III. To account for this force discrepancy, an inertial term is added to the post-yield damper force for the MNS model. When the damper force is on the positive force post-yield curve (i.e., quadrants I or II), the final damper force is determined as

$$f = \begin{cases} f_{py}^{+}(\dot{x}) & \ddot{x} \geq 0; \text{increasing phase} \\ f_{py}^{+}(\dot{x}) + m_0\ddot{x} & \ddot{x} < 0; \text{decreasing phase} \end{cases} \tag{3.4}$$

When the damper force is on the negative force post-yield curve (i.e., quadrants III and IV), the damper force is

$$f = \begin{cases} f_{py}^{-}(\dot{x}) & \ddot{x} < 0; \text{increasing phase} \\ f_{py}^{-}(\dot{x}) + m_0\ddot{x} & \ddot{x} \geq 0; \text{decreasing phase} \end{cases} \tag{3.5}$$

In Equations (3.4) and (3.5) m_0 is a mass to account for the above force discrepancy. The parameter m_0 can be estimated by equating the product of the measured acceleration $\ddot{x}$ and m_0 to the experimental force discrepancy between the increasing and decreasing phases.

3.5.3 Criteria for Mode Changes

When the damper force *f* from the Maxwell element reaches the post-yield curve, the nonlinear slider in the MNS model is activated and the mode changes from the pre-yield to the post-yield state. Mathematically, this condition is expressed as

$$|f| = \left|f_{py}(\dot{x})\right| \tag{3.6}$$

where f_{py} is associated with either the positive or negative force post-yield curve. If *f* reaches $f_{py}^{+}(\dot{x})$ or $f_{py}^{-}(\dot{x})$, then the damper force is determined by Equation (3.4) or Equation (3.5), respectively, in the post-yield mode. Equation (3.6) implies that the generated damper force is always bounded by the positive and negative force post-yield curves in the MNS model. The transition from the post-yield mode to the pre-yield mode occurs when the following velocity equation is satisfied during the post-yield mode:

$$\dot{x} = \dot{y} \tag{3.7}$$

where, $\dot{y}$ is calculated from

$$\dot{y} = \frac{\dot{f}}{k} + \frac{f}{c} \tag{3.8}$$

Equation (3.8) is obtained by rearranging Equation (3.1) to arrive at an expression for y and then taking the time derivative of y. The value for $\dot{y}$ is calculated by substituting the damper force f and the time derivative of the damper force, $\dot{f}$, from the post-yield mode into Equation (3.8). To obtain a smooth transition from the post-yield mode to the pre-yield mode, during the post-yield mode the pre-yield mode variables y and z of the MNS model are continuously updated by solving Equation (3.1) for z and y using the force f developed in the damper during the post-yield mode. The details of the state determination during the pre- and post-yield mode are given in Appendix 2.

3.6 Identification of Model Parameters

3.6.1 Particle Swarm Optimization

The parameters of the damper models are identified in such a manner that the errors between the response prediction by the models and the experimental data is minimized. The particle swarm optimization (PSO) algorithm was used to identify the parameters. The PSO concept is motivated from the social behavior of a swarm of animals such as a flock of birds or school of fish (Kennedy and Eberhart 1995). In the PSO algorithm, a particle is defined as a set of the model parameters to be identified (see Tables 3.3 through 3.5). The initial position (i.e., the initial parameters of the model)

of the particles is assigned in a random manner. Each parameter of the particle is assigned a random number from a uniform distribution over the possible range of the parameter. Thus, the range of the parameter needs to be established. In the MNS model, the range of parameters is determined based on the initial guess of the model parameters described in Section 3.5.1 and 3.5.2. Each particle in the PSO roams on a hyper-plane of variables to be identified according to a specific velocity rule to find the best solution for the values of the model parameters. During the simulation, a particle adjusts its position based on its own experience and the experiences of its neighbors, and the best previous position experienced by itself and its neighbors. This method is considered the "less sensitive to local minimization problems" and is known to be more accurate than other traditional optimization methods (Ye and Wang 2007).

In the PSO algorithm, the position of a particle is defined by the following equations:

$$pv_i(j+1) = w(j)pv_i(j) + g_1 r_1(j)[pbest_i(j) - px_i(j)] + g_2 r_2(j)[gbest(j) - px_i(j)] \quad (3.9)$$

$$px_i(j+1) = pv_i(j+1) + px_i(j) \quad (3.10)$$

where, px_i and pv_i are the position and velocity of the i^{th} particle, respectively, and j is the iteration index. g_1 and g_2 are learning factors, which are defined as $g_1 = g_2 = 2$ in this study. r_1 and r_2 are random numbers that are uniformly distributed between zero and one. $pbest_i$ is the position of the i^{th} particle that has the best solution in the history

of i^{th} particle. $gbest$ is the best solution among all the particles and all iterations, and referred to as the global best solution. w is an inertia weight, which is defined as the following linear decreasing function:

$$w(j) = w_{max} - (w_{max} - w_{min})\frac{j}{j_{max}} \tag{3.11}$$

where w_{max} and w_{min} are the final weight and the initial weight, respectively, and j_{max} is the maximum iteration number selected for the search. In this study, the inertia weight w is set to vary from 0.9 at the beginning of the search to 0.4 at the end of the search (i.e., $w_{max} = 0.9$ and $w_{min} = 0.4$). The entire solution procedure for the PSO is summarized in Figure 3.15.

An example of the PSO is illustrated in Figure 3.16. The objective function to be minimized is given as: $F(x_1, x_2) = 100(x_2 - x_1^2)^2 + (1 - x_1)^2$, where x_1 and x_2 are real numbers. The analytical solution for this example is $x_1 = x_2 = 1$. As can be shown in Figure 3.16, 30 particles in the swarm are initially distributed randomly on a plane consisting of the variable x_1 and x_2. As the iteration continues, the particles move toward the optimal solution, and finally, most of the particles are located near the optimal solution after 100 iterations. The solution using the PSO is $x_1 = x_2 = 1.00$, which is the same as the analytical solution.

3.6.2 Parameter Identification of MR Damper Model

In this study, the normalized root mean square (RMS) error, E^{RMS}, is used as the objective function F to be minimized for the optimization of the model parameters.

$$E^{RMS} = \frac{\sqrt{\sum_i^N \left(f_i^e - f_i^p\right)^2}}{\sqrt{\sum_i^N (f_i^e)^2}} \tag{3.12}$$

In Equation (3.12), f_i^e, f_i^p and N are the experimental damper force, the predicted damper force by the damper model, and the number of data samples considered, respectively. If $E^{RMS} = 0$, the predicted damper force is exactly the same as the experimental value. The parameters for the model are always dependent on the selected experimental data set. The target experimental data set for the identification of the model parameters needs to be representative of the expected range of response of the damper. The velocity of the damper is considered as one of the important factors that characterizes the damper force, and it is therefore desirable that the selected data set includes a proper range of velocity. Four different sinusoidal characterization tests with excitation frequency of 0.5Hz, 1.0Hz, 2.0Hz and 3.0Hz, and amplitude of 25.4mm per each, were therefore chosen to generate experimental data over a range of velocities for the model identification. The velocities associated with the tests include maximum values up to 479 mm/sec.

Table 3.3 summarizes the identified parameters for the MNS model for various current levels using the PSO algorithm. The number of particles and the maximum iteration number for the PSO algorithm are $N_s = 50$ and $j_{max} = 150$, respectively. As

noted previously, the performance of the MNS model was compared with the Bouc-Wen and hyperbolic tangent models, the parameters for these models are also identified using the PSO algorithm with the same experimental data set, number of particles and iteration numbers as those for the MNS model. The identified parameters for the Bouc-Wen and hyperbolic tangent models are presented in Tables 3.4 and 3.5 for 0.0A and 2.5A current levels. Figure 3.17 illustrates convergence of the PSO algorithm applied to identify the parameters for the three damper models when the damper current I is 2.5A. The normalized RMS errors after 150 iterations are 0.0242 for the MNS model, 0.0375 for the Bouc-Wen model and 0.0274 for the hyperbolic tangent model. These results show the superior performance of the MNS model over the other models. In particular, the difference in the normalized RMS error for the MNS model between the initial and final iteration is much less than that of the hyperbolic tangent and the Bouc-Wen models. This means the initial estimation of parameters for c and k, and a, b, n, $\dot{x}_t$, and m_0 for the MNS model established using Equations (3.2), (3.3), (3.4) and (3.5) are close to their final optimal values.

3.7 Comparison of MR Damper Models under Constant Current

Figure 3.18 compares the post-yield behavior of the MR damper and model prediction. The experimental data points shown are from five sinusoidal tests with the different frequencies of 0.2Hz, 0.5Hz, 1Hz, 2Hz and 3Hz. The amplitude of the sine wave is 25.4 mm. The data points identified in Figure 3.18 represent the measured damper force corresponding to the maximum velocity in each sinusoidal test when the

acceleration is zero (see Figures 3.7 (b) and 3.8 (b)). The curve showing the prediction by each model describes the quasi-static behavior of the MR damper, which is a trace of damper force under constant velocity. It is noticeable that the experimental data for I=0.0A shown in Figure 3.18 (a) has a shear thickening behavior, while the one for I=2.5A in Figure 3.18 (b) shows a shear thinning behavior. As can be seen, the MNS model shows better agreement with the experimental data due to the ability of the model to account for the properties of a Non-Newtonian fluid with shear thinning or shear thickening behavior. The damper force-velocity curves for the hyperbolic tangent and the Bouc-Wen models have an almost linear relationship and thereby show a discrepancy with the experimental damper force.

Figures 3.20 ~ 3.22 show the prediction of damper force using the three different MR damper models, where they are compared to experimental data with a damper current input of I=0.0A. The Gaussian white noise-based displacement history with a bandwidth of 2Hz shown in Figure 3.19 was used as the input displacement. The experimental data clearly shows the shear thickening behavior as shown in Figure 3.20 (c). The prediction made by the MNS model (Figure 3.20) shows good agreement with the experimental data. However, damper forces predicted by the Bouc-Wen model (Figure 3.21) and hyperbolic tangent model (Figure 3.22) both show some discrepancy with the experimental data, especially when the velocity is high due to the shear thickening of the MR fluid. The post-yield force-velocity behavior of these two models is almost linear in the force-velocity curves due to the linear dashpot in the models; thus, the predicted maximum damper forces by the Bouc-Wen and hyperbolic tangent models

are less than the experimental data. The superior performance of the MNS model over the two existing models can be observed as well in Tables 3.6 and 3.7, where comparisons of the normalized RMS errors and maximum (minimum) damper forces are provided, respectively.

In Figures 3.24 ~ 3.26, the responses of the MR damper models are compared to the experimental data with the Gaussian white noise displacement input shown in Figure 3.23 and a current input of I=2.5A. The MNS model predicts the damper force accurately, and has the smallest normalized RMS error and maximum (minimum) damper force errors among the models listed in Tables 3.6 and 3.7, respectively.

An assessment of MR damper models subject to demand from earthquake ground motion involved using a pre-defined displacement input, where the displacement history is obtained from a numerical simulation of the 2-story linear elastic shear building structure shown in Figure 3.27. In the simulation, the MR dampers are analytically modeled using the MNS model. The structural properties are as follows: $m_1 = 8.08 \times 10^2\ \mathrm{kN \cdot s^2/m}$, $m_2 = 5.80 \times 10^2\ \mathrm{kN \cdot s^2/m}$, $k_1 = 5.486 \times 10^4\ \mathrm{kN/m}$, and $k_2 = 9.732 \times 10^4\ \mathrm{kN/m}$. The diagonal braces are assumed to be axially rigid and a 5% viscous damping ratio for modes 1 and 2 is used. The 1994 Northridge earthquake record at the Canoga Park station (360 component) is used as the ground motion shown in Figure 3.28. By utilizing the procedure proposed by Somerville et al. (1997), the ground motion is scaled up by a scale factor of 3.33 to simulate the intensity of the DBE, where the variables for the DBE response spectrum are chosen as S_{DS}=1.0g and S_{DI}=0.6g based on the deterministic limit for the maximum

considered earthquake ground motion (ICC 2003). It is assumed that there are eight dampers in the 1st story and one damper in the 2nd story of the structure. The maximum story drifts of the building from time history analysis are 1.22% and 0.85% for the 1st and the 2nd stories, respectively. Figure 3.29 shows the numerically obtained displacement history of the first story MR damper when a constant current of I=2.5A is used. This displacement history is then imposed on the damper in the laboratory test setup by the servo-hydraulic actuator with a current input of I=2.5A to obtain the experimental damper force time history. The displacement input is pre-defined; thus, it should be noted that this test is different from a typical real-time hybrid simulation, where the damper displacement is sequentially determined by numerical integration of the equations of motion during the simulation. To eliminate a possible displacement error from any delayed response of the hydraulic actuator, the measured displacement of the damper in the test setup is used as the input for the MNS, Bouc-Wen and hyperbolic tangent models. Shown in Figure 3.30 is the comparison of damper force from the experiment and that predicted by the MNS model. The shear thinning behavior in the experimental data is shown to be accurately predicted by the MNS model. The prediction by the Bouc-Wen and hyperbolic tangent models are presented in Figures 3.31 and 3.32. Due to the linear relationship in the post-yield behavior of the Bouc-Wen and hyperbolic tangent models, errors in damper forces are more significant than for the MNS model. The MNS model shows a smaller normalized RMS error in Table 3.6, and the maximum (minimum) damper forces of the MNS model in Table 3.7 exhibits less

discrepancy from the experimental results as well. These results demonstrate the superior performance of the MNS model over the existing damper models.

3.8 Summary

A newly developed MR damper model called the Maxwell Nonlinear Slider model has been introduced for the prediction of the dynamic behavior of a large-scale MR damper. In the MNS model the pre-yield and post-yield behavior of the MR damper is independently described. This makes it easy to estimate model parameters from characterization test data. The MNS model utilizes the Hershel-Bulkley model to describe the post-yield behavior, which has the ability to account for the properties of a non-Newtonian fluid, i.e., the shear thinning or shear thickening behavior of the MR fluid. This is a feature of the MNS model that the Bouc-Wen and hyperbolic tangent models do not possess. The Bouc-Wen and hyperbolic tangent models have a linear relationship between velocity and damper force when the damper is in the post-yield mode. The MNS model exhibited good agreement with experimental data for both pre-yield and post-yield behavior and was overall more accurate than the Bouc-Wen and hyperbolic tangent models.

The modeling of the large-scale MR damper under constant current was described in this chapter, which is used to simulate the dynamic behavior of an MR damper in the passive mode. The dynamics of an MR damper associated with variable current input for the semi-active control of an MR damper is discussed in Chapter 4.

Table 3.1 Characterization test matrix: amplitude and frequency combinations for sinusoidal test with DC power supply (the number in the table indicates the maximum velocity in mm/sec)

Freq. (Hz)	Amplitude (mm)		
	2.54	25.4	152.4
0.1	-	16	-
0.2	-	32	-
0.5	8	80	479
1.0	-	160	-
2.0	32	319	-
3.0	-	479	-
5.0	80	-	-

Table 3.2 Input data for random displacement characterization test

Case	Bandwidth (Hz)	Max. disp. (mm)	Max. vel. (mm/sec)	RMS* of disp. (mm)	Duration (sec)
1	2	50.0	441	18.0	20
2	4	30.0	543	11.0	20
3	5	10.1	110	3.2	300
4	25	2.3	120	0.6	300
5	50	1.3	105	0.3	300

* RMS: Root Mean Square

Table 3.3 Identified parameters for MNS damper model

Current I (Amps)	c (kN s/m)	k (kN/m)	Positive force post-yield curve				Negative force post yield curve				m_0 (kNs^2/m)
			a (kN)	b (kN s/m)	n	$\dot{x}_t^+$ (m/s)	a (kN)	b (kN s/m)	n	$\dot{x}_t^-$ (m/s)	
0.0	10,000	100,000	7.5	243.5	1.62	0.010	-7.3	-235.6	1.60	-0.010	0.50
0.5	11,000	100,000	53.1	162.5	0.85	0.010	-53.1	-162.5	0.85	-0.010	0.50
1.0	12,000	118,000	91.5	122.5	0.52	0.010	-96.0	-134.9	0.60	-0.010	1.60
1.5	12,000	118,000	126.7	152.1	0.58	0.010	-126.7	-152.1	0.58	-0.010	1.50
2.0	11,491	110,030	148.5	166.3	0.66	0.003	-146.8	-182.1	0.71	-0.003	1.05
2.5	12,278	112,890	138.5	161.8	0.46	0.017	-133.5	-171.8	0.46	-0.012	1.04

Table 3.4 Identified parameters for Bouc-Wen model

Current I (Amps)	k_0 (kN/m)	k_1 (kN/m)	c_0 (kN·s/m)	c_1 (kN·s/m)	x_0 (m)	α (kN/m)	β (m^{-2})	γ (m^{-2})	n	A
0.0	29.39	1.39	133.3	123370	0.30	0.9	39.97	2184.3	7.22	779.7
2.5	10.36	1.21	209.0	11651	0.12	170.9	5.92	610.7	4.80	650.5

Table 3.5 Identified parameters for hyperbolic tangent model

Current I (Amps)	k_0 (kN/m)	k_1 (kN/m)	c_0 (kN.s/m)	c_1 (kN.s/m)	m_0 (kN.s^2/m)	f_0 (kN)	Vref (m/s)
0.0	2.45	226895	125.7	173.3	0.589	2.4	0.00818
2.5	4.58	100404	186.0	563.2	1.682	174.2	0.01387

Table 3.6 Comparison of normalized RMS error of MR damper models

Damper input displacement	Current I (Amps)	Normalized RMS error		
		Bouc-Wen model	Hyperbolic tangent model	MNS model
Gaussian white noise input	0.0	0.1291	0.0992	0.0688
	2.5	0.0420	0.0409	0.0370
Earthquake response input	2.5	0.0473	0.0528	0.0465

Table 3.7 Comparison of minimum and maximum damper force of MR damper models

			Experimental damper force (kN)	Predicted damper force (kN)		
				Bouc-Wen model	Hyperbolic tangent model	MNS model
Gaussian white noise input	I=0.0A	Min	-74.1	-61.2 (-17.5%)*	-59.2 (-20.1%)	-74.2 (0.1%)
		Max	63.4	54.3 (-14.4%)	53.2 (-16.0%)	64.4 (1.5%)
	I=2.5A	Min	-259.1	-271.4 (4.7%)	-267.9 (3.4%)	-258.3 (-0.3%)
		Max	261.0	268.7 (3.0%)	266.2 (2.0%)	254.6 (-2.4%)
Earthquake response input	I=2.5A	Min	-260.0	-269.4 (3.7%)	-265.1 (2.1%)	-257.1 (-1.0%)
		Max	254.0	272.0 (7.1%)	269.3 (6.1%)	256.3 (0.9%)

* Numbers in parenthesis denote the percent difference compared to the experimental force

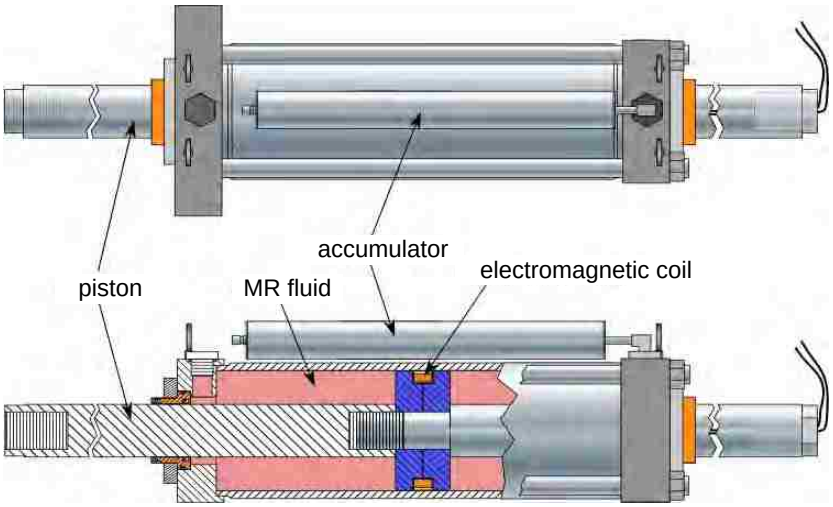

Figure 3.1 Schematic of 2nd generation large-scale MR damper manufactured by Lord Corporation (after Bass and Christenson 2007)

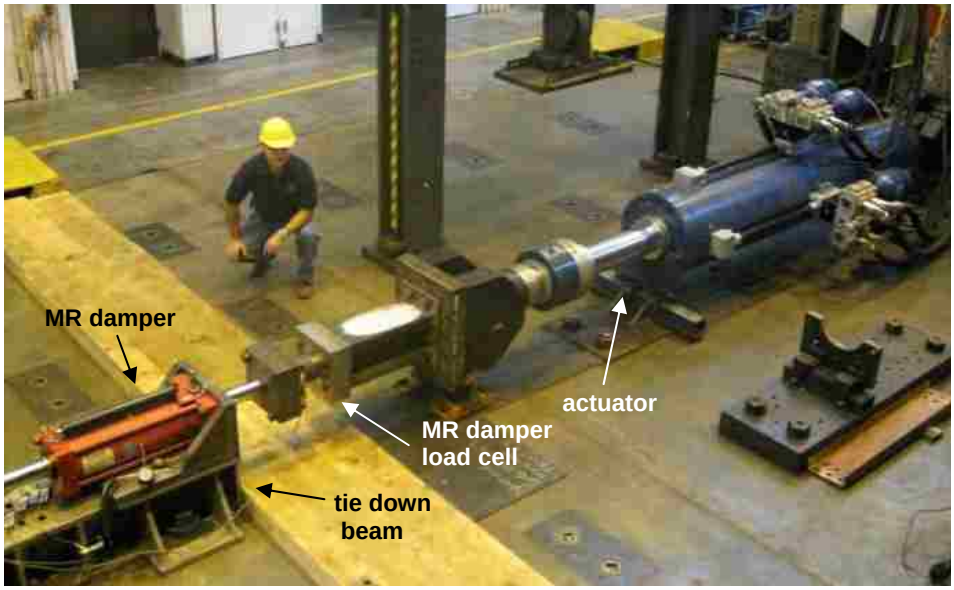

Figure 3.2 Photograph of experimental setup for MR damper characterization tests

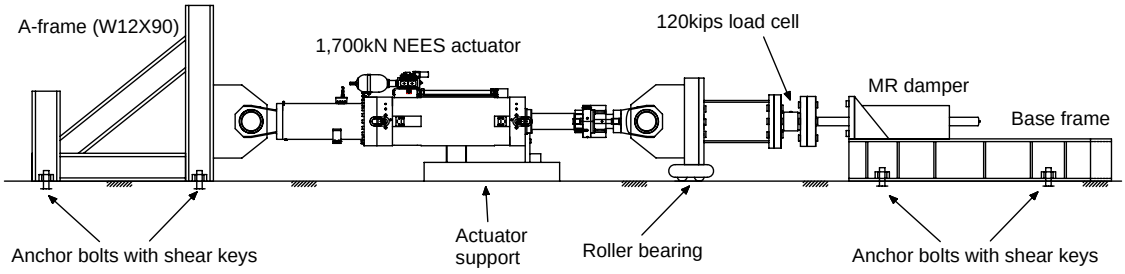

Figure 3.3 Schematic of experimental test setup

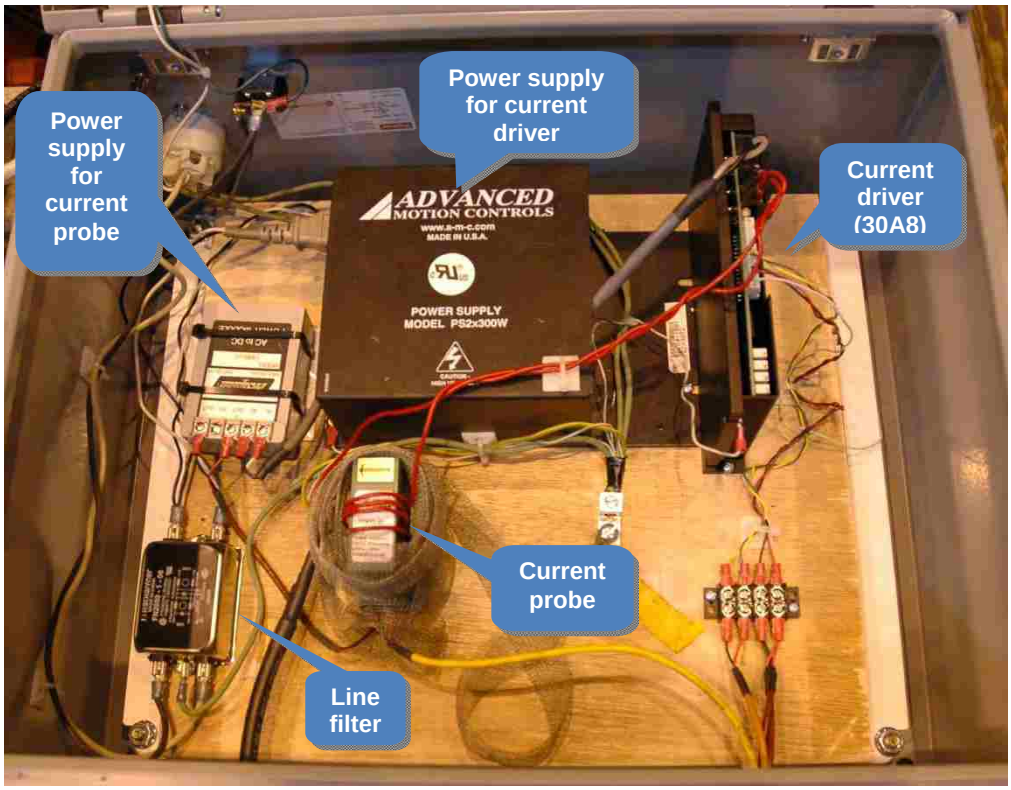

Figure 3.4 Photograph of electrical hardware controlling the current into MR damper

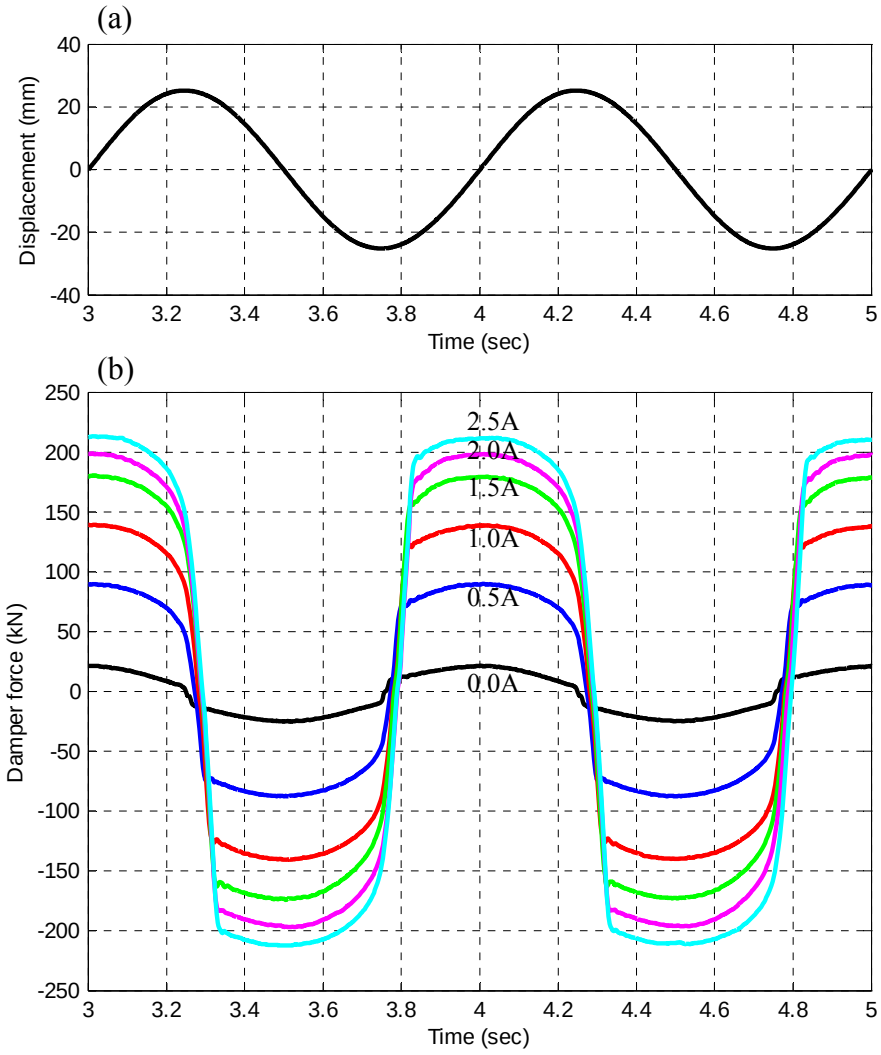

Figure 3.5 Response of MR damper under sinusoidal displacement input with various constant current levels (frequency=1.0Hz, amplitude=25.4mm): (a) time history of input damper displacement; (b) time history of damper force

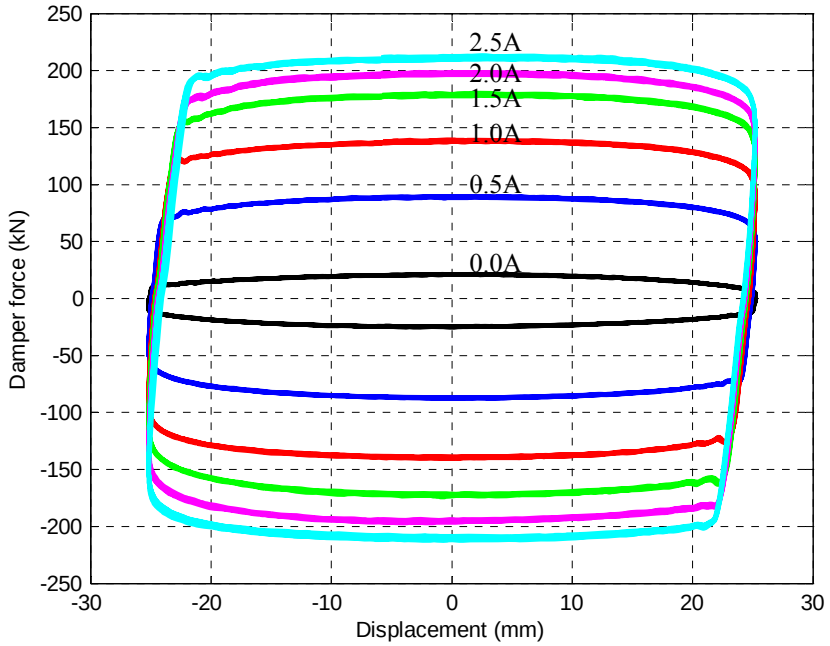

(a)

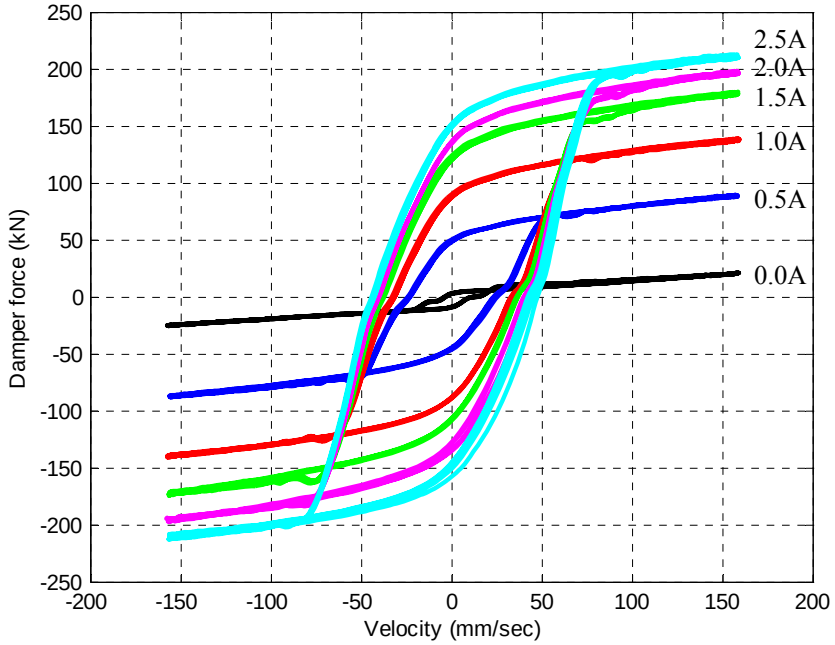

(b)

Figure 3.6 Response of MR damper under sinusoidal displacement input with various constant current levels (frequency=1.0Hz, amplitude=25.4mm): (a) force-displacement relationship; (b) force-velocity relationship

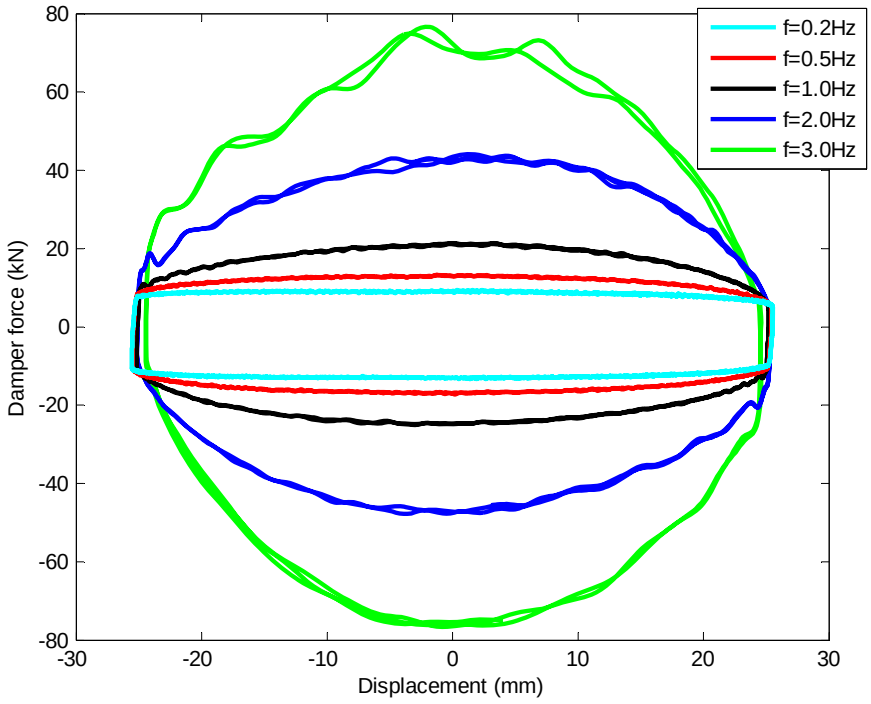

(a)

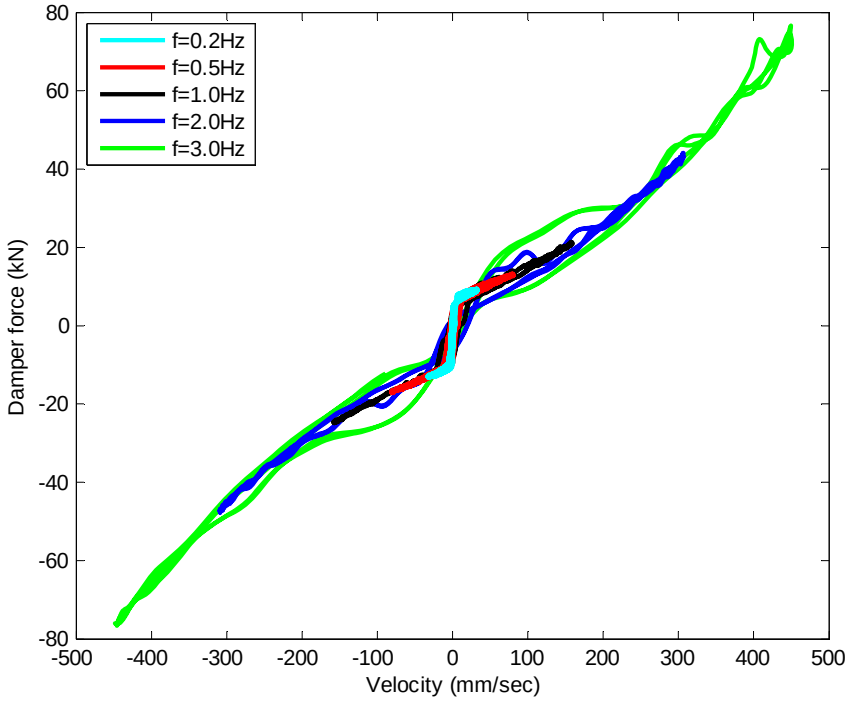

(b)

Figure 3.7 MR damper responses under sinusoidal displacement input with various frequency inputs (amplitude=25.4mm, I=0.0A): (a) force-displacement relationship; (b) force-velocity relationship

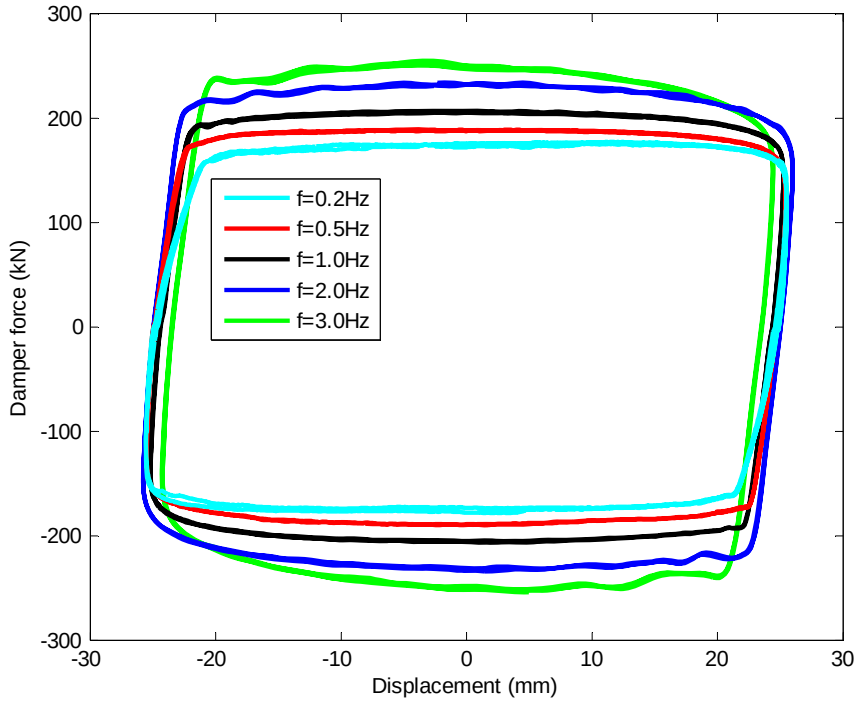

(a)

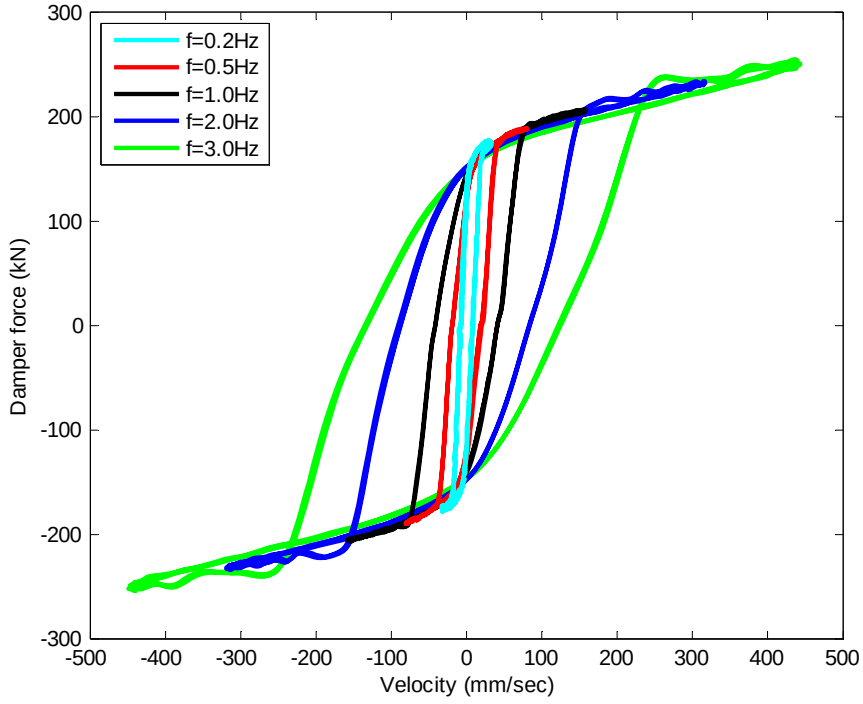

(b)

Figure 3.8 MR damper responses under sinusoidal displacement input with various frequency inputs (amplitude=25.4mm, I=2.5A): (a) force-displacement relationship; (b) force-velocity relationship

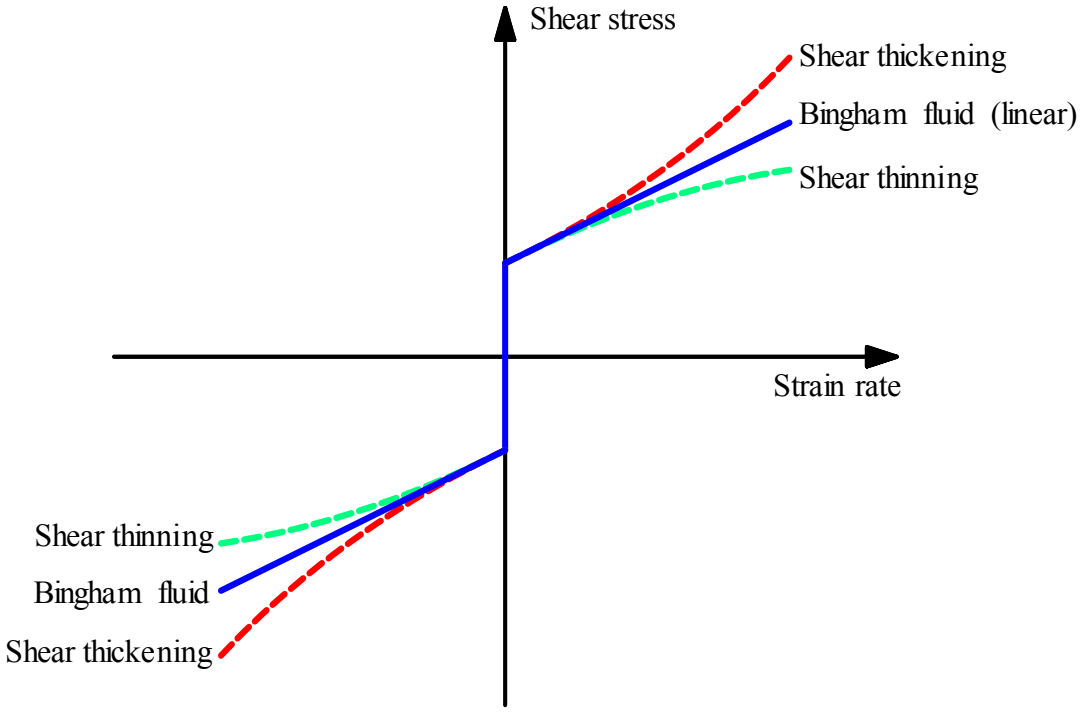

Figure 3.9 Visco-plasticity behavior of MR fluid

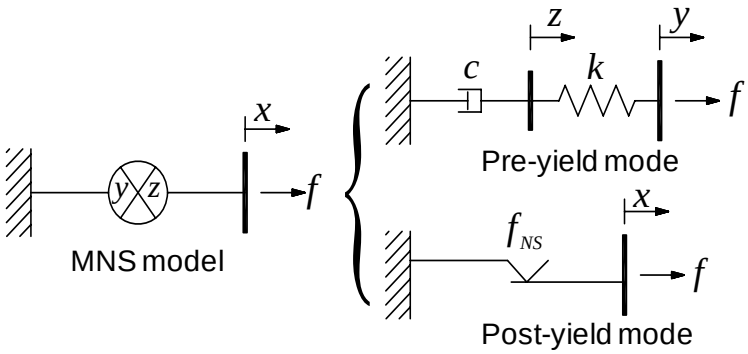

Figure 3.10 Proposed phenomenological MR damper model: Maxwell Nonlinear Slider (MNS) MR damper model

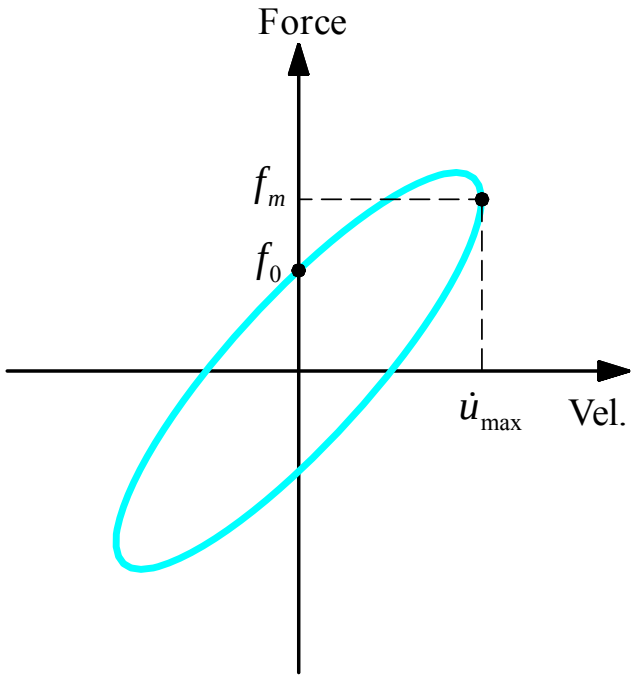

Figure 3.11 Force-velocity relationship of Maxwell element under harmonic motion

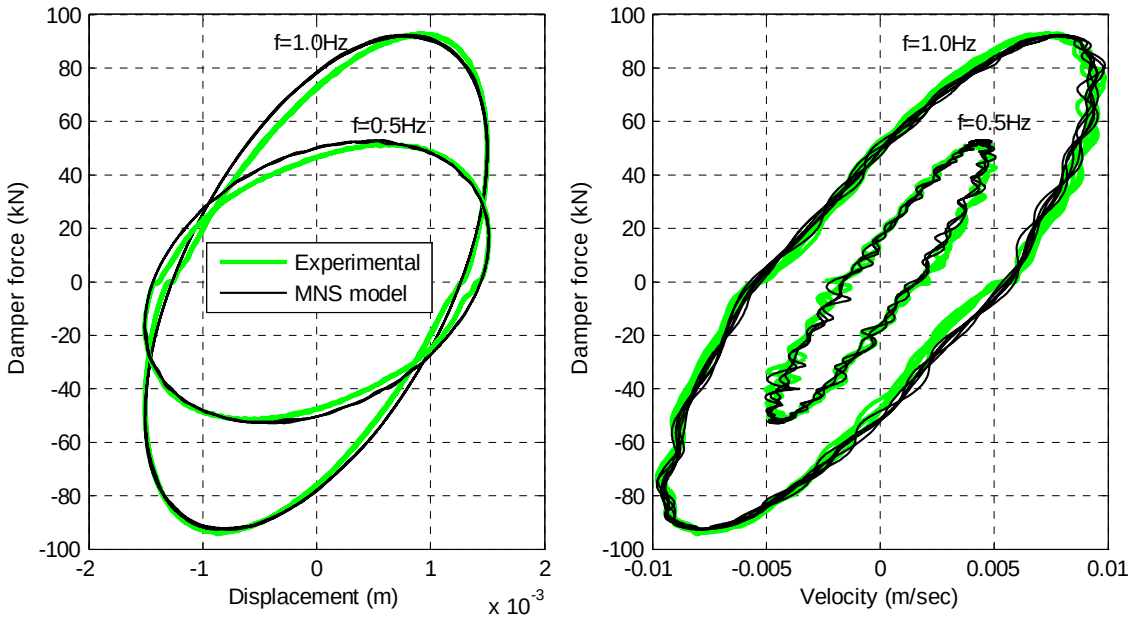

(a) (b)

Figure 3.12 Comparison of pre-yield behavior of MR damper (I=2.5A): (a) force-displacement relationship; (b) force-velocity relationship

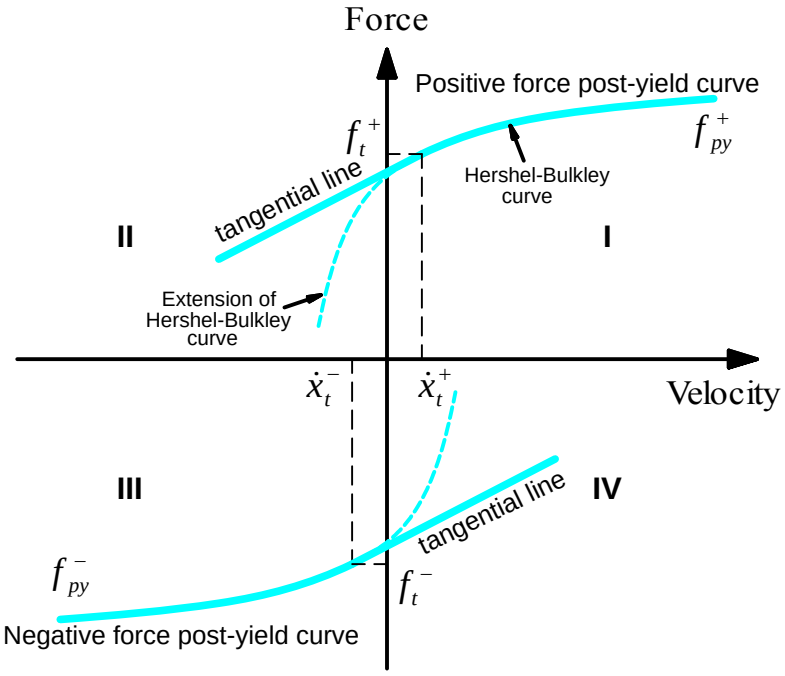

Figure 3.13 Pre-defined post-yield curves of MNS model

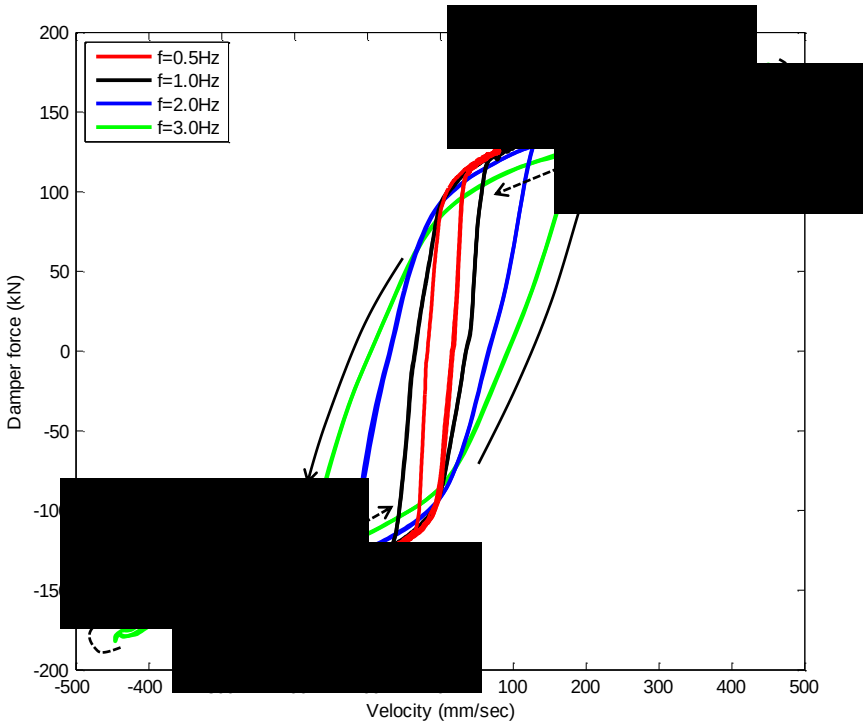

(a)

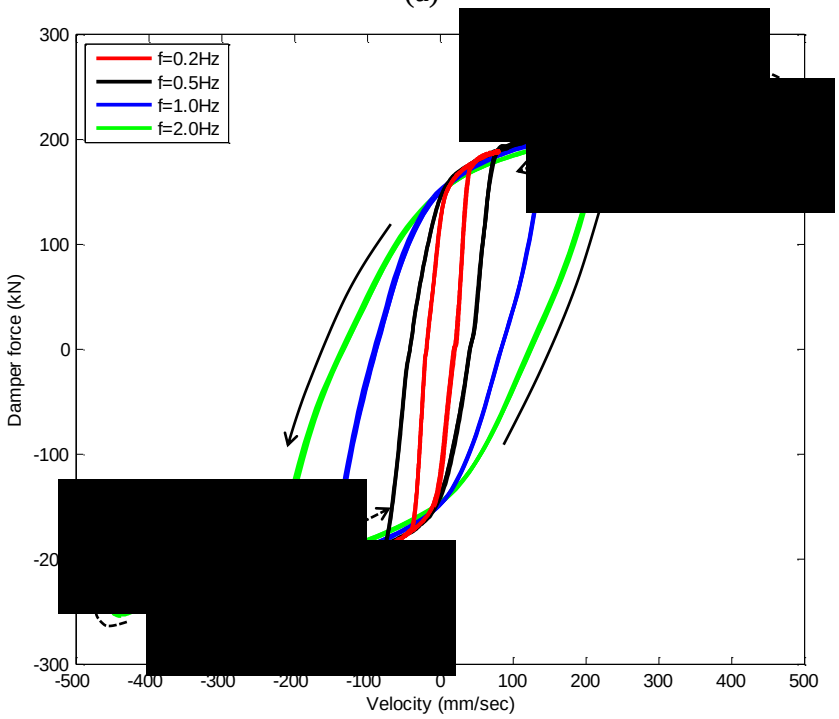

(b)

Figure 3.14 Experimental force-velocity relationship of MR damper under sinusoidal displacement input with various frequencies (amplitude=25.4mm): (a) I=1.0A; (b) I=2.5A

1) Set the iteration index j to zero. Initialize randomly the swarm S_w of N_S particles such that the position $px_i(0)$ and velocity $pv_i(0)$ of each particle meets the prescribed conditions (i.e., the range of parameters). Also, initialize the inertia weight $w(0)$.

2) Evaluate the fitness of each particle $F(px_i(j))$, where F is an objective function to be minimized.

3) Compare the personal best of each particle $pbest_i\ (\ j\ )$ to its current fitness and set $pbest_i\ (\ j\ )$ to the better performance

$$pbest_i(j) = \begin{cases} pbest_i(j-1) & \text{if } F(px_i(j)) \geq F(pbest_i(j-1)) \\ px_i(j) & \text{otherwise} \end{cases}$$

4) Set the global best $gbest(j)$ to the position of the particle with the best fitness within the swarm

$$gbest(\ j\ ) = \min\{F(pbest_1(\ j\ )), F(pbest_2(\ j\ )), \ldots, F(pbest_{N_s}(\ j\ ))\}$$

5) Change the velocity vector for each particle according to Equation (3.9), then the velocity of each particle is updated according to the following relation

$$pv_i\ (j+1)\ = \begin{cases} V_{max} & \text{if } pv_i\ (j+1)\ >\ V_{max} \\ -V_{max} & \text{if } pv_i\ (j+1) < -V_{max} \\ pv_i(j+1) & \text{otherwise} \end{cases}$$

where V_{max} is a constant in order to control excessive roaming of particles.

6) Move each particle to its new position, according to Equation (3.10).

7) Update the inertia weight according to Equation (3.11).

8) Let $j = j + 1$.

9) Go to step 2), and repeat until the stop criteria are met. The stop criteria can be that the maximum iteration number is reached or the minimum value for the objective function has been obtained.

Figure 3.15 Solution procedure for the PSO algorithm

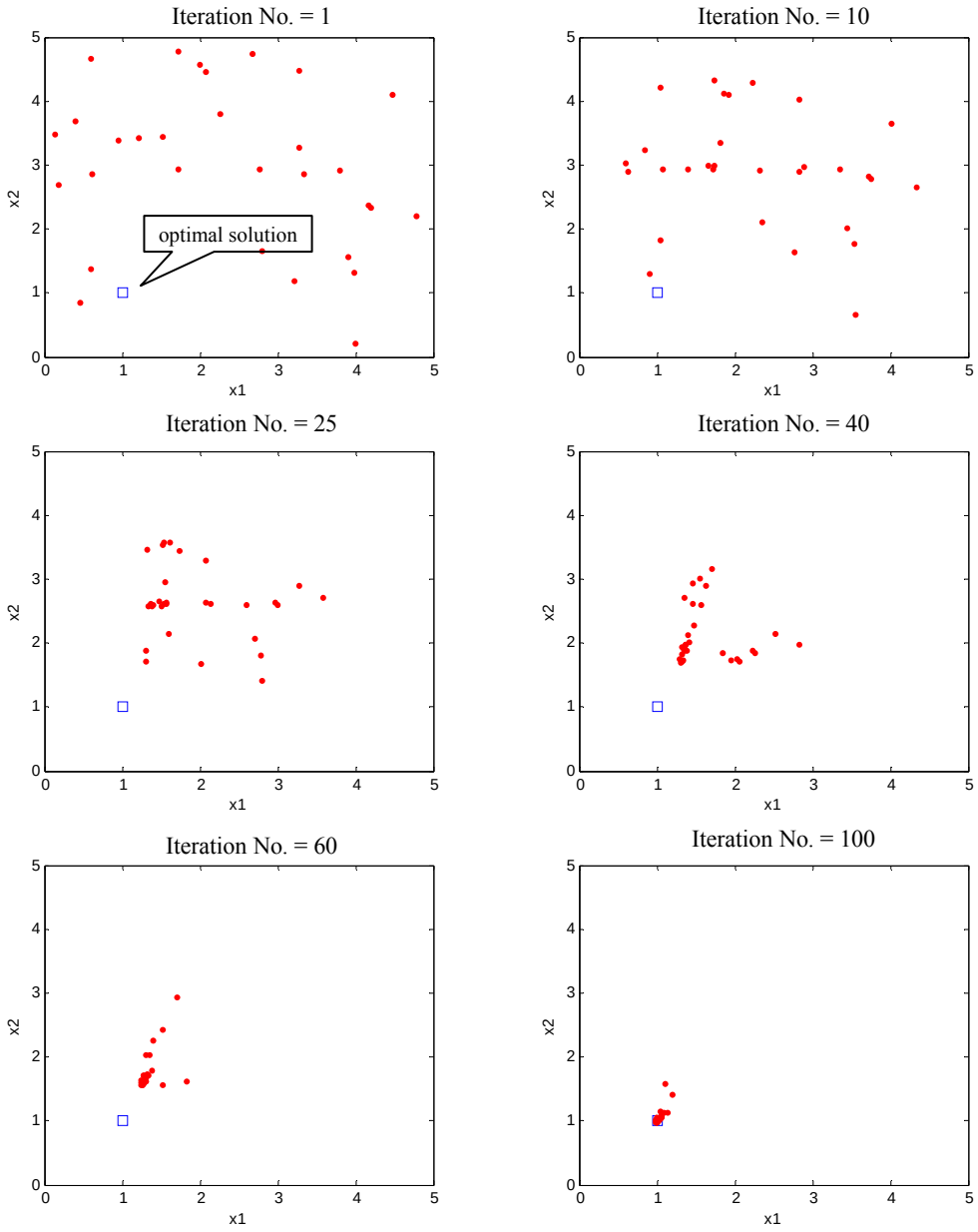

Figure 3.16 Graphical illustration of the PSO algorithm

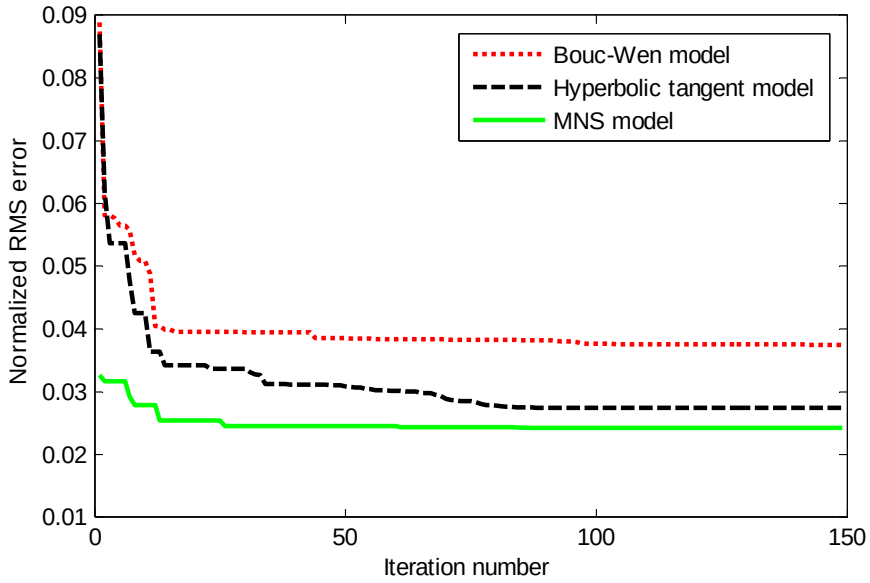

Figure 3.17 Convergence characteristics of normalized RMS error for MR damper models using the PSO algorithm (I=2.5A)

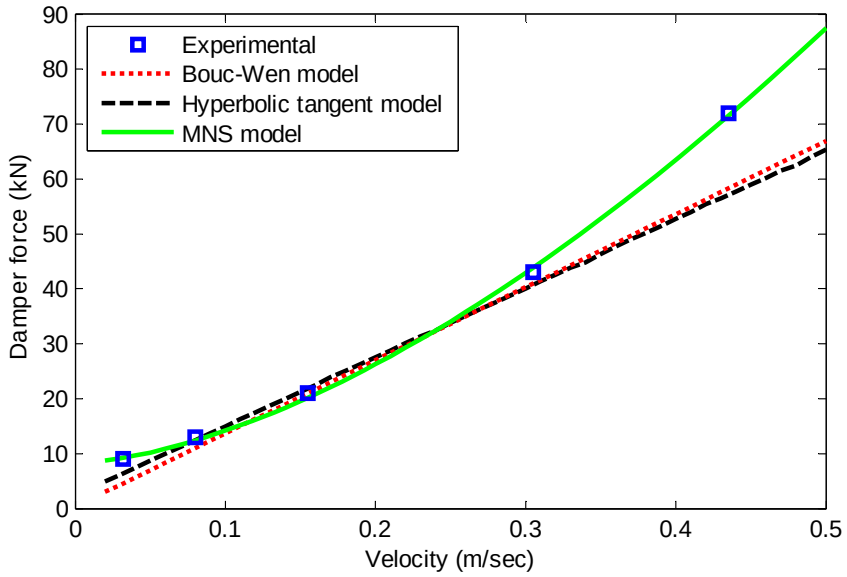

(a)

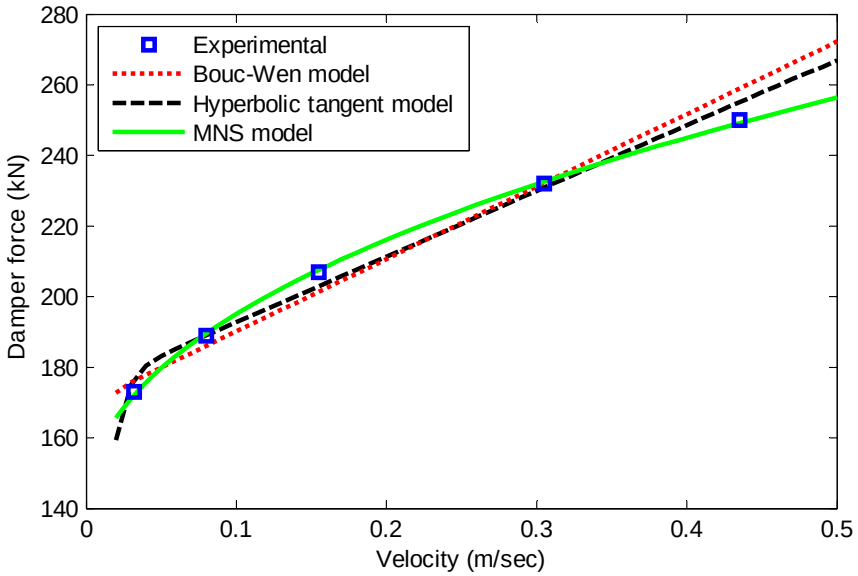

(b)

Figure 3.18. Quasi-static behavior of damper models and comparison with sinusoidal test results: (a) I=0.0A; (b) I=2.5A

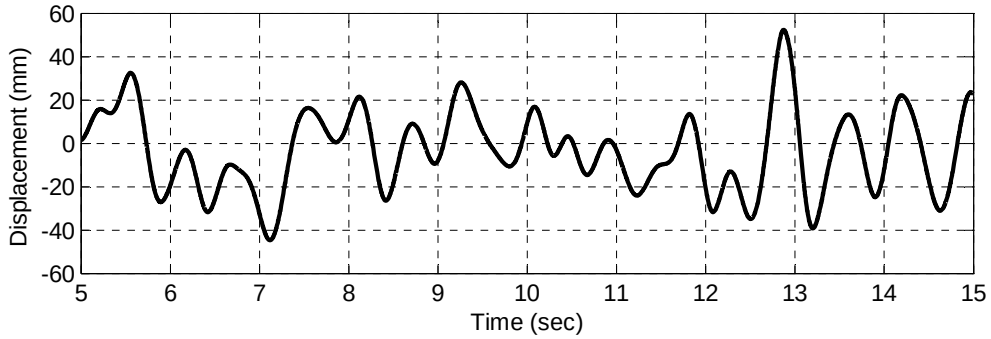

Figure 3.19 Gaussian white noise input displacement with 2.0Hz bandwidth

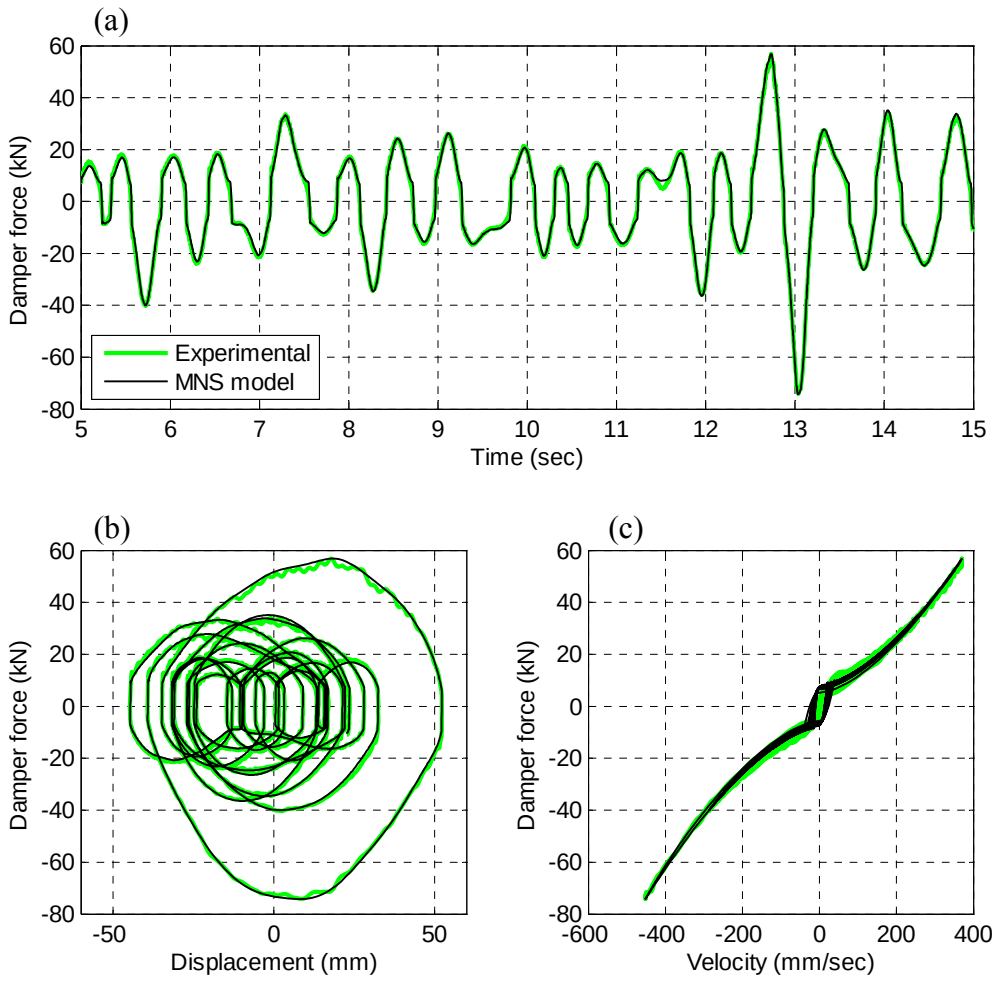

Figure 3.20 Comparison of predicted damper force by MNS model with experimental data under the displacement input of Figure 3.19 (I=0.0A): (a) damper force time history; (b) force-displacement relationship; (c) force-velocity relationship

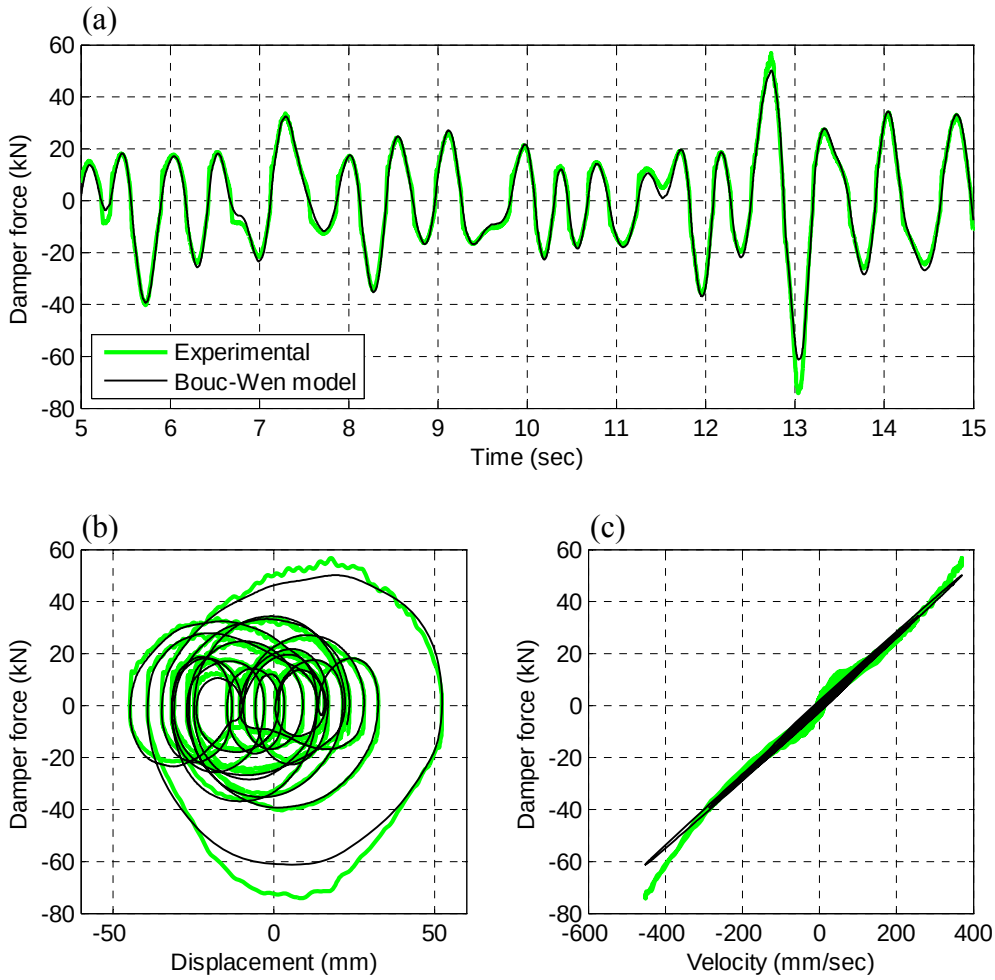

Figure 3.21 Comparison of predicted damper force by Bouc-Wen model with experimental data under the displacement input of Figure 3.19 (I=0.0A): (a) damper force time history; (b) force-displacement relationship; (c) force-velocity relationship

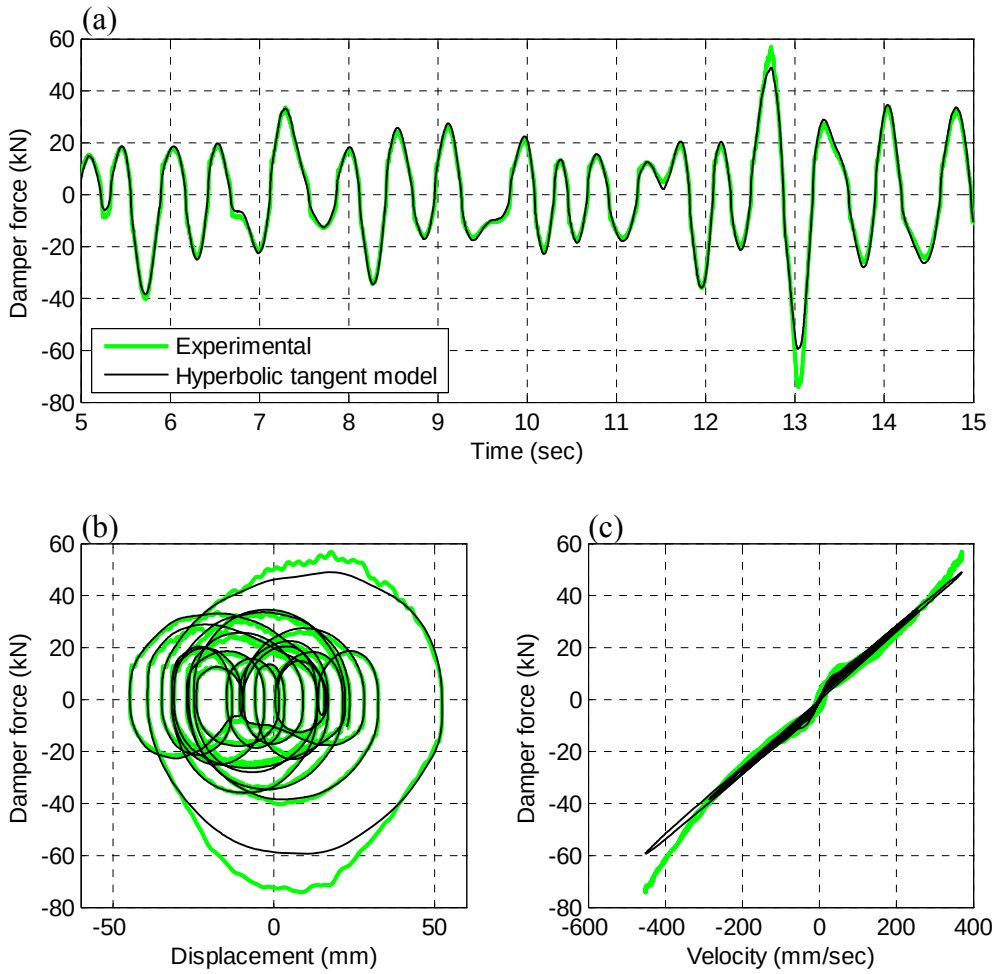

Figure 3.22 Comparison of predicted damper force by hyperbolic tangent model with experimental data under the displacement input of Figure 3.19 (I=0.0A): (a) damper force time history; (b) force-displacement relationship; (c) force-velocity relationship

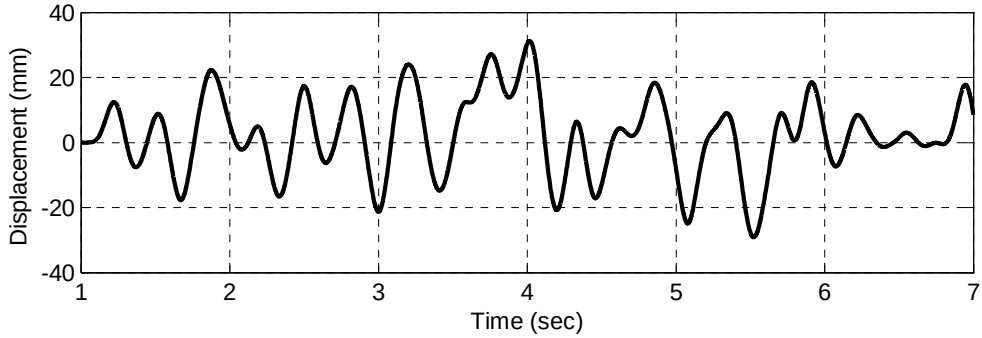

Figure 3.23 Gaussian white noise input displacement with 4.0Hz bandwidth

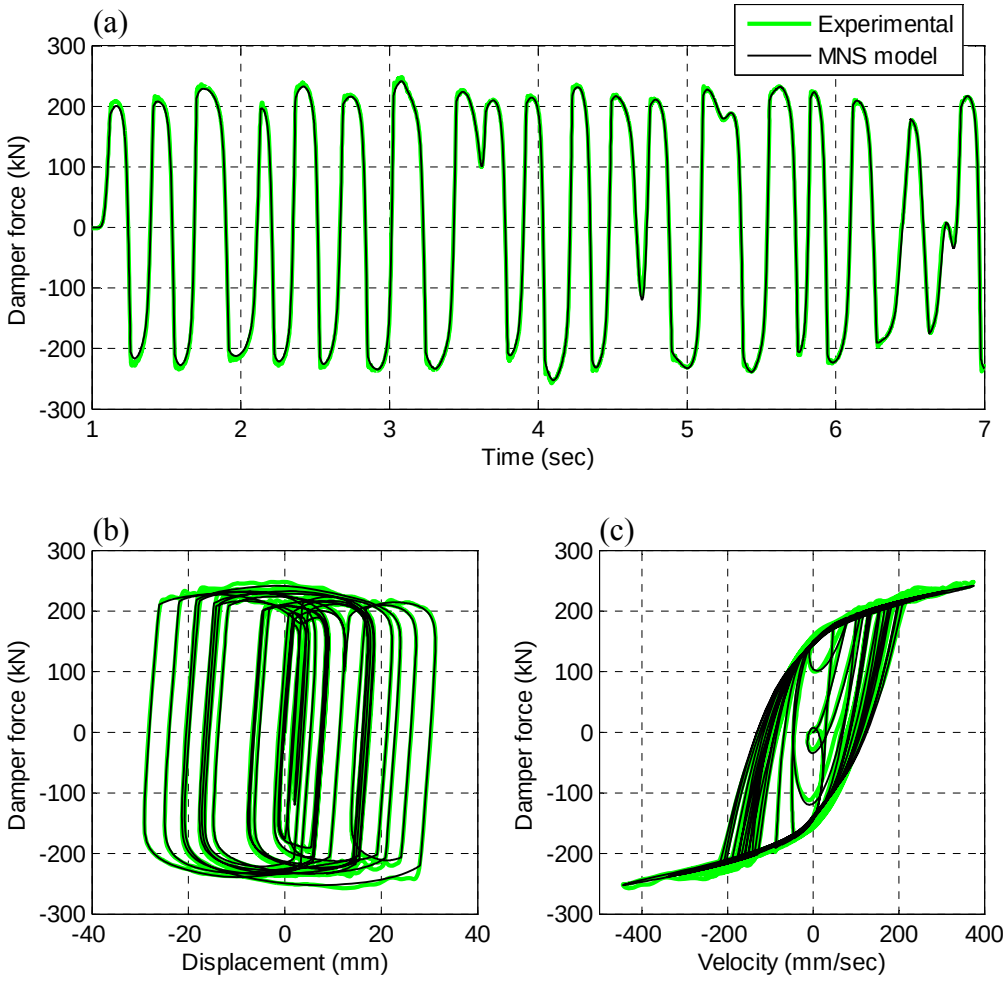

Figure 3.24 Comparison of predicted damper force by MNS model with experimental data under the displacement input of Figure 3.23 (I=2.5A): (a) damper force time history; (b) force-displacement relationship; (c) force-velocity relationship

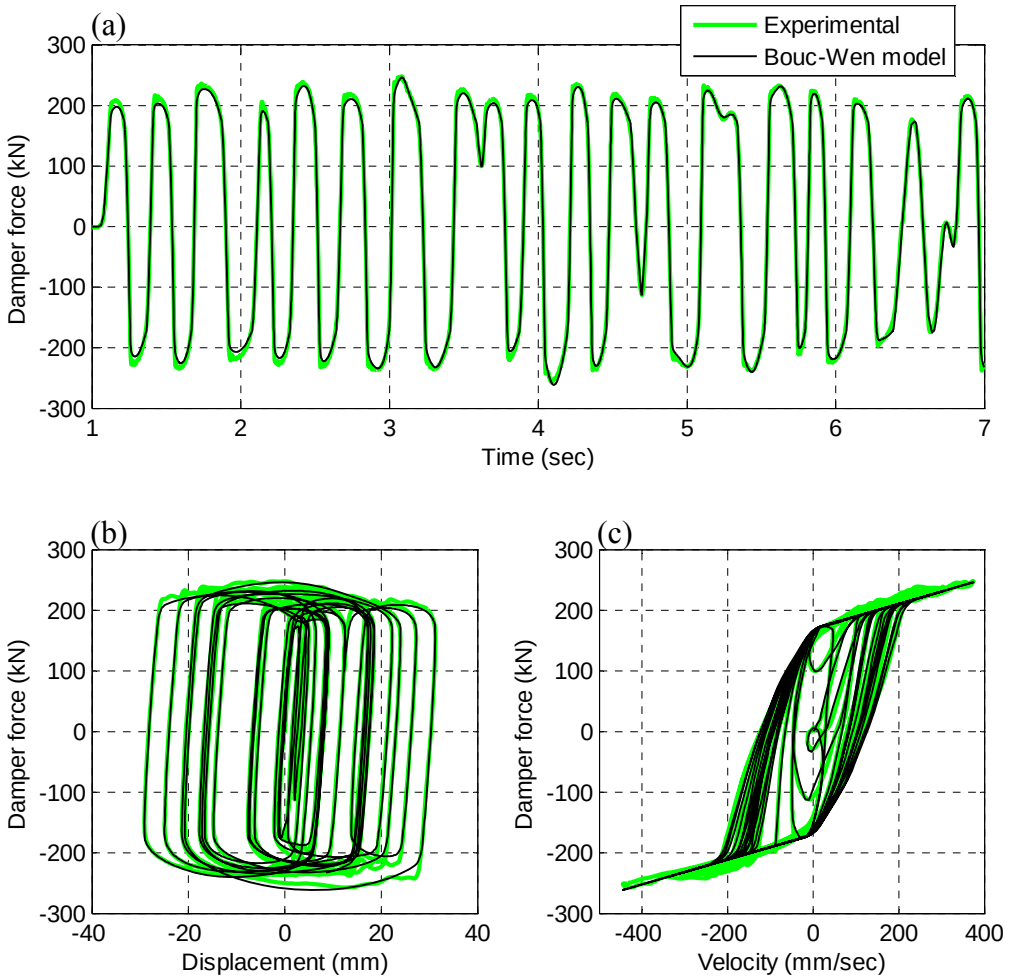

Figure 3.25 Comparison of predicted damper force by Bouc-Wen model with experimental data under the displacement input of Figure 3.23 (I=2.5A): (a) damper force time history; (b) force-displacement relationship; (c) force-velocity relationship

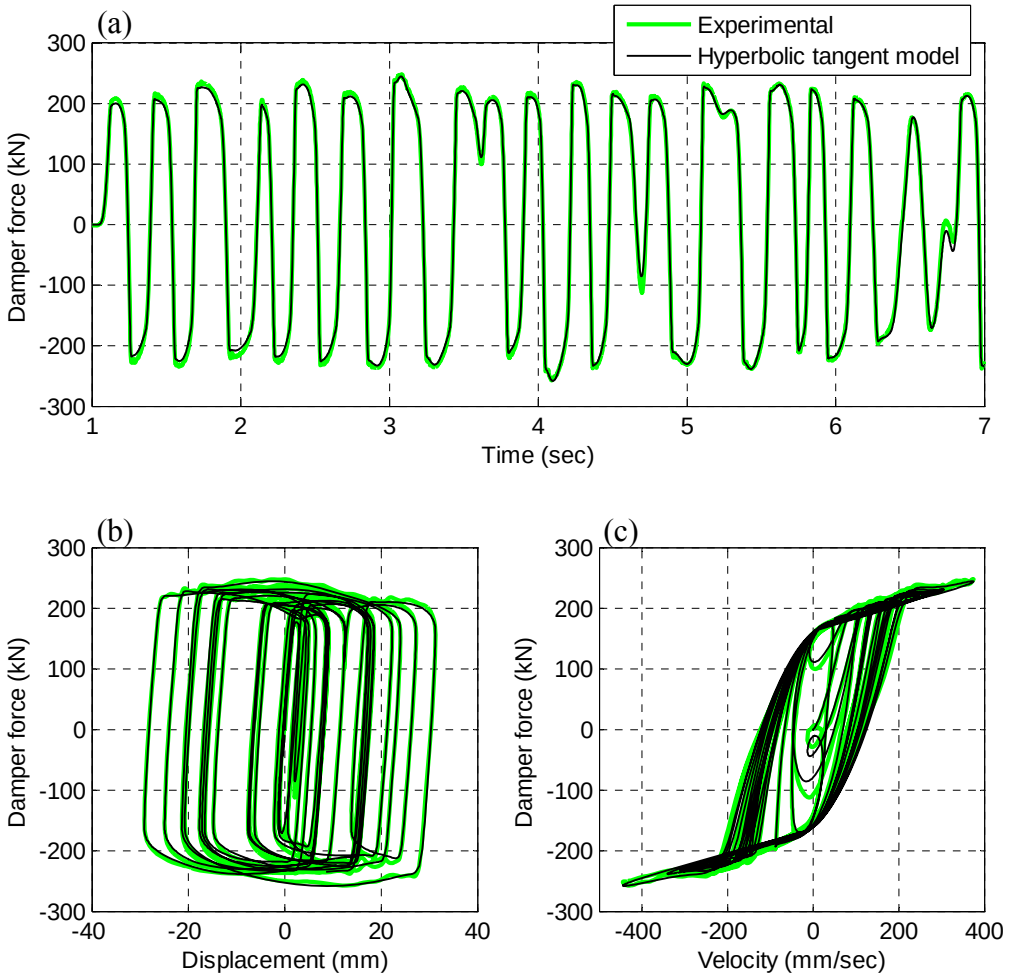

Figure 3.26 Comparison of predicted damper force by hyperbolic tangent model with experimental data under displacement input of Figure 3.23 and I=2.5A (a) damper force time history; (b) force-displacement relationship; (c) force-velocity relationship

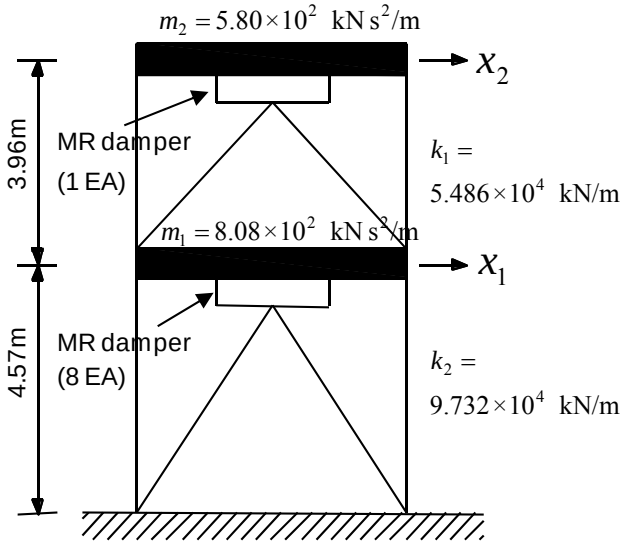

Figure 3.27 Two-story shear building structure with MR dampers

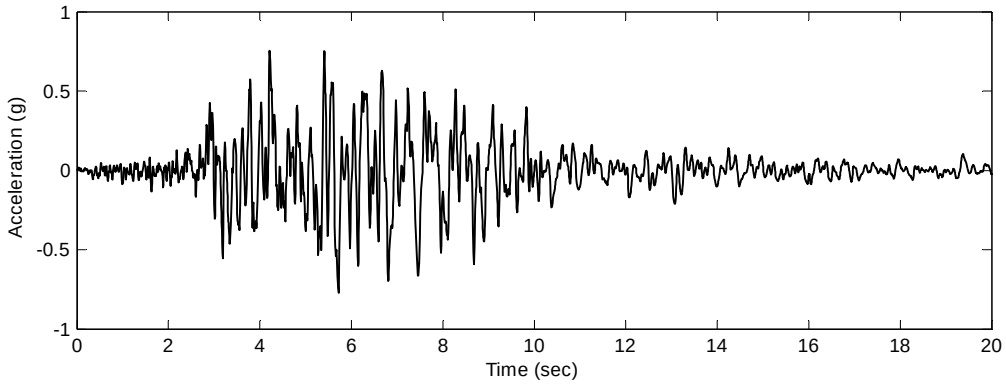

Figure 3.28 Scaled input ground motion (1994 Northridge) with scale factor of 3.33

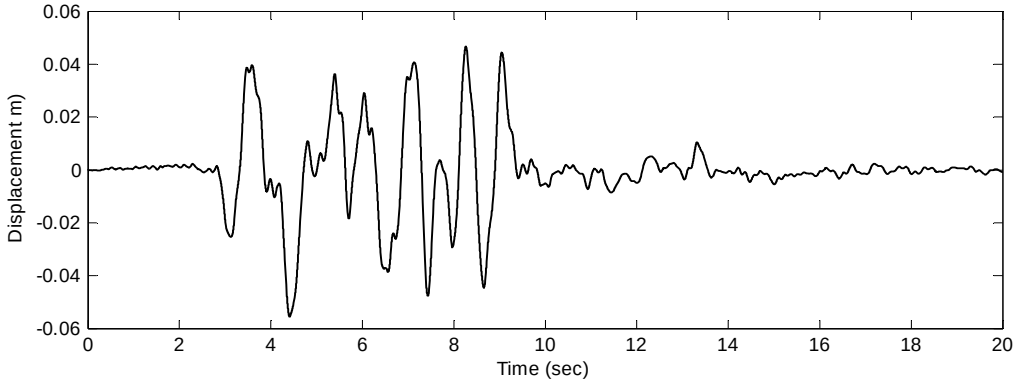

Figure 3.29 Displacement history of MR damper in the 1st story

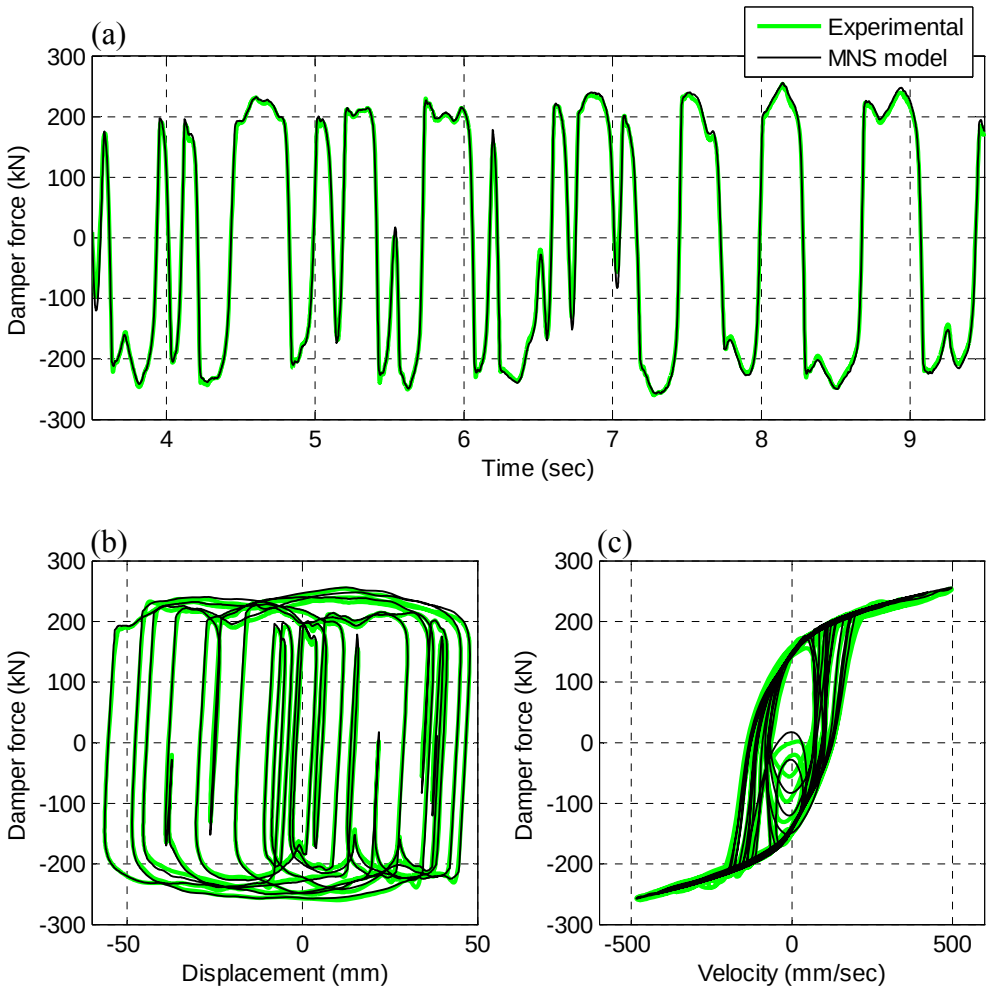

Figure 3.30 Comparison of predicted damper force by MNS model with experimental data under earthquake response input (I=2.5A): (a) damper force time history; (b) force-displacement relationship; (c) force-velocity relationship

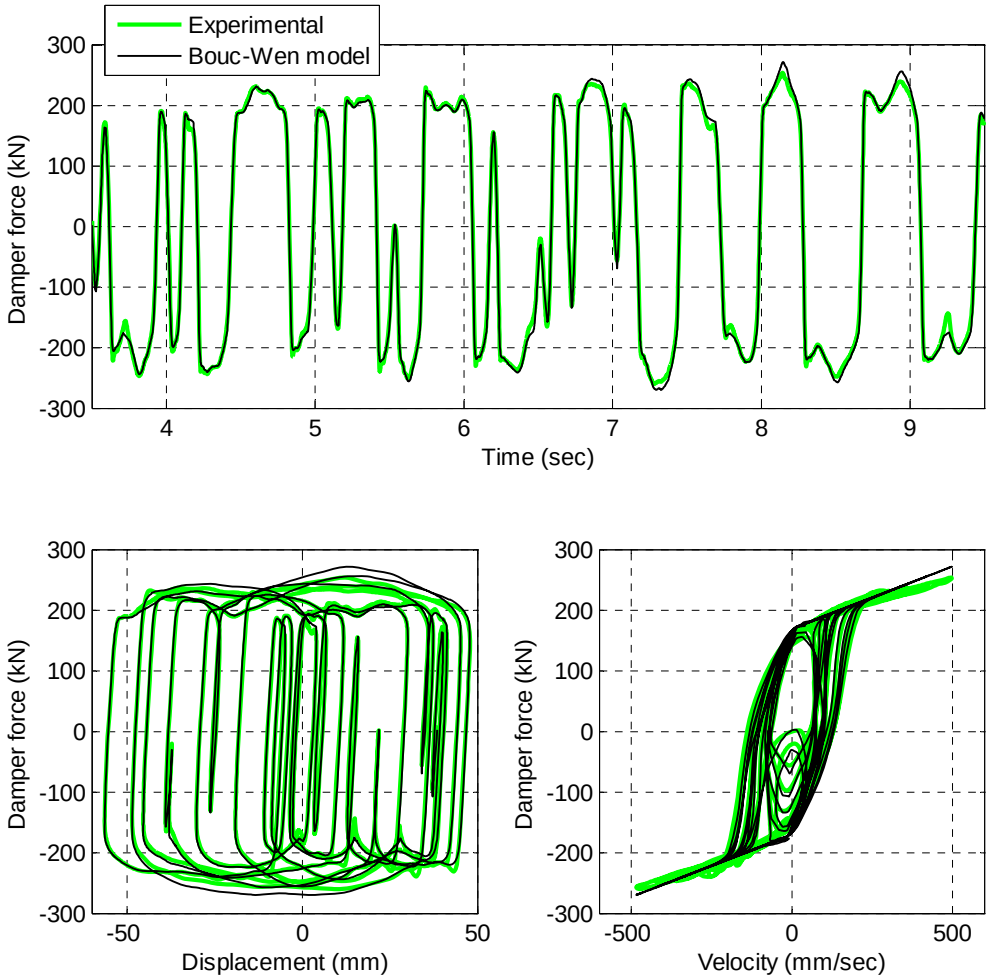

Figure 3.31 Comparison of predicted damper force by Bouc-Wen model with experimental data under earthquake response input (I=2.5A): (a) damper force time history; (b) force-displacement relationship; (c) force-velocity relationship

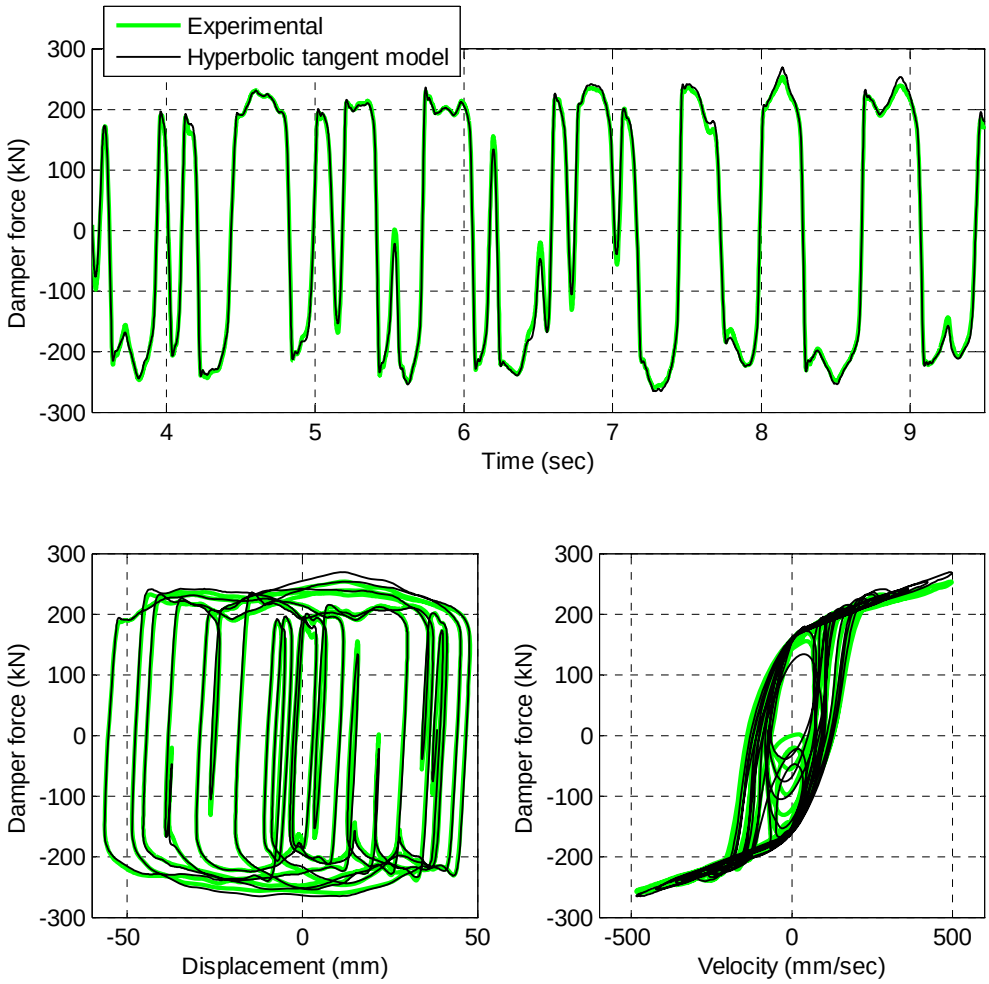

Figure 3.32 Comparison of predicted damper force by hyperbolic tangent model with experimental data under earthquake response input (I=2.5A): (a) damper force time history; (b) force-displacement relationship; (c) force-velocity relationship

Chapter 4

Modeling of a Large-Scale Magneto-Rheological Damper for Seismic Hazard Mitigation: Semi-Active Mode

4.1 General

As noted in Chapter 1, an MR damper contains MR fluid, which has iron carbonate particles suspended in the carrier liquid. The MR damper force depends on the magnetic field around the MR fluid as well as the velocity of the damper. When there is no magnetic field applied to the MR fluid, the iron particles are suspended uniformly in the MR fluid by a strong surface active agent (Shiraishi et al 2004). Under a magnetic field, the iron particles become aligned and form chain-like clusters.

The electromagnetic coil in the MR damper controls the magnetic flux around the MR fluid by changing the current in the coil. To investigate the behavior of an MR damper under variable current, the relationship between the current in the coil and the magnetic flux generated by the coil needs to be studied. In this chapter, electromagnetic theory including the eddy current effect and the magnetization behavior of materials is used to describe the dynamics of an MR damper associated with variable current input. A nonlinear differential equation relating the coil current to the MR damper force is used to describe the damper behavior under variable current. The solution to the differential equation is used to determine an equivalent static current and the associated damper force. The predicted damper force is compared to experimental damper forces from several tests.

4.2 Dynamics of Current Driver

The command current needs to be developed quickly in the electromagnetic coil of the damper to avoid control problems caused by delay in the current in the coil. Due to the inductance of the electromagnetic coil, the current in the coil changes slowly if a voltage driven power supply is used (Yang 2001). To obtain a quick change in the current in the coil, a current driver (see Figure 2.8) based on a pulse width modulation (PWM) servo amplifier is used in this study. The amplifier is manufactured by Advanced Motion Controls (30A8) and is shown in Figure 4.1.

The identification of the current driver is conducted by applying a band-limited Gaussian white noise command to the current driver. Figure 4.2 shows the frequency response of the current driver obtained from these characterization tests, which shows the relationship between the input command current into the current driver and the current developed in the coil by the current driver. Input command currents to the current driver are band-limited white noise (100Hz) with three different levels of root mean square (RMS) command current equal to 0.3A, 0.6A, and 1.2A. The amplitude response of the current driver shows an apparent nonlinear behavior and dependence on the input command current, while the phase angle response does not appear to be sensitive to the amplitude of the input command current.

Yang (2001) proposed a differential equation to describe a current driver based on the duty cycle of a PWM servo-amplifier with a PI controller, where

$$\frac{L}{\tilde{\beta}\tilde{\gamma}}\ddot{I} + \frac{(R_L + \tilde{\beta}\tilde{\eta})}{\tilde{\beta}\tilde{\gamma}}\dot{I} + I = \frac{I_{com}}{\tilde{\beta}} + \frac{\tilde{\eta}}{\tilde{\beta}\tilde{\gamma}}\dot{I}_{com} \tag{4.1}$$

In Equation (4.1) I = current output developed in the coil; I_{com} = command current into the current driver; L = inductance of coil; R_L = resistance of coil; $\tilde{\beta}$ = sensitivity of the current sensing; and $\tilde{\gamma}$, $\tilde{\eta}$ = parameters associated with PI gains for the current driver. Based on Equation (4.1), the following transfer function for the current driver of this study is proposed

$$G(s) = \frac{235s + 44522}{s^2 + 302s + 44522} \tag{4.2}$$

where s is the Laplacian variable. $G(s)$ of Equation (4.2) is called *current driver model* in this study. The current driver model correlates the input command current with the current developed in the coil, i.e., $I(s) = G(s)I_{com}(s)$. The coefficients of Equation (4.2) are obtained by utilizing the system identification toolbox in MATLAB (2009) and applying it to an experimental data set consisting of I_{com} and I as the input and output for Equation (4.1). In Figure 4.2, the solid black line is the frequency response represented by Equation (4.2). A good match is observed with the data, however Equation (4.2) fits the low amplitude response data better (i.e., RMS command current values of 0.3A and 0.6A). Thus, Equation (4.2) may not work well when the command current is large. Figure 4.3 shows the step response of the current driver as well as the predicted response using the proposed current driver model in Equation (4.2). Due to

the dynamics of the current driver, overshooting can be observed in Figure 4.3 in both the step-up and step-down response. The rise time of the current driver is measured to be about 17 msec, while the settling time is about 8 msec. The model represented by Equation (4.2) has a faster response for a step-up response than the measured response, and predicts well the measured step-down response.

4.3 Dynamics of Electromagnetism of MR Damper

According to Faraday's law, a change in the magnetic flux due to the damper coil induces a counter-electromotive force in the electric conductors near the annular gap between the piston head and cylinder housing of the damper, creating an eddy current. This eddy current generates a new magnetic flux that opposes the original magnetic flux by the current in the coil (Lenz's law). The new magnetic flux slows the formation of the magnetic field around the annular gap, creating a slow response of an MR damper under a variable current input (Takesue et al. 2004). To understand the dynamics of an MR damper better, it is necessary to investigate the dynamic behavior of the magnetic field in the damper associated with variable current. Figure 4.4 shows a schematic of the magnetic field around the electromagnetic coil. The total average magnetic flux around the annular gap can consist of two parts: i) magnetic flux due to the electromagnetic coil, ϕ_0; and ii) the induced magnetic flux due to the eddy current of the electric conductor around the annular gap, ϕ_{eddy}, that is,

$$\phi_t = \phi_0 + \phi_{eddy} \tag{4.3}$$

where, ϕ_t is the total average magnetic flux around the annular gap. The magnetic flux of a wire is proportional to the current in the wire according to electromagnetic theory. Therefore, the generated magnetic flux due to the damper coil can be written as follows.

$$\phi_0 = \kappa I \tag{4.4}$$

where κ is a constant and I is the current developed in the coil of the damper. Ignoring the electric potential term, the density of the eddy current is proportional to the time derivative of the magnetic vector potential (Takesue et al. 2004). Thus, the magnetic flux due to the eddy current can be expressed as

$$\phi_{eddy} = -\frac{1}{\nu}\frac{d\phi_t}{dt} \tag{4.5}$$

where ν is a constant. The negative sign in Equation (4.5) implies that the magnetic flux due to the eddy current is induced in the direction opposite to the change in total magnetic flux. In Equation (4.5), the effect of the eddy current in the cylinder housing, which is generated when the damper piston moves with current in the coil, is ignored for simplicity. Substitution of Equations (4.4) and (4.5) into (4.3) leads to the following differential equation.

$$\frac{d\phi_t}{dt} + \nu\,\phi_t = \nu\kappa I \tag{4.6}$$

The same magnetic flux ϕ_t can be generated by supplying a static current into the damper coil. This current is referred to as the *equivalent static current* in this study. If the eddy current due to the movement of the piston of the MR damper is ignored, ϕ_t is proportional to the equivalent static current, i.e.,

$$\phi_t = \kappa I_{eq} \tag{4.7}$$

where I_{eq} is the equivalent static current. Substituting Equation (4.7) into Equation (4.6) gives

$$\dot{I}_{eq} = \nu\left(I - I_{eq}\right) \tag{4.8}$$

Equation (4.8) is exactly the same as the first order filter equation proposed by Spencer et al. (1997) to account for the dynamics of MR dampers associated with variable current input. The equivalent static current can be directly used for the prediction of the MR damper force under a variable current because the parameters of an MR damper model are identified from characterization tests involving a constant current input. The equivalent static current I_{eq} is determined by numerically integrating Equation (4.8). In this study, the forward Euler method was used, along with a time step of 1/1024 sec and the appropriate initial condition for I_{eq}.

The MR damper model has a set of identified parameters corresponding to several values of constant current input (e.g., see Table 3.3). The parameter set for an

equivalent static current other than the current levels listed in Table 3.3 can be obtained using linear interpolation.

Figure 4.5 illustrates a block diagram of an MR damper model under variable current input. The command current (I_{com}) is input into the current driver, and the generated current from the current driver (i.e., the current developed in the damper coil by the current driver, I) goes into the damper, causing the dynamics of the electromagnetism around the annular gap in the damper. The next block in Figure 4.5 is introduced to account for the dynamic response of the electromagnetism by converting the input current to the equivalent static current I_{eq}. The damper force is finally determined from the interpolated model parameters at the given equivalent static current along with the displacement, velocity and acceleration inputs imposed on the mechanical MR damper model.

4.4 Step Response of MR Damper

Figure 4.6 shows a step response from tests when the MR damper is subjected to a step current input of I=2.5A, while the piston of the damper moves at a constant velocity of $\dot{x}$=50 mm/sec. The constant ν in Equation (4.8) can be obtained from nonlinear optimization theory by minimizing the RMS error of the predicted damper force developed under the step current input. For a selected ν value, the time history for the equivalent static current under the step current input is determined by solving Equation (4.8), where the zero equivalent static current is used as the initial condition. The parameters of the MNS model for a constant current input equal to the equivalent

static current is then determined, and the MR damper force is calculated with the model parameters. The RMS error of Equation (3.12), which is related to ν, is evaluated and the optimal ν value is determined by minimizing the RMS error with respect to ν. The PSO algorithm is used to find the optimal ν value, where a particle is defined to be a one-dimensional variable consisting of ν. After 100 iterations with 50 particles, the optimal ν value for the experimental step response plotted in Figure 4.6 is identified to be $\nu = 2.39$.

As can be seen in Figure 4.6, the predicted response using the solution of the first order filter (it is referred to as the *MNS model with the first order filter*) with the optimal value of $\nu = 2.39$ shows a large discrepancy compared to the experimental results, especially for the damper force associated with the step-down response. Moreover, the step-down response of the MR damper appears to be slower than the step-up response. The time for reaching 95% of the final damper force is measured to be about 0.92 sec during the step-up response and 1.75 sec during the step-down response.

The major reason for the difference in 0.92 sec and 1.75 sec is thought to be due to nonlinear magnetization behavior of the materials around the annular gap and MR fluid itself. Due to hysteresis of the magnetization, the piston head and cylinder housing around the annular gap can develop a residual magnetic field after the applied magnetic field has been removed. This nonlinear hysteretic behavior can affect not only the induction of the eddy current, but it can also disturb the formation of the total magnetic field. In addition, the hysteretic magnetization response of the MR fluid, which is directly related to the clustering of iron particles in the fluid, makes it difficult to

accurately predict the damper force. To obtain a better prediction for the damper force under a variable current the following nonlinear differential equation that relates the coil current to the equivalent static current is proposed:

$$\dot{I}_{eq} = \alpha(\dot{I}_r)(I - I_{eq}) \tag{4.9}$$

The function $\alpha()$ is determined from the Equations (4.10) and (4.11):

$$\alpha(\dot{I}_r) = \begin{cases} \beta^+ \dot{I}_r + \alpha_1 & \text{if } \dot{I}_r \geq 0 \\ \beta^- \dot{I}_r + \alpha_1 & \text{if } \dot{I}_r < 0 \end{cases} \tag{4.10}$$

$$\dot{I}_r = \alpha_0 (I - I_r) \tag{4.11}$$

where, α_0, α_1, β^+ and β^- are constants which can be obtained by utilizing nonlinear optimization theory to minimize the error between the model predicted and experimental measured damper force. I_r in Equation (4.11) is the reference current that can simulate the dynamics of the electromagnetism to account for the eddy current effect, while Equation (4.10) is used to accommodate the effect of a residual magnetic field due to the nonlinear hysteretic behavior of the magnetization in the damper. In this study, the solution of Equation (4.9) is obtained from the numerical integration utilizing the forward Euler method. The PSO algorithm is employed for the identification of the parameters, where using the experimental data associated with the damper force plotted in Figure 4.6, results in $\alpha_0 = 18.90$, $\alpha_1 = 1.61$, $\beta^+ = 0.11$ and $\beta^- = -0.34$. In this case, a particle consists of four variables, i.e., α_0, α_1, β^+ and β^-. Like the first order

filter case, 50 particles and 100 iterations were used to find the optimal values for these parameters. As can be seen in Figure 4.6, the MNS model with the nonlinear equation based on Equation (4.9) for the dynamics of electromagnetism, which is referred to as the *variable current MNS model*, shows better prediction for damper force developed under a step current than the first order filter. The equivalent static current of Equation (4.9) was obtained using the numerical integration method similar to that described for Equation (4.8).

4.5 Experimental Assessment of MNS Model

4.5.1 Predefined Input

To validate the MNS model with variable current, a pre-defined displacement and current that mimics the demand on the damper associated with the response of a structure to an earthquake with a semi-active controller is used in this section. The 2-story shear building structure in Figure 3.27 subjected to the ground motion shown in Figure 3.28 is used in conjunction with the semi-active controller based on the linear quadratic regulator (LQR). Equation (4.9) with the parameters identified from the step response data is employed to account for the effect of the dynamics of the MR damper associated with a variable current during the numerical simulation. Figure 4.7 shows the displacement response of the MR damper in the first story along with the corresponding command current generated by the semi-active controller. These are used as pre-defined inputs to the damper in the test setup prescribed in Chapter 3 (see Figures 3.2 and 3.3) to obtain the experimental damper force shown in Figure 4.8 (a).

In order to match the results better between the predicted damper forces and the experimental data for this pre-defined displacement input, new parameter sets for the first order filter of Equation (4.8) and the proposed method of Equation (4.9) are identified using the PSO algorithm applied to the pre-defined displacement input. The newly identified parameters are $\nu = 10.9$ for the first order filter; and $\alpha_0 = 24.96$, $\alpha_1 = 3.57$, $\beta^+ = 0.31$, $\beta^- = -0.30$ for Equation (4.9). Figure 4.8 (a) shows the comparison of damper force history during the time when a strong response is observed. The predicted damper forces by the MNS model with the first order filter and the variable current MNS model show good agreement with the experimental damper force. However, the normalized RMS error of the variable current MNS model has a lower value (0.0503) than the one for the MNS model with the first order filter (0.0871), which demonstrates a better performance for the proposed method based on Equation (4.9). The predicted current using the current driver model based on the transfer function of Equation (4.2) has good agreement with the measured current in the damper coil as shown in Figure 4.8 (b). Figure 4.8 (c) shows the comparison of the equivalent static currents from the first order filter and Equation (4.9) with the current predicted by the current driver model $G(s)$ of Equation (4.2). In Figure 4.9, close-up views of Figure 4.8 are illustrated between *t*=7.0 sec and 7.6 sec. Good prediction of the damper force by the variable current MNS model can be observed in Figure 4.9 (a). The equivalent static currents of the first order filter and Equation (4.9) always lag behind the predicted current by the current driver model, as can be observed in Figure 4.9 (c), so that they can account for the time lag of the MR damper associated with a variable current input.

Figure 4.10 illustrates the damper force-displacement relationship of both models. The variable current MNS model track the experimental data well, while the MNS model with the first order filter estimates the damper force less accurately, especially in the second and fourth quadrants in Figure 4.10 (b) where the command current is zero and a drop in damper force occurs during the experiments.

4.5.2 Real-Time Hybrid Simulation

To further assess the variable current MNS damper model, a real-time hybrid simulation is conducted for the structure shown in Figure 4.11 and the measured experimental results compared to the numerical results from a time history analysis of the structure. The structure represents a 3-story, 6-bay office building located in Southern California (Chae et al. 2010). The moment resisting frame (MRF) of the building is designed to satisfy strength requirements of the International Building Code (ICC 2006). In the real-time hybrid simulation the building structure is reduced to 0.6 scale and one large-scale MR damper is installed in the 3rd story to limit the story drift of the scaled building structure to less than 2.0%. The sliding mode controller (SMC) is used as the semi-active controller for the large-scale MR damper. By taking the advantage of symmetry in the floor plan of the structure, only one-quarter of the floor plan is considered in the hybrid simulation and the numerical simulation of the building response. The real-time hybrid simulation involves two substructures: i) the experimental substructure consisting of an MR damper and a hydraulic actuator as shown in Figure 3.2; and ii) the analytical substructure that includes the remaining

structural components of the building such as the moment resisting frame (MRF) and gravity frames to consider the P-Δ effect, as shown in Figure 4.12. The lean-on column represents the gravity frames that are tributary to the MRF. The tributary mass associated with one-quarter of the structure is placed on the lean-on column, along with the tributary gravity loads to capture the P-Δ effect induced by the gravity loads. The lean-on column is connected to the MRF through rigid links to simulate the effects of a rigid diaphragm (i.e., the floor slab), where the MRF and lean-on column have the same horizontal degree of freedom at each respective floor level. The seismic weights of one-quarter of the structure are $W_1 = W_2 = 991.8$ kN, $W_3 = 721.0$kN. The beams and columns of the MRF are modeled using a concentrated plastic hinge element. The lean-on column is modeled using a linear elastic beam-column element with an area of 3.61×10^{-2}m^2 and a moment of inertia of 1.448×10^{-4} m^4, which are obtained from the summation of the area and moment of inertia of the gravity columns in the associated one-quarter of the building floor plan, respectively. The natural frequencies based on the initial stiffness of the structure are f_1=0.95Hz, f_2=2.84Hz, and f_3=6.36Hz. Rayleigh damping with a 5% damping ratio for the 1st and 2nd mode is used.

The explicit unconditionally stable CR integration algorithm (Chen et al. 2009), a robust nonlinear finite element code, called HybridFEM (Karavasilis et al. 2009), and an inverse compensation scheme to minimize actuator delay (Chen and Ricles 2010) are integrated together and used in the real-time hybrid simulation to compute the structural response based on feedback restoring forces from the experimental and analytical substructures. More details about these aspects of real-time hybrid simulation are

discussed in Chapter 11. The 1989 Loma Prieta earthquake (Hollister station, HSP090 component) scaled to the DBE level (scale factor = 2.04) is used as a ground motion.

For the numerical simulations, the variable current MNS model was implemented into HybridFEM and HybridFEM was used to model and conduct a time history analysis of the above structure.

Figure 4.13 compares the story drifts. Good agreement in the story drifts are observed between the real-time hybrid simulation (RTHS) and the pure numerical simulation. The same variable current MNS model parameters derived from pre-defined earthquake response and pre-defined command current data (Section 4.5.1) were used (i.e., $\alpha_0 = 24.96$, $\alpha_1 = 3.57$, $\beta^+ = 0.31$, $\beta^- = -0.30$). Figure 4.14 compares the damper response from the real-time hybrid simulation and numerical simulation. The predicted damper force by the variable current MNS model matches well with the experimental damper force obtained from the real-time hybrid simulation; the command current of the numerical simulation also shows good agreement with that from the real-time hybrid simulation. The results shown in Figure 4.13 and 4.14 demonstrate the robustness and accuracy of the variable current MNS MR damper model.

4.8 Summary

In this chapter, the dynamics of an MR damper associated with variable current input was studied by utilizing electromagnetism theory to consider the effect of eddy currents and hysteretic magnetization of the damper materials. Prediction of damper force under variable current was made based on solving a nonlinear differential

equation which relates the current developed in the damper coil to an equivalent static current which is used as the current input to the MNS model. The parameters for the coefficients of the differential equation were optimally identified from the pre-defined earthquake response and command current data as given in Section 4.5.1. The response of the variable current MNS model with these parameters showed good agreement with the measured damper response from experimental results based on the predefined input for the damper as well as a real-time hybrid simulation, demonstrating the robustness of the variable current MNS MR damper model.

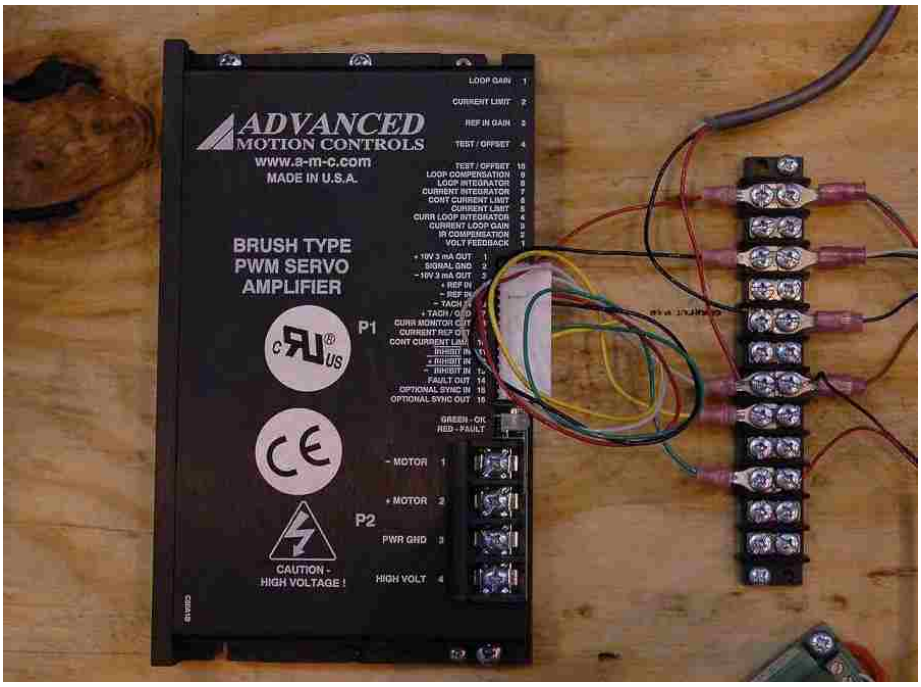

Figure 4.1 Current driver manufactured by Advanced Motion Controls

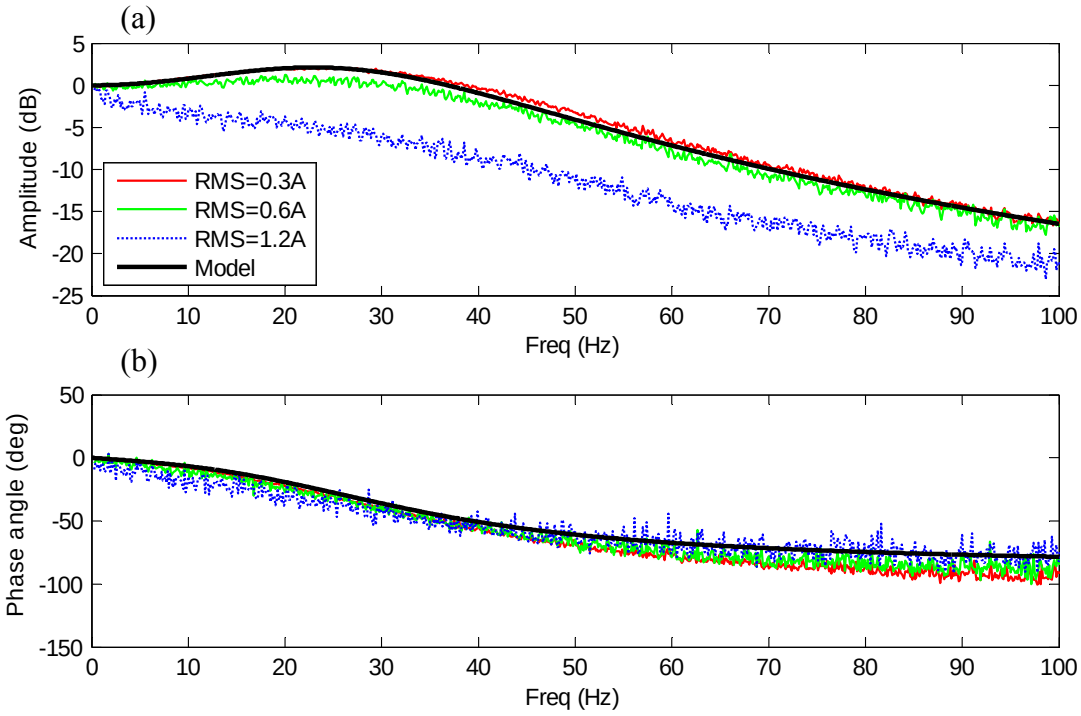

Figure 4.2 Frequency response of current driver under Gaussian white noise with bandwidth of 100Hz and with various RMS amplitudes: (a) amplitude response; (b) phase angle response

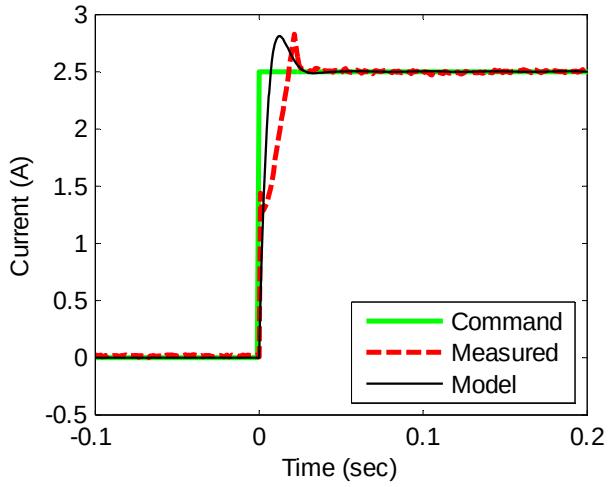

(a)

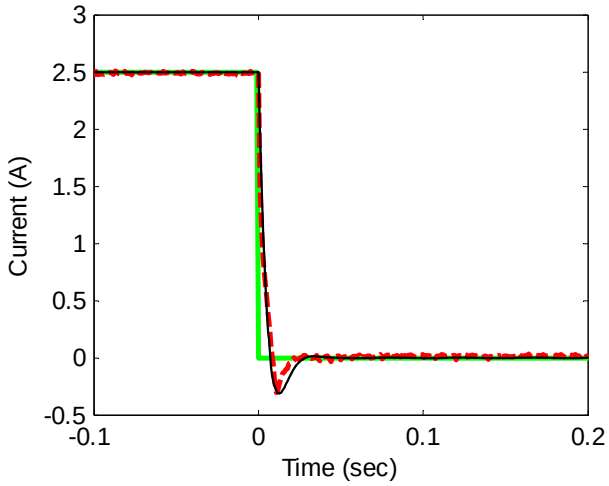

(b)

Figure 4.3 Step response of current driver: (a) step-up response; (b) step-down response

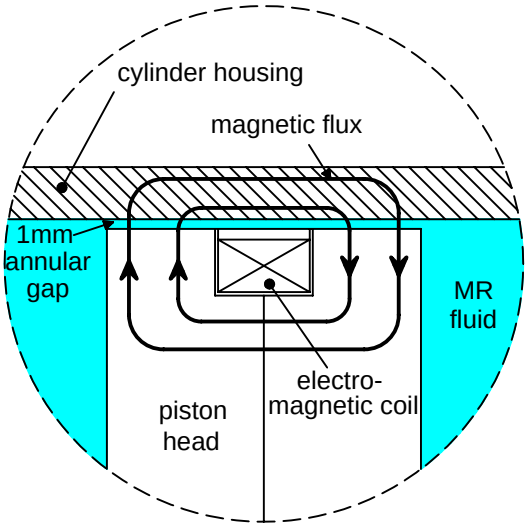

Figure 4.4 Schematic of magnetic flux around the annular gap of MR damper

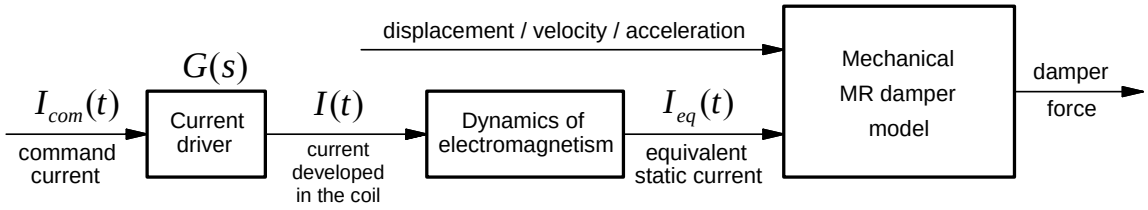

Figure 4.5 Block diagram for MR damper model under variable current

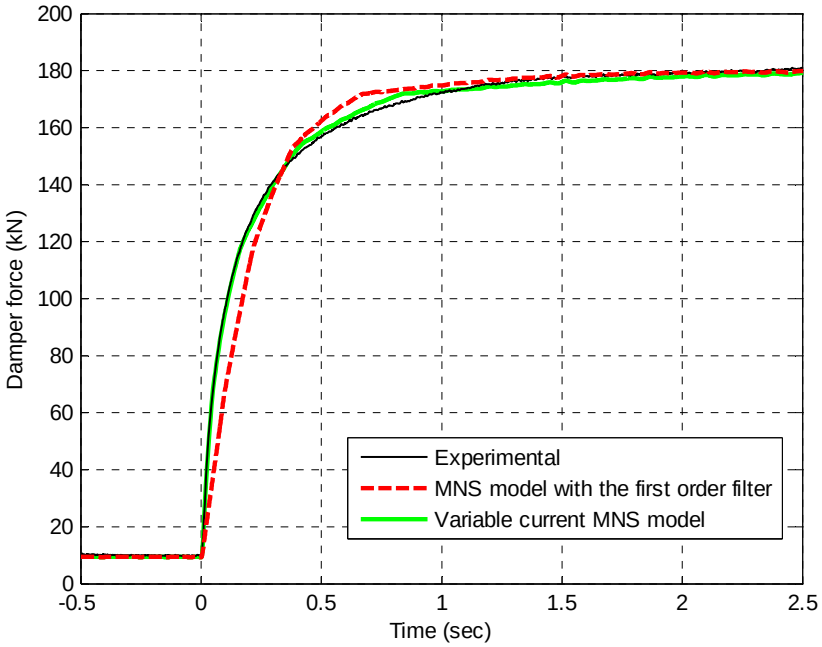

(a)

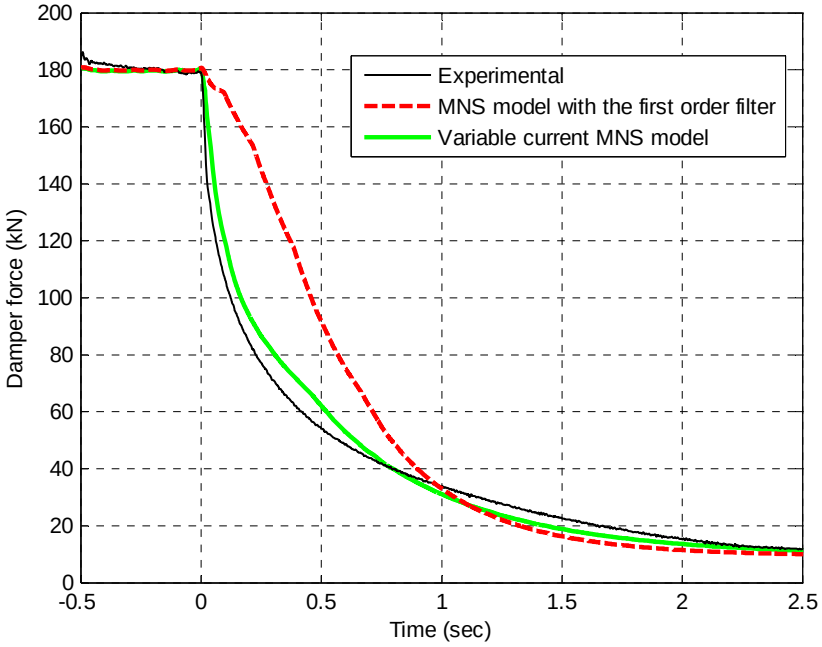

(b)

Figure 4.6 Response of MR damper under step current input: (a) step-up response; (b) step-down response

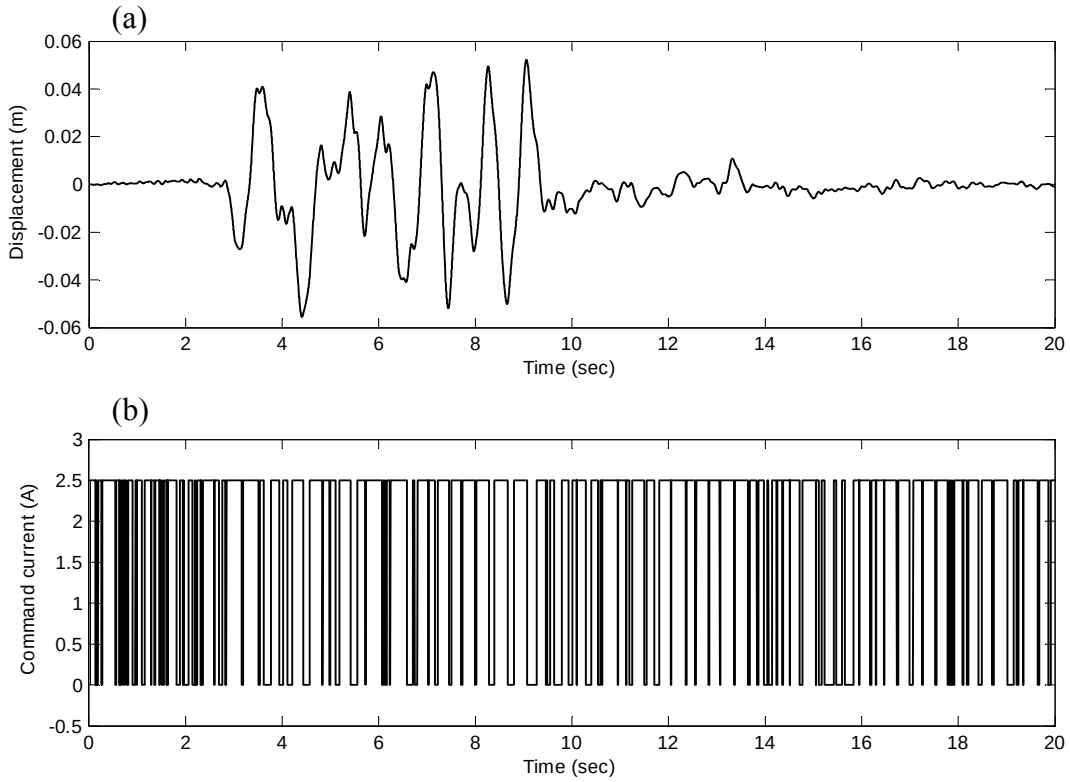

Figure 4.7 Input data of MR damper for the semi-active control: (a) displacement input; (b) current input

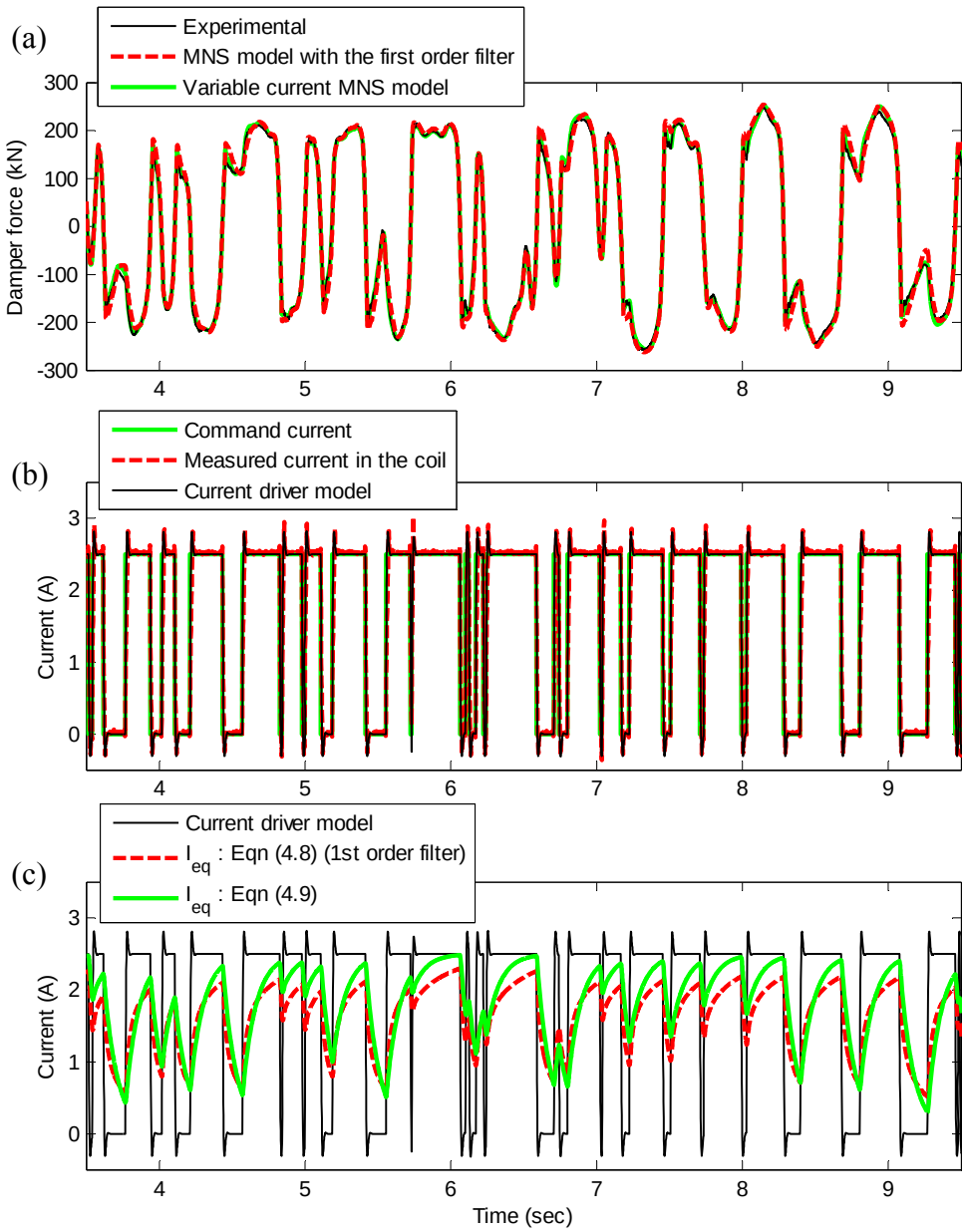

Figure 4.8 Comparison of response of semi-actively controlled MR damper with model predictions: (a) time history of damper force; (b) current; (c) equivalent static current

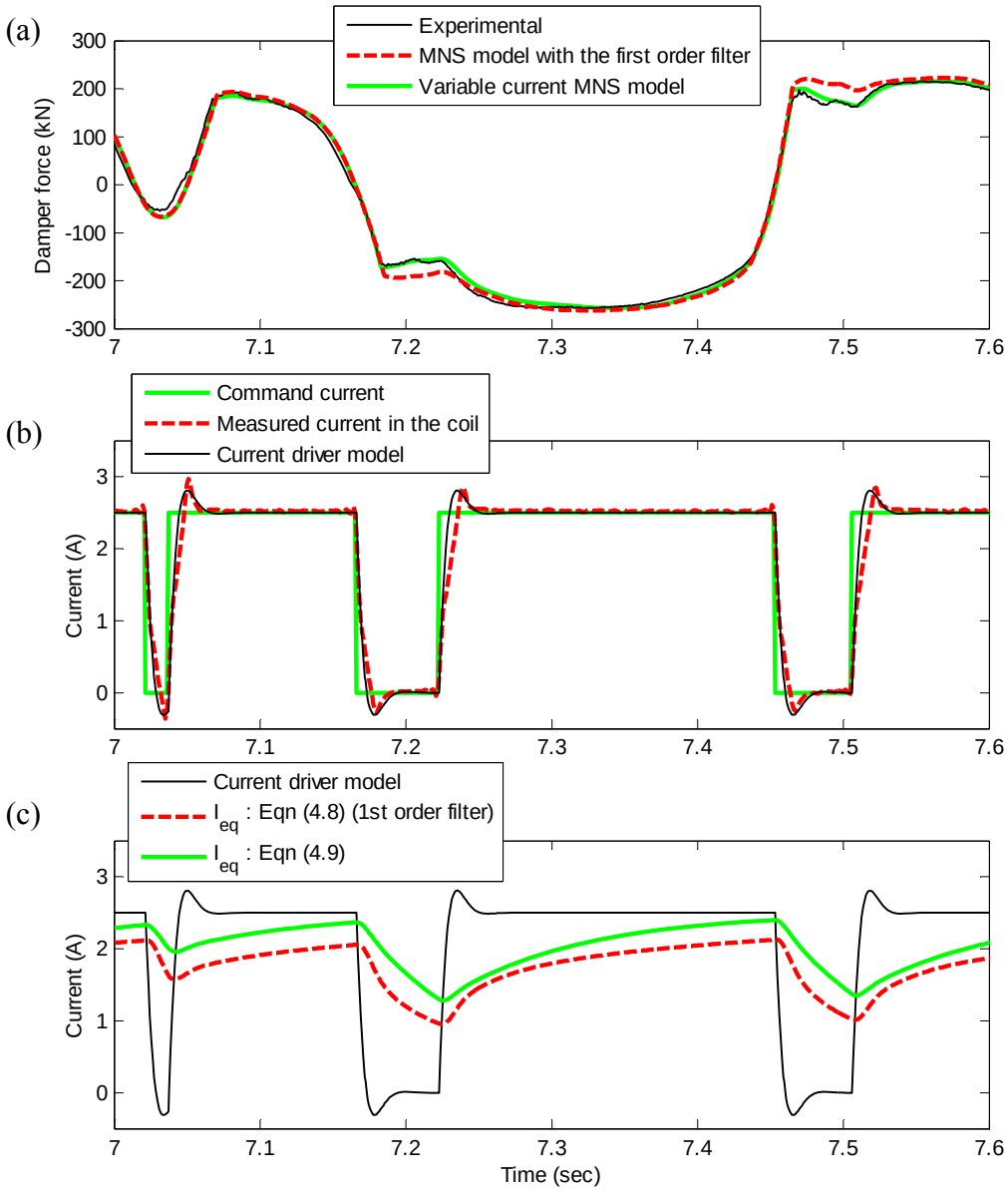

Figure 4.9 Comparison of response of semi-actively controlled MR damper with model predictions (close-up view of Figure 4.8): (a) time history of damper force; (b) current; (c) equivalent static current

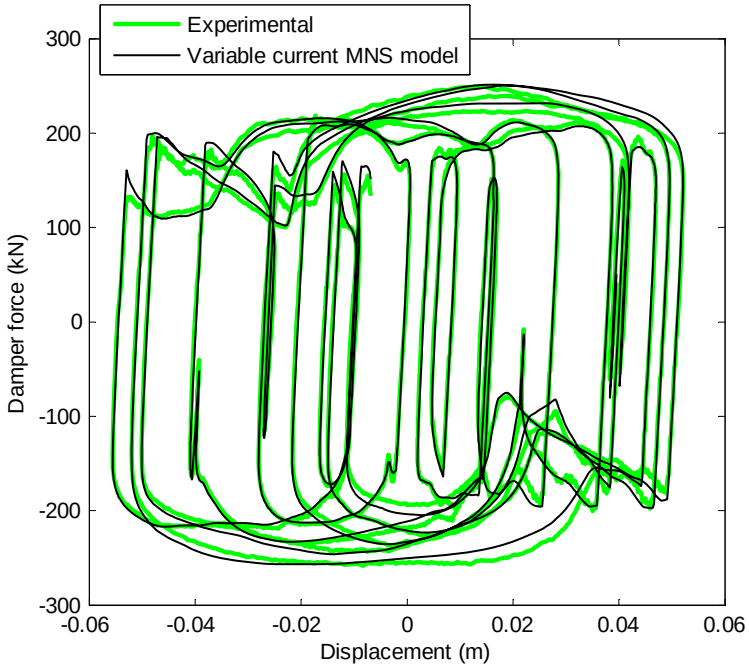

(a)

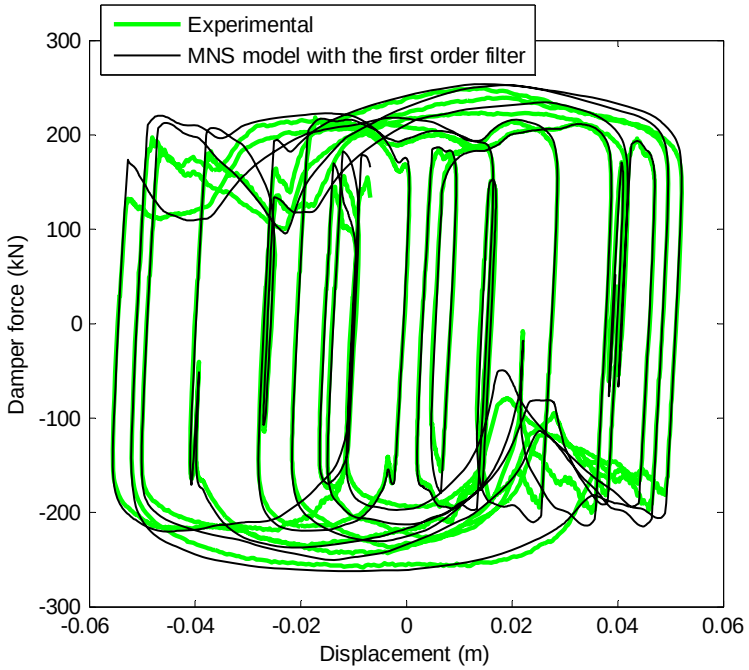

(b)

Figure 4.10 Hysteresis loop of MR damper with semi-actively controlled input data: (a) variable current MNS model; (b) MNS model with the first order filter

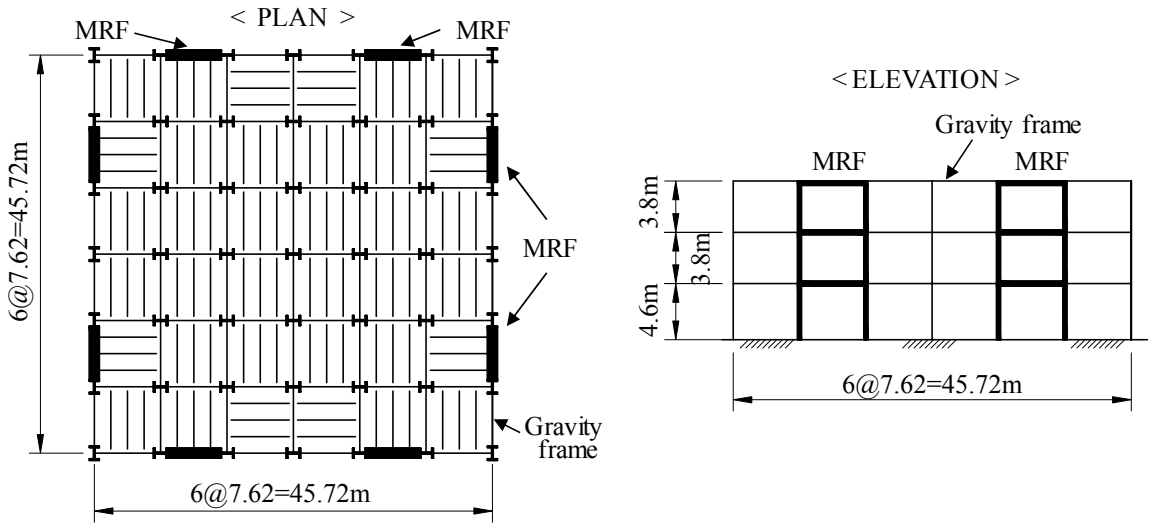

Figure 4.11 Prototype building structure for real-time hybrid simulation

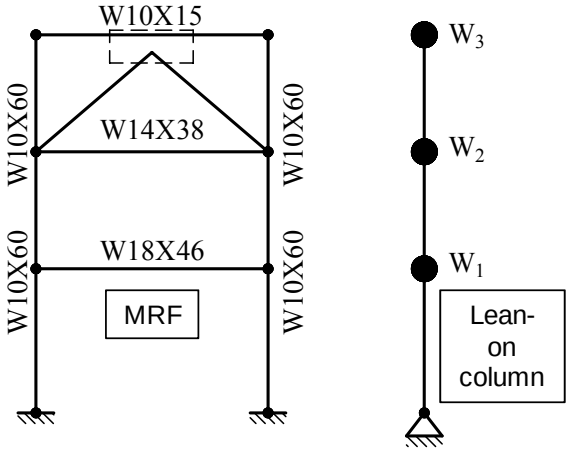

Figure 4.12 Analytical substructure for real-time hybrid simulation

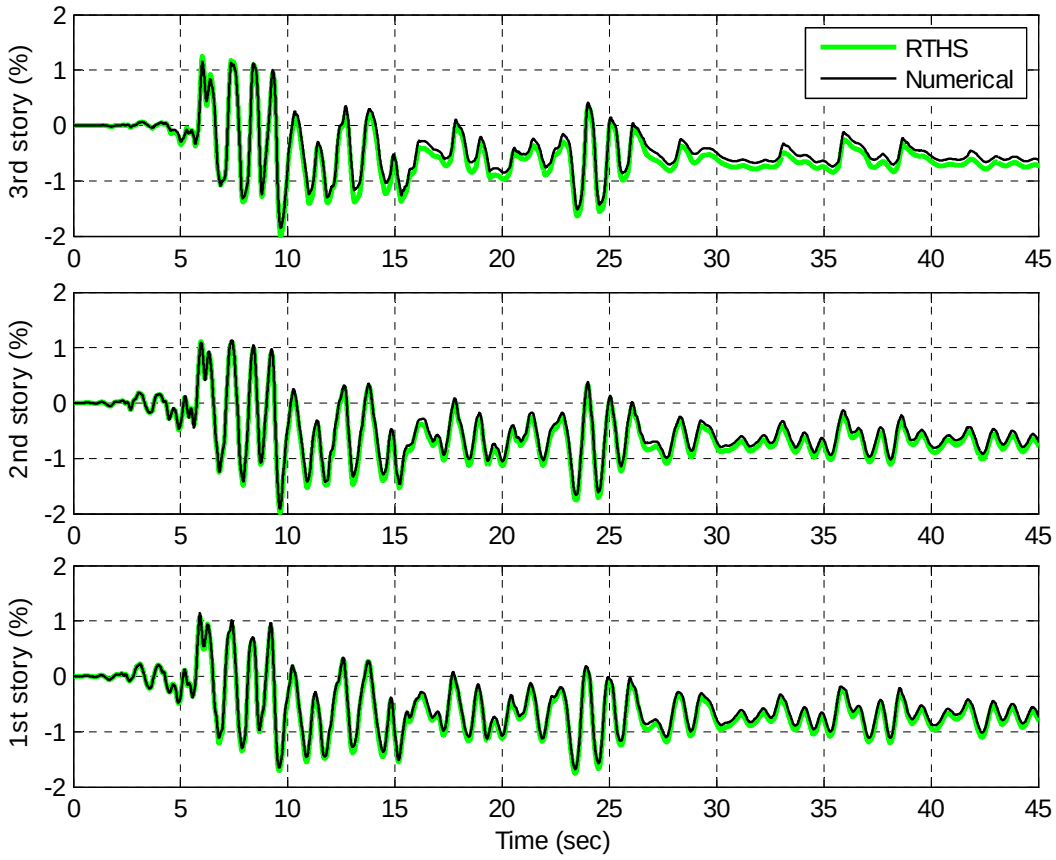

Figure 4.13 Comparison of story drifts between the real-time hybrid simulation (RTHS) and the numerical simulation under the 1989 Loma Prieta earthquake ground motion with sliding mode controller

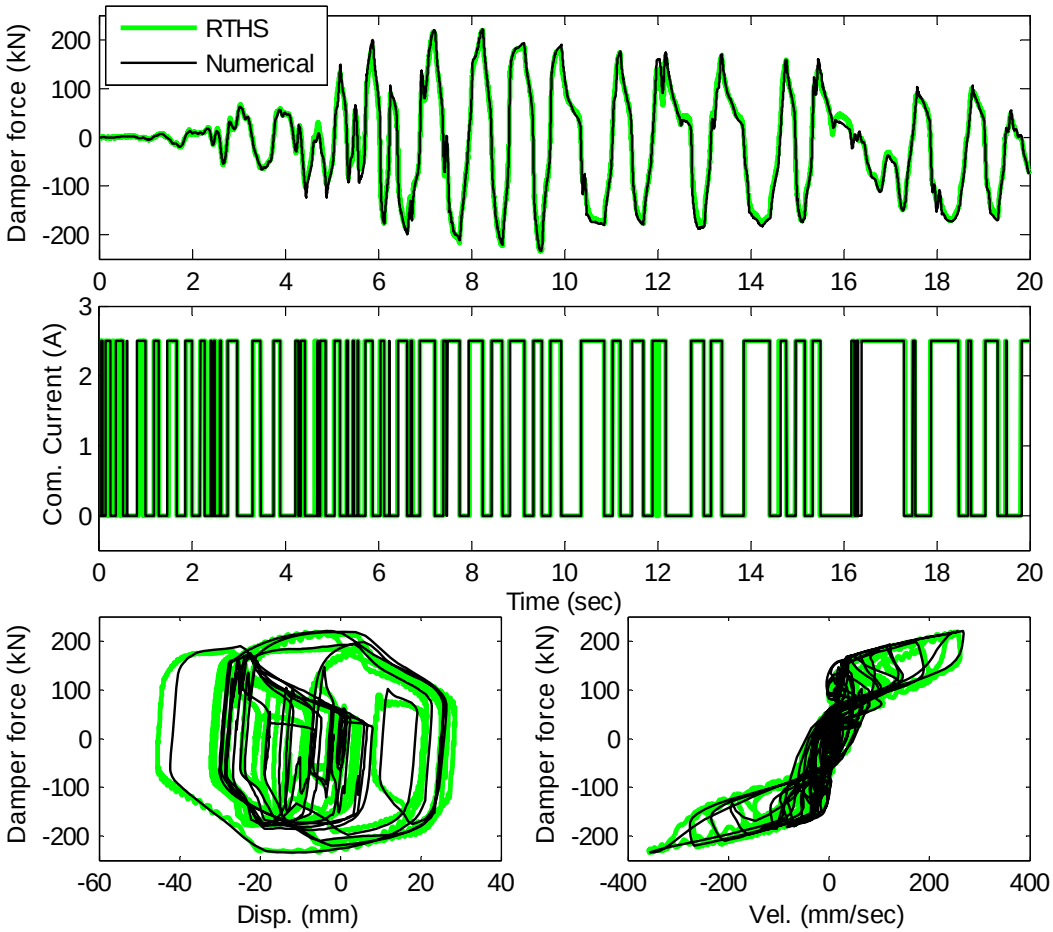

Figure 4.14 Comparison of damper response under the 1989 Loma Prieta earthquake ground motion with sliding mode controller: (a) time history of damper force; (b) time history of command current; (c) force-displacement relationship; (d) force-velocity relationship

Chapter 5

Equivalent Linear System for SDOF Structure with MR dampers

5.1 General

It is well-known that supplemental damping devices increase the energy dissipation capacity of structures, reducing the seismic demand on the primary structure (Constantinou et al. 1998; Soong and Dargush 1997). A structural system with supplemental dampers is often represented by an equivalent linear system. Kwan and Billington (2003) derived optimal equations for the equivalent period and damping ratio of SDOF systems with various nonlinear hysteresis loops based on time history analysis and regression analysis. Symans and Constantinou (1998) studied the dynamic behavior of SDOF systems with linear or nonlinear viscous fluid dampers and derived an equation for the equivalent damping ratio of the nonlinear viscous fluid damper. Ramirez et al (2002) proposed a simplified method to estimate displacement, velocity and acceleration for yielding structures with linear or nonlinear viscous dampers. Lin and Chopra (2003) investigated the behavior of SDOF systems with a brace and nonlinear viscous damper by transforming the system to an equivalent linear Kelvin model.

Fan (1998) investigated the behavior of non-ductile reinforced concrete frame buildings with viscoelastic dampers. He derived an equivalent elastic-viscous model based on the complex stiffness and energy dissipation of the viscoelastic system, and proposed a simplified design procedure for a structure with viscoelastic dampers. Lee et

al. (2005 and 2009) applied this method to structures with elastomeric dampers and validated the simplified design procedure with numerical simulation results.

In this chapter a systematic analysis procedure for use in the design of structures with MR dampers is developed, which is called the *simplified analysis procedure*. The procedure is similar to that developed by Lee et al. (2005 and 2009). A quasi-static MR damper model for determining the loss factor and the effective stiffness of an MR damper is introduced and incorporated into the procedure to predict the behavior of an SDOF structure with an MR damper. The procedure is evaluated by comparing the predicted response by the procedure to that of a nonlinear time history analysis of an SDOF structure. The procedure provides a basic methodology for a performance-based design procedure for structures with MR dampers. This procedure will be presented in Chapter 6.

5.2 Quasi-Static MR Damper Models

The quasi-static behavior of an MR damper is one that describes the behavior of an MR damper under constant velocity. The MR damper force is closely related to the velocity and the quasi-static behavior has a unique relationship between velocity and damper force.

The first quasi-static model is a simple frictional model shown in Figure 5.1. The force-displacement loop is of a rectangular shape and the damper force and is described as follows:

$$f = \text{sign}(\dot{u}) f_0 \tag{5.1}$$

where u is the damper displacement. The second quasi-static model is the Bingham MR damper model shown in Figure 5.2. As discussed in Chapter 2, the Bingham plasticity model is comprised of a linear dashpot in parallel with a friction element; where, the damper force is obtained as

$$f = \text{sign}(\dot{u}) f_0 + C\dot{u} \tag{5.2}$$

In Equation (5.2) C is a dashpot coefficient. Due to its simplicity, the Bingham model has been used frequently to describe the dynamic behavior of a small scale MR damper.

The last quasi-static MR damper model considered is the Hershel-Bulkley model shown in Figure 5.3. The damper force is given as

$$f = \text{sign}(\dot{u})\{f_0 + C|\dot{u}|^n\} \tag{5.3}$$

This model consists of a friction element in parallel with a nonlinear viscous dashpot. This damper model can simulate both a simple frictional model and the Bingham model by adjusting the values for C and n (i.e. $C = 0$ for the simple frictional model, $n = 1$ for Bingham model). It should be noted that the values of f_0, C, and n are dependent on the current in the damper.

5.3 Energy Dissipation of Quasi-Static MR Damper Model

For the simplified analysis procedure developed in this chapter, the energy dissipation of an MR damper is characterized by a quasi-static model. Since the Hershel-Bulkley model can account for the behavior of the simple frictional model and the Bingham model by adjusting the values of C and n, the energy dissipation of the quasi-static MR damper model is calculated based on the Hershel-Bulkley model.

Suppose that the MR damper is subjected to a harmonic displacement motion

$$u(t) = u_0 \sin(\omega t) \tag{5.4}$$

where, u_0 is the amplitude of displacement and ω is the excitation frequency of the damper. The energy dissipated by the damper over one cycle of the harmonic motion is equal to

$$E_{MRD} = \int_0^{\frac{2\pi}{\omega}} f(t)\dot{u}(t)dt \tag{5.5}$$

Substitution of Equations (5.3) and (5.4) into Equation (5.5), and evaluation of the resulting integral results in

$$E_{MRD} = 4f_0u_0 + 2^{n+2}C\gamma(n)u_0^{1+n}\omega^n \tag{5.6}$$

where

$$\gamma(n) = \frac{\Gamma^2\left(1+\frac{n}{2}\right)}{\Gamma(2+n)} \tag{5.7}$$

In Equation (5.7) Γ() is the gamma function (Soong and Constantinou 1994). For the simple frictional model, the energy dissipation during one cycle of harmonic motion can be obtained by setting $C = 0$, whereby

$$E_{MRD} = 4f_0u_0 \tag{5.8}$$

By inserting $n = 1$ into Equation (5.6), the dissipated energy of the Bingham model can be calculated as

$$E_{MRD} = 4f_0u_0 + \pi C\omega u_0^2 \tag{5.9}$$

When the MR damper is semi-actively controlled, the force-deformation hysteresis loop stays within that of a passive controlled MR damper as shown in Figure 5.4. During the semi-active control of an MR damper, the command current for the damper is between the minimum and maximum currents (I_{min} and I_{max}). Thus, the hysteresis loop under the semi-active control mode is bounded by the hysteresis loops for the two passive controlled cases with constant current inputs of $I = I_{min}$ and $I = I_{max}$. Since the area within the hysteresis loop for a semi-active controlled MR damper is smaller than that for passive control with $I = I_{max}$, the energy dissipated by

the semi-active controlled MR damper E_{MRD}^{SA} is defined as a linear interpolation between the energy dissipated under passive mode with the current on and with the current off:

$$E_{MRD}^{SA} = \varphi E_{MRD}^{max} + (1-\varphi)E_{MRD}^{min} \quad (0 \le \varphi \le 1) \tag{5.10}$$

where E_{MRD}^{min} and E_{MRD}^{max} are the energy dissipation of the passive controlled MR damper defined in Equation (5.6) with $I = 0$ and $I = I_{max}$, respectively. φ is a constant between zero and one whose value needs to be established from experimental observations of the damper characteristics associated with the semi-active control law.

5.4 Equivalent Stiffness of MR Damper

The equivalent stiffness of the MR damper, k_{eq}, is used for estimating the equivalent damping ratio and the effective stiffness of a structure with MR dampers. Since the MR damper effects the period of the structure, the equivalent stiffness of the MR damper needs to be defined appropriately. In this dissertation, two different approaches are described for determining the equivalent stiffness of an MR damper. These two approaches are illustrated in Figure 5.5, and include: i) secant stiffness method, k_{sec}; and ii) a method based on the root mean square (RMS) displacement of damper (hereafter, referred as to the *RMS stiffness method*), k_{RMS}. The secant stiffness of a passive controlled MR damper, k_{sec}, is determined by the maximum displacement of the damper and its corresponding damper force, where

$$k_{sec} = f_0/u_0 \tag{5.11}$$

where, f_0 is the damper force when the damper displacement is equal to the maximum displacement u_0, and is dependent of the current of the damper.

For the RMS stiffness method of a passive controlled MR damper, the equivalent stiffness is obtained from the RMS displacement of the MR damper and its corresponding damper force. The RMS displacement, u_{RMS}, for a harmonic motion is

$$u_{RMS} = \sqrt{\frac{\omega}{2\pi}\int_0^{2\pi/\omega} u(t)^2 dt} = \frac{\sqrt{2}}{2}u_0 \tag{5.12}$$

The velocity of the damper is determined by differentiating Equation (5.4) with respect to time

$$\dot{u}(t) = u_0\omega\cos(\omega t) \tag{5.13}$$

From Equations (5.4) and (5.12), it is apparent that when $\sin(\omega t) = \sqrt{2}/2$, $u(t) = u_{RMS} = \sqrt{2}/2$. The velocity at the time when $u = u_{RMS}$ is therefore obtained by substituting $\omega t = \pi/4$ into Equation (5.13), whereby

$$\dot{u}(u = u_{RMS}) = u_0\omega\sqrt{2}/2 \tag{5.14}$$

The damper force corresponding to u_{RMS} is obtained by substituting Equation (5.14) into Equation (5.3), whereby

$$f(u = u_{RMS}) = f_0 + C\left(\frac{\sqrt{2}}{2}u_0\omega\right)^n \tag{5.15}$$

Finally, the equivalent stiffness based on the RMS stiffness method, k_{RMS}, is defined as

$$k_{RMS} = \frac{f(u = u_{RMS})}{u_{RMS}} = \frac{\sqrt{2}f_0}{u_0} + C\left(\frac{u_0}{\sqrt{2}}\right)^{n-1}\omega^n \tag{5.16}$$

Since $u_{RMS} < u_0$ and $f(u = u_{RMS}) > f_0$, k_{RMS} is always greater than k_{sec}. Note that both k_{sec} and k_{RMS} depend on the displacement of the damper, which means the effective period of the structure with an MR damper will depend on the amplitude of the structural response.

The equivalent stiffness of the semi-active controlled MR damper k_{eq}^{SA} can be obtained either from the secant stiffness method (k_{sec}^{SA}) or the RMS stiffness method (k_{RMS}^{SA}) as well. The damper force of the semi-active controlled MR damper is always lower than the passive controlled MR damper with $I = I_{max}$; thus, $k_{sec}^{SA} \leq k_{sec}^{max}$ and $k_{RMS}^{SA} \leq k_{RMS}^{max}$ as shown in Figure 5.5, where k_{sec}^{max} and k_{RMS}^{max} are the secant stiffness and the RMS stiffness of the passive controlled MR damper with $I = I_{max}$. The equivalent stiffness of the semi-active controlled MR damper k_{eq}^{SA} is expressed as a linear interpolation between the stiffness at maximum current and zero current

$$k_{eq}^{SA} = \chi k_{eq}^{max} + (1-\chi)k_{eq}^{min} \quad (0 \le \chi \le 1) \tag{5.17}$$

where k_{eq}^{min} and k_{eq}^{max} are the equivalent stiffness of the passive controlled MR damper with $I = 0$ and $I = I_{max}$, respectively , which is determined from either k_{sec} or k_{RMS}. χ is a constant between zero and one, whose value needs to be established from experimental observations of the damper characteristics associated with the semi-active control law.

Both constants φ and χ for the semi-active controlled MR damper depend on the control algorithm for the MR damper. The hysteresis loop of the semi-active MR damper needs to be appropriately defined based on the characteristics of a specified semi-active control algorithm. In this dissertation, the equivalent linear system for structures with MR dampers and the simplified analysis procedure is based on the passive controlled MR damper with $I = I_{max}$ (i.e., $\varphi = \chi = 1.0$). The determination of φ and χ for the semi-active controlled MR damper is not studied in this dissertation, and remains for a future study. The assumption of using $\varphi = \chi = 1.0$ in the design of a structure with semi-active controlled MR dampers is evaluated and presented in Chapter 9.

5.5 Equivalent Linear System for SDOF Structure with MR Damper and Diagonal Bracing

Figure 5.6 shows an SDOF system with an MR damper and diagonal bracing. This model could represent an equivalent SDOF model of an MDOF structural system

with MR dampers and bracing. The equilibrium equation of the SDOF system is expressed as

$$m\ddot{x} + c\dot{x} + k_0 x = -m\ddot{x}_g - f(x, y) \tag{5.18}$$

$$f(x, y) = k_{br} y \tag{5.19}$$

where, $f(x, y)$ is an MR damper force that is determined by the relative motion of x and y, and where y is the diagonal brace deformation in the horizontal direction. In Figure 5.6, k_0 is the lateral stiffness of the frame and k_{br} is the lateral stiffness of the diagonal bracing in terms of the global displacement DOF x. The mass and the dashpot coefficient for viscous damping of the system is represented by m and c, respectively.

The MR damper in Figure 5.6 is assumed to be passively controlled. The energy dissipation of the passive MR damper in the SDOF system is obtained by using a procedure similar to the one presented in Section 5.4. The SDOF system is assumed to be subjected to a harmonic excitation, where

$$x = x_0 \sin(\omega t) \tag{5.20}$$

The damper displacement and velocity, u_d and $\dot{u}_d$, respectively, are expressed as

$$u_d = x - y \tag{5.21}$$

$$\dot{u}_d = \dot{x} - \dot{y} \tag{5.22}$$

Although x is a harmonic motion, the damper displacement u_{d0} is not harmonic because the nonlinear damper force results in a non-harmonic displacement y. For the simplicity of estimating the response of the SDOF system, the assumption is made that

> *The maximum displacement, u_{d0}, and velocity, $\dot{u}_{d0}$, of the MR damper occur when x and $\dot{x}$ are a maximum, respectively.*

This assumption greatly simplifies the estimate of the maximum displacement and velocity of MR damper. When the damper reaches its maximum displacement, the velocity of the damper $\dot{u}_d$ is equal to zero and the damper force becomes f_0 from Equation (5.3). The diagonal bracing deformation y becomes $y = f_0/k_{br}$ from Equation (5.19). Therefore, considering the above assumption, the maximum displacement of damper u_{d0} is determined by substituting the diagonal bracing deformation into Equation (5.21)

$$u_{d0} = x_0 - f_0/k_{br} \tag{5.23}$$

When the velocity of the damper reaches a maximum value, the damper has a maximum damping force f_{max} as can be seen in Figure 5.3 (a). The time derivative of f when $f = f_{max}$ is zero. Hence, at this instant $\dot{y}$ is zero from the time derivative of Equation (5.19). Considering the above assumption and Equation (5.22), the maximum damper velocity $\dot{u}_{d0}$ has the same value as the maximum velocity $\dot{x}_0$

$$\dot{u}_{d0} = \dot{x}_0 = x_0\omega \tag{5.24}$$

The above assumption, Equations (5.23) and (5.24) are always true when the simple frictional MR damper model, i.e., Equation (5.1), is used as an MR damper model. Figure 5.7 shows a mechanical model for the simple frictional model combined with a diagonal bracing in series, which is subjected to a harmonic motion. Figure 5.8 shows the force-displacement relationship for the simple frictional model and the simple frictional model combined with a diagonal bracing in series (e.g., combined structure). The time history of displacements for the combined structure is presented in Figure 5.9. During the transition from point O to point A, all the deformation of the combined structure is in the spring (i.e., diagonal bracing) and the frictional element is not deformed (i.e., $u_d = 0$). When the force developed in the spring reaches f_0, then the slip in the frictional element occurs and the spring has a constant deformation of f_0/k_{br} during the slip of the frictional element. The damper displacement and velocity during the slip are expressed as follows:

$$u_d = x - y = x_0 \sin(\omega t) - sign(\dot{u}_d) f_0/k_{br} \tag{5.25}$$

$$\dot{u}_d = x_0\omega\cos(\omega t) \tag{5.26}$$

The slip continues until x reaches its maximum value of x_0 at point B. Right after the point B, the direction of x changes and the friction element is locked again. All the deformation is in the spring until the force of the spring reaches $-f_0$ at point C.

Between point B and point C, the damper displacement is constant and equal to be $u_d = x_0 - f_0/k_{br}$. After point C, a reverse slip begins in the friction element and the damper velocity becomes negative where the damper displacement is obtained to be $u_d = x - y = x_0 \sin(\omega t) + f_0/k_{br}$ from Equation (5.25). The slip of the friction element continues until x reaches its negative maximum at point D. After point D, the friction element is locked and has a constant displacement of $u_d = -x_0 + f_0/k_{br}$ until the spring force becomes f_0 at point E. The slip in the frictional element begins at point E and continues to the point A of the next cycle.

It is obvious that the maximum damper displacement is obtained to be $u_{d0} = x_0 - f_0/k_{br}$, from Figure 5.9 and Equation (5.25), and it occurs at the same time with the maximum displacement of x. The maximum damper velocity is equal to the maximum velocity of x (i.e., $\dot{u}_{d0} = \dot{x}_0 = x_0\omega$), as can be determined from Equation (5.26), and it occurs at $t = \pi/\omega$ when the maximum velocity of x occurs.

When the Hershel-Bulkley model is used, it may be difficult to get an analytical solution for the damper displacement due to the highly nonlinear terms in Equation (5.3). The above assumption was made based on the observation from the simple frictional model and makes it easy to derive a linearized system for structures with MR dampers.

Equations (5.23) and (5.24) provide basic information to enable the equivalent damping ratio and stiffness of the system to be calculated, making it possible to estimate the response of the structure using these structural properties and a response

spectrum. Substituting the maximum damper displacement of u_{d0} for the displacement amplitude u_0 into Equation (5.6) results in

$$E_{MRD} = 4f_0 u_{d0} + 2^{n+2} C\gamma(n) u_{d0}^{n+1} \omega^n \tag{5.27}$$

The strain energy of the MR damper is calculated from the equivalent stiffness of the damper and the maximum damper displacement

$$E_S = \frac{1}{2} k_{eq} u_{d0}^2 \tag{5.28}$$

where the equivalent stiffness k_{eq} of the MR damper can be selected to be either k_{sec} or k_{RMS}. The loss factor η of the MR damper by definition is

$$\eta = \frac{1}{2\pi} \frac{E_{MRD}}{E_S} = \frac{4\{f_0 + C\gamma(n)(2u_{d0}\omega)^n\}}{\pi k_{eq} u_{d0}} \tag{5.29}$$

The equivalent damping ratio of the system, ξ_{eq}, is calculated by utilizing the lateral force energy (LFE) method (Sause et al. 1994) and is given as

$$\xi_{eq} = \frac{\eta}{2} \frac{F_d u_{d0}}{F x_0} + \xi_i \tag{5.30}$$

where, F is the force applied to the SDOF, F_d is the force developed in the damper and ξ_i is the inherent damping ratio of the SDOF system. Theoretically, this method is exactly the same as the one proposed by Chopra (2001) to determine ξ_{eq}. F and F_d can be expressed in terms of the stiffness and displacement

$$F = k_{total}x_0, \quad F_d = k_{eq}u_{d0} \tag{5.31}$$

where, the stiffness of system, k_{total}, is

$$k_{total} = k_0 + \frac{k_{br}k_{eq}}{k_{br} + k_{eq}} \tag{5.32}$$

By substituting Equations (5.29) and (5.27) into Equation (5.28)

$$\xi_{eq} = \frac{\eta}{2}\frac{k_{eq}u_{d0}^2}{k_{total}x_0^2} + \xi_i = \frac{2\{f_0 + C\gamma(n)(2u_{d0}\omega)^n\}u_{d0}}{\pi k_{total}x_0^2} + \xi_i \tag{5.33}$$

Because k_{total} and u_{d0} are a function of x_0, ξ_{eq} of Equation (5.33) is a function of x_0 and ω for a given structural system and MR damper properties. If the excitation frequency is equal to the effective frequency of the system, ω_{eff}

$$\omega = \omega_{eff} = \sqrt{\frac{k_{total}}{m}} \tag{5.34}$$

then ξ_{eq} is a function of only the maximum displacement of the system x_0. Therefore, an iterative method needs to be utilized to estimate the maximum displacement x_0 of the system via a response spectrum, where the response of structure is characterized by an effective period T_{eff} and the equivalent damping ratio ξ_{eq}. Once the maximum displacement x_0 is determined, the maximum damper force can be calculated using Equations (5.24) and (5.3)

$$f_{max} = f_0 + C\dot{u}_{d0}^n = f_0 + C\left(x_0\omega_{eff}\right)^n \tag{5.35}$$

Figure 5.10 summarizes the solution procedure for estimating the maximum displacement x_0 and the maximum damper force f_{max} for an SDOF system consisting of an MR damper and lateral load resisting frame of stiffness k_0. In this study, this prediction procedure is referred as to the *simplified analysis procedure*.

5.6 Assessment of Simplified Analysis Procedure

To assess the accuracy of the simplified analysis procedure, the linear-elastic SDOF structure shown in Figure 5.6(a) is analyzed as the period is varied. The analysis results are compared to the results from nonlinear time history analysis of the structure, where the nonlinearity comes from the MNS MR damper model. The comparison was

made with the response statistics of the nonlinear time history analysis of the SDOF system involving the ensemble of the 44 ground motions listed in Appendix 3. The response spectrum for the simplified analysis procedure is based on the design response spectrum in the IBC code (ICC 2003). The structure is assumed to be located on stiff soil (site class D) in Southern California. The spectral response acceleration parameters at short periods and 1.0 sec period are based on the deterministic limit for maximum considered earthquake ground motion in the IBC code (ICC 2003) and equal to $S_{DS} = 1.0g$ and $S_{D1} = 0.6g$, respectively. The equivalent damping ratio of structures with supplemental damping devices will have a larger damping ratio than 5% which is used for a typical design spectrum. Therefore, it is required to reduce the spectral acceleration of the response spectrum by using a damping reduction factor, such as B_S and B_1 from FEMA (2000b), for damping ratios greater than 5%.

The properties for the MR damper are given as: $f_0 = 138.5$ kN , $C = 161.8$ kN sec/m and $n = 0.46$. These properties represent the Hershel-Bulkley curve of the MNS model with a current input of 2.5A, where $a = f_0$ and $b = C$ (see Equation (3.3) and Table 3.3). One MR damper is installed between the diagonal bracing and the beam of the frame. The ratio of horizontal brace stiffness to the story stiffness k_0 , α, is assumed to be 10 so that k_{br} can be obtained from known values for k_0 and α. The inherent damping of the system is assumed to be $\xi_i = 5\%$. The period of structure without the MR damper is

$$T_n = 2\pi\sqrt{m/k_0} \tag{5.36}$$

The assessment of the simplified analysis procedure was performed for three different values for the equivalent damping ratio, namely, $\xi_{eq} = 0.10$, 0.20, and 0.30. Six different periods are chosen for each value of ξ_{eq}, namely, T_n=0.5, 1.0, 1.5, 2.0, 2.5, and 4.0 sec. To define the structural properties, either k_0 or m needs to be specified for a given period T_n. Table 5.1 summarizes the values for mass corresponding to the selected natural periods and equivalent damping ratios. For a given equivalent damping ratio ξ_{eq} and a period T_n, the mass of the SDOF system can be determined iteratively using the simplified analysis procedure given in Figure 5.10. The unknown variables are m, k_0, and x_0. There are three known equations to solve these variables: i) T_n from Equation (5.36), which is a function of m and k_0; ii) ξ_{eq} from Step 5 of the simplified analysis procedure, which is a function of m, k_0, and x_0; and iii) the updated value for x_0 from Step 6 of the simplified analysis procedure, which is a function of m, k_0, and current x_0. The value of the mass depends on what the equivalent stiffness of damper is based on (i.e., secant stiffness or RMS stiffness). The values for mass in Table 5.1 are obtained using the secant stiffness method.

With the damper and structural properties defined, a series of nonlinear time history analysis involving the MNS model is performed and compared to the estimation by the simplified analysis procedure. The 44 ground motions listed in Appendix 3 are scaled to the DBE. The procedure proposed by Somerville et al. (1997) was used to scale each ground motion, where

$$SF = \prod_{i=1}^{4} \left(\frac{S_a^{target}(T_i)}{S_a^{record}(T_i)} \right)^{\alpha_i} \tag{5.37}$$

In Equation (5.37) SF is a scale factor for a given earthquake, and $S_a^{target}(T_i)$ and $S_a^{record}(T_i)$ are the spectral accelerations of the target hazard spectrum (i.e., the design response spectrum in the IBC code) and a given ground motion at the period T_i, respectively. α_i are weight factors with values of 0.1, 0.3, 0.3, and 0.3 associated with four periods. A total of six different periods for the structural system, T_n, were selected. For each period T_n, four different values of T_i are selected as shown in Table 5.2 to get the median spectrum of the 44 ground motions to match the target response spectrum near the period T_n. Hence, each ground motion has six different scale factors, one for each T_n. Figures 5.11 through 5.16 show the response spectrum for the ground motions that are scaled to the DBE level for the six different periods of the structure (T_n).

Figure 5.17 compares estimations from the simplified analysis procedure with the nonlinear time history analysis (NTHA) results for the maximum displacement and the maximum damper force. The MNS model presented in Chapter 3 is used for the time history analysis. The simplified analysis procedure shows good agreement with the NTHA results. The vertical lines in the NTHA represent the range of one standard deviation above and below the median value of the response for the 44 ground motions. The median value of the maximum displacement of the NTHA closely matches the estmation from the simplified analysis procedure using the RMS stiffness method when the equivalent damping ratios are 10% and 20%. The secant stiffness method provides a

more conservative estimation of the response, and better agreement with the NTHA when the equivalent damping ratio is 30%, while the RMS stiffness method underestimates the displacement from the NTHA results, especially when the period is long.

In terms of the MR damper force, the secant and RMS stiffness methods provide a similar estimation for the maximum damper force f_{max}. They both show good agreement with the median value from the NTHA up to T_n =1.5sec. However, as the period of the structural system gets longer, the maximum damper force from the NTHA is larger than the estimation from the simplified analysis procedure.

The discrepancies noted between the median NTHA and the estimation from the simplified analysis procedure are attributed to the use of the pseudo-velocity in calculating the RMS stiffness as well as the maximum damper force. The simplified analysis procedure uses a pseudo-velocity from the response spectrum for the calculation of the maximum damper force as can be observed in Step 8 of Figure 5.10. The maximum damper velocity is assumed to be equal to the maximum velocity of x that is obtained from the pseudo-velocity of x.

The pseudo-velocity response spectrum becomes constant when the effective period of structure is greater than T_S. T_S is defined by FEMA (2000b) as:

$$T_S = \frac{S_{D1}B_S}{S_{DS}B_1} \tag{5.38}$$

where B_S and B_1 are the damping reduction factors. T_S is equal to 0.65 sec, 0.72 sec, and 0.81 sec for the cases of ξ_{eq} =0.10, 0.20, and 0.30, respectively. When $T_{eff} > T_S$, the maximum velocity from the response spectrum is in accordance with FEMA (2000b)

$$\dot{x}_0 = \frac{S_{D1}}{2\pi B_1} \tag{5.39}$$

Therefore, the maximum damper force, when $T_{eff} > T_S$, is obtained by substituting Equation (5.39) into Equation (5.35) via Equation (5.24), whereby:

$$f_{max} = f_0 + C\left(\frac{S_{D1}}{2\pi B_1}\right)^n \tag{5.40}$$

Thus, f_{max} is independent of the effective period. This explains why the maximum damper force is shown to be a constant value for the longer periods in Figure 5.17. In addition, Hudson (1962) found that for longer periods the use of pseudo-velocity introduces more appreciable error, and for damping values 20% or more significant differences can also exist (Clough and Penzein, 1993). To avoid errors introduced by the use of pseudo-velocity, the relative velocity response spectrum can be used instead.

Although the maximum damper force is underestimated when the period is long, the results from the simplified analysis procedure appear to be sufficient close to the results of NTHA for design purpose.

5.7 Summary

In this chapter a systematic procedure for estimating the response of an SDOF system with diagonal bracing and a passive MR damper was developed. The purpose of this simplified analysis procedure is to enable the design of structures with MR dampers without performing a nonlinear time history analysis. The simplified analysis procedure is based on an effective period and equivalent damping ratio. The equations describing the energy dissipation for a structure with an MR damper under a harmonic motion are developed based on the Hershel-Bulkley visco-plasticity model. Two different approaches for determining the equivalent stiffness of an MR damper are presented, the secant and RMS stiffness methods, and are incorporated into the equation for equivalent damping ratio as well as the equation for determining the effective period of the SDOF system.

The accuracy of the simplified analysis procedure was assessed by comparing the estimated response from this procedure with the results of nonlinear time history analyses of linear SDOF systems with a passive MR damper. Good agreement was observed, although the maximum damper force is underestimated when the structure has a long period. The simplified analysis procedure for an SDOF system will be extended to MDOF systems in the next chapter.

The energy dissipation and equivalent stiffness of a semi-active MR damper was also discussed in this chapter. The factors to describe the reduced energy dissipation and equivalent stiffness (i.e., φ and χ) were introduced based on an assumed hysteresis loop for the semi-active MR damper. These constants are dependent on the semi-active

control algorithm used for the MR damper. The dynamic behavior of structures with semi-active controlled MR dampers will be investigated in Chapter 9 and the result will be discussed and compared to that predicted by the simplified analysis procedure based on the properties of the passive MR damper.

Table 5.1 Mass for SDOF analysis

Equivalent damping ratio	Mass, m (kN sec^2/m)					
	T_n=0.5 sec	T_n=1.0 sec	T_n=1.5 sec	T_n=2.0 sec	T_n=2.5 sec	T_n=3.0 sec
$\xi_{eq} = 10\%$	419	670	1005	1340	1675	2010
$\xi_{eq} = 20\%$	174	247	371	494	618	741
$\xi_{eq} = 30\%$	120	148	223	297	371	445

Table 5.2 Selected T_i for scaling of ground motions (sec)

T_i	Period of structure without MR damper					
	T_n=0.5 sec	T_n=1.0 sec	T_n=1.5 sec	T_n=2.0 sec	T_n=2.5 sec	T_n=3.0 sec
T_1	0.2	0.5	1.0	1.0	1.5	2.0
T_2	0.3	0.6	1.2	1.2	1.8	2.2
T_3	0.4	0.8	1.3	1.7	2.2	2.5
T_4	0.5	1.0	1.5	2.0	2.5	3.0

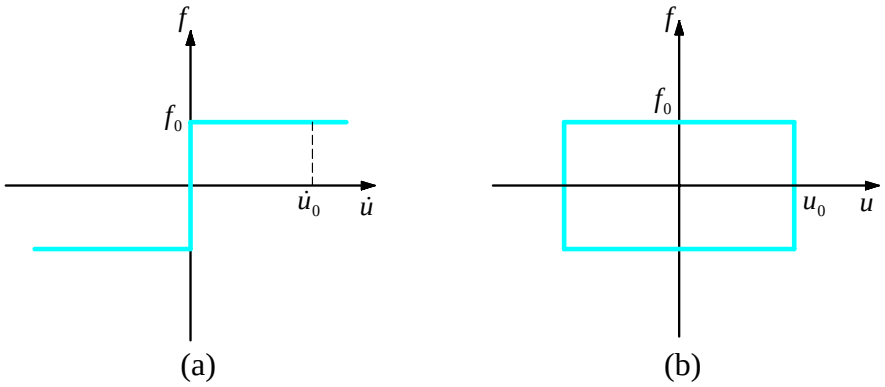

Figure 5.1 Simple frictional model for MR damper: (a) force-velocity relationship; (b) force-displacement relationship

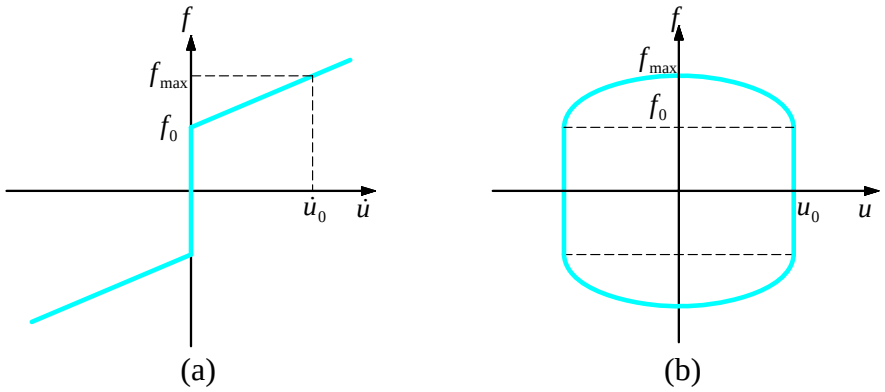

Figure 5.2 Bingham MR damper model: (a) force-velocity relationship; (b) force-displacement relationship

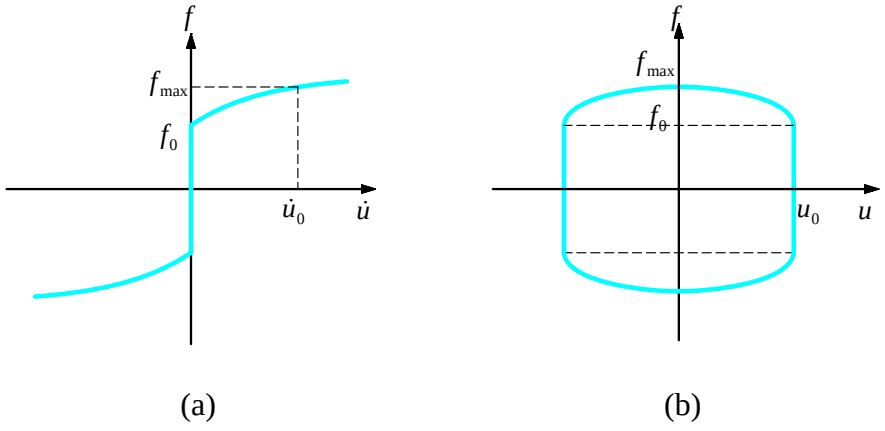

Figure 5.3 Hershel-Bulkley MR damper model: (a) force-velocity relationship; (b) force-displacement relationship

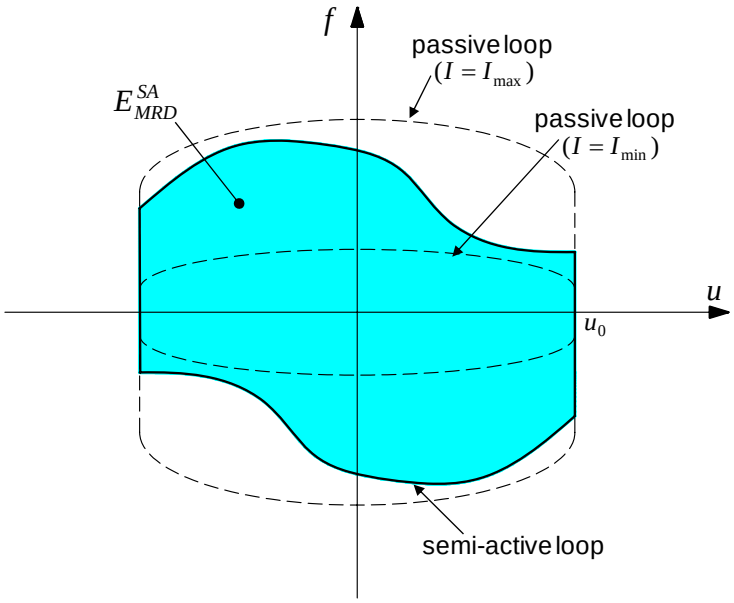

Figure 5.4 Energy dissipation by semi-active controlled MR damper

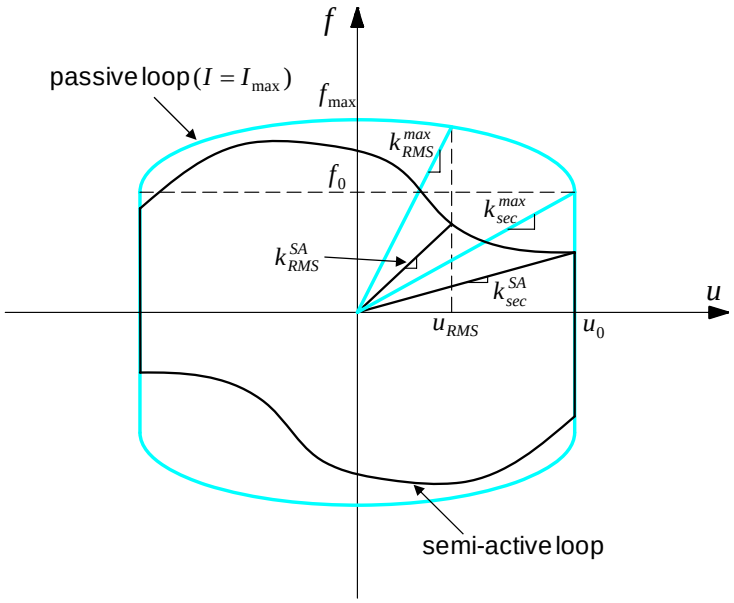

Figure 5.5 Graphical representations of secant stiffness and RMS stiffness of MR damper

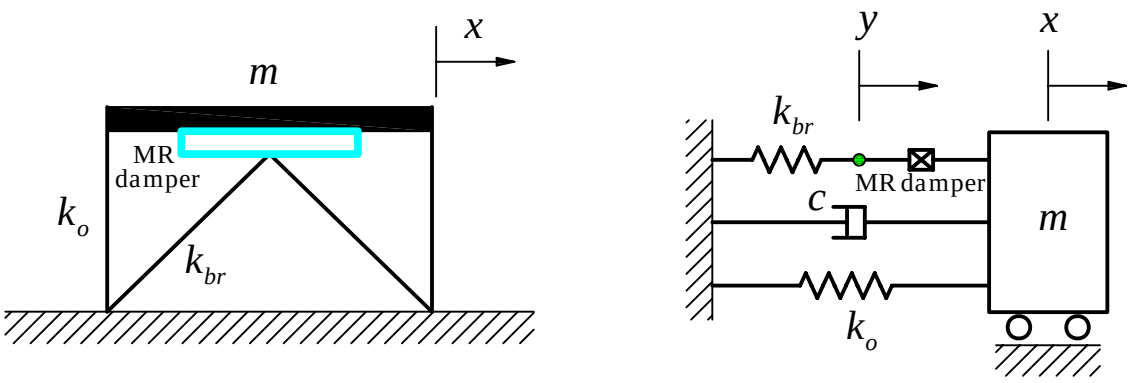

(a) (b)

Figure 5.6 (a) schematic of equivalent SDOF system with MR damper and brace; (b) mechanical model

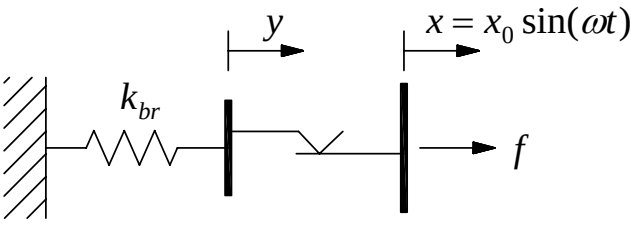

Figure 5.7 Simple frictional model combined with diagonal bracing in series

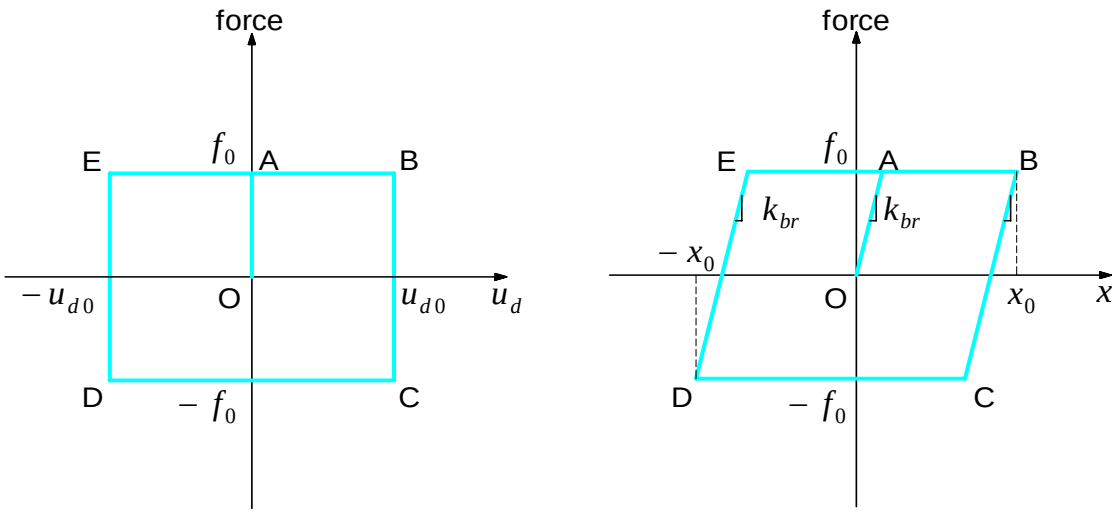

(a) (b)

Figure 5.8 Force-displacement relationship: (a) for simple frictional model; (b) for combined structure

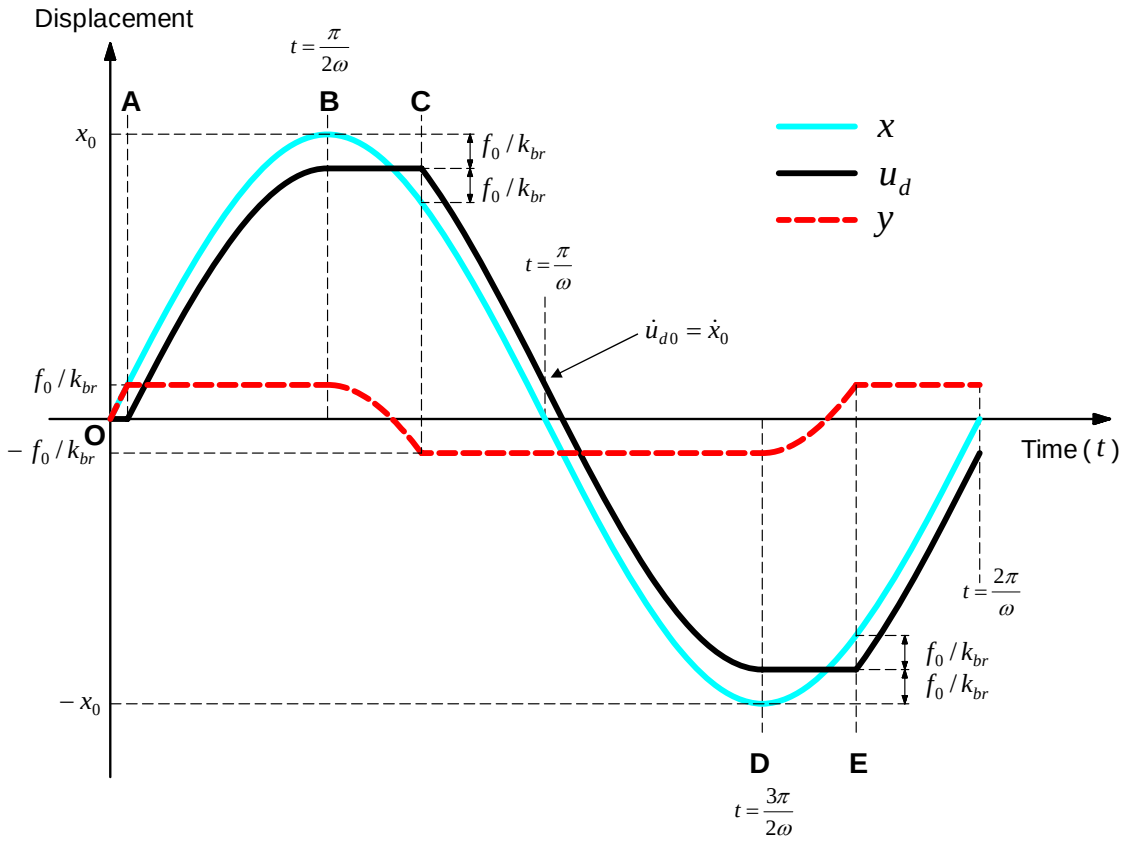

Figure 5.9 Displacement time history for simple frictional model combined with diagonal bracing in series

Given:

MR damper properties: f_0, C, n

Structural properties: m, k_0, k_{br}, ξ_i

Step 1. Assume x_0 and set $\omega_{eff} = \omega_n = \sqrt{k_0/m}$

Step 2. Determine the maximum damper displacement

$$u_{d0} = x_0 - f_0/k_{br}$$

Step 3. Calculate the damper equivalent stiffness, k_{eq}

For secant stiffness: $k_{eq} = k_{sec} = f_0/u_{d0}$

For RMS stiffness: $k_{eq} = k_{RMS} = \frac{\sqrt{2}f_0}{u_{d0}} + C\left(\frac{u_{d0}}{\sqrt{2}}\right)^{n-1}\omega_{eff}^n$

Step 4. Revise the effective frequency and effective period

$$\omega_{eff} = \sqrt{\frac{k_{total}}{m}}, \text{ where } k_{total} = k_0 + \frac{k_{br}k_{eq}}{k_{br}+k_{eq}}$$

$$T_{eff} = 2\pi/\omega_{eff}$$

Step 5. Calculate the equivalent damping ratio

$$\xi_{eq} = \frac{2\left\{f_0 + C\gamma(n)\left(2u_{d0}\omega_{eff}\right)^n\right\}u_{d0}}{\pi k_{total}x_0^2} + \xi_i$$

Step 6. Find the maximum displacement from the response spectrum

$$x_0^{new} = S_d(T_{eff}, \xi_{eq})$$

Step 7. Check convergence: if $\Delta x_0 = x_0^{new} - x_0 >$ tolerance, then set $x_0 = x_0^{new}$ and go to **Step 2**, and repeat **Step 2** ~ **Step 7** until x_0 converges.

Step 8. Set $x_0 = x_0^{new}$ and determine the maximum damper force, f_{max}

$$f_{max} = f_0 + C\dot{u}_{d0}^n = f_0 + C\left(x_0\omega_{eff}\right)^n$$

Figure 5.10 Simplified analysis procedure for estimating the response of an SDOF system with lateral load resisting frame of stiffness k_0 and an MR damper

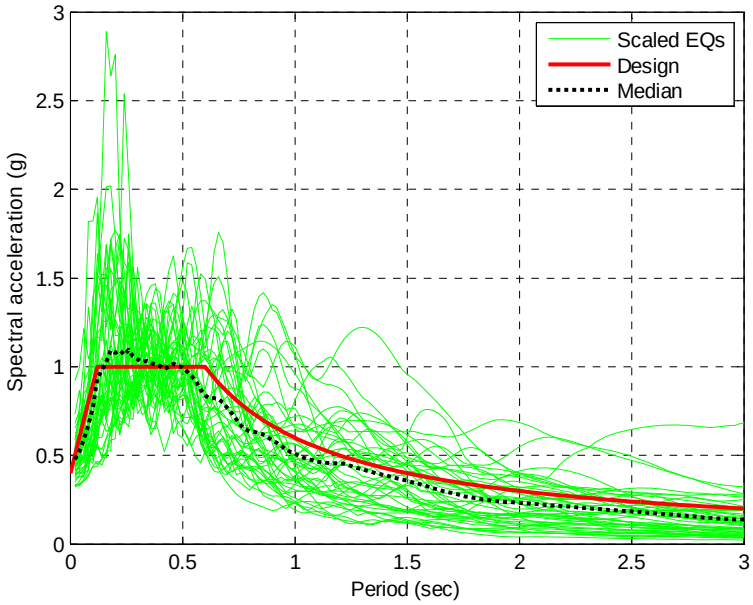

Figure 5.11 Response spectrum of scaled ground motions to DBE response spectrum (T_n=0.5sec)

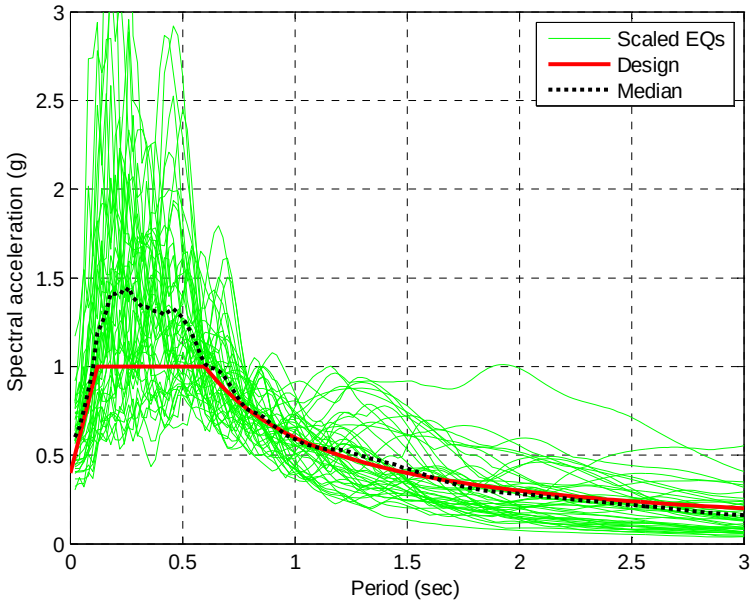

Figure 5.12 Response spectrum of scaled ground motions to DBE response spectrum (T_n=1.0sec)

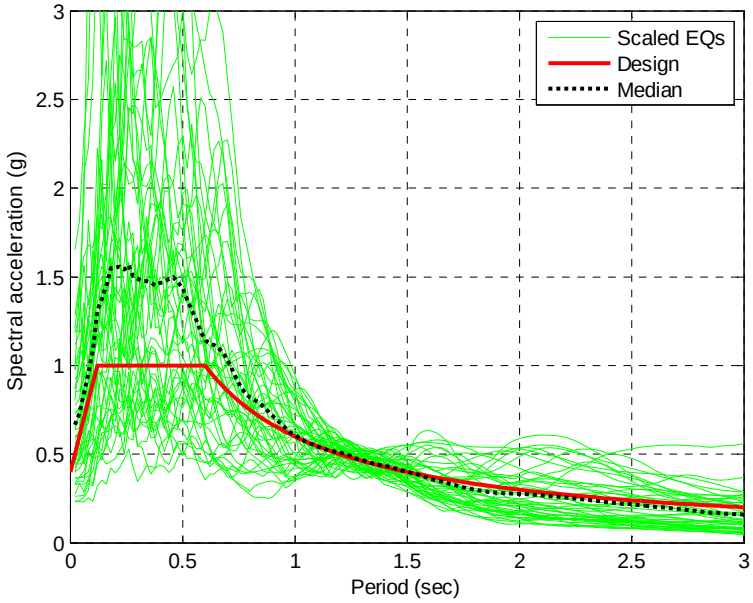

Figure 5.13 Response spectrum of scaled ground motions to DBE response spectrum (T_n=1.5sec)

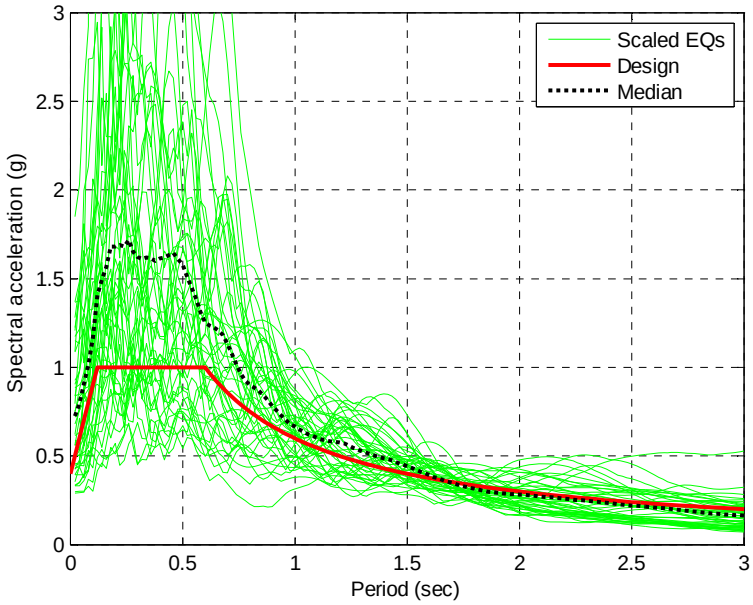

Figure 5.14 Response spectrum of scaled ground motions to DBE response spectrum (T_n=2.0sec)

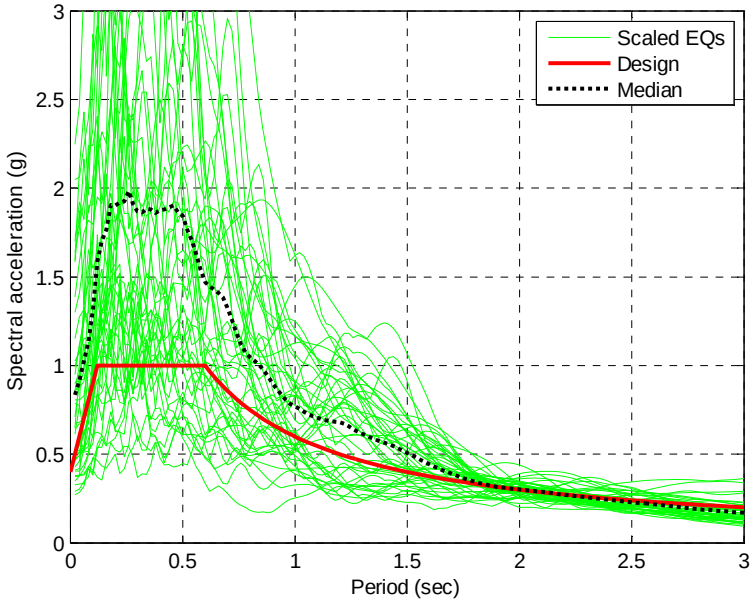

Figure 5.15 Response spectrum of scaled ground motions to DBE response spectrum (T_n=2.5sec)

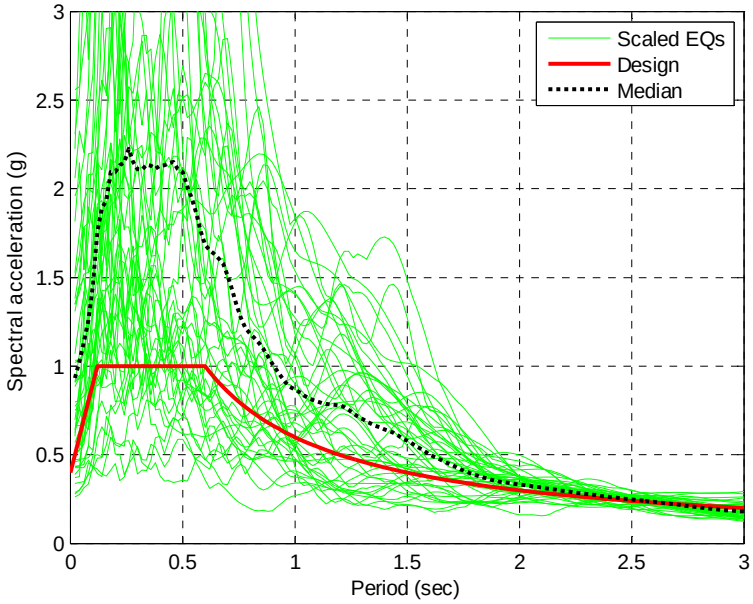

Figure 5.16 Response spectrum of scaled ground motions to DBE response spectrum (T_n=3.0sec)

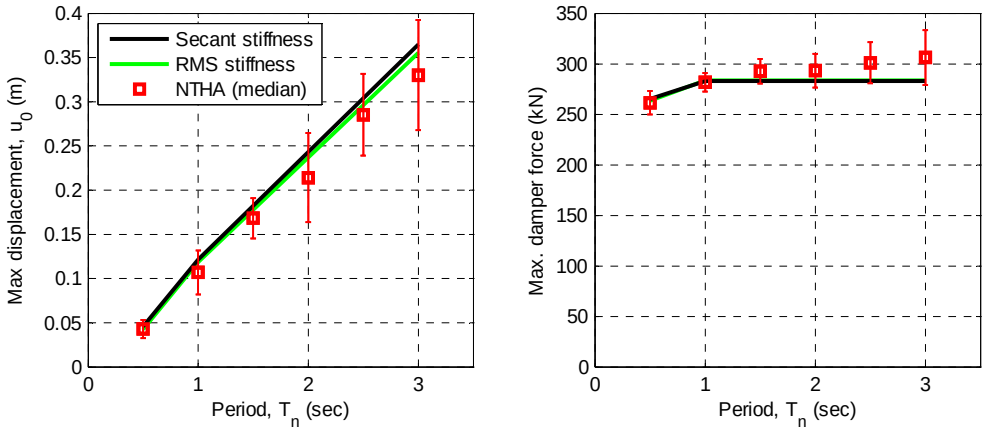

(a) $\xi_{eq} = 10\%$

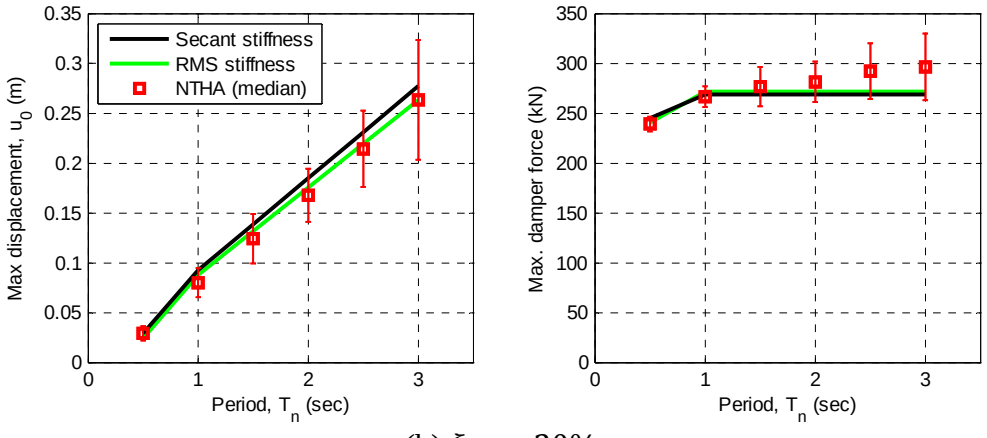

(b) $\xi_{eq} = 20\%$

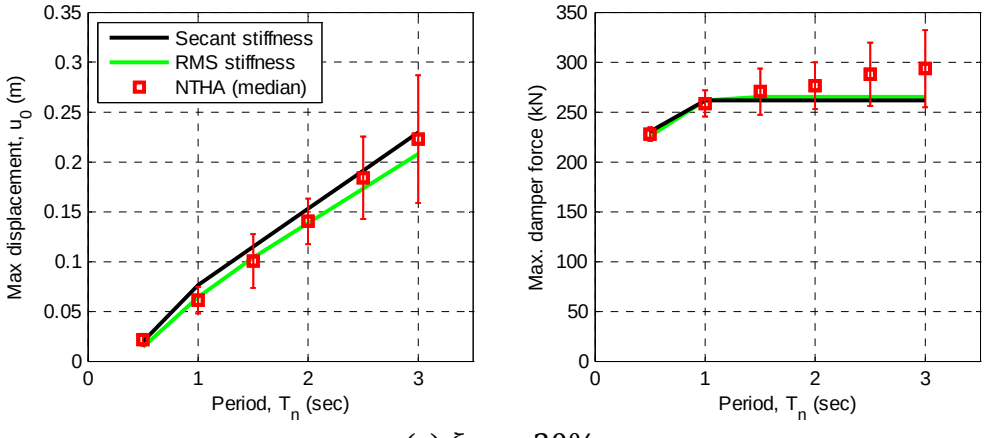

(c) $\xi_{eq} = 30\%$

Figure 5.17 Comparison of SDOF maximum displacement and damper force between the simplified analysis procedure (with secant stiffness and RMS stiffness methods) and the nonlinear time history analysis (vertical line of NTHA shows the range one standard deviation above and below the median response)

Chapter 6

Performance-Based Design Procedure for Structures with MR Dampers

6.1 General

In this chapter, a simplified design procedure (SDP) similar to the one developed by Lee et al. (2005 and 2009) is formulated for structures with passive MR dampers. The equivalent stiffness and damping ratio of MDOF structures are calculated by extending the simplified analysis procedure presented in Chapter 5. The procedure is incorporated into the design of a structure with MR dampers to satisfy specified performance objectives for the structure. A performance-based design procedure for a 3-story building structure with MR dampers is demonstrated in this chapter based on the SDP.

6.2 Equivalent Stiffness and Damping Ratio

In order to obtain an effective period for an MDOF structure with MR dampers, the combined stiffness of the MR dampers and diagonal bracing needs to be added to the global stiffness of the structure; thus, the global effective stiffness of the MDOF system is given as

$$\mathbf{K_{eff}} = \mathbf{K_0} + \mathbf{K_{brsystem}} \tag{6.1}$$

where $\mathbf{K_0}$ is the stiffness of the structure without braces and MR dampers, and $\mathbf{K_{brsystem}}$ is the stiffness associated with the braces and MR dampers. The structure is assumed to have *N* DOF, thus the dimension of $\mathbf{K_{eff}}$ is $N \times N$. The combined stiffness of the brace and MR damper at *i*-th MR damper location, $\mathrm{K}^i_{\mathrm{brsystem}}$, is

$$\mathrm{K}^i_{\mathrm{brsystem}} = \frac{k^i_{br} k^i_{eq}}{k^i_{br} + k^i_{eq}} \tag{6.2}$$

where, k^i_{br} and k^i_{eq} are the horizontal stiffness of the diagonal bracing and MR damper at the *i*-th MR damper location. k^i_{eq} can be calculated utilizing either the secant or RMS stiffness method. The individual combined stiffnesses based on Equation (6.2) are appropriately assembled to form $\mathbf{K_{brsystem}}$. The effective periods and mode shapes of the structure can then be calculated by performing an eigenvalue analysis.

The equivalent damping ratio of an MDOF system can be expressed using the lateral force energy method (Sause et al 1994), where

$$\xi_{eq} = \frac{1}{2} \frac{\sum_{i=1}^{L} \eta_i F^i_d u^i_d}{\mathbf{F}^{\mathrm{T}} \mathbf{x_0}} + \xi_{in} \tag{6.3}$$

where, η_i and u^i_d is the loss factor and damper displacement of the *i*-th MR damper, respectively. *L* is the number of MR dampers. Since the damper displacement is unique for each MR damper, the loss factor of each individual MR damper, which is a function

of damper displacement, is unique for each damper. η_i is obtained from Equation (5.29). ξ_{in} in Equation (6.3) is the inherent damping ratio and $\mathbf{x_0}$ is the vector of the displacements of the structure that develop under the lateral force **F**. The individual damper force F_d^i and the lateral force vector **F** are defined as

$$F_d^i = k_{eq}^i u_d^i, \qquad \mathbf{F} = \mathbf{K_{eff}} \mathbf{x_0} \tag{6.4}$$

Equation (6.3) can be also expressed in matrix form, where

$$\xi_{eq} = \frac{1}{2} \frac{\mathbf{u_d^T} \boldsymbol{\eta} \mathbf{k_{eq}} \mathbf{u_d}}{\mathbf{x_0^T} \mathbf{K_{eff}} \mathbf{x_0}} + \xi_{in} \tag{6.5}$$

where, $\boldsymbol{\eta}$ and $\mathbf{k_{eq}}$ are $L \times L$ diagonal matrices with diagonal terms that are defined as $[\eta_1 \ \eta_2 \ \cdots \ \eta_L]$ and $[k_{eq}^1 \ k_{eq}^2 \ \cdots k_{eq}^L]$, respectively. $\mathbf{u_d}$ is the damper displacement vector, that is, $\mathbf{u_d} = [u_d^1 \ u_d^2 \ \cdots u_d^I]^{\mathrm{T}}$.

6.3 Simplified Design Procedure for MDOF Structures with MR Dampers

In the SDP developed by Lee et al. (2005 and 2009), the supplemental damper properties are represented by β, which is the ratio of the damper stiffness per story in the global direction to the lateral load resisting frame story stiffness, k_0, without dampers and braces. The structural system with dampers is converted into a linear elastic system characterized by the initial stiffness of the structure, α (the ratio of brace

stiffness per story in the global direction to the lateral load resisting frame story stiffness k_0), β, and η. By conducting elastic-static analysis with equivalent lateral forces (ELF), the expected member forces and story drift are determined and checked against the design requirements.

Since the loss factor of an MR damper depends on the displacement of the structure, i.e., η is no longer constant as for elastomeric dampers (Lee et al. 2005 and 2009), the SDP for elastomeric damper needs to be modified appropriately for structures with MR dampers. The loss factor η is associated with the energy dissipation of the damper over a cycle. For purpose of calculating the energy dissipation over a cycle of displacement, the property of the MR damper (i.e., f_0, C, and n) are assumed to remain constant. The impact of this assumption in performance prediction by the SDP is assessed in Chapter 9.

Figure 6.1 summarizes the SDP for structures with MR dampers. In Step 1, the seismic performance objectives and associated design criteria are established for the design of the structure. In Step 2, the structure is designed without MR dampers in accordance with the design code selected in Step 1 to satisfy the strength requirement for the members in the structure; In Step 3, the MR dampers are incorporated into the design of the structure to satisfy the specified performance objectives. The response of the structure is estimated in terms of the α, β, and a constant loss factor η based on the simple frictional MR damper model. Then, the required MR damper sizes are determined in Step 4 based on the β value that meets the design criteria and performance objectives in Step 1. Since the simple frictional damper model does not

account for the velocity dependent behavior of an MR damper, the story drift and member strength of the structure are checked using a more sophisticated MR damper model (i.e., Hershel-Bulkley model). A simplified analysis procedure is employed to predict more accurately the response of the structure based on the selected MR damper properties in Step 4. The design is then revised with final member sizes and MR damper sizes are selected (location, number, force capacity, etc). If the performance objectives cannot be met in an economical manner, then the performance objectives and/or structural system design need to be revised as indicated in Figure 6.1.

6.3.1 Preliminary Estimation Using Frictional MR Damper Model

The simple frictional model for a passive MR damper discussed in Chapter 5 is used for the preliminary estimate of the response of the structure with MR dampers. By inserting $C = 0$ into Equation (5.29), the loss factor of the simple frictional model becomes

$$\eta = \frac{4f_0}{\pi k_{eq} u_{do}} \tag{6.6}$$

If the secant stiffness is used, the equivalent stiffness of a simple frictional model is

$$k_{eq} = f_0 / u_{d0} \tag{6.7}$$

Therefore, the loss factor of a simple frictional model is obtained by substituting Equation (6.7) into Equation (6.6) resulting in

$$\eta = \frac{4}{\pi} \tag{6.8}$$

Since the loss factor is constant, the equivalent damping ratio from Equation (6.5) for a structure with MR dampers using the simple frictional model has the following form

$$\xi_{eq} = \frac{2}{\pi} \frac{\mathbf{u_d^T k_{eq} u_d}}{\mathbf{x_0^T K_{eff} x_0}} + \xi_{in} \tag{6.9}$$

In the SDP proposed by Lee et al. (2005), the damper displacement can be expressed in terms of $\mathbf{x_0}$:

$$\mathbf{u_d} = \left(\frac{\alpha}{\alpha + \beta}\right) \mathbf{H x_0} \tag{6.10}$$

where, $\mathbf{H}$ is a $L \times N$ matrix that associates the total brace and damper deformation with $\mathbf{x_0}$. In Equation (6.10) it is assumed that α and β are constant among all floors. If $\mathbf{x_0}$ is chosen to be proportional to the j-th modal vector (e.g., $\boldsymbol{\phi}_j$) as in the modal strain energy method (Chang et al. 1992), then by substituting (6.10) into (6.9), Equation (6.9) can be rewritten as

$$\xi_{eq} = \frac{2}{\pi}\left(\frac{\alpha}{\alpha+\beta}\right)^2 \frac{\boldsymbol{\phi}_j^{\mathrm{T}}\mathbf{H}^{\mathrm{T}}\mathbf{k_{eq}}\mathbf{H}\boldsymbol{\phi}_j}{\boldsymbol{\phi}_j^{\mathrm{T}}\mathbf{K_{eff}}\boldsymbol{\phi}_j} + \xi_{in} \tag{6.11}$$

Equation (6.11) implies that since $\boldsymbol{\phi}_j$, $\mathbf{k_{eq}}$ and $\mathbf{K_{eff}}$ are uniquely determined for a given α and β, the equivalent damping ratio is a function of only the design variables α and β, not the displacement. Hence, iteration is not necessary to obtain the maximum displacement of the structure when a frictional model is used for the MR dampers.

Once the maximum damper displacement is determined for a given α and β, the maximum damper force of the i-th MR damper can be obtained from Equations (6.7) and (6.10)

$$f_{max}^i = k_{eq}^i u_{d0}^i = \frac{\alpha\beta}{\alpha+\beta} k_0^i u_0^i \tag{6.12}$$

where, k_0^i is the story stiffness and u_0^i is the deformation across the diagonal bracing and damper in the story where the i-th MR damper is installed.

6.3.2 Simplified Analysis Procedure for MDOF Structures with MR Dampers

The simplified analysis procedure provides a methodology for calculation of the structural response of an MDOF system with MR dampers. It uses either the equivalent lateral force method (ELF) or the response spectrum analysis (RSA) method. In the simplified analysis procedure, the maximum structural displacements are determined by the equal displacement rule, which is a well-known empirical rule that is used to assess

the maximum displacement of nonlinear structures subjected to earthquake ground motions. In the equal displacement rule, the maximum displacement of a nonlinear structure is assumed to be the same as that of a linear structure with an initial tangent stiffness of the nonlinear structure, regardless of the ductility of structure. The equal displacement rule is only applicable to structures that lie in the low-frequency and medium frequency spectral regions (Newmark and Hall 1973).

The simplified analysis procedure utilizing either the ELF or the RSA is summarized in Figures 6.2 and 6.3, respectively. Once the maximum displacements and MR damper forces are obtained, the required strength of the members in the MDOF structure can be determined by applying the maximum displacements and damper forces to the structure, as well as the gravity design loads.

6.4 Performance-Based Design of a 3-Story Building with MR Dampers

6.4.1 Prototype Building Structure

An example of the SDP for a 3-story building with MR dampers is provided in this section. The prototype structure used for this study is shown in Figure 6.5. It consists of a 3-story, 6-bay building and represents a typical office building located in Southern California. The floor plan of the prototype building is square in plan, 150ft (=45.72m) by 150ft (=45.72m), with columns spaced at 25ft (=7.62m). Lateral loads are resisted by a total of eight moment resisting frames (MRFs) on the perimeter of the building and eight damped braced frames (DBFs) inside the building. MR dampers are installed in the DBFs to control the drift of the building by adding supplemental

damping to the structure. The DBFs have continuous columns, with pin connections at each end of the beams and diagonal bracing. A rigid diaphragm system is assumed to exist at each floor level and the roof of the building to transfer the floor inertia loads to the MRFs and DBFs. The floor slab, which is assumed to be a rigid diaphragm, is supported on the beams of the MRFs, DBFs, and gravity frames. The height of each story is 12.5ft (=3.81m). The building has a basement where a point of inflection is assigned at $1/3^{rd}$ of the height of the column from the column base. This point is modeled as a hinge support in the analysis model for the building (see Figure 7.1).

6.4.2 Simplified Design Procedure

Figure 6.6 illustrates the SDP for the 3-story building structure. In the procedure, the MRFs are designed to satisfy the strength requirements of the current building seismic code (ICC 2006, AISC 2008). That is, they carry the full seismic base shear of the building. The strength contribution from the DBFs and MR dampers is not considered when the MRFs are designed since the DBFs and MR dampers are intended only to control the story drift of the building system. The DBF members are designed by imposing the displacement and damper force demands on the DBF. The following sections describe the details of the SDP for the performance-based design of the 3-story building structure.

6.4.2.1 Performance Objectives (Step 1)

The seismic performance is quantified in terms of story drift and member plastic rotation (Lee et al 2009). Table 6.1 summarizes performance levels recommended by FEMA (2000b) for steel moment frames. In this example, three different performance objectives for the prototype structure are considered:

- Limit the story drift to 1.5% under the DBE ground motion
- Limit the story drift to 3.0% under the MCE ground motion
- Design strength of members in the DBF shall not be exceeded by the demand imposed by the DBE ground motion

The MCE ground motion is represented by a response spectra that has a 2% probability of exceedance in 50 years, and the DBE ground motion is 2/3rd the intensity of the MCE ground motion. (FEMA 2000a). The performance objectives of 1.5% story drift satisfies the life safety performance level under the DBE. The 3% story drift satisfies the collapse prevention level under the MCE, as defined in Table 6.1. To minimize the damage and repair cost to the DBF structure, the DBF structure is intended to remain elastic under the DBE.

6.4.2.2 Design of MRFs and Gravity Frames (Step 2)

As noted in Figures 6.1 and 6.6, Step 2 of the SDP involves designing the structure without the dampers (i.e., the MRFs and gravity frames) to satisfy the strength requirement of current building seismic codes, in this case, the International Building Code (IBC) (ICC 2006) along with the AISC Steel Construction Manual (AISC 2008).

Design loads and load combinations are determined in accordance with the ASCE/SEI 7-05 (2006). The dead loads are summarized in Tables 6.2 and 6.3, and the live loads in Table 6.4. Live load reduction was considered in determining the live loads. The gravity frames are designed first to resist the gravity loads. The MRFs are then designed to satisfy the lateral strength requirement without any contribution from the DBFs to the lateral resistance. The drift requirement for the structure (ASCE/SEI 7-05) is not checked in the design of the MRFs.

The member forces of the MRF structure are obtained by conducting an elastic-static analysis of an analytical model developed using SAP2000, where the equivalent lateral force procedure is utilized to for the preliminary design. The response modification factor is selected as $R = 8.0$ in accordance with the IBC (ICC 2006) for special steel moment resisting frames. The prototype building is for office occupancy, resulting in Seismic Use Group II with an occupancy importance factor, I_E, equal to 1.0. The building is assumed to be located on stiff soil, which corresponds to Site Class D. The deterministic limits on the maximum considered earthquake ground motion (ICC 2006) are used to determine the design response spectrum, where the spectral acceleration for short period, S_S, and for a 1 second period, S_1, are taken as 1.5g and 0.6g, respectively. Based on these values, along with the site classification, the site coefficients F_a and F_v are equal to 1.0 and 1.5, respectively, resulting in the short period design spectral response acceleration S_{DS} and the design spectral response at one second S_{D1} being equal to 1.0g and 0.6g, respectively. The design response spectrum based on

these values is shown in Figure 6.7. The inherent damping ratio ξ_{in} of the prototype building structure is assumed to be 5.0%.

The controlling load combinations considered in the design are as follows (ASCE/SEI 7-05, Section 2.3.2):

$$\text{GRAV1} = 1.2D + 1.6L + 0.5L_r \tag{6.13}$$

$$\text{GRAV2} = 1.2D + 1.6L_r + 0.5L \tag{6.14}$$

$$\text{EQ1} = 1.2D + 1.0E + 0.5L \tag{6.15}$$

$$\text{EQ2} = 0.9D + 1.0E \tag{6.16}$$

where D=dead load; L=live load; L_r=roof live load; E=earthquake load. The earthquake load considers the effect of the horizontal and vertical seismic loads, E_h and E_v, respectively, where

$$E = E_h + E_v \quad \text{(for EQ1)} \tag{6.17}$$

$$E = E_h - E_v \quad \text{(for EQ2)} \tag{6.18}$$

where

$$E_h = \rho Q_E \tag{6.19}$$

$$E_v = 0.2 S_{DS} D \tag{6.20}$$

where S_{DS} is the short period design spectral response which is defined to be 1.0 as above; ρ is the redundancy factor, which is taken as 1.3 for Seismic Design Category D; Q_E is the effect of horizontal seismic forces. By substituting Equations (6.17) through (6.20) into Equations (6.15) and (6.16), the load combinations involving earthquake loads are redefined as follows:

$$\text{EQ1} = 1.4D + 1.3Q_E + 0.5L \tag{6.21}$$

$$\text{EQ2} = 0.7D + 1.3Q_E \tag{6.22}$$

Effective seismic weights are determined based on the ASCE/SEI 7-05 (Section 12.7.2). The partition load of 20 psf is added to the total dead load of Table 6.2 for the 1st and 2nd floors, resulting in the final effective seismic weights listed in Table 6.5. In the analysis model for the equivalent lateral force procedure, the gravity frame is modeled as a lean-on column with the gravity loading to account for the P-delta effect on the structure. Since the prototype structure has a symmetric floor plan, only one-quarter of the floor plan is considered in the model.

The seismic base shear is determined from the fundamental period and design response spectrum given in Figure 6.7. If the fundamental period obtained from a structural model is larger than the upper limit of the fundamental period in ASCE/SEI 7-05 (Section 12.8.2), the upper limit prescribed in ASCE/SEI 7-05 is used for the seismic base shear. An iteration procedure is required to determine the final seismic base shear by updating the member sizes and comparing the fundamental periods

obtained from the structural model and the IBC. The upper limit of the fundamental period for the prototype building is calculated as $T_{max} = C_U C_t h_n^x = 0.71$ sec, where $C_U = 1.4$, $C_t = 0.028$ (steel moment-resisting frame), and $x = 0.8$, according to ASCE/SEI 7-05. The height above the base to the highest level of the structure is $h_n = 37.5$ ft.

The beams and columns are designed based on criteria from the AISC Steel Construction Manual (AISC 2008). The Load and Resistance Factor Design (LRFD) interaction equations for member axial force and moment are utilized for checking the ratio of demand to capacity as follows

$$\frac{P_u}{\phi_c P_n} + \frac{8}{9}\frac{M_u}{\phi_b M_n} \leq 1.0 \quad \text{for} \quad \frac{P_u}{\phi_c P_n} \geq 0.2 \tag{6.23}$$

$$\frac{P_u}{2\phi_c P_n} + \frac{M_u}{\phi_b M_n} \leq 1.0 \quad \text{for} \quad \frac{P_u}{\phi_c P_n} < 0.2 \tag{6.24}$$

where, P_u is the factored axial load in the member; P_n is the nominal axial load capacity of the member; ϕ_c is a strength reduction factor for axial compression; M_u is the factored moment in the member, which is obtained using the general second-order elastic analysis method (AISC 2008); M_n is the nominal moment capacity of the member; and ϕ_b is a strength reduction factor for flexure.

The prototype building structure is intended to provide the basis for an MRF and DBF which can be constructed for future laboratory tests with MR dampers. Due to laboratory constraints, the prototype building structure and resulting MRF and DBF

were designed at 0.6-scale. The reduced 0.6-scale and full scale structures have the same material; thus, the scale factor for stress is 1.0. The amplitude of acceleration is the same for reduced scale and full scale structures. By employing dimensional analysis, scale factors for various physical quantities are listed in Table 6.6.

Table 6.7 summarizes the final member sizes for the MRF and the gravity frame of the scaled structure, respectively. The required column size at the first story is extended over the height of the building in MRFs, gravity frames, and DBFs.

The doubler plate in the panel zone of the MRF was designed based on the AISC Steel Construction Manual (AISC 2008) and FEMA 350 (2000a) to satisfy the panel zone shear strength. The thicknesses of the doubler plate are 25mm, 25mm, and 8mm for the panel zones at the beam-column joints of the 1st, 2nd, and roof floors, respectively.

6.4.2.3 Determination of α and β Using Frictional MR Damper Model (Step 3)

Step 3 of the SDP develops a preliminary design of the system with dampers by selecting α and β values and using the simple frictional damper model. The MRF design being completed, the story drift of the scaled structure is estimated using the simple frictional MR damper model for selected values of α and β. The stiffness matrix of one MRF and the tributary gravity frames including the P-Δ effect are obtained using SAP2000. The story stiffness k_0 associated with the stiffness matrix is given in Table 6.8. The tributary weights and masses for the scaled structure are listed in Table 6.9. A value of $\alpha = 10$ is assumed for the preliminary design. The ELF method is employed to

obtain the story drift. The fundamental period of structure can be obtained from the mass matrix and $\mathbf{K_{eff}}$. The equivalent lateral force is then determined based on the fundamental period, the equivalent damping ratio defined in Equation (6.11), and the time-scaled response spectrum from FEMA (2000b). Since the equivalent damping ratio is uniquely defined for a given α and β, the ELF used in this step does not involve an iteration procedure. The response modification factor and the deflection amplification factor are assumed to be $R = 1.0$ and $C_d = 1.0$ (linear elastic), respectively, since the equal displacement rule is used. The contribution of the DBF is not considered in this step.

Figure 6.8 shows the response of the structure for various β values, where the structure consisting of MRF, gravity frames, and frictional MR dampers combined with diagonal braces is subjected to the DBE ground motion. Based on Figure 6.8(a), a value of $\beta = 0.3$ is selected in order to satisfy the performance objective of 1.5% story drift, where the predicted story drifts are 0.91%, 1.33%, and 1.48% for the 1st, 2nd, and 3rd stories, respectively.

6.4.2.4 Preliminary Determination of MR Damper Capacity (Step 4)

In Step 4 of the SDP, the approximate size and number of MR dampers are determined from the β value determined in Step 3. Preliminary values for the required damper forces using Equation (6.12) with $\beta = 0.3$ are calculated to be 243kN, 238kN, and 129kN for the 1st, 2nd, and 3rd stories MR dampers, respectively. The preliminary sizes for the MR dampers are selected based on these required damper forces. The

large-scale MR damper studied in Chapter 3 with a current input of 2.5A can generate a 200kN damper force at a velocity of 0.1m/sec. For the preliminary design one large-scale MR damper is selected to be located in each story of the DBF.

6.4.2.5 Elastic-Static Analysis with Hershel-Bulkley Quasi-Static MR Damper Model (Step 5)

In Step 5, the story drifts and the damper forces are calculated using a more sophisticated quasi-static MR damper model, i.e., the Hershel-Bulkley model, along with the simplified analysis procedure provided in Figures 6.2 and 6.3. During this step of the SDP, the size, number, and location of the MR dampers can be further revised to satisfy the performance objectives with an optimum layout of MR dampers. The predicted story drifts and damper forces are then imposed on the DBF structure to calculate member forces needed for a preliminary design of the DBF members. The story drifts and damper forces from the preliminary design of the combined structural system (i.e., MRF, DBF, MR dampers, and gravity frames) are determined and imposed on the DBF to check the strength of the DBF members. If all the strength requirements and performance objectives for the building structure are satisfied, the design can be finalized. Otherwise, the design needs to be revised (through one or more iterations) until the design is satisfactory.

Step 5.1) Calculation of preliminary story drifts and damper forces

Table 6.10 summarizes the calculated story drifts and maximum damper forces of the scaled building structure under the DBE using the ELF (Figure 6.2) and the RSA (Figure 6.3) methods with one large-scale MR damper in each story. In this prediction, the contribution of the MR dampers but not the members of the DBF is included. The MR damper properties presented in Chapter 3 were used, namely, $f_0 = 138.5\,\text{kN}$, $C = 161.8\,\text{kN sec/m}$, and $n = 0.46$ (Hershel-Bulkley curve at a 2.5A constant current input). The secant stiffness method was shown in Chapter 5 to provide reasonably conservative response prediction results compared to the RMS stiffness method. Hence, the secant stiffness method is used for the damper equivalent stiffness to obtain the results given in Table 6.10.

As can be observed in Table 6.10, when three MR dampers are used the story drifts based on the RSA method are less than 1.5%, satisfying the performance objective for drift under the DBE ground motion. Included in Table 6.10 is the case where the building structure is designed without MR dampers. The use of the three MR dampers is shown to significantly reduce the story drift. The structure without dampers develops a story drift which exceeds the maximum allowable story drift (2.0%) for the prototype building structure (Occupancy Category III) according to the IBC (ICC 2006).

The results of the ELF method are more conservative than the RSA method. One of the reasons is that the total seismic weight of structure is considered in the ELF procedure which is simulating the first mode forces. The RSA method is expected to be more accurate than the ELF method. Consequently, the RSA method with the damper

stiffness based on the secant stiffness is used to develop the final design for the structure.

For future tests which will involve the 0.6-scale structure, only two large-scale MR dampers are available. Hence, an investigation was conducted to determine the optimum location of two MR dampers. Using the above MRF design along with a value of $\alpha = 10$ for the braces, the expected story drift under the DBE was calculated using the simplified analysis procedure for various locations of the dampers. The results are given in Tables 6.11 and Table 6.12, where two MR dampers and one MR damper are used, respectively. From these results, the optimal damper location that satisfies the 1.5% story drift limit for the DBE appears to be the case where one MR damper is installed in each of the 2nd and 3rd stories. With this MR damper configuration, the preliminary design of the DBF structure is performed as follows.

Step 5.2) Preliminary design of DBF

MR dampers are assumed to be mounted between the top of the diagonal braces and at the beam-to-column joint. The DBF must be designed to meet the performance objectives where the members remain elastic under the DBE ground motion. To comply with this requirement, the force demands on the members of the DBF are determined. These demands are determined by subjecting the DBF to the expected design drift while also developing the corresponding force in each MR damper.

The maximum MR damper force does not necessarily occur at the same time as the maximum displacement of the structure. If the maximum damper displacement is

assumed to occur at the same time as the building reaches the maximum displacement, as stated in the assumption in Chapter 5, the damper force corresponding to the maximum displacement of the structure is f_0 according to the Hershel-Bulkley quasi-static MR damper model, which is less than the maximum damper force f_{max} (see Figure 5.3(b)). Instead of using f_0 to determine the DBF member design forces, the predicted maximum MR damper forces are applied to the DBF structure produce a more conservative DBF design.

The calculated maximum displacements and damper forces (Table 6.11, case [0 1 1]) from Step 5.1 of the procedure are imposed on the DBF to obtain the DBF member forces as shown in Figure 6.9. The damper forces are applied as self-equilibrating forces at the second and third stories of the structure, while the lateral displacements are applied to the DBF as prescribed displacements. A rigid floor slab is assumed, whereby the displacements in the DBF are the same as the combined system.

The DBF member forces are obtained by performing an elastic-static analysis with the above mentioned ASCE7-05 load combinations of factored dead loads, live loads, and earthquake loads. The earthquake loads Q_E in the load combinations for the DBF design are the maximum displacements and damper forces as explained above. The member sizes are selected to satisfy the strength requirement based on the interaction equations for axial force and bending moment, Equations (6.23) and (6.24). The resulting preliminary member sizes for the scaled DBF structure are shown in Table 6.13. The beam size is determined based on the gravity load only. The axial force in the DBF beams due to the lateral loads is not considered in the DBF design since a

rigid diaphragm is assumed, which is attached to both ends of the beams. Thus, the beams in the DBF structure have the same sizes as those of the gravity frames.

Step 5.3) Calculation of revised story drifts and damper forces for combined structure

With the preliminary DBF structure designed in Step 5.2, the story drifts and damper forces are revised for the combined structure (i.e., MRF, gravity frames, DBF, and MR dampers) using the simplified analysis procedure summarized in Figure 6.3. The effective stiffness and effective period of the structure are revised accordingly, considering the contribution of the DBF structure. Table 6.14 summarizes the predicted story drifts and damper forces of the combined building structure under the DBE ground motion.

Step 5.4) Revision of strength check for DBF structure

Since the DBF designed in Step 5.2 is a preliminary design based on the incomplete building structure, the revised story drifts and damper forces in Step 5.3, which considers all of the structural components of the building structure, are imposed on the DBF structure to check the final member strength. The demand-to-capacity ratios for the DBF structure with the member sizes in Table 6.13 are summarized in Table 6.15 based on Equations (6.23) and (6.24). The design of the braces was controlled by stiffness, $\alpha = 10$, and not strength, hence, the demand-to-capacity ratios for the braces are small in Table 6.15.

6.4.2.6 Final Design Check

In this step, the strength requirement and the performance objectives for the complete building structure designed using the aforementioned procedure are checked. If the structure does not satisfy these criteria, the structure needs to be revised until the design is satisfactory.

The MRF of the building structure was initially designed to satisfy the strength requirement without the DBF and MR dampers in Step 2. Therefore, the MRF satisfies the strength requirement within the final combined structure since the seismic base shear resisted by the MRF in Step 5 is smaller than that used in Step 2 due to the additional lateral force resisting systems, i.e., the DBF and MR dampers.

Three performance objectives, as stated previously, are considered in this building design: i) 1.5% story drift under the DBE; ii) 3.0% story drift under the MCE; and, iii) linear-elastic behavior of the DBF under the DBE. The calculated response of the final 0.6-scale building structure with MR dampers under the DBE and MCE ground motions are provided in Table 6.14 and Table 6.16, respectively. The story drifts under the DBE ground motion satisfy the 1.5% story drift limit, and those under the MCE ground motion satisfy the 3.0% story drift. The linear-elastic behavior of the DBF under the DBE is assured by the demand-to-capacity ratios in Table 6.15, which are less than 1.0.

The natural periods of the final 0.6-scale building structure are summarized in Table 6.17 along with the damping ratios. Those values are identified from the simplified analysis procedure of Figure 6.3 for the final scaled building structure. Since

the equivalent damping ratio and the effective stiffness of the building structure depend on the displacement amplitude, the natural periods and the equivalent damping ratios of the building structure under the DBE and MCE ground motions are different as listed in Table 6.17.

6.5 Summary

In this chapter, a simplified design procedure (SDP) for structures with passive MR dampers was presented. To calculate the story drifts and MR damper forces of the MDOF structure, the SDP was based on an equivalent damping ratio and effective stiffness for an MDOF structure with MR dampers. The SDP is used in the performance-based design of a 3-story building structure with MR dampers. The MRF was designed to satisfy the strength requirement of the current building seismic code. The DBF and MR dampers are intended to control the story drift of the building. The DBF was designed by imposing the maximum displacements and MR damper forces on the DBF, which were predicted from the simplified analysis procedure utilizing the Hershel-Bulkley quasi-static MR damper model. The maximum displacements and the maximum MR damper forces were assumed to occur concurrently in the SDP and its effect on the design of members will be assessed in Chapter 7 using the nonlinear time history analysis.

The designed structure will be used to numerically and experimentally assess the performance of various control strategies for MR dampers. In order to validate the proposed SDP, the results of a series of nonlinear time history analyses for the 3-story

building structure with passive controlled MR dampers are given in Chapter 7. The performance of the building with semi-active controlled MR dampers will be discussed in Chapter 9 and this performance will be compared to that of the building with passive MR dampers.

Table 6.1 Structural performance levels for steel moment frames (FEMA 2000b)

Type	Structural performance level		
	Immediate Occupancy	Life safety	Collapse prevention
Primary*	Minor local yielding at a few places. No fractures. Minor buckling or observable permanent distortion of members	Hinges form. Local buckling of some beam elements. Severe joint distortion; isolated moment connection fractures, but shear connections remain intact. A few elements may experience partial fracture.	Extensive distortion of beams and column panels. Many fractures at moment connections, but shear connections remain intact.
Secondary**	Same as primary.	Extensive distortion of beams and column panels. Many fractures at moment connections, but shear connections remain intact.	Same as primary.
Drift	0.7% transient; negligible permanent	2.5% transient; 1% permanent	5% transient or permanent

* Primary elements and components: elements and components that provide the capacity of the structure to resist collapse under seismic forces

** Secondary elements and components: other elements and components than primary ones

Table 6.2 Dead load for 1st and 2nd floors

Item	Description	Unit weight (psf)
Slab	3.5"light weight concrete on 2" metal deck	43
Deck	2"-18 gage metal deck	3
Ceiling	suspended acoustical tile	3
Flooring	carpet	3
Systems	mechanical/electricity/plumbing	10
Fireproofing	spray on cementitious	3
Cladding	25psf exterior cladding projected onto floor plan	10
Structure	beams/girders/columns/bracing	15
Total	-	**90**

Table 6.3 Dead load for 3rd floor (roof)

Item	Description	Unit weight (psf)
Deck	1.5" Type B metal deck	3
Finish	Insulation and water proofing	11
Ceiling	suspended acoustical tile	3
Systems	mechanical/electricty/plumbing	10
Fireproofing	spray on cementitious	3
Cladding	25psf on exterior walls	5
Structure	beams/girders/columns…	15
Equipment	mechanical equipment on roof	30
Total	-	**80**

Table 6.4 Live loads

Floor level	Unreduced live load L_0 (psf)
1	70
2	70
3 (roof)	20

Table 6.5 Effective seismic weights

Floor level	Seismic weight (psf)
1	110
2	110
Roof	80

Table 6.6 Scale factors

Quantity	Dimension	Scale Factor
Length, width, height	L	λ=0.6
Area	L^2	λ^2
Elastic section modulus *S*	L^3	λ^3
Plastic section modulus *Z*	L^3	λ^3
Moment of inertia	L^4	λ^4
Stress	S	1
Force	$F=S\cdot L^2$	λ^2
Moment	$F\cdot L$	λ^3
Displacement	D=L	λ
Velocity	V=L/T	$\lambda^{1/2}$
Acceleration	$A=L/T^2$	1
Mass	F/A	λ^2
Time	T	$\lambda^{1/2}$

Note: L=Length, S=Stress, F=force, T=time, A=acceleration

Table 6.7 Member sizes for MRF and gravity frame of 0.6-scale building structure

Story (or Floor Level)	MRF		Gravity Frame	
	Column	Beam	Column	Beam
1	W8X67	W18X46	W10X30	W8X40
2	W8X67	W14X38	W10X30	W8X40
3	W8X67	W10X17	W10X30	W8X40

Table 6.8 Story stiffness of 0.6-scale building considering one MRF and tributary gravity frames

	Story stiffness (kN/m)
1st story	25,231
2nd story	16,729
3rd story	8,008

Table 6.9 Tributary weights and masses for 0.6-scale building structure

Floor level	Weight (kN)	Mass (kN·sec^2/m)
1	991.2	101.0
2	991.2	101.0
Roof	720.9	73.5

Table 6.10 Preliminary response of 0.6-scale building structure (without DBF) under DBE

Story	No dampers		With three MR dampers (one MR damper in each story)			
	Story drift (%)		Story drift (%)		Maximum MR damper force (kN)	
	RSA*	ELF*	RSA	ELF	RSA	ELF
1	1.89	2.27	1.06	1.33	217.4	219.9
2	2.29	2.90	1.21	1.62	219.7	227.4
3	2.74	3.34	1.27	1.72	228.9	229.9

*RSA: response spectrum analysis method; ELF: equivalent lateral force method

Table 6.11 Preliminary response of 0.6-scale building structure (without DBF) under DBE with *two MR dampers*

Story	Number of dampers and locations					
	[1 1 0]*		[1 0 1]		**[0 1 1]**	
	Story drift (%)	Damper force (kN)	Story drift (%)	Damper force (kN)	Story drift (%)	Damper force (kN)
1	1.18	224.7	1.20	220.1	**1.32**	-
2	1.43	223.5	1.51	-	**1.37**	**222.4**
3	1.90	-	1.52	233.7	**1.41**	**232.0**

* [1 1 0] means one MR damper is installed in the 1st and 2nd story, and no MR damper in the 3rd story

Table 6.12 Preliminary response of 0.6-scale building structure (without DBF) under DBE with *one MR damper*

Story	Number of dampers and locations					
	[1 0 0]		[0 1 0]		[0 0 1]	
	Story drift (%)	Damper force (kN)	Story drift (%)	Damper force (kN)	Story drift (%)	Damper force (kN)
1	1.44	229.2	1.53	-	1.56	-
2	1.89	-	1.70	228.3	1.80	-
3	2.32	-	2.20	-	1.80	239.5

Table 6.13 Member sizes for DBF structure

Story (or Floor level)	Column	Beam	Diagonal bracing
1	W10X33	W10X30	-
2	W10X33	W10X30	W6X20
3	W10X33	W10X30	W6X20

Table 6.14 Response of 0.6-scale building structure under DBE with two MR dampers (case [0 1 1])

Story	Story drift (%)	Damper force (kN)
1	1.18	-
2	1.35	222.9
3	1.41	233.6

Table 6.15 The ratio of demand-to-capacity for DBF members

Story (or Floor level)	Column (W10X33)	Beam (W10X30)	Brace (W6X20)
1	0.955	0.521	-
2	0.303	0.576	0.270
3	0.079	0.354	0.283

Table 6.16 Response of 0.6-scale building structure under MCE with two MR dampers (case [0 1 1])

Story	Story drift (%)	Damper force (kN)
1	1.91	-
2	2.32	244.4
3	2.57	261.6

Table 6.17 Natural periods and damping ratios of the final 0.6-scale building structure

Mode No.	Without MR dampers		With MR dampers			
			DBE level		MCE level	
	Period (sec)	ξ_{in} (%)	T_{eff} (sec)	ξ_{eq} (%)	T_{eff} (sec)	ξ_{eq} (%)
1	0.94	5.0	0.85	20.4	0.88	16.2
2	0.30	5.0	0.28	15.5	0.29	12.1
3	0.13	5.0	0.13	6.3	0.13	6.5

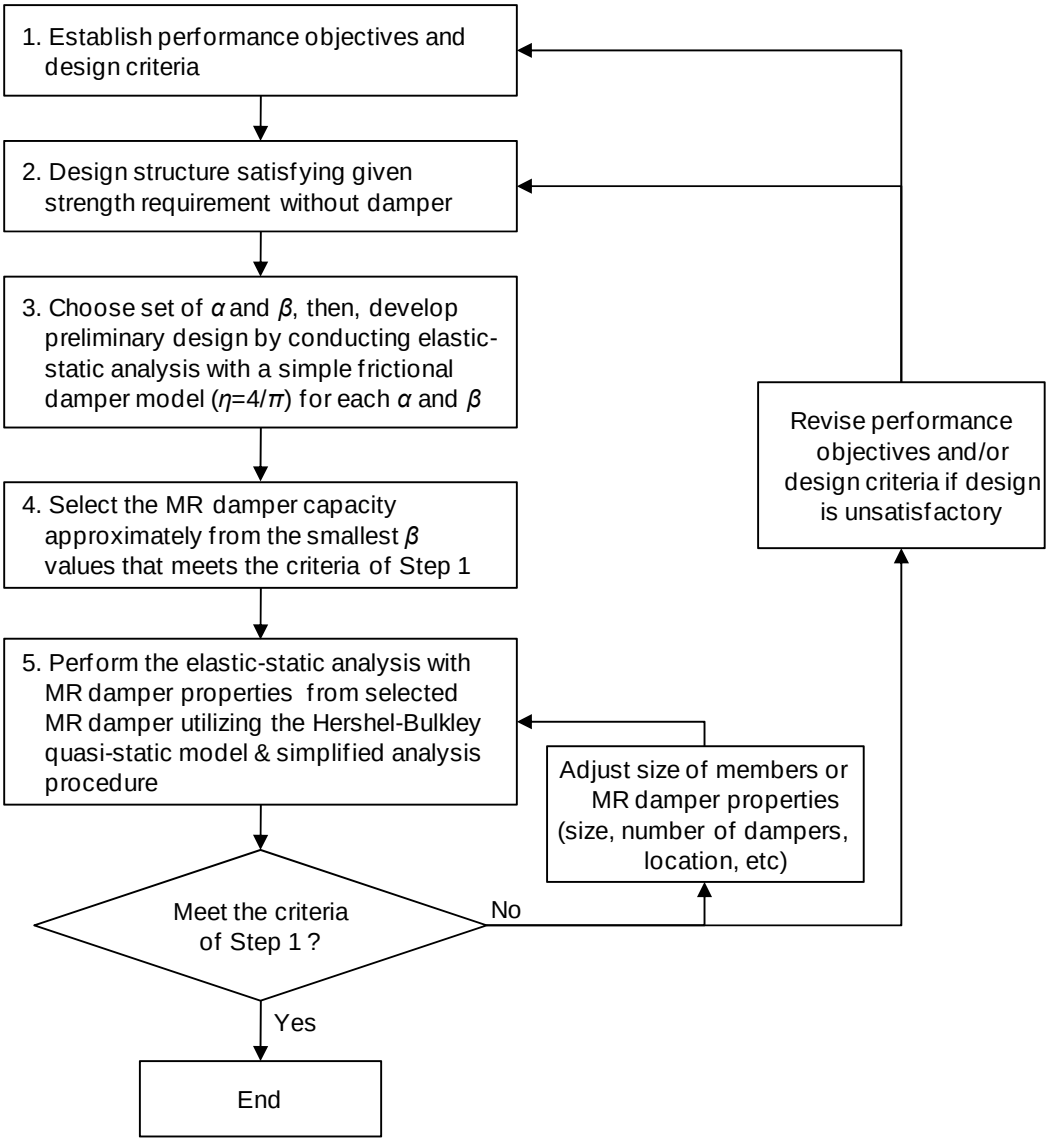

Figure 6.1 General simplified design procedure (SDP) for structures with MR dampers

Given:

MR damper properties: f_0^i, C_i, n_i (i: index of MR damper)
Structural properties: $\mathbf{M}$, $\mathbf{K_0}$, k_{br}^i, ξ_{in}

Step 1. Assume $\mathbf{x_0}$ and set $\omega_{eff} = \omega_n^1$ (fundamental frequency of structure without MR dampers)

Step 2. Determine maximum damper displacements

$$u_{d0}^i = u_0^i - f_0^i/k_{br}^i$$

u_0^i: maximum deformation of damper and bracing at the i-th MR damper

Step 3. Calculate equivalent stiffness of MR dampers (secant or RMS stiffness)

For secant stiffness: $k_{eq}^i = f_0^i/u_{d0}^i$

For RMS stiffness: $k_{eq}^i = \frac{\sqrt{2}f_0^i}{u_{d0}^i} + C_i\left(\frac{u_{d0}^i}{\sqrt{2}}\right)^{n_i-1}\left(\omega_{eff}\right)^{n_i}$

Step 4. Determine $\mathrm{K}_{\mathrm{brsystem}}^i = \frac{k_{br}^i k_{eq}^i}{k_{br}^i + k_{eq}^i}$ for each damper and update $\mathbf{K_{eff}}$

Step 5. Update the fundamental effective period $T_{eff} = 2\pi/\omega_{eff}$

ω_{eff} ← eig($\mathbf{K_{eff}}$, $\mathbf{M}$), where $\mathbf{M}$ is a mass matrix of the structure

Step 6. Calculate equivalent damping ratio using the lateral force energy method

$$\xi_{eq} = \frac{1}{2}\frac{\sum_{i=1}^{L}\eta_i k_{eq}^i (u_{d0}^i)^2}{\mathbf{x_0^T K_{eff} x_0}} + \xi_{in} \quad \text{where } \eta_i = \frac{4\left\{f_0^i + C_i\gamma(n_i)\left(2u_{d0}^i\omega_{eff}\right)^{n_i}\right\}}{\pi k_{eq}^i u_{d0}^i}$$

Step 7. Determine seismic base shear from response spectrum based on T_{eff} and ξ_{eq}

$V = C_S W$ (C_S: seismic response coefficient; W: effective seismic weight)

Step 8. Compute equivalent lateral forces

$$F_j = C_{vj} V$$

(F_j: equivalent lateral force; C_{vj}: vertical distribution factor for j-th floor)

Step 9. Update $\mathbf{x_0}$ by performing elastic-static analysis with equivalent lateral forces

Step 10. Repeat **Step 2** ~ **Step 9** until $\mathbf{x_0}$ convergence is achieved.

Step 11. Determine maximum damper force for each damper

$$f_{max}^i = f_0^i + C_i\left(u_0^i\omega_{eff}\right)^{n_i}$$

Figure 6.2 Simplified analysis procedure used to design MDOF structures with passive MR dampers utilizing equivalent lateral force (ELF) method

Given:

MR damper properties: f_0^i, C_i, n_i (i: index of MR damper)

Structural properties: $\mathbf{M}$, $\mathbf{K_0}$, k_{br}^i, ξ_{in}^j (inherent damping ratio of the j-th mode)

Step 1. Assume $\mathbf{x_0}$ and set $\omega_{eff}^1 = \omega_n^1$ (fundamental frequency of structure without MR dampers)

Step 2. Determine maximum damper displacements

$$u_{d0}^i = u_0^i - f_0^i / k_{br}^i$$

u_0^i: maximum deformation of damper and bracing at the i-th MR damper

Step 3. Calculate equivalent stiffness of MR dampers (secant or RMS stiffness)

For secant stiffness: $k_{eq}^i = f_0^i / u_{d0}^i$

For RMS stiffness: $k_{eq}^i = \frac{\sqrt{2} f_0^i}{u_{d0}^i} + C_i \left(\frac{u_{d0}^i}{\sqrt{2}}\right)^{n_i - 1} \left(\omega_{eff}\right)^{n_i}$

Step 4. Determine $\mathrm{K}_{\mathrm{brsystem}}^i = \frac{k_{br}^i k_{eq}^i}{k_{br}^i + k_{eq}^i}$ for each damper and update $\mathbf{K_{eff}}$

Step 5. Update modal frequency ω_{eff}^j and modal vector $\boldsymbol{\phi}_j$ ($j = 1, \ldots, N$)

ω_{eff}^j , $\boldsymbol{\phi}_j$ ← eig($\mathbf{K_{eff}}$, $\mathbf{M}$), where $\mathbf{M}$ is a mass matrix of the structure

Step 6. Calculate loss factor of MR damper

$\eta_i = \frac{4\left\{f_0^i + C_i \gamma(n_i) \left(2 u_{d0}^i \omega_{eff}^1\right)^{n_i}\right\}}{\pi k_{eq}^i u_{d0}^i}$ where ω_{eff}^1 is the fundamental modal frequency

Step 7. Perform modal analysis from Figure 6.4

Step 8. Apply modal combination rule (SRSS, CQC, etc) to get the final displacement $\mathbf{x_0}$ and velocity of MR damper $\dot{u}_{d0}^i$

$\mathbf{x_0}$ = function of ($\mathbf{x_0^1}, \ldots, \mathbf{x_0^N}$), $\dot{u}_{d0}^i$ = function of ($\dot{u}_{d0}^{i1}, \ldots, \dot{u}_{d0}^{iN}$)

Step 9. Repeat **Step 2** ~ **Step 8** until $\mathbf{x_0}$ convergence is achieved.

Step 10. Calculate maximum damper force

$$f_{max}^i = f_0 + C\left(\dot{u}_{d0}^i\right)^n$$

Figure 6.3 Simplified analysis procedure used to design MDOF structures with passive MR dampers utilizing response spectrum analysis (RSA) method

Step 7. For j=1 to N-th mode

Substep 1. Assume modal displacement vector $\mathbf{x_0^j}$

Substep 2. Determine maximum damper displacement u_{d0}^{ij}

$$u_{d0}^{ij} = u_0^{ij} - f_0^i/k_{br}^i$$

u_0^{ij}: maximum deformation of damper and bracing at the i-th MR damper in mode j

Substep 3. Calculate equivalent modal damping ratio ξ_{eq}^j

$$\xi_{eq}^j = \frac{1}{2}\frac{\sum_{i=1}^{L}\eta_i k_{eq}^i (u_{d0}^{ij})^2}{\mathbf{x_0^{jT}K_{eff}x_0^j}} + \xi_{in}^j$$

Substep 4. Find maximum modal displacement (x_0^j) from response spectrum

$$x_0^j = S_d(T_{eff}^j, \xi_{eq}^j) \text{ where } T_{eff}^j = 2\pi/\omega_{eff}^j$$

Substep 5. Update modal displacement vector $\mathbf{x_0^j}$

$$\mathbf{x_0^j} = \Gamma_j x_0^j \boldsymbol{\phi}_j$$

$\boldsymbol{\phi}_j$: mode vector; $\Gamma_j = \boldsymbol{\phi}_j^T \mathbf{1}/M_j$; $\mathbf{1}$: unit vector; M_j: modal mass (=$\boldsymbol{\phi}_j^T \mathbf{M} \boldsymbol{\phi}_j$)

Substep 6. Repeat Substep 2 ~ 5 until $\mathbf{x_0^j}$ convergence is achieved

Sbustep 7. Calculate maximum damper velocity at i-th MR damper $\dot{u}_{d0}^{ij}$

$$\dot{u}_{d0}^{ij} = u_0^{ij}\omega_{eff}^j$$

Figure 6.4 Modal analysis method for the simplified analysis procedure utilizing response spectrum analysis (RSA) method

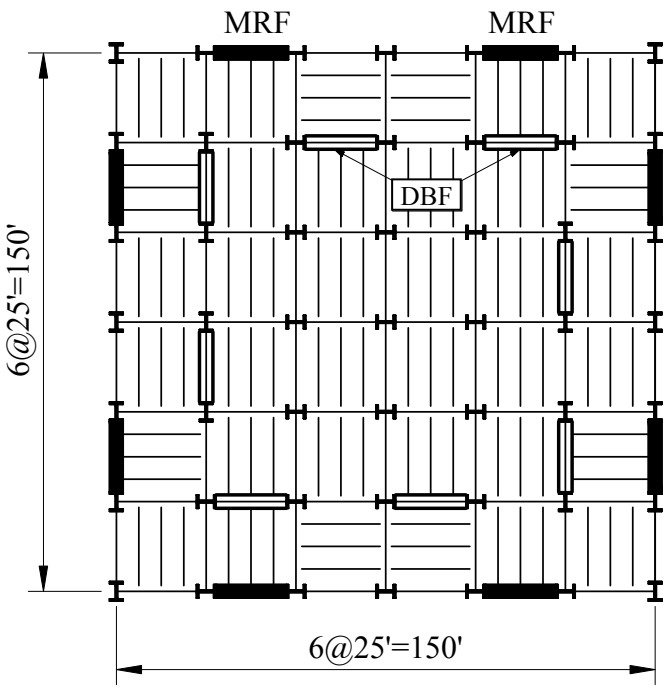

(a) floor plan

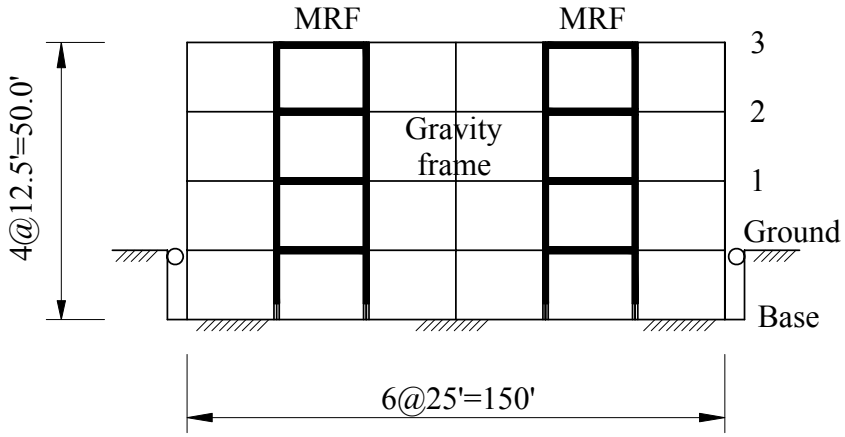

(b) elevation

Figure 6.5 Full-scale building structure

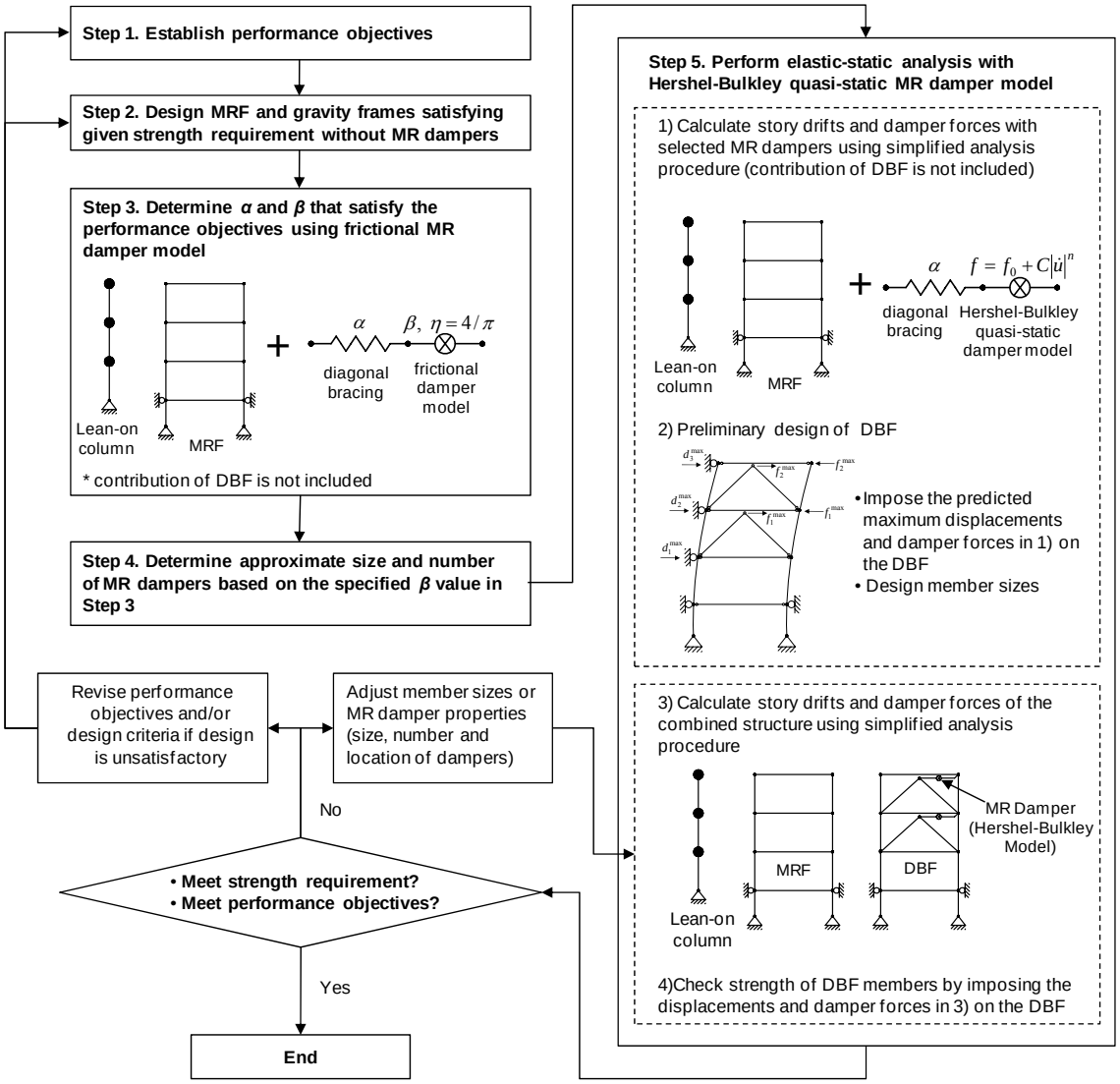

Figure 6.6 Simplified design procedure for 3-story building with MR dampers

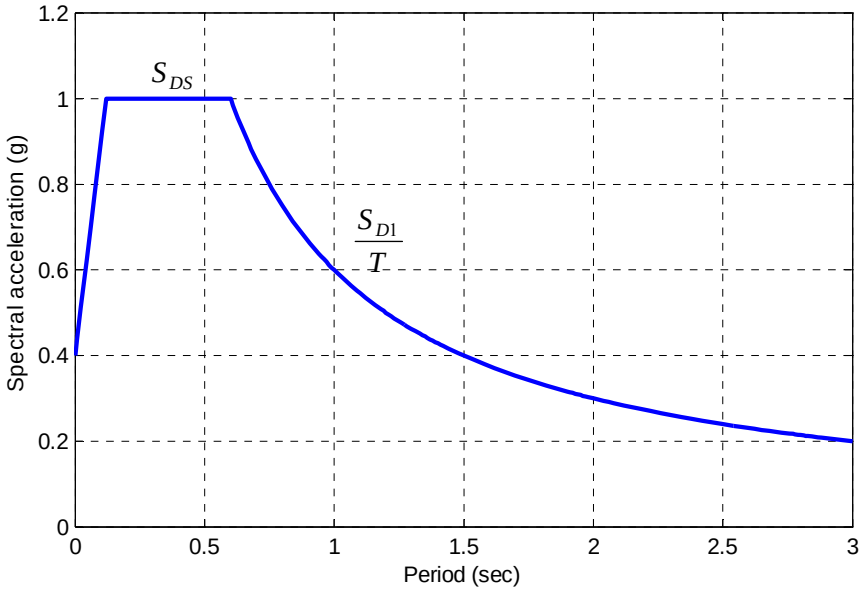

Figure 6.7 Design earthquake response spectrum (ICC 2006)

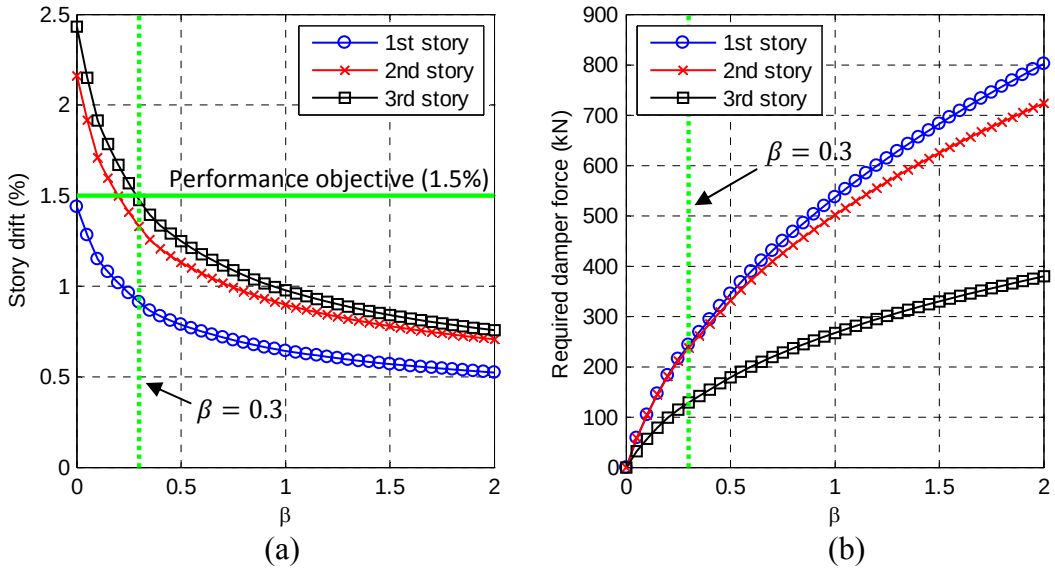

Figure 6.8 Response under DBE for various β values utilizing the simple frictional MR damper model ($\alpha = 10$): (a) story drift response; (b) required MR damper force

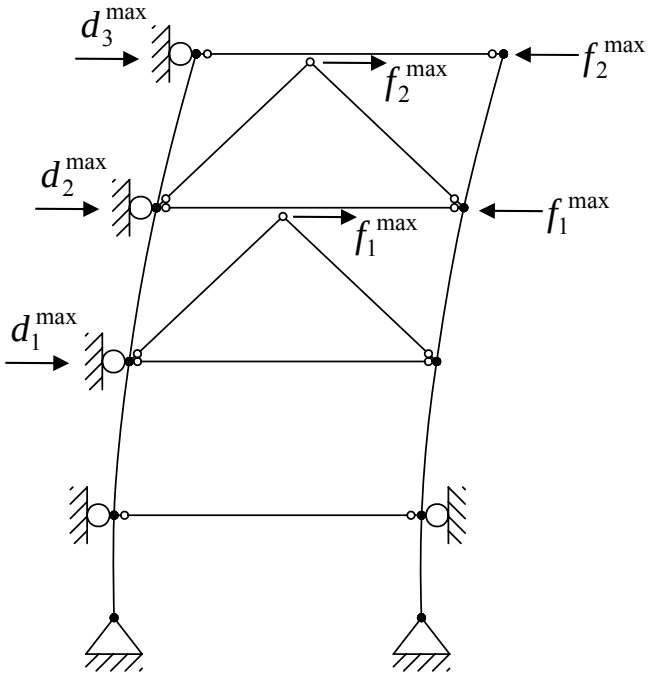

Figure 6.9 Application of maximum displacements (d_i^{max}) and MR damper forces (f_i^{max}) to the DBF structure for the design of DBF members

Chapter 7

Assessment of Simplified Design Procedure

7.1 General

In this chapter, the simplified design procedure (SDP) proposed in Chapter 6 is assessed by comparing the expected behavior with results from a series of nonlinear time history analyses (NTHA) using OpenSees. The calculated responses from the SDP are compared to the results of the NTHA and the accuracy of the SDP is assessed.

7.2 Nonlinear Analytical Modeling Using OpenSees

The scaled building presented in Chapter 6 is modeled using OpenSees (2009). The OpenSees model is shown in Figure 7.1. The member sizes for the MRF and DBF are illustrated in Figure 7.2. The beams and columns of the MRF structure are modeled with a distributed plasticity force-based beam-column element with five fiber sections along the element length. The cross section of the element is discretized into 18 fibers, including 12 fibers for the web and 3 fibers each for the top and bottom flanges. Each fiber is modeled with a bilinear stress-strain relationship with a small post-yielding stiffness, where the elastic modulus and the yield stress of the steel are $E = 2 \times 10^8\ \mathrm{kN/m^2}$ and $F_y = 345{,}000\ \mathrm{kN/m^2}$, respectively. The strain-hardening ratio (the post-yielding modulus over the elastic modulus) is assigned to be 0.01. The beam-column joints are modeled using a four-sided panel zone element, where shear and symmetric column bending deformations are considered (Seo et al. 2009). The doubler

plate in the panel zone is included in the model of the panel zone. The force-based fiber element is also used to model the columns of the DBF. The beams and braces of the DBF are modeled using linear elastic truss elements. An elastic beam-column element with geometric stiffness is used to model the lean-on column. The section properties of the lean-on column is obtained by taking the sum of the section properties of each gravity column within the tributary area of the MRF and the DBF. The MNS MR damper model is implemented in OpenSees as a new *material* with a zero length element. The MR damper is assumed to be located between the top of the brace and the beam-column joint. The parameters that appear in Table 3.3 are used for the MNS model. The MR dampers are passive controlled with a constant current input of 2.5A.

The gravity loads in Table 6.9 from the tributary gravity frames (i.e., one-quarter of the floor plan) are applied to the lean-on column to account for the P-Δ effect of the building. Included in Table 6.9 is also the mass of each floor. Only horizontal ground motion is applied to the building; so only the horizontal mass is defined at each floor level, and this mass is located at the lean-on column. A rigid floor diaphragm is assumed; hence, the top node of the panel zone element in the MRF and the beam-column joint in the DBF are horizontally constrained to the node of the lean-on column at each floor level, while the vertical and rotational dofs are released.

Rayleigh damping is used to model the inherent damping of the building with a 5% damping ratio for the 1st and 2nd modes.

7.3 Results of Nonlinear Time History Analyses

An ensemble of 44 ground motions listed in Appendix 3 is scaled to the DBE and MCE levels using the procedure by Somerville et al. (1997). The fundamental effective periods of the structure with MR dampers are estimated to be around 0.85 sec and 0.88 sec under the DBE and MCE, respectively (see Table 6.17). The T_i values listed in Table 5.2 for T_n=1.0 sec are used for scaling the ground motions to the DBE and MCE levels.

Statistical results (median value and standard deviation) for the maximum story drifts along with the residual story drifts are summarized in Table 7.1. The median value of the maximum story drift is less than 1.5% under the DBE and less than 3.0% under the MCE. The performance of the structure therefore complies with the performance objectives. The median maximum residual story drift is 0.22% and 0.63% under the DBE and MCE, respectively, both occurring in the 3rd story of the structure. In Table 7.2, the median value and standard deviation for the maximum and residual beam plastic rotations of the MRF are summarized. The beams developed yielding at each floor level, but the plastic rotations under the DBE are considered to be small and under the MCE are considered to be modest and would not lead to local buckling and strength degradation of the beams. In Tables 7.3 and 7.4, the median value and standard deviation for the maximum and residual column plastic rotations for the MRF and DBF are provided, respectively. The MRF structure was designed to satisfy the requirement of *strong column-weak beam*. This is consistent with the results of the NTHA, where the columns in the 2nd and 3rd stories remained elastic and yielding developed at only the ground level of the first story column. The column plastic rotation at the ground

level is small under both the DBE and MCE, leading to a small residual drift in the structure, as noted above. The DBF column has behavior similar to that of the MRF column, but the amount of plastic rotation at the column base is not as large for both the DBE and MCE ground motions. In Table 7.5, the statistics for the maximum MR damper forces are summarized. The median values are 231.9kN and 241.5kN in the 2nd and 3rd story dampers, respectively, under the DBE. Under the MCE, larger velocities developed in the dampers leading to larger median maximum damper forces of 248.4kN and 260.2kN in the 2nd and 3rd stories, respectively. The median and standard deviation for the maximum MR damper forces are larger in the 3rd story than the 2nd story.

7.4 Comparison of NTHA Response with Expected Response from the Simplified Design Procedure

The time history response of the structure is given in Figures 7.3 through 7.8 for selected ground motions. The response under the 1992 Landers and 1995 Kobe earthquakes are selected from among the responses to the 44 records in the ensemble of ground motions. Results from these ground motions scaled to the DBE and MCE levels are given, respectively. The responses calculated using the SDP are given in Figures 7.3 through 7.8. Figures 7.9 and 7.10 compare the story drift from the SDP with the median values for maximum story drift from the NTHA under the DBE and MCE ground motions. The response based on the RSA and ELF methods are both given in Figures 7.9 and 7.10, where the secant stiffness method was utilized to obtain the equivalent stiffness of the MR dampers.. Table 7.6 summarizes the story drifts from the SDP under

the DBE and MCE using the RSA and ELF methods. Although a slight underestimation of the 3rd story drift under the DBE is observed in Figure 7.9, the story drifts using the RSA method in the SDP show good agreement with the median maximum story drifts from the NTHA. The RSA method results also show good agreement with the median values from the NTHA under the MCE, see Figure 7.10. The results calculated using the ELF are a conservative estimate of drift response for both DBE and MCE ground motions. The ELF results exceed the median plus one standard deviation NTHA results, and therefore represent story drifts that are approximately in the 84th percentile or greater.

Figure 7.11 compares the maximum MR damper forces from the SDP with the median maximum MR damper forces from the NTHA. Maximum damper forces from both the RSA and ELF methods are summarized in Table 7.7. The MR damper forces from the RSA method are slightly smaller than the median NTHA results for the DBE. However, the differences between the RSA and the NTHA are 3.9% and 3.3% for the MR dampers in the 2nd and 3rd stories, respectively. The differences for MR damper forces from the ELF method are 0.0% and 3.0% for the MR dampers in the 2nd and 3rd stories, respectively, compared to the results of the NTHA. For the MCE the differences between the median NTHA results and the RSA method for the MR damper forces in the 2nd and 3rd stories are 1.6% and 0.5% respectively, and 3.0% and 0.2% for the ELF method, respectively. Both the RSA and ELF results show reasonably good agreement with the median results from the NTHA for the maximum MR damper forces.

In the RSA method, the damper force is based on the total damper velocity which is obtained from the combination of the modal damper velocities (see Figures 6.3 and 6.4). If the maximum damper force is determined from the combination of the modal damper forces (i.e., $f_{max} = \text{function}(f_{max}^{i})$, where f_{max}^{i} is the maximum damper force of the i-th mode), the damper forces under the DBE would be estimated by the SRSS (Square Root of the Sum of the Squares) modal combination rule to be 297.5kN and 313.7kN for the MR dampers in the 2nd and 3rd stories, respectively. These values are too conservative compared to the median maximum damper forces from the NTHA (Table 7.5). This is the reason why the maximum damper force in the RSA method is determined from the total damper velocity, not by a combination of the modal damper forces.

Since the MR damper is in series with the braces in the DBF, the axial forces in the braces are proportional to the MR damper forces. Thus, the actual force demand on the brace members is slightly higher than the forces from the SDP. Figure 7.12 shows the histogram of MR damper forces obtained from the NTHA with the 44 ground motions. The bell-shaped solid line represents a lognormal distribution of the MR damper force based on the mean and standard deviation of the logarithmic values of the MR damper forces in each story. Figure 7.12 shows that if a safety factor ($\rho_s = 1.3$) for the horizontal earthquake load is considered for the design of the diagonal bracing, the factored damper forces from the SDP are considerably higher than the median of the maximum damper forces from the NTHA. Thus, the design based on the factored SDP

damper forces using $\rho_s = 1.3$ can assure an elastic behavior of the diagonal bracing in the DBF.

The linear elastic behavior of the DBF columns is confirmed by checking the plastic rotation developed in the columns. In the first story, some plastic rotation did develop at the base of the column under the DBE. However, the median is zero and the standard deviation is 0.0005 radians for the maximum plastic rotation. The median and standard deviation of the maximum plastic rotation in the 2nd and 3rd stories columns are zero under the DBE ground motion, as given in Table 7.4, which indicates a linear elastic behavior of these columns.

In the SDP described in Chapter 6, the DBF is designed assuming that the maximum damper forces and the maximum displacements of the structure occur at the same time. Figure 7.13 provides time histories for normalized story drifts, damper forces, and the moment and axial force at the base of the 1st story DBF column under the 1992 Landers earthquake scaled to the DBE level. These results represent a typical response of the structure to the DBE or MCE ground motions. The structural response is divided by the maximum value of the response so that the normalized value is between -1.0 and 1.0. The 1st story column axial force is primarily associated with the MR damper forces in the 2nd and 3rd stories, while the column base moment is primarily associated with the 1st story drift. The maximum values of the story drift of the 2nd and 3rd stories and the damper forces do not occur concurrently in Figures 7.13 (a) and (b) . When the maximum 2nd and 3rd story drifts occur at around *t*=12.2 sec, the damper force is about 70% of the maximum damper force. It is also observed that the local maximum

moment occurs ahead of the local maximum axial force in some cases, and vice-a-versa in other cases. Comparing Figures 7.13 (c), (a), and (b) however it is apparent that the maximum 1st story drift and the maximum damper forces at the 2nd and 3rd stories occur at the same time, and that these response quantities appear to be in phase with each other. Consequently, the column axial force and moment at the base of the column in the 1st story are in phase with their maximum values occurring simultaneously, as shown in Figure 7.13(d).

Figure 7.14 shows the time history of the demand-to-capacity ratio for the column at the base of the DBF under the 1992 Landers earthquake scaled to the DBE level. Since the ratio of the factored axial force to the axial force capacity exceeded 0.2 (i.e., $P_u/\phi_c P_n > 0.2$), when the column was designed, Equation (6.23) is used to plot the demand-to-capacity ratio. The axial force and moment of the column are obtained from the NTHA and combined with the dead and live loads in accordance with Equation (6.21). Since the maximum moment and the maximum axial force occur at almost the same time (as discussed above), the maximum value of the demand-to-capacity ratio is close to the design value. Thus, applying the maximum damper force along with the maximum displacement for designing the members of the DBF structure does not appear to be too conservative. For the design of the upper story columns, where the dampers are located in the story, the assumption that the maximum damper force and story drift occur simultaneously is conservative.

7.5 Probability of Exceedance

The probability of the maximum responses under the DBE or MCE exceeding the responses from the SDP was determined. The probability distribution for the maximum damper forces, story drifts, residual drifts, member plastic rotations, and residual plastic rotations were determined to be best represented by a lognormal distribution. The probability of exceeding a prescribed response level was thus obtained by using the cumulative distribution along with the lognormal mean and standard deviation of the maximum values for the response quantity.

In Table 7.8 the probabilities of the damper forces exceeding the damper forces from the SDP, $P(f_{max} > f_{SDP})$, are summarized As previously observed in Figure 7.12, the predicted damper forces from the SDP are less than the median maximum values from the NTHA. The results in Table 7.8 indicate that the probability of the maximum damper forces exceeding the design damper forces from the SDP is 0.926 and 0.834 at the 2nd and 3rd stories, respectively, under the DBE, and 0.999 and 0.999 under the MCE when there is no safety factor (i.e., $\rho_s = 1.0$) is used for determining the damper force from the SDP. However, when the value of $\rho_s = 1.3$ is used, then $P(f_{max} > f_{SDP})$ is significantly lower, and equal to 1.11×10^{-16} and 8.39×10^{-12} for the 2nd and 3rd stories under the DBE, and 5.65×10^{-8} and 8.58×10^{-6} under the MCE. The use of $\rho_s = 1.3$ produces very conservative design forces associated with the maximum damper forces, and possibly investigations of using smaller values of ρ_s that are in between 1.0 and 1.3 are warranted.

Table 7.9 summarizes the probability of the maximum story drift exceeding the story drift limits used in the design of the building. The probability of exceeding the 1.5%

story drift limit under the DBE and MCE and the 3.0% story drift limit under the DBE and MCE are given. The θ_{SDP} value of 1.5%, which is the targeted performance under the DBE, shows a maximum probability of exceedance of 0.444 in the 3rd story, indicating that the probability of exceeding the performance objective of 1.5% story drift under the DBE is reasonably acceptable. The probability of exceeding the 1.5%.story drift under the MCE ranges from 0.725 (1st story) to 0.930 (3rd story). The probability of exceeding the drift limit 3.0% (the target drift used in the design of the structure under the MCE) under an MCE ground motion ranges from 0.094 (1st story) to 0.194 (3rd story); only a small probability of exceedance is observed. Under a DBE ground motion, the probability of exceeding the 3.0% story drift ranges from 9.05×10^{-5} (1st story) to 3.58×10^{-4} (3rd story), which is small as expected.

Performance levels for a steel moment frame recommended by FEMA (2000b) are described in Table 6.1. The story drift limits are equal to 0.007, 0.025, and 0.05 rads. for the Immediate Occupancy (IO), Life Safety (LS), and Collapse Prevention (CP) levels, respectively. Table 7.10 summarizes the probability of the maximum story drift exceeding these story drift limits under the DBE and MCE. The probability of the maximum drift exceeding 0.007 rads. under the DBE is high, and therefore, the building with MR dampers will not achieve the IO level under the DBE. The probability of exceeding the drift associated with the LS level of performance is 0.006 in the 2nd and 3rd stories under the DBE and 0.402 in the 3rd story under the MCE. The probability of exceeding the drift of 0.05 rads. associated with the CP level of performance is a maximum value of 4.92×10^{-8} (2nd story) under the DBE and 0.005 (3rd story) under the

MCE. These are considered to be small probabilities of exceedance for these levels of seismic hazard. More discussion related to collapse prevention is given in Chapter 10.

In Table 7.11, the probability of the maximum residual story drift exceeding the residual drift limits for various structural performance levels in Table 6.1 is summarized. For the IO level, the negligible residual story drift in the table is assumed to be 0.2% in this study, which is the drift associated with the required plumbness for the construction of steel frames (AISC 2005). The cause of the residual drift under the DBE is the yielding of the beams and at the base of the 1st story columns in the MRF. The probability of exceeding the residual drift of 0.002 in the 3rd story is 0.794 under the DBE and 0.946 under the MCE, which means the likelihood of achieving IO level is low under the DBE and MCE. The probability of exceeding the residual drift of 1% in the 3rd story associated with the LS level is 0.263 under the DBE and 0.616 under the MCE. The probability of exceeding the 5% residual drift is considerably low under the DBE and MCE so that the CP performance level can be achieved with a small probability of exceedance. The probability of collapse will be discussed more in Chapter 10.

In Tables 7.12 through 7.15, the probability of maximum beam plastic rotation, beam residual plastic rotation, column plastic rotation, and column residual plastic rotation of the MRF structure exceeding three different levels of the plastic rotation (0.005 rads., 0.01 rads., and 0.03 rads.) are provided. The results in Table 7.12 indicate that there is a probability of 0.302 (3rd floor) to 0.376 (2nd floor) among the floors that the maximum plastic rotation in the beams of the MRF will exceed 0.005 rads., and

0.102 (3rd floor) to 0.144 (2nd floor) that 0.01 rads. will be exceeded under the DBE. A plastic rotation of 0.005 rads. is considered to be insignificant, and is associated with initial yielding in the beam. At a plastic rotation of 0.01 rads. the beams will develop significantly more yielding, however for seismic compact sections, the beams will not develop local buckling and no deterioration in strength to have occurred. At a plastic rotation of 0.03 rads. the beams will typically have developed their maximum capacity, and local flange buckling and web distortion is expected, leading to the onset of a degradation in capacity with any increase in amplitude of cyclic deformations. Table 7.12 indicates that the probability of exceeding 0.03 rads. of plastic rotation in the beams is 0.007 (3rd floor) to 0.012 (2nd floor) under the DBE and 0.043 (1st floor) to 0.068 (3rd floor) under the MCE. The probability of the maximum beam residual plastic rotations in the MRF (Table 7.13) exceeding the selected values are less than the probability of the maximum beam plastic rotations in the MRF exceeding the selected values by an average of 2.

The probability of exceeding 0.005 rads. of plastic rotation in the MRF columns in the 2nd and 3rd story is essentially zero, and very unlikely under both the DBE and MCE, complying with the design criteria of a weak beam-strong column response. The columns in the 1st story develop yielding at the base of the column. Table 7.14 indicates that the probability of exceeding the selected values of column plastic rotation of 0.005 rads. are 0.277 and 0.589 under the DBE and MCE, respectively, implying that there is a reasonable chance that yielding will occur at the base of the columns in the MRF under the DBE and MCE. The probability of column plastic rotation exceeding 0.01

rads. is 0.067 and 0.318 under the DBE and MCE, respectively, while the probability of exceeding 0.03 rads. is 0.017 and 0.057 under the DBE and MCE. Plastic rotations of 0.01 rads. and 0.03 rads. will lead to more significant yielding at the base of the 1st story columns, however, because column sections are compact with small flange and web slenderness it is expected that local buckling at the base of the columns will not occur. Therefore the column damage is expected to be minor. Permanent residual plastic rotations at the base of the 1st story columns are small, where the results in Table 7.15 indicate a low probability of 0.001 under the DBE of exceeding 0.01 rads.

In Tables 7.16 and 7.17, the probability of maximum column plastic rotation and column residual plastic rotation of the DBF structure exceeding the three selected levels of plastic rotation (0.005, 0.01, and 0.03) are summarized. Like the MRF, the columns in the DBF developed plastic rotation at only the base of the 1st story column. Only under the MCE is any plastic rotation expected, where the probability of exceeding 0.005 rads., 0.01 rads., and 0.03 rads. is 0.109, 0.046, and 0.008. These probabilities are less than those for the MRF. No yielding under the DBE is expected in the columns, meeting the performance objective used in the design of the DBF where the DBF should remain elastic during the DBE.

7.6 Summary

In this chapter, the simplified design procedure (SDP) was assessed by comparing the results from the analyses used in the SDP with the results of nonlinear time history analyses. The MNS MR damper model was implemented into the

OpenSees computer program and statistics for the response to DBE and MCE ground motions were obtained from a series of nonlinear time history analyses using 44 different ground motions. The story drifts and maximum MR damper forces from the SDP showed good agreement with the median values from the nonlinear time history analyses, confirming the robustness of the simplified analysis procedure used in the SDP. The probability of the responses exceeding specified values was also evaluated using results from the nonlinear time history analyses, further confirming the analysis used in the SDP.

Table 7.1 Median and standard deviation of story drift from nonlinear time history analysis

Story	DBE		MCE	
	Max story drift (%)	Residual story drift (%)	Max story drift (%)	Residual story drift (%)
1	1.18 (0.35)*	0.11 (0.21)	1.86 (0.85)	0.42 (0.62)
2	1.35 (0.36)	0.17 (0.26)	2.10 (0.85)	0.57 (0.66)
3	1.46 (0.33)	0.22 (0.27)	2.32 (0.84)	0.63 (0.69)

* Value in () indicates standard deviation of response

Table 7.2 Median and standard deviation of MRF beam plastic rotation from nonlinear time history analysis

Floor	DBE		MCE	
	Max plastic rotation (rad %)	Residual plastic rotation (rad %)	Max plastic rotation (rad %)	Residual plastic rotation (rad %)
1	0.35 (0.37)*	0.16 (0.27)	1.05 (0.86)	0.49 (0.63)
2	0.37 (0.33)	0.27 (0.31)	1.20 (0.84)	0.68 (0.72)
Roof	0.31 (0.30)	0.18 (0.30)	1.17 (0.86)	0.67 (0.78)

* Value in () indicates standard deviation of response

Table 7.3 Median and standard deviation of MRF column plastic rotation from nonlinear time history analysis

Story	Location along column	DBE		MCE	
		Max plastic rotation (rad %)	Residual plastic rotation (rad %)	Max plastic rotation (rad %)	Residual plastic rotation (rad %)
1	bottom	0.07 (0.25)*	0.06 (0.19)	0.62 (0.76)	0.41 (0.59)
	top	0.00 (0.00)	0.00 (0.00)	0.00 (0.01)	0.00 (0.01)
2	bottom	0.00 (0.00)	0.00 (0.00)	0.00 (0.00)	0.00 (0.00)
	top	0.00 (0.00)	0.00 (0.00)	0.00 (0.01)	0.00 (0.01)
3	bottom	0.00 (0.00)	0.00 (0.00)	0.00 (0.00)	0.00 (0.00)
	top	0.00 (0.00)	0.00 (0.00)	0.00 (0.00)	0.00 (0.00)

* Value in () indicates standard deviation of response

Table 7.4 Median and standard deviation of DBF column plastic rotation from nonlinear time history analysis

Story	Location along column	DBE		MCE	
		Max plastic rotation (rad %)	Residual plastic rotation (rad %)	Max plastic rotation (rad %)	Residual plastic rotation (rad %)
1	bottom	0.00 (0.05)*	0.00 (0.04)	0.08 (0.40)	0.07 (0.35)
	top	0.00 (0.00)	0.00 (0.00)	0.00 (0.00)	0.00 (0.00)
2	bottom	0.00 (0.00)	0.00 (0.00)	0.00 (0.00)	0.00 (0.00)
	top	0.00 (0.00)	0.00 (0.00)	0.00 (0.00)	0.00 (0.00)
3	bottom	0.00 (0.00)	0.00 (0.00)	0.00 (0.00)	0.00 (0.00)
	top	0.00 (0.00)	0.00 (0.00)	0.00 (0.00)	0.00 (0.00)

* Value in () indicates standard deviation of response

Table 7.5 Median and standard deviation of maximum damper force from nonlinear time history analysis

Story	Maximum damper force (kN)	
	DBE	MCE
1	-	-
2	231.9 (6.4)*	248.4 (7.3)
3	241.5 (8.3)	260.2 (9.4)

* Value in () indicates standard deviation of response

Table 7.6 Maximum story drift calculated by simplified analysis procedure

Story	Story drift (%)			
	DBE		MCE	
	RSA	ELF	RSA	ELF
1	1.18	1.47	1.91	2.40
2	1.35	1.81	2.32	3.09
3	1.41	1.92	2.57	3.38

Table 7.7 Maximum MR damper force calculated by simplified analysis procedure

Story	Maximum damper force (kN)			
	DBE		MCE	
	RSA	ELF	RSA	ELF
1	-	-	-	-
2	222.9	231.8	244.4	255.9
3	233.6	234.2	261.6	260.8

Table 7.8 Probability of maximum damper force f_{max} exceeding the predicted damper force from SDP (f_{SDP})

Story	$P(f_{max} \geq f_{SDP})$			
	DBE		MCE	
	$\rho_s = 1.0$	$\rho_s = 1.3$	$\rho_s = 1.0$	$\rho_s = 1.3$
1	-	-	-	-
2	0.926	1.11×10^{-16}	0.999	5.65×10^{-8}
3	0.834	8.39×10^{-12}	0.999	8.58×10^{-6}

Table 7.9 Probability of maximum story drift (θ_{max}) exceeding the performance objectives for story drift in SDP

Story	$P(\theta_{max} \geq \theta_{SDP})$			
	θ_{SDP} = 1.5%		θ_{SDP} = 3.0%	
	DBE	MCE	DBE	MCE
1	0.166	0.725	9.05×10^{-5}	0.094
2	0.330	0.852	5.67×10^{-4}	0.135
3	0.444	0.930	3.58×10^{-4}	0.194

Table 7.10 Probability of maximum story drift (θ_{max}) exceeding selected levels of story drift

Story	IO level $P(\theta_{max} \geq 0.007)$		LS level $P(\theta_{max} \geq 0.025)$		CP level $P(\theta_{max} \geq 0.05)$	
	DBE	MCE	DBE	MCE	DBE	MCE
1	0.981	0.997	0.001	0.208	3.59×10^{-9}	0.003
2	0.996	0.999	0.006	0.295	4.92×10^{-8}	0.004
3	0.999	0.999	0.006	0.402	3.90×10^{-9}	0.005

IO: Immediate Occupancy
LS: Life Safety
CP: Collapse Prevention

Table 7.11 Probability of maximum residual story drift ($\theta_{res,max}$) exceeding selected levels of residual story drift

Story	IO level $P(\theta_{res,max} \geq 0.002)$		LS level $P(\theta_{res,max} \geq 0.01)$		CP level $P(\theta_{res,max} \geq 0.05)$	
	DBE	MCE	DBE	MCE	DBE	MCE
1	0.575	0.827	0.161	0.491	0.015	0.162
2	0.721	0.904	0.203	0.574	0.012	0.176
3	0.794	0.946	0.263	0.616	0.018	0.154

Table 7.12 Probability of maximum beam plastic rotation ($\theta_{pl,MRF}^{beam}$) of MRF exceeding selected levels of plastic rotation

Floor	$P(\theta_{pl,MRF}^{beam} \geq 0.005)$		$P(\theta_{pl,MRF}^{beam} \geq 0.01)$		$P(\theta_{pl,MRF}^{beam} \geq 0.03)$	
	DBE	MCE	DBE	MCE	DBE	MCE
1	0.353	0.885	0.130	0.530	0.010	0.043
2	0.376	0.946	0.144	0.633	0.012	0.048
3	0.302	0.912	0.102	0.599	0.007	0.068

Table 7.13 Probability of maximum beam residual plastic rotation ($\theta_{res,MRF}^{beam}$) of MRF exceeding selected levels of residual plastic rotation

Floor	$P(\theta_{res,MRF}^{beam} \geq 0.005)$		$P(\theta_{res,MRF}^{beam} \geq 0.01)$		$P(\theta_{res,MRF}^{beam} \geq 0.03)$	
	DBE	MCE	DBE	MCE	DBE	MCE
1	0.168	0.490	0.062	0.264	0.007	0.056
2	0.293	0.600	0.120	0.379	0.015	0.115
3	0.176	0.619	0.061	0.339	0.006	0.060

Table 7.14 Probability of maximum column plastic rotation ($\theta_{pl,MRF}^{col}$) of MRF exceeding selected levels of plastic rotation

Story	$P(\theta_{pl,MRF}^{col} \geq 0.005)$		$P(\theta_{pl,MRF}^{col} \geq 0.01)$		$P(\theta_{pl,MRF}^{col} \geq 0.03)$	
	DBE	MCE	DBE	MCE	DBE	MCE
1	0.277	0.589	0.067	0.318	0.017	0.057
2	0.000	0.000	0.000	0.000	0.000	0.000
3	0.000	0.000	0.000	0.000	0.000	0.000

Table 7.15 Probability of maximum column residual plastic rotation ($\theta_{res,MRF}^{col}$) of MRF exceeding certain levels of residual plastic rotation

Story	$P(\theta_{res,MRF}^{col} \geq 0.005)$		$P(\theta_{res,MRF}^{col} \geq 0.01)$		$P(\theta_{res,MRF}^{col} \geq 0.03)$	
	DBE	MCE	DBE	MCE	DBE	MCE
1	0.010	0.353	0.001	0.043	9.85×10^{-6}	5.88×10^{-5}
2	0.000	0.000	0.000	0.000	0.000	0.000
3	0.000	0.000	0.000	0.000	0.000	0.000

Table 7.16 Probability of maximum column plastic rotation ($\theta_{pl,DBF}^{col}$) of DBF exceeding selected levels of plastic rotation

Story	$P(\theta_{pl,DBF}^{col} \geq 0.005)$		$P(\theta_{pl,DBF}^{col} \geq 0.01)$		$P(\theta_{pl,DBF}^{col} \geq 0.03)$	
	DBE	MCE	DBE	MCE	DBE	MCE
1	0.000	0.109	0.000	0.046	0.000	0.008
2	0.000	0.000	0.000	0.000	0.000	0.000
3	0.000	0.000	0.000	0.000	0.000	0.000

Table 7.17 Probability of maximum column residual plastic rotation ($\theta_{res,DBF}^{col}$) of DBF exceeding selected levels of residual plastic rotation

Story	$P(\theta_{res,DBF}^{col} \geq 0.005)$		$P(\theta_{res,DBF}^{col} \geq 0.01)$		$P(\theta_{res,DBF}^{col} \geq 0.03)$	
	DBE	MCE	DBE	MCE	DBE	MCE
1	0.000	0.205	0.000	0.068	0.000	0.011
2	0.000	0.000	0.000	0.000	0.000	0.000
3	0.000	0.000	0.000	0.000	0.000	0.000

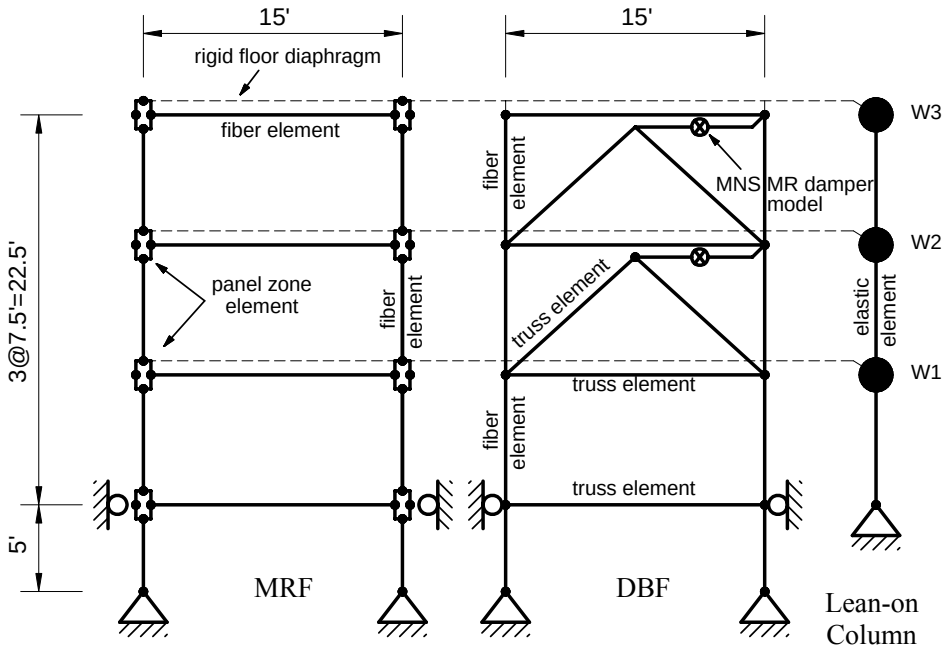

Figure 7.1 OpenSees model for 0.6-scale building structure

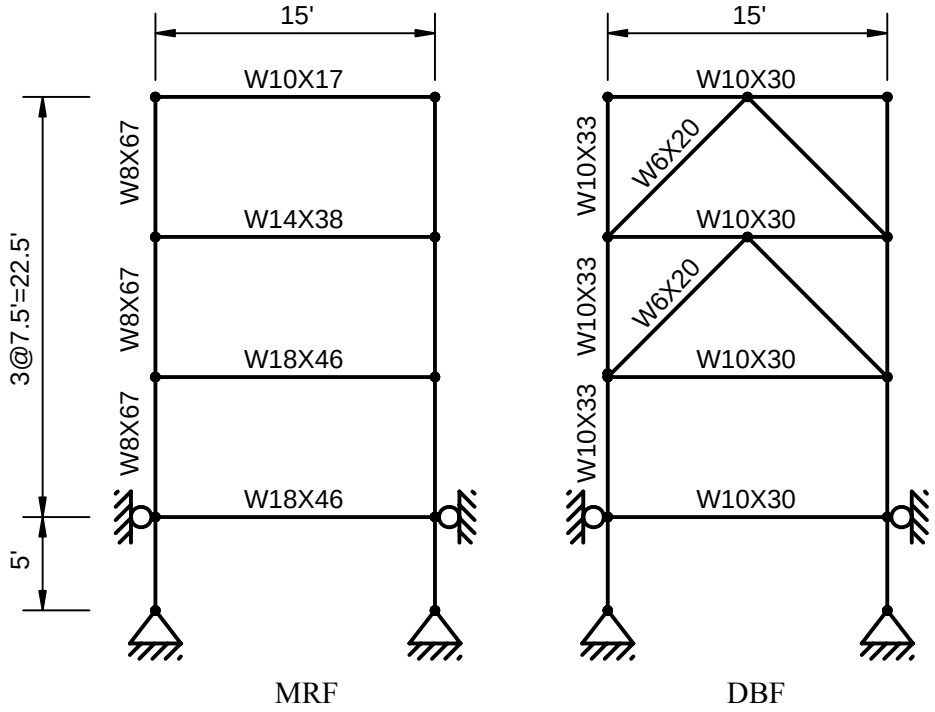

Figure 7.2 Member size of 0.6-scale building structure

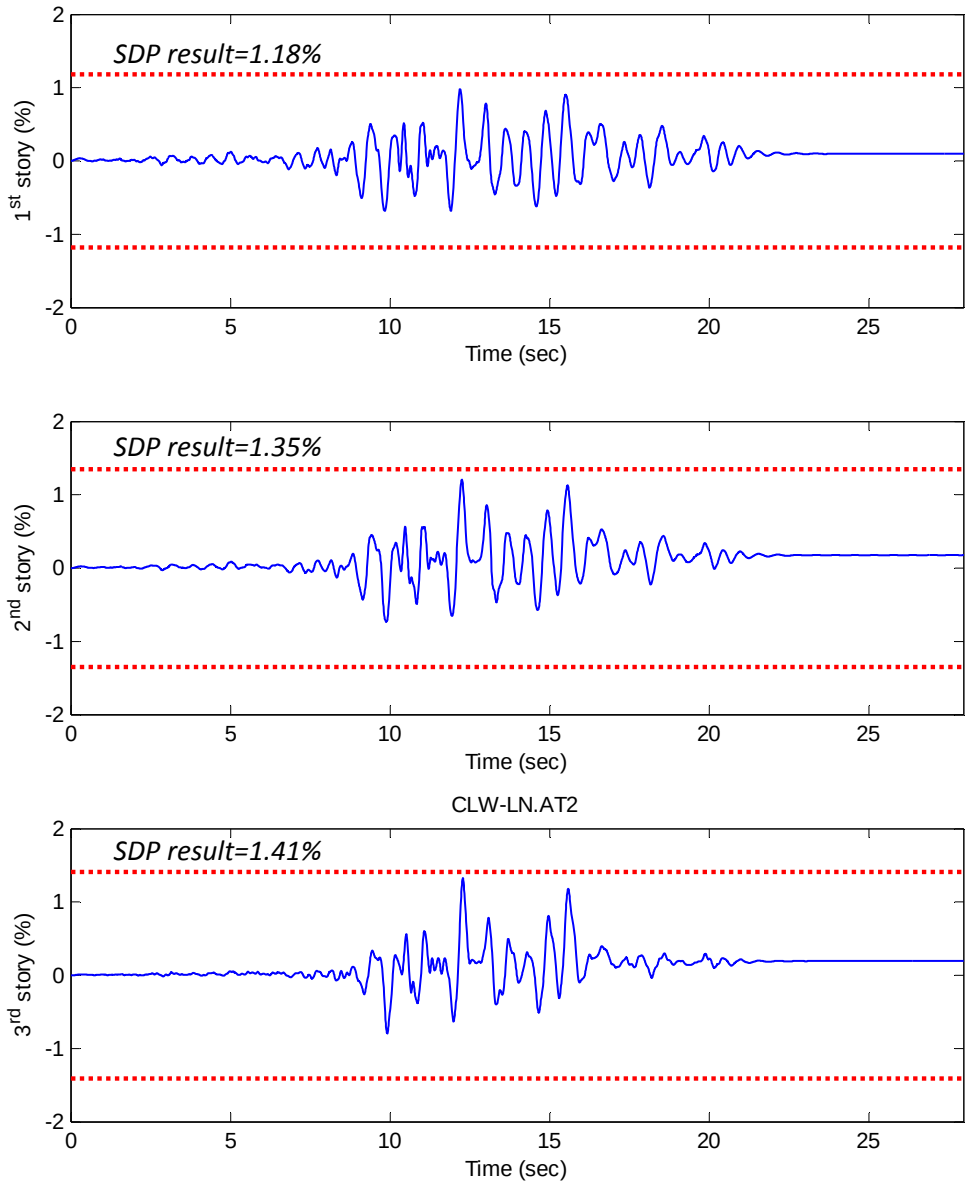

Figure 7.3 Time history story drift response compared to results from SDP (DBE level, EQ: Landers, 1992, Coolwater, longitudinal direction)

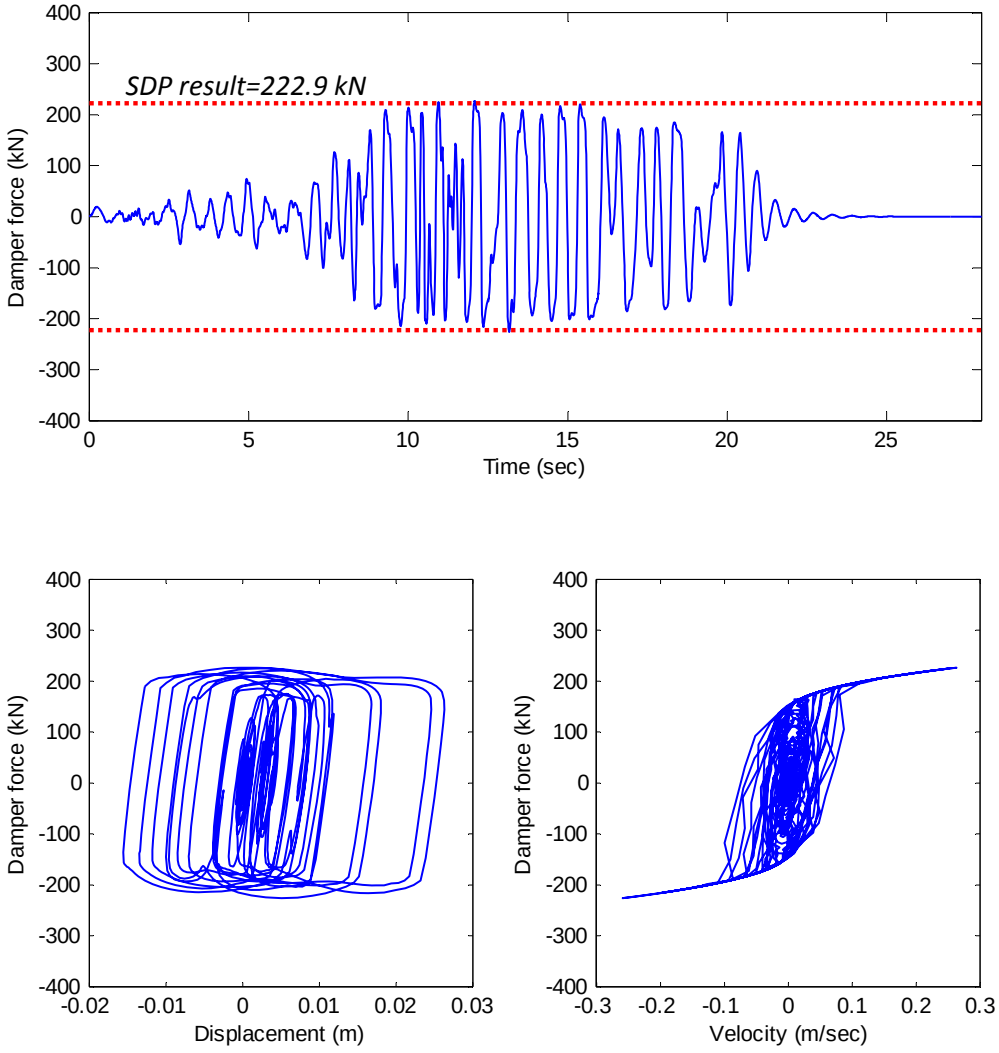

Figure 7.4 Time history response of MR damper in the 2nd story compared to result from SDP (DBE level, EQ: Landers, 1992, Coolwater, longitudinal direction)

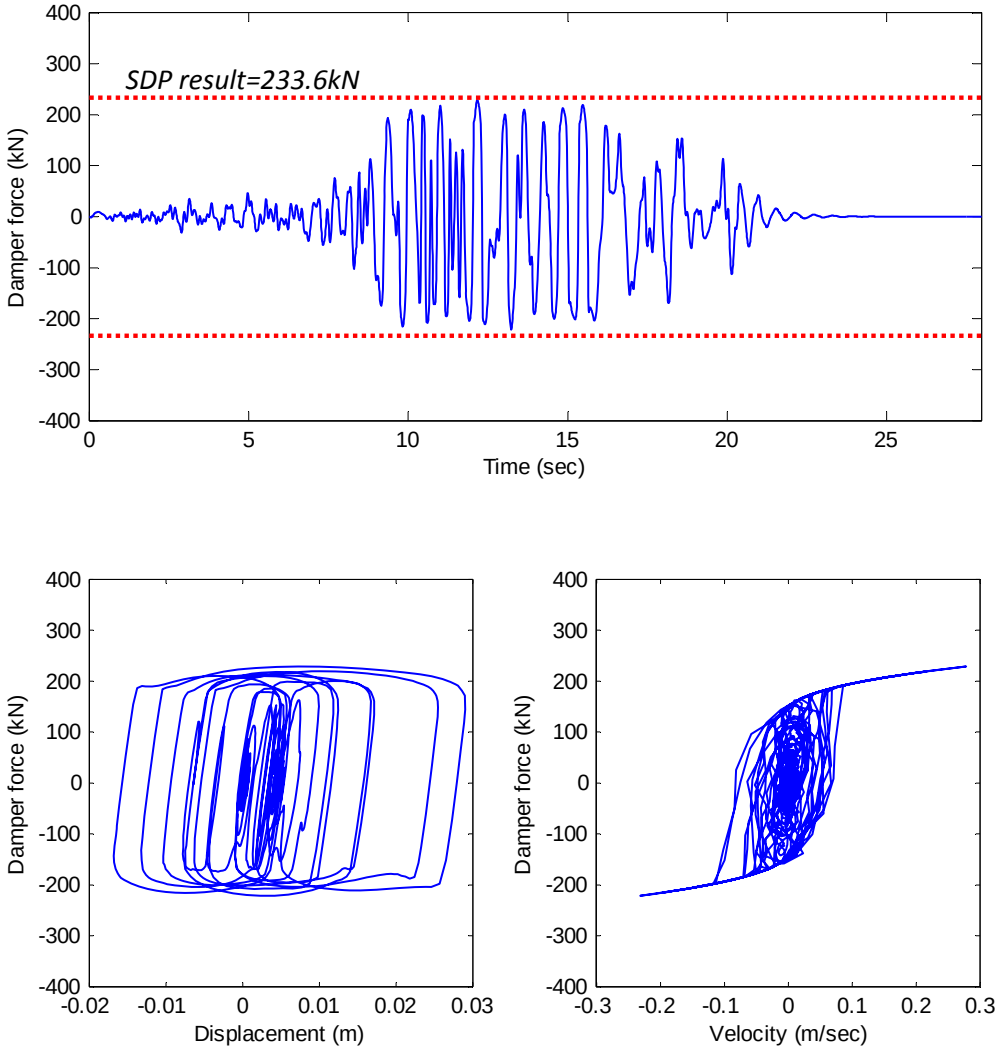

Figure 7.5 Time history response of MR damper in the 3rd story compared to result from SDP (DBE level, EQ: Landers, 1992, Coolwater, longitudinal direction)

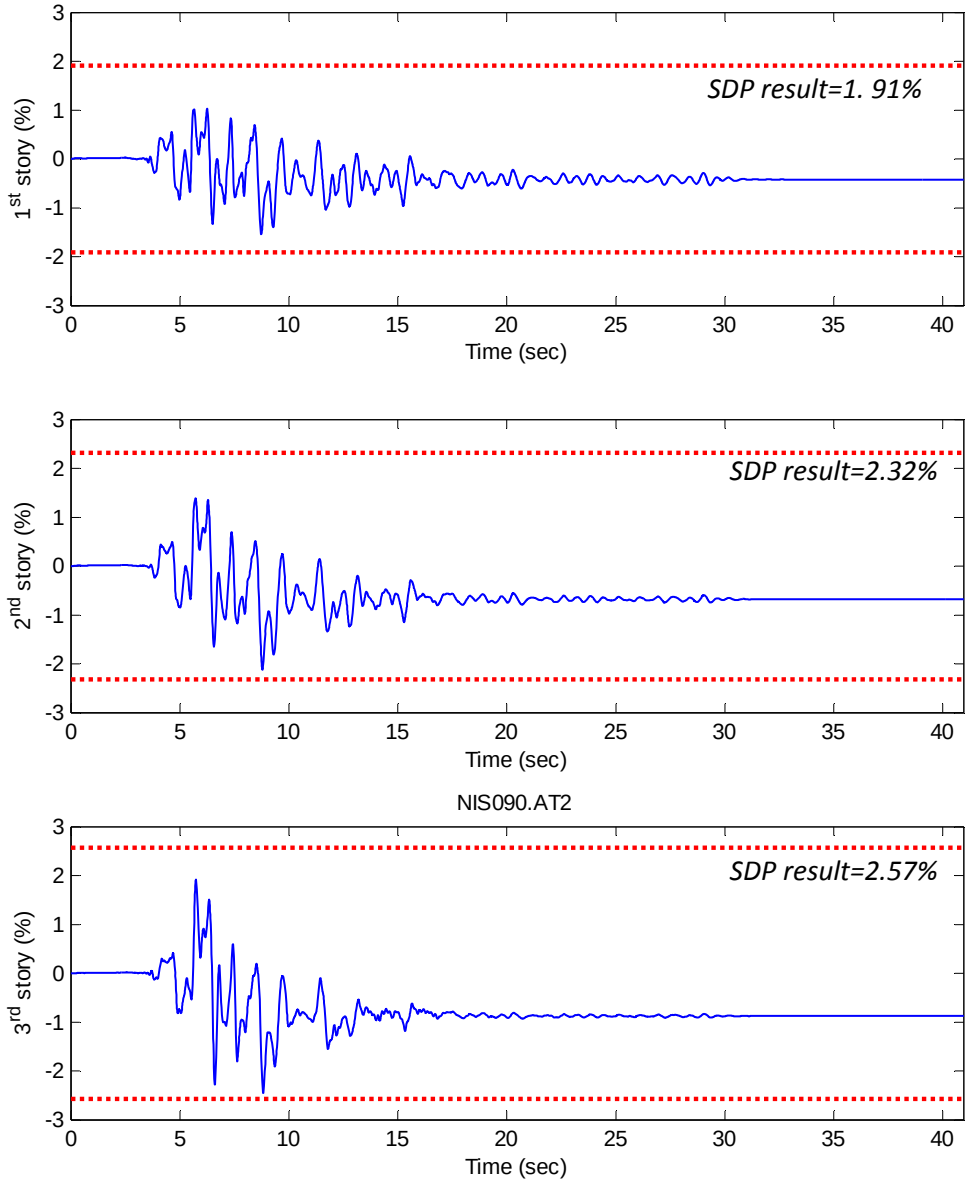

Figure 7.6 Time history story drift response compared to results from SDP (MCE level, EQ: Kobe, 1995, Nishi-Akashi, 090 component)

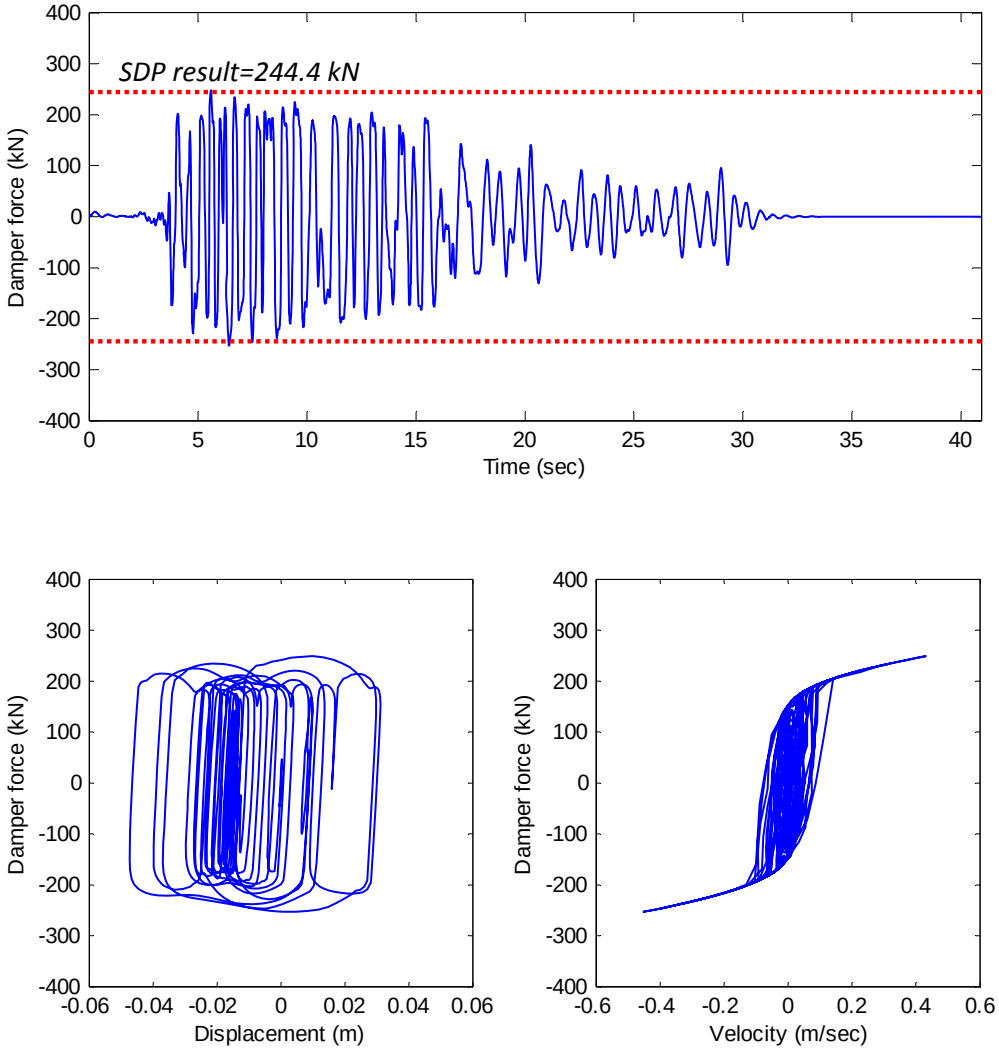

Figure 7.7 Time history response of MR damper in the 2nd story compared to result from SDP (MCE level, EQ: Kobe, 1995, Nishi-Akashi, 090 component)

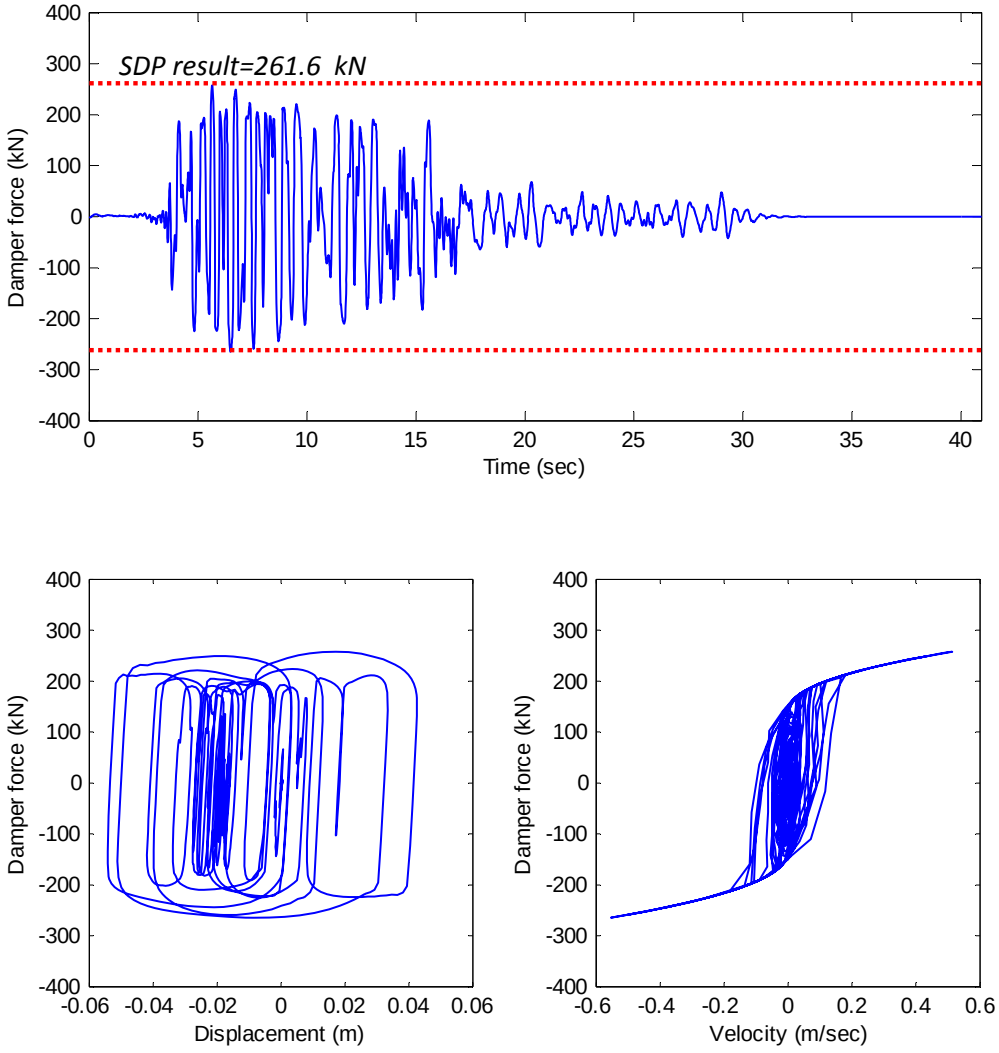

Figure 7.8 Time history response of MR damper in the 3rd story compared to result from SDP (MCE level, EQ: Kobe, 1995, Nishi-Akashi, 090 component)

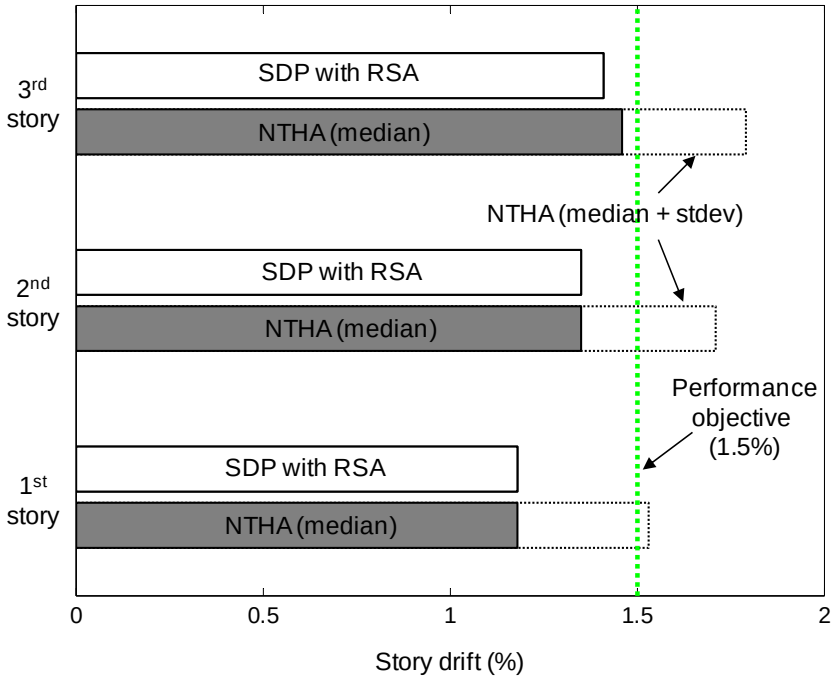

(a)

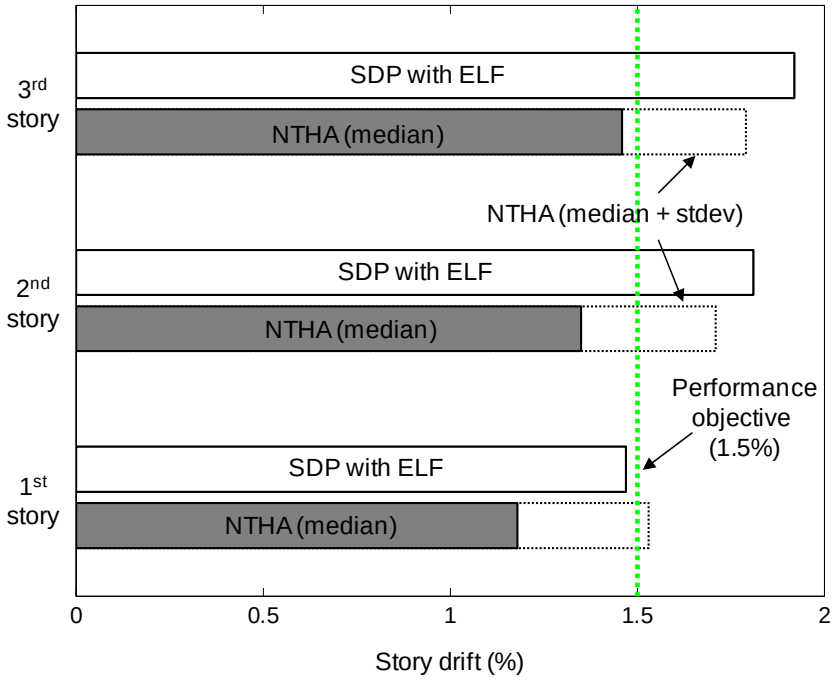

(b)

Figure 7.9 Comparison of story drift between SDP and NTHA under DBE: (a) with RSA method; (b) with ELF method

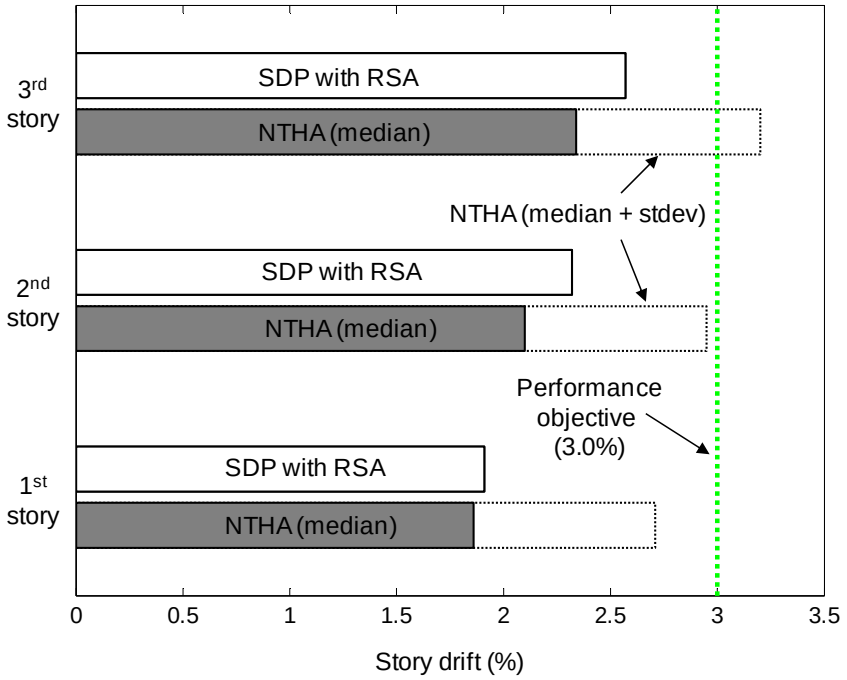

(a)

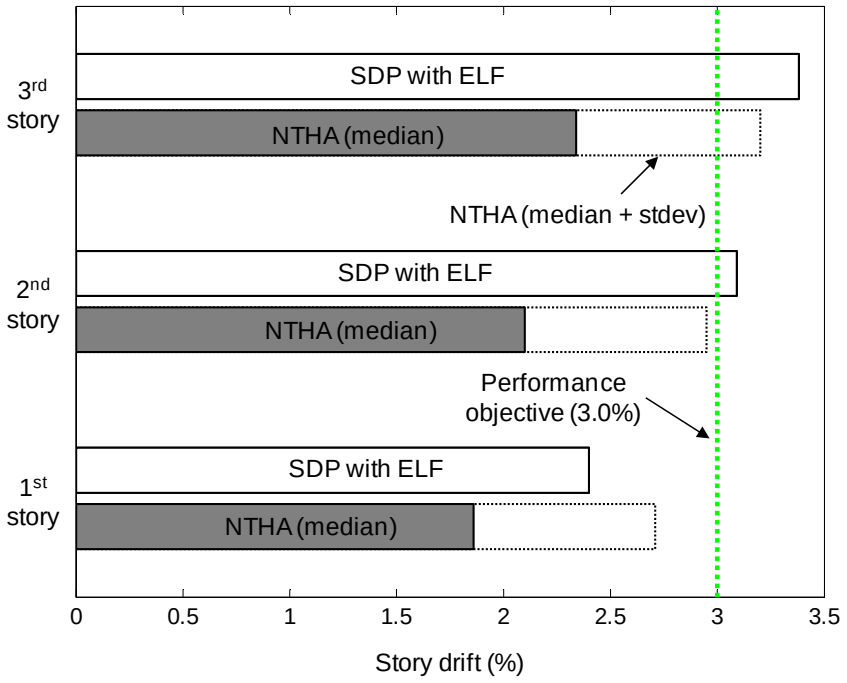

(b)

Figure 7.10 Comparison of story drift between SDP and NTHA under MCE: (a) with RSA method; (b) with ELF method

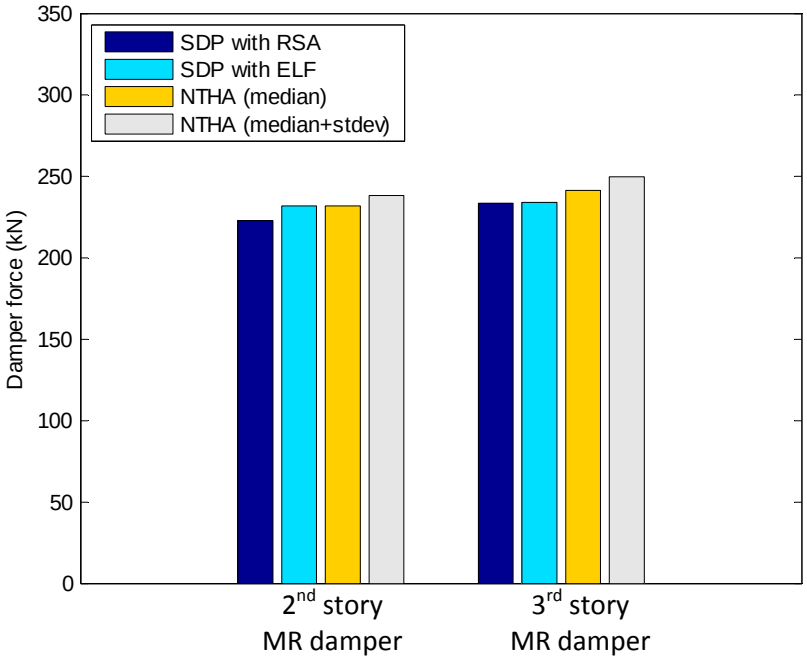

(a)

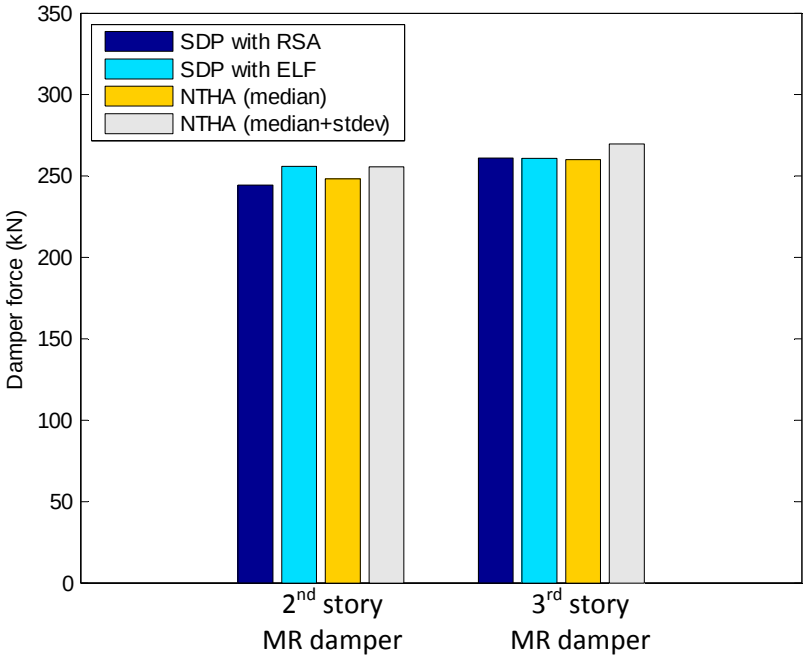

(b)

Figure 7.11 Comparison of MR damper force between SDP and NTHA: (a) DBE level; (b) MCE level

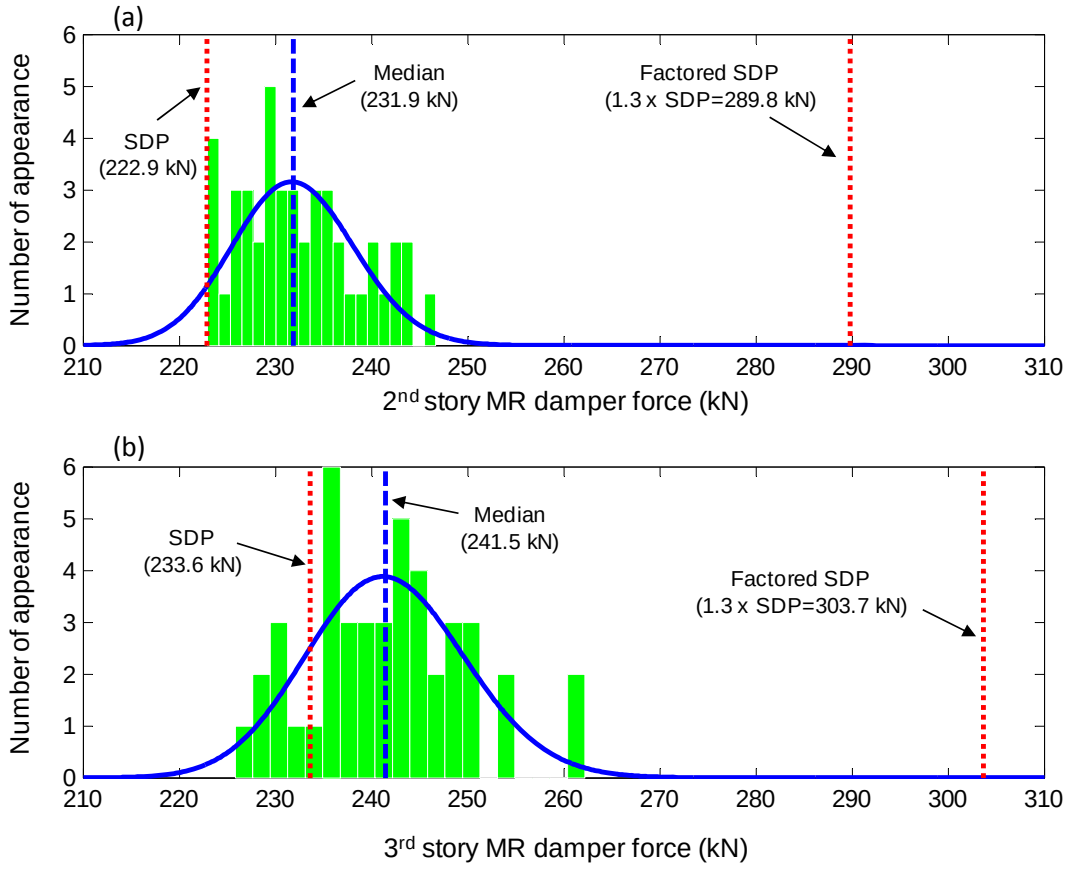

Figure 7.12 Histogram of MR damper forces compared with results from SDP: (a) 2nd story MR damper force; (b) 3rd story MR damper force

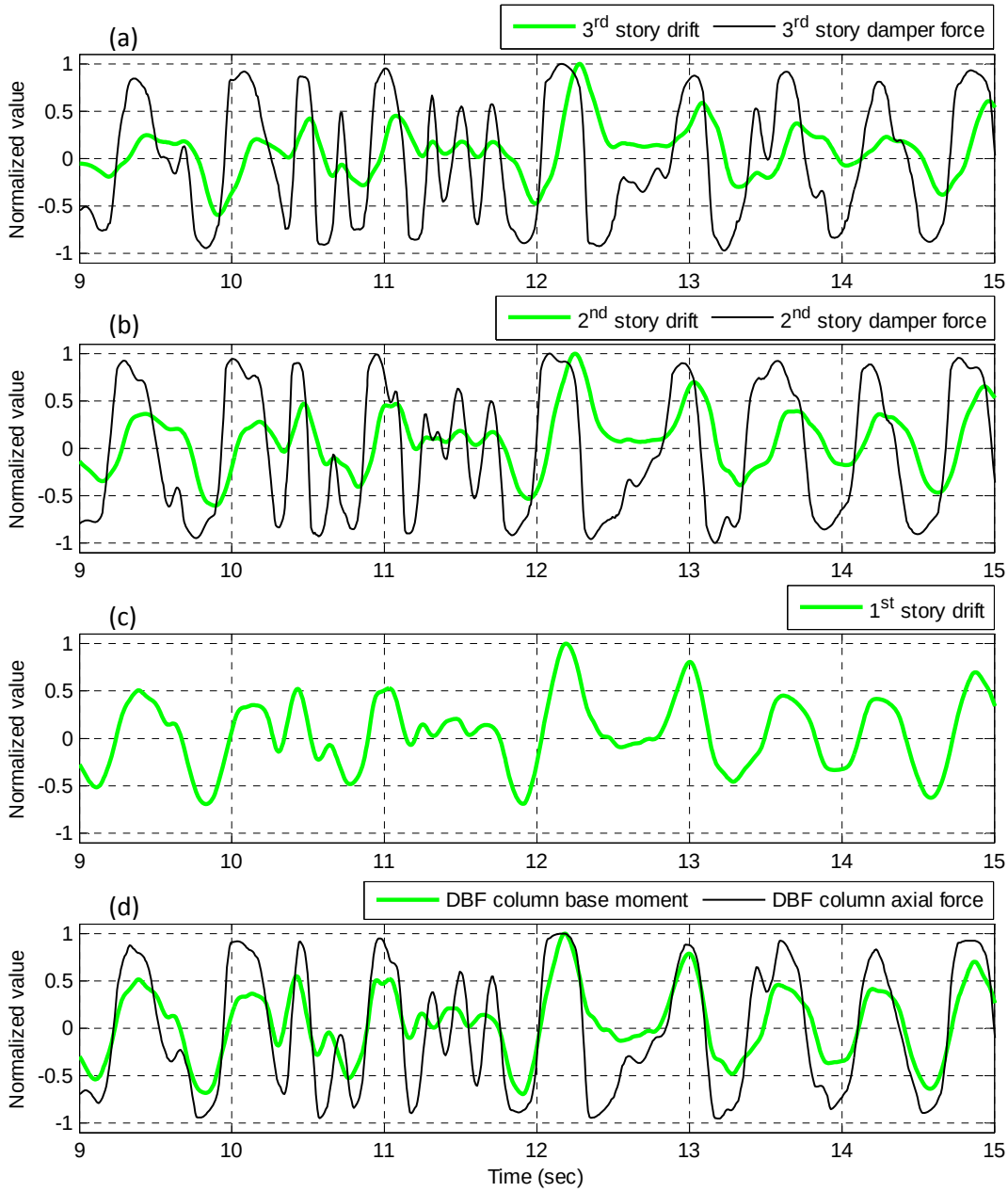

Figure 7.13 Comparison of normalized structural responses (DBE level, EQ: Landers, 1992, Coolwater, longitudinal direction): (a) 3rd story drift and 3rd story MR damper force; (b) 2nd story drift and 2nd story MR damper force; (c) 1st story drift; (d) Moment and axial force at the base of the 1st story DBF column

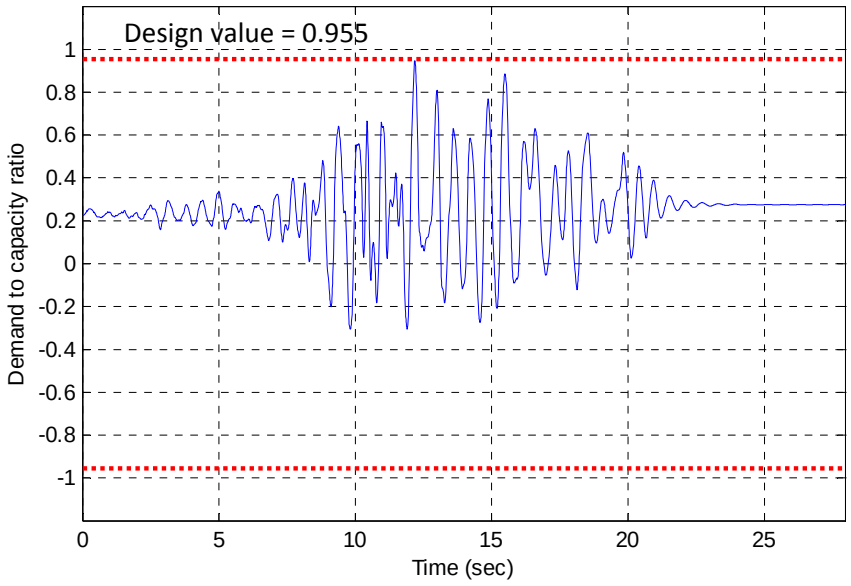

Figure 7.14 Demand to capacity ratio at the DBF column base under the 1992 Landers earthquake ground motion (Coolwater station, longitudinal direction) scaled to DBE

Chapter 8

Phase Angle Control

8.1 General

This chapter introduces a new controller for semi-active controlled MR dampers which overcomes a limitation of the existing controllers described in Chapter 2. The performance of the linear quadratic regulator (LQR) and the sliding mode control (SMC) depends on proper selection of the weighting matrices **Q** and **R** along with the gradient vector of the sliding surface **S** (see Chapter 2), respectively. Proper selection of these parameters can be a challenging task for the design of semi-active controllers for real structures. An alternative control algorithm called *phase angle control* (PAC) is developed in this chapter based on the concept of an impulse response function. PAC does not require any user-defined parameters.

8.2 Phase Angle Control (PAC)

Figure 8.1 shows a SDOF system with an MR damper. The MR damper is connected to the mass m in parallel with a spring k and a viscous dashpot c. A free-body diagram of the SDOF system is given in Figure 8.1 (b), where $f_s(t)$, $f_c(t)$, $f(t)$, $f_I(t)$, and $p(t)$ are the spring force, force in viscous dashpot, MR damper force, inertia force, and applied external force, respectively. A time varying damper force can be represented as a sequence of infinitesimally short impulses $f(\tau)d\tau$, where the response of a linear SDOF system to one of these impulses at time τ is given by

$$du(t) = f(\tau)h(t-\tau)d\tau \tag{8.1}$$

where, $h(t-\tau)$ is the unit impulse response function, $f(\tau)$ is the damper force at time τ, and $t \geq \tau$. The objective of the PAC controller is to maximize the effect of $f(\tau)d\tau$ on reducing the structural response. Figure 8.2 illustrates how the phase angle controller works with the impulse from the damper. In the PAC, the controller considers the effect of damper force impulse at time τ to determine the command current into the MR damper at time τ.

Using PAC, the command current at time τ is determined by comparing the phase angles of the impulse response and the hypothetical free vibration response from the displacement $u(\tau)$ and velocity $\dot{u}(\tau)$ at time τ. At time τ, the phase angle of $du(t)$, $\phi_d(\tau)$, is either 0 or π, depending on the sign of $f(\tau)$. For an SDOF system, the phase angle of the free vibration at time τ is determined from the following free vibration response for a given $u(\tau)$ and $\dot{u}(\tau)$:

$$u(t) = e^{-\xi_{in}\omega_n(t-\tau)}\left[u(\tau)\cos\omega_D(t-\tau) + \frac{\dot{u}(\tau)+\xi_{in}\omega_n u(\tau)}{\omega_D}\sin\omega_D(t-\tau)\right] \tag{8.2}$$

where ω_n is the natural frequency of system, ξ_{in} is the damping ratio, and $\omega_D = \omega_n\sqrt{1-\xi_{in}^2}$. The phase angle of the system $\phi_s(\tau)$ under free vibration is

$$\phi_s(\tau) = \tan^{-1}\left(-\frac{u(\tau)\omega_D}{\dot{u}(\tau)+\xi_{in}\omega_n u(\tau)}\right) \tag{8.3}$$

The period of $du(t)$ is equal to the natural period of the SDOF system. If the absolute value of the difference of the two phase angles, $|\phi_s(\tau)-\phi_d(\tau)|$, is π, then the impulse response and the free vibration are completely out of phase, and generating a damper force as large as possible at this time is effective on reducing the future response. The maximum reduction of the response is expected when the phase angle difference is π, while the maximum amplification of the response occurs when the phase angle difference is 0. Thereby, a simple control law can be established by sending the maximum current to the MR damper when the phase angle difference is in the range between $\pi/2$ and $3\pi/2$, and the minimum current for other cases.

If the Hershel-Bulkley quasi-static MR damper model (see Figure 5.3) is used, the command current of PAC always yields the maximum current when $\xi_{in} = 0$, as can be observed in Figure 8.3. $\phi_d = \pi$ if $\dot{u} > 0$, and $\phi_d = 0$ otherwise. If $\xi_{in} = 0$, the phase angle of the SDOF system ϕ_s is determined based on the sign of u and $\dot{u}$, where the range of ϕ_s are provided on each quadrant of Figure 8.3 along with the value of ϕ_d. It is obvious that the difference of ϕ_s and ϕ_d is between $\pi/2$ and $3\pi/2$ on all the quadrants so that the command current is always a maximum when $\xi_{in} = 0$.

Figure 8.4 illustrates the phase angle diagram of the SDOF system with the Hershel-Bulkley quasi-static MR damper model when $\xi_{in} > 0$. Unlike the case of $\xi_{in} = 0$, the term $\xi_{in}\omega_n u(\tau)$ in Equation (8.3) creates the shaded area shown in Figure 8.4. In this region, the impulse response due to the MR damper is in phase with the free vibration response determined from u and $\dot{u}$ so that the command current is zero. Zero command current is applied after the peak value of u occurs and is kept until the state of $\dot{u}$ and u is out of the shaded area. For a small value of ξ_{in} the slope of $1/\xi_{in}\omega_n$ is large and the portion of the shaded area is small compared to the unshaded area, implying that the command current is mostly maximum for PAC when the Hershel-Bulkley quasi-static MR damper model is used.

The idea for SDOF systems can be extended to MDOF systems. In general, the contribution of the fundamental mode of a building structure is dominant under earthquake loading and controlling the fundamental mode will reduce the structural response. The first mode phase angle of a MDOF system at a given instant of time is determined by

$$\phi_{s1}(\tau) = \tan^{-1}\left(-\frac{q_1(\tau)\omega_{D1}}{\dot{q}_1(\tau) + \xi_1\omega_1 q_1(\tau)}\right) \tag{8.4}$$

where the modal displacement $q_1(\tau)$ and velocity $\dot{q}_1(\tau)$ are calculated as,

$$q_1(\tau) = \frac{\boldsymbol{\phi}_1^{\mathrm{T}}\mathbf{M_s}\mathbf{x}(\tau)}{\boldsymbol{\phi}_1^{\mathrm{T}}\mathbf{M_s}\boldsymbol{\phi}_1} \tag{8.5}$$

$$\dot{q}_1(\tau) = \frac{\boldsymbol{\phi}_1^{\mathrm{T}} \mathbf{M_s} \dot{\mathbf{x}}(\tau)}{\boldsymbol{\phi}_1^{\mathrm{T}} \mathbf{M_s} \boldsymbol{\phi}_1} \tag{8.6}$$

In the above equations ω_1 is the first mode natural frequency, ξ_{in}^1 is the first mode damping ratio, $\omega_{D1} = \omega_1\sqrt{1-(\xi_{in}^1)^2}$, $\boldsymbol{\phi}_1$ is the first mode vector, $\mathbf{x}(\tau)$ is the MDOF system displacement vector, $\dot{\mathbf{x}}(t)$ the MDOF system velocity vector, and $\mathbf{M_s}$ the mass matrix of the MDOF system associated with the DOF in $\mathbf{x}(\tau)$. The first modal damper force F_1 can be obtained by multiplying the damper force vector by the first mode vector:

$$F_1(\tau) = \boldsymbol{\phi}_1^{\mathrm{T}} \boldsymbol{\Lambda} \mathbf{f} = \sum_{i=1}^{I} p_i f_i(\tau) \tag{8.7}$$

where, $\boldsymbol{\Lambda}$ is the MR damper location matrix defined in Equation (2.11) and p_i is a constant associated with the i^{th} MR damper force, $f_i(\tau)$. The phase angle of the impulse response due to $p_i f_i(\tau)$ at time t is represented by $\phi_{d1}^i(\tau)$, and is either 0 or π, depending on the sign of $p_i f_i(\tau)$. That is,

$$\phi_{d1}^i(\tau) = \begin{cases} 0 & \text{if } p_i f_i(\tau) \geq 0 \\ \pi & \text{otherwise} \end{cases} \tag{8.8}$$

Therefore, a control law similar to the one for an SDOF system can be applied to MDOF systems, where:

$$I_c^i = \begin{cases} I_{max} & \text{if } \frac{\pi}{2} < \left|\phi_{s1}(t) - \phi_{d1}^i(t)\right| < \frac{3\pi}{2} \\ 0 & \text{otherwise} \end{cases} \tag{8.9}$$

8.3 Summary

In this chapter, a new semi-active controller, called phase angle control (PAC), was developed based on the response of the structure due to an impulse from an MR damper. In PAC, the phase angle of the impulse response due to an MR damper and the phase angle of the free vibration response of the structure due to the current displacement and velocity are calculated at a given time instant. Then, the command current into the damper is determined based on the absolute difference of the two phase angles.

Unlike the LQG and SMC, user-defined parameters are not required for PAC, which makes PAC attractive to use as a semi-active controller. The performance of PAC for controlling the seismic response of the structure described in Chapter 6 will be evaluated in Chapter 9 along with other semi-active controllers described in Chapter 2.

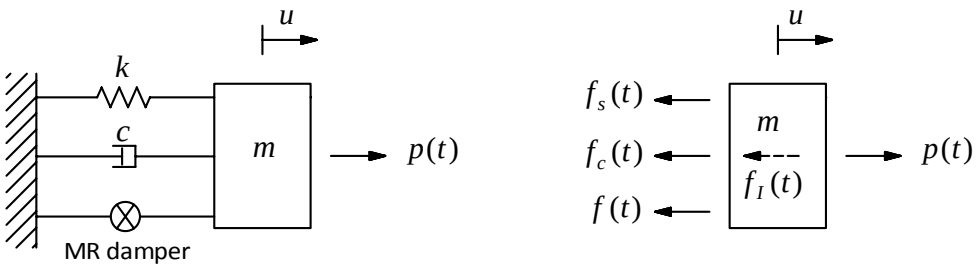

Figure 8.1 SDOF system with MR damper: (a) mechanical model; (b) free-body diagram

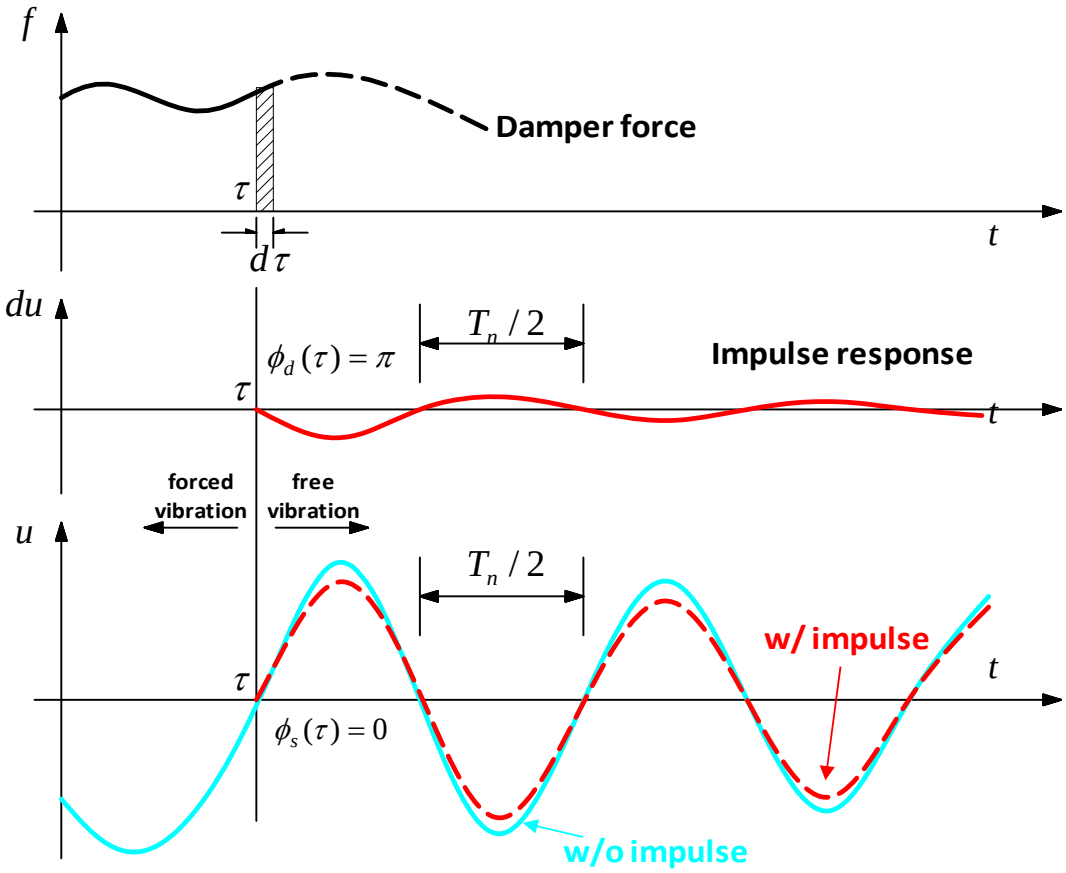

Figure 8.2 Impulse response of SDOF system due to damper

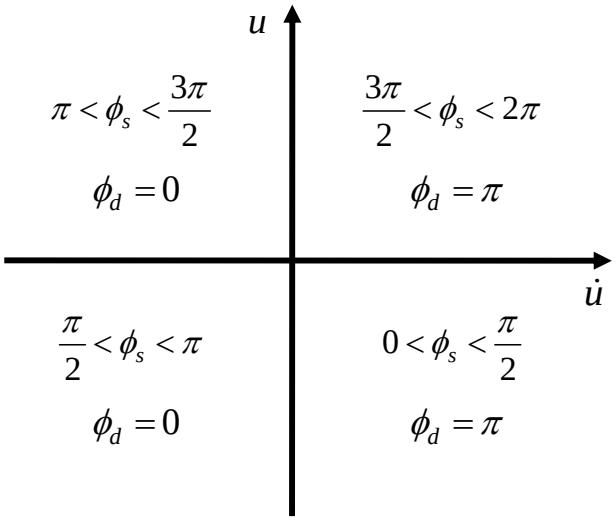

Figure 8.3 Phase angle diagram of SDOF system (Hershel-Bulkley quasi-static model, $\xi_{in} = 0$)

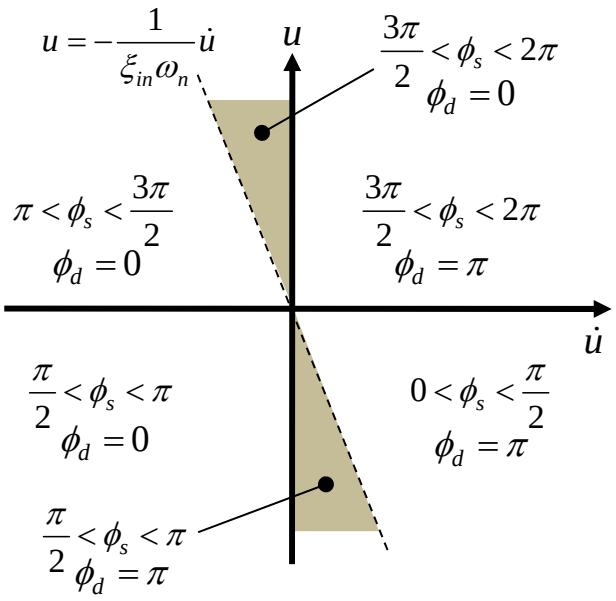

Figure 8.4 Phase angle diagram of SDOF system (Hershel-Bulkley quasi-static model, $\xi_{in} > 0$)

Chapter 9

Comparison of MR Damper Controllers

9.1 General

In this chapter, the four different semi-active controllers presented previously in Chapter 2 are evaluated by comparing the performance of a controlled structure using these controllers with that of the same structure using a passive controller. The four semi-active controllers include: (1) linear quadratic regulator (LQR); (2) sliding mode control (SMC); (3) decentralized bang-bang control (DBB); and, (4) phase angle control (PAC). The building structure designed in Chapter 6 is used for the comparison. The performance of these four semi-active controllers and the passive controller is numerically investigated using the ensemble of ground motions listed in Appendix 3, where the ground motions are scaled to the DBE and MCE levels. The MR dampers are modeled using the MNS model. Structural response statistics are processed and compared.

Since semi-active controllers rely on feedback data and properties of the structure, the effect of uncertainty in the structural properties used in the control design and the effect of noise corruption of feedback data are studied in this chapter. In addition, the effect of the response time of the MR dampers associated with variable current input is evaluated.

9.2 Structural Modeling Using OpenSees

The scaled building structure designed in Chapter 6 is used in the evaluation of the performance of the various structural controllers. The OpenSees model for this structure is shown in Figure 7.1. The modeling for the MRF, DBF, gravity frames, and inherent damping of the structure is described in Chapter 7.2. The four semi-active controllers are incorporated into the OpenSees along with the MNS MR damper model. During the nonlinear time history analysis the feedback of the state vector (e.g., displacements and velocities) and the MR damper forces are fed into the semi-active controllers and processed to determine the command current into the MR dampers. The variable current MNS model with the parameters listed in Table 3.3 along with the parameters provided in Chapter 4 for the dynamics of MR dampers associated with variable current (i.e., $\alpha_0 = 24.96, \alpha_1 = 3.57, \beta^+ = 0.31, \beta^- = -0.30$) is used to simulate the semi-active behavior of the MR dampers.

9.3 Implementation of Semi-Active Controllers in the Analysis Model

To design the semi-active controllers considered in this chapter, structural properties and information about the MR dampers (i.e., number, size, and the location of dampers in the structure) need to be defined. In the analysis model for the numerical analysis, the rotational and vertical inertia forces are ignored and only horizontal mass is assigned in the model as provided in Table 6.9. The mass of each MR damper is assumed to be 0.5 kN-sec^2/m, including the self weight of the damper, fixtures, and tributary length of the diagonal bracing. This mass is assigned to the top of the diagonal bracing. Therefore, there are five nonzero masses in the structure; three at the floors and

two at the MR dampers. For the design of the semi-active controllers, the system properties are given as follows:

$$\mathbf{M_s} = \begin{bmatrix} 101.0 & 0 & 0 & 0 & 0 \\ 0 & 101.0 & 0 & 0 & 0 \\ 0 & 0 & 73.5 & 0 & 0 \\ 0 & 0 & 0 & 0.5 & 0 \\ 0 & 0 & 0 & 0 & 0.5 \end{bmatrix} \text{kN} \cdot \text{sec}^2/\text{m} \tag{9.1}$$

$$\mathbf{K_s} = \begin{bmatrix} 3.3104 & -1.3901 & 0.2177 & -1.8300 & 0.4222 \\ -1.3901 & 2.7009 & -0.4031 & 0.4209 & -1.5774 \\ 0.2177 & -0.4031 & 0.2211 & 0 & -0.0004 \\ -1.8300 & 0.4209 & 0 & 1.8301 & -0.4215 \\ 0.4222 & -1.5774 & -0.0004 & -0.4215 & 1.5772 \end{bmatrix} \times 10^5 \text{kN/m} \tag{9.2}$$

$$\mathbf{x} = \begin{bmatrix} u_1 \\ u_2 \\ u_3 \\ u_2^b \\ u_3^b \end{bmatrix} \qquad \mathbf{\Lambda} = \begin{bmatrix} 0 & 0 \\ -1 & 0 \\ 0 & -1 \\ 1 & 0 \\ 0 & 1 \end{bmatrix} \qquad \mathbf{f} = \begin{bmatrix} f_2 \\ f_3 \end{bmatrix} \tag{9.3}$$

where, u_i is the horizontal displacement of the i^{th} floor; u_j^b is the horizontal displacement of the top of the diagonal bracing at the j^{th} story; and f_j is the MR damper force at the j^{th} story. The stiffness matrix $\mathbf{K_s}$ of Equation (9.2) is obtained from the initial tangent stiffness of the building structure by performing static condensation on the full stiffness matrix, where the initial tangent stiffness matrix is extracted from OpenSees. With the matrices defined in Equations (9.1) through (9.3), the semi-active controllers are designed according to the procedures presented in Chapter 2.4 and Chapter 8.

One of the challenges associated with the design of a semi-active controller is to define the user-defined parameters such as $\mathbf{Q}$ and $\mathbf{R}$ for the LQR, and $\mathbf{Q_s}$ for the SMC. In this study, $\mathbf{Q}$ is based on the recommendation of Chang and Zhou (2002), and $\mathbf{R}$ is selected to be small in order that an aggressive controller design is achieved, where $\mathbf{f}_{\text{opt}}$ is large:

$$\mathbf{Q} = \begin{bmatrix} \mathbf{K_s} & \mathbf{0} \\ \mathbf{0} & \mathbf{M_s} \end{bmatrix} \quad \mathbf{R} = 1 \times 10^{-15} \begin{bmatrix} 1 & 0 \\ 0 & 1 \end{bmatrix} \tag{9.4}$$

The $\mathbf{Q_s}$ matrix for the quadratic minimization in the SMC is assigned to be the identity matrix

$$\mathbf{Q_s} = \mathbf{I}_{10\times 10} \tag{9.5}$$

A series of nonlinear time history analysis were conducted using OpenSees. The ground motions listed in Appendix 3 were selected and scaled to the DBE and MCE levels. A total 44 ground motions are used for each control scheme and the statistics from the responses of the structure to the 44 ground motions are compared.

The semi-active controllers require feedback of the state vector and measured MR damper forces. While the damper force and the acceleration can be easily measured using a load cell and accelerometer, respectively, the displacement and velocity of the structure may be difficult to obtain directly. Hence sensors may not be able to provide full-state feedback data. In order to resolve this problem, researchers have used an

estimator, or an observer, of the state vector that predicts the full-state feedback from the measured information obtained from a limited number of sensors (Yang et al. 1995, Dyke et al. 1996, Carrion and Spencer 2007).

It should be noted that an estimator or observer is not used in this study. Full-state feedback is assumed to be available to remove any unwanted errors coming from the estimator or the observer when the performance of each semi-active controller is assessed. Therefore, the performance comparison is made here under the ideal situation where full-state feedback data is directly achievable. The effect of sensor noise on the performance of semi-active controllers is investigated in the Section 9.6.

9.4 Comparison of Control Strategies

Figures 9.1 through 9.4 compare the story drift achieved in the structure with passive and semi-active controllers under the 1999 Duzce earthquake (Bolu, 90 component, Turkey). The earthquake ground motion is scaled to the DBE level. Table 9.1 summarizes the maximum story drift and Table 9.2 the residual story drift under this earthquake. For passive control, a constant current of 2.5A is supplied to the MR damper, while variable currents from 0.0A to 2.5A are fed into the MR dampers for the semi-active controllers. As can be observed in Tables 9.1 and 9.2, the semi-active controllers perform equal to or better than passive control under this selected ground motion. In particular, the LQR controller results in 12%, 6%, and 2% less story drift for the 1st, 2nd, and 3rd story, respectively, than passive control. Moreover, the residual drift of the 1st story is reduced by 30% compared to the passive control. Figures 9.5 and 9.6

compare the damper response and command current for the 2nd story and the 3rd story MR dampers, respectively, when the LQR controller is used. The LQR command current for the 2nd story MR damper is continuously turned on around the time of the maximum response (at 8.5 sec), so the damper forces for the passive and LQR controllers are almost same at that time. Meanwhile, the LQR command current for the 3rd story MR damper is frequently turned off and on near the time of the maximum response so that the LQR damper force is less than the passive control damper force. The differences result in better performance of LQR controller compared with the passive control. In the cases of the DBB and PAC, the story drifts are almost the same as those for the passive control, while the SMC shows a slightly better performance than the passive control (see Tables 9.1 and 9.2).

Under the Duzce earthquake, the LQR controller shows the best performance among the five controllers. Although a specific controller may work well for a selected ground motion, it may not work well for other ground motions due to the variability among the records in the ensemble of ground motions. It is therefore necessary to evaluate the performance of the controllers by comparing the statistics for the response of the structure. This involves subjecting the structure to an ensemble of ground motions that have the same intensity level.

The statistical response (median and standard deviation) of the structure with the above controllers are compared in Tables 9.3 through 9.12 for both the DBE and MCE levels. The response includes maximum story drift, beam and column maximum plastic rotations, and maximum absolute velocity and maximum absolute acceleration.

Included in these tables is the response of the uncontrolled structure (i.e., without MR dampers) and the response of the structure with passive control. The median and standard deviation values of structural responses are obtained from the response of the structure to the 44 ground motions that are scaled to the DBE and MCE levels. The MR damper is shown to reduce the response, where the statistics for the maximum responses in Table 9.3 through 9.12 for the structure with MR dampers are shown to be smaller than the response of the structure without MR dampers.

However, it is observed that semi-active controllers do not significantly improve the performance of the structure compared to the performance with passive control. Both the median and standard deviation for maximum story drift are similar for the passive and various semi-active controllers. For example, the largest reduction compared to the passive control case in the maximum median story drift under the DBE ground motion is about 6 % (SMC) in the 1st story. However, the story drifts for the 2nd and 3rd stories of the structure with the SMC are 3 % and 4 %, respectively, larger than those for passive control.

A graphical comparison of the story drift is given in Figures 9.7 and 9.8 for the DBE and MCE levels, respectively. The dashed line in the figure indicates the story drift from the simplified design procedure (SDP). It is observed that the benefit of MR dampers is clearly demonstrated and the performance of the structure with semi-active controllers is similar to that of the structure with passive control. Consequently, the story drift from the SDP has the same accuracy for both the semi-active controllers and passive control. Similar tendencies also can be observed in the beam and column

maximum plastic rotations listed in Tables 9.4 through 9.10, where the statistics are about the same for the structures with passive and semi-active controllers. It is noteworthy that semi-active controllers do not always result in a better structural performance than the passive control case.

The median and standard deviation of the maximum absolute velocity and maximum absolute acceleration are compared in Tables 9.11 and 9.12 for the DBE and MCE levels, respectively. With MR dampers, the velocity and acceleration are generally reduced compared to the structure without dampers. Although the LQR and SMC semi-active controllers result in a slight reduction for the 1st and 2nd floors median maximum absolute velocity, the velocity is almost the same at each floor level for all five controllers. In terms of the absolute acceleration, the SMC appears to reduce the acceleration the most. The SMC reduces the absolute floor acceleration of the 2nd floor by 10% compared to passive control under the DBE. However, the improvement for other floors is not significant, e.g., about a 2% reduction for both the 1st and 3rd floors under the DBE. Similar results are observed in the responses under the MCE. A graphical comparison of the absolute velocity and the absolute acceleration is given in Figures 9.9 through 9.12 for the DBE and MCE levels.

The statistical comparison of the maximum MR damper force for the various controllers is summarized in Table 9.13. As expected, the passive controller has the largest maximum MR damper force among the various controllers, while the standard deviation of the passive controller is observed to be smaller than that of the semi-active controllers. Since the command current varies between I=0.0A and I=2.5A during semi-

active control of the MR damper, a reduced damper force is observed for the semi-active controller and a wider range of the MR damper forces can be expected compared to the passive control case.

Overall, the statistics of the response show that passive control produces a similar improvement in structural performance compared to the semi-active controllers. For passive control, feedback data such as displacement, velocity and damper force is not required, which is an advantage of using passive control.

9.5 Sensitivity of Semi-Active Controllers on the Uncertainty of Stiffness

Semi-active controllers require a decision block for determining the command current for the MR damper. The decision block is designed based on the structural properties as well as the user-defined parameters for the semi-active controller. Hence, the performance of semi-active controllers may be affected by any discrepancies in the structural properties used in the design of the controller.

The initial tangent stiffness of a building can be estimated from design data or identified by utilizing various system identification techniques. One of the structural properties used in most of the semi-active controller discussed in Chapter 2 is the structural stiffness $\mathbf{K_s}$. The identified stiffness however may differ from the actual stiffness of the building so that the performance of semi-active controllers may be affected by this discrepancy in stiffness. In this section, the effect of perturbed structural stiffness on the performance of semi-active controllers is investigated. The perturbed

stiffness matrix representing the uncertainty of the structural properties is obtained using the following equation (Moon et al. 2002):

$$\mathbf{K_s^*} = (1 + \epsilon)\mathbf{K_s} \tag{9.6}$$

where, ϵ is a perturbation factor. Five different values for ϵ are used here, including: -20%, -10%, 0%, 10%, and 20%. When ϵ= 0%, the semi-active controllers are designed with the correct stiffiness matrix. Figures 9.13 and 9.14 show the effect of a perturbed stiffness on the semi-active controllers, where the median of the maximum story drift and absolute acceleration from the results of the nonlinear time history analysis with the 44 ground motions are compared for the DBE and MCE levels, respectively. Since the decentralized bang-bang controller (DBB) does not utilize the structural stiffness matrix for determining the command current, it is excluded in the comparison. As can be observed in Figures 9.13 and 9.14, the overall response does not vary too much with respect to the perturbed stiffness, implying the performance of semi-active controllers is not significantly affected by a perturbation of the stiffness.

9.6 Effect of Noise in Feedback Signal

Since the semi-active controllers require feedback data to determine the command current for MR dampers, the performance of a semi-active controller may be affected by noise in the feedback data from sensors.. In this section, the effect of noise in the feedback data is investigated by adding artificial noise to the full-state feedback

data. The artificial noise is based on Gaussian noise with a bandwidth of 512Hz. Scaled artificial noise is added to the displacement, velocity, and damper force feedback during the nonlinear time history analysis. In the investigation, structural response is from nonlinear time history analyses where the damper forces are based on command currents determined from feedback signals corrupted by noise. The amplitude of the noise is based on a selected signal-to-noise ratio (SNR), where the SNR is defined as

$$\mathrm{SNR} = 20 \log_{10} \left(\frac{\mathrm{RMS}_{\mathrm{signal}}}{\mathrm{RMS}_{\mathrm{noise}}} \right) \tag{9.7}$$

where $\mathrm{RMS}_{\mathrm{signal}}$ and $\mathrm{RMS}_{\mathrm{noise}}$ are the root mean square (RMS) values of the signal and the scaled noise, respectively. The RMS value of each sensor signal (displacement, velocity, damper force), $\mathrm{RMS}_{\mathrm{signal}}$, is calculated from the response of the structure with passive control. The RMS value of each signal is averaged over the structural response from the 44 ground motions. For example, the RMS values of the three floor displacements are calculated from the nonlinear time history analysis using 44 ground motions, where passive control is used, then, the three RMS floor displacements are averaged to get the RMS value for all displacement sensors. For a selected SNR, the corresponding value for $\mathrm{RMS}_{\mathrm{noise}}$ is obtained. For the study, values for the SNR of 10, 20, and 40 dB were selected. Table 9.14 summarizes the RMS values for the noise level in each sensor ($\mathrm{RMS}_{\mathrm{noise}}$) based on Equation (9.7) for the nonlinear time history analyses under the DBE and MCE ground motions. The noise with the RMS values listed in Table 9.14 are added to the feedback signal of sensors during the nonlinear

time history analyses of the structure with semi-active controllers to investigate the effect of the sensor noise on the performance of the controllers. Figure 9.15 illustrates a displacement signal corrupted by various noise levels. The original signal was obtained from the 2nd floor displacement of the building subjected to the 1994 Northridge earthquake scaled to the DBE.

Figures 9.16 and 9.17 show the performance of the semi-active controllers under various noise levels in the feedback data for the DBE and MCE levels, respectively, where the median values for the maximum story drift and absolute acceleration for the various semi-active controllers are plotted as a function of the SNR. For the 3rd story drift, the LQR and SMC semi-active controllers appear to be most affected by the noise level associated with the structural response to the DBE; however, overall the effect of noise on the performance of semi-active controllers is not otherwise significant. Under the MCE, the 2nd and 3rd story drift associated with the SMC appears to be affected by the noise level, however, similar to the structural response to the DBE the overall effect of noise on the performance of semi-active controllers under the MCE is not otherwise significant. Even when the noise level is high, it does not result in a significant change in the performance for each of the semi-active controllers for the DBE and MCE events.

9.7 Effect of Response Time Associated with Dynamics of an MR Damper

The response time of an MR damper under variable current is related to the electro-magnetism of the MR fluid and the material around the MR damper as discussed in Chapter 4. A quick response of an MR damper subjected to a variable current is

defined as one with a fast rise time of the MR damper force. The rise time of an MR damper under constant velocity is defined as the time required to make the transition from the initial state to 95% of the final state (Koo et al. 2006). As mentioned in Chapter 4, the rise time of the large-scale MR damper in this study is about 0.92 sec when a step command current from 0.0A to 2.5A is fed into the MR damper while the damper is subjected to a constant velocity of V=50mm/sec. In this section, the effect of the response time of the MR damper force on the performance of the semi-active controllers is studied. The study involves conducting numerical simulations, where the rise time of the MR damper force is systematically varied.

The dynamics of an MR damper is described by Equation (4.9) in Chapter 4. By appropriately adjusting the parameters in the equation, the rise time of the MR damper can be changed as desired. The damper force response of an MR damper from the MNS model with five different rise times is shown in Figure 9.18, where the linear ramp displacement with a constant velocity of V=50mm/sec is imposed on the model, while the step current from 0.0A to 2.5A is applied at time zero. The parameters in Equation (4.9) corresponding to each rise time T_r for the model are listed in Table 9.15. The parameters for T_r=0.27sec. are exactly the same as those used in the previous numerical simulations, which mimics the dynamics of the physical MR damper under semi-active control mode as in Chapter 4. The use of the values related to the parameters for T_r=0.27sec. were intended to describe the behavior of the MR damper under a semi-active control mode where a frequent change of the input current, i.e., either 0.0A or

2.5A, is expected. The parameters for other rise times are selected by setting $\beta^+ = \beta^- = 0$ for simplicity, which is exactly the same as a 1st order filter as follows:

$$\dot{I}_{eq} = \alpha_1(I - I_{eq}) \tag{9.8}$$

The solution of Equation (9.8) under a step current input from 0.0A to 2.5A at time $t = 0$ is obtained as

$$I_{eq} = 2.5[1 - \exp(-\alpha_1 t)] \tag{9.9}$$

Among five rise time cases, two cases ($T_r = 0.05$sec and 0.10sec represent a fast MR damper and the two cases of $T_r = 0.50$sec and 1.00sec represent a slow MR damper.

The performance of semi-active controllers with various rise times is compared to that of a passive control in Figures 9.19 and 9.20 for the DBE and MCE levels, respectively, where the story drift and absolute acceleration are plotted against the damper force rise time. The SMC appears to be most sensitive to the rise time in the damper force. In Figures 9.19 and 9.20 an increase in the 3rd story drift is observed to occur with a slow rise time. In the case of the SMC, the 3rd story drift increased from 1.43% to 1.59% for the DBE and from 2.25% to 2.44% for the MCE when the rise time was changed from 0.05sec to 1.0sec. The 2nd story drift decreases from 2.25% to 2.13% under the MCE for the SMC. The 2nd floor acceleration associated with the SMC semi-active controller appears to be affected the most by the damper rise time, where the

acceleration ranges from 0.45g to 0.5g under the DBE and from 0.6g to 0.68g under the MCE when the rise time is increases from 0.5sec to 1.0sec. It appears that the overall performance of semi-active controllers is not significantly affected by the rise time and is similar to that of a passive controller. Even in some cases, a better performance is achieved with a slow rise time (e.g, 2nd floor acceleration for the LQR and PAC under the DBE, and 1st and 2nd story drifts for the SMC under the MCE).

9.8 Summary

The performance of a 3-story building structure with large-scale MR dampers and various MR damper controllers was studied by conducting numerical simulations. 44 ground motions were selected and scaled to both the DBE and MCE levels. Numerical simulations with the MNS MR damper model were conducted using this ensemble of ground motions. Statistical results for response show that the overall performance of the structure with semi-active controllers is similar to response with passive control for the 3-story structure studied. Even if an MR damper with a fast response time is used, it is observed that the improvement in structural performance from the use of semi-active controllers is not significant compared to the passive control case.

The effects of a perturbed stiffness (i.e., uncertainty in the structural stiffness properties used to design the semi-active controller) as well as noise-corrupted feedback signals on the performance of semi-active controllers was also investigated. The

statistical results show that the performance of semi-active controllers is not significantly affected by a perturbed stiffness or noise in the feedback signals.

Table 9.1 Maximum story drift under the 1999 Duzce earthquake, Turkey, DBE level

Story	Maximum story drifts (%)				
	Passive	LQR	SMC	DBB	PAC
1	1.43	**1.26**	1.32	1.43	1.37
2	1.74	**1.64**	1.72	1.77	1.74
3	1.72	**1.68**	1.72	1.79	1.77

Table 9.2 Residual story drift under the Duzce earthquake, Turkey, DBE level

Story	Residual story drifts (%)				
	Passive	LQR	SMC	DBB	PAC
1	0.77	**0.54**	0.65	0.79	0.70
2	0.90	**0.69**	0.88	0.95	0.87
3	0.85	**0.67**	0.88	0.91	0.83

Table 9.3 Median and standard deviation values of maximum story drift and residual story drift, DBE level

		1st story	2nd story	3rd story
Maximum story drift (%)	No damper	1.36 (0.62)*	1.89 (0.73)	2.61 (0.74)
	Passive	1.18 (0.35)	1.35 (0.36)	1.46 (0.33)
	LQR	1.14 (0.36)	1.35 (0.37)	1.50 (0.34)
	SMC	1.11 (0.37)	1.39 (0.41)	1.52 (0.37)
	DBB	1.19 (0.36)	1.36 (0.37)	1.51 (0.33)
	PAC	1.15 (0.36)	1.33 (0.37)	1.52 (0.33)
Residual story drift (%)	No damper	0.15 (0.27)	0.21 (0.30)	0.26 (0.31)
	Passive	0.11 (0.21)	0.17 (0.26)	0.22 (0.27)
	LQR	0.12 (0.22)	0.19 (0.27)	0.23 (0.28)
	SMC	0.12 (0.22)	0.21 (0.28)	0.26 (0.30)
	DBB	0.11 (0.22)	0.18 (0.27)	0.23 (0.28)
	PAC	0.11 (0.22)	0.17 (0.27)	0.21 (0.28)

* Value in () denotes standard deviation of response

Table 9.4 Median and standard deviation values of maximum story drift and residual story drift, MCE level

		1st story	2nd story	3rd story
Maximum story drift (%)	No damper	2.22 (1.18)*	2.92 (1.29)	3.74 (1.21)
	Passive	1.86 (0.85)	2.10 (0.85)	2.32 (0.84)
	LQR	1.83 (0.85)	2.08 (0.85)	2.33 (0.83)
	SMC	1.88 (0.84)	2.11 (0.88)	2.33 (0.86)
	DBB	1.87 (0.86)	2.11 (0.85)	2.39 (0.84)
	PAC	1.88 (0.86)	2.11 (0.85)	2.38 (0.84)
Residual story drift (%)	No damper	0.45 (0.72)	0.47 (0.77)	0.44 (0.79)
	Passive	0.42 (0.62)	0.57 (0.66)	0.63 (0.69)
	LQR	0.40 (0.62)	0.54 (0.65)	0.61 (0.68)
	SMC	0.38 (0.62)	0.57 (0.65)	0.65 (0.67)
	DBB	0.44 (0.62)	0.58 (0.65)	0.64 (0.68)
	PAC	0.39 (0.62)	0.59 (0.65)	0.65 (0.68)

* Value in () denotes standard deviation of response

Table 9.5 Median and standard deviation values of MRF beam maximum plastic rotation and residual plastic rotation, DBE level

		1st floor	2nd floor	3rd floor
Maximum plastic rotation (rad %)	No damper	0.68 (0.38)*	1.16 (0.76)	1.62 (0.75)
	Passive	0.35 (0.37)	0.37 (0.33)	0.31 (0.30)
	LQR	0.35 (0.38)	0.39 (0.35)	0.35 (0.32)
	SMC	0.36 (0.40)	0.42 (0.39)	0.34 (0.34)
	DBB	0.36 (0.38)	0.40 (0.34)	0.37 (0.31)
	PAC	0.34 (0.38)	0.37 (0.34)	0.36 (0.31)
Residual plastic rotation (rad %)	No damper	0.22 (0.29)	0.31 (0.31)	0.32 (0.33)
	Passive	0.16 (0.27)	0.27 (0.31)	0.18 (0.30)
	LQR	0.16 (0.28)	0.28 (0.32)	0.24 (0.31)
	SMC	0.17 (0.29)	0.35 (0.34)	0.23 (0.32)
	DBB	0.16 (0.28)	0.28 (0.32)	0.19 (0.31)
	PAC	0.15 (0.28)	0.28 (0.31)	0.21 (0.31)

* Value in () denotes standard deviation of response

Table 9.6 Median and standard deviation values of MRF beam maximum plastic rotation and residual plastic rotation, MCE level

		1st floor	2nd floor	3rd floor
Maximum plastic rotation (rad %)	No damper	1.45 (1.24)*	2.31 (1.25)	2.82 (1.24)
	Passive	1.05 (0.86)	1.20 (0.84)	1.17 (0.86)
	LQR	1.05 (0.86)	1.18 (0.84)	1.21 (0.84)
	SMC	1.09 (0.87)	1.26 (0.88)	1.21 (0.89)
	DBB	1.06 (0.87)	1.23 (0.85)	1.23 (0.86)
	PAC	1.08 (0.87)	1.23 (0.84)	1.21 (0.86)
Residual plastic rotation (rad %)	No damper	0.46 (0.73)	0.53 (0.79)	0.47 (0.84)
	Passive	0.49 (0.63)	0.68 (0.72)	0.67 (0.78)
	LQR	0.48 (0.63)	0.71 (0.71)	0.70 (0.75)
	SMC	0.51 (0.64)	0.74 (0.70)	0.74 (0.73)
	DBB	0.51 (0.63)	0.72 (0.72)	0.70 (0.77)
	PAC	0.51 (0.63)	0.75 (0.71)	0.72 (0.76)

* Value in () denotes standard deviation of response

Table 9.7 Median and standard deviation values of MRF column maximum plastic rotation and residual plastic rotation, DBE level

		1st story	2nd story	3rd story
Maximum plastic rotation (rad %)	No damper	0.13 (0.49)*	0.00 (0.04)	0.00 (0.02)
	Passive	0.07 (0.25)	0.00 (0.00)	0.00 (0.00)
	LQR	0.05 (0.25)	0.00 (0.00)	0.00 (0.00)
	SMC	0.03 (0.25)	0.00 (0.00)	0.00 (0.00)
	DBB	0.06 (0.26)	0.00 (0.00)	0.00 (0.00)
	PAC	0.06 (0.26)	0.00 (0.00)	0.00 (0.00)
Residual plastic rotation (rad %)	No damper	0.10 (0.30)	0.00 (0.04)	0.00 (0.00)
	Passive	0.06 (0.19)	0.00 (0.00)	0.00 (0.00)
	LQR	0.05 (0.19)	0.00 (0.00)	0.00 (0.00)
	SMC	0.02 (0.19)	0.00 (0.00)	0.00 (0.00)
	DBB	0.05 (0.19)	0.00 (0.00)	0.00 (0.00)
	PAC	0.04 (0.19)	0.00 (0.00)	0.00 (0.00)

* Value in () denotes standard deviation of response

Table 9.8 Median and standard deviation values of MRF column maximum plastic rotation and residual plastic rotation, MCE level

		1st story	2nd story	3rd story
Maximum plastic rotation (rad %)	No damper	0.90 (1.06)*	0.08 (0.20)	0.00 (0.16)
	Passive	0.62 (0.76)	0.00 (0.00)	0.00 (0.00)
	LQR	0.55 (0.76)	0.00 (0.00)	0.00 (0.00)
	SMC	0.57 (0.74)	0.00 (0.00)	0.00 (0.00)
	DBB	0.61 (0.76)	0.00 (0.00)	0.00 (0.00)
	PAC	0.61 (0.76)	0.00 (0.00)	0.00 (0.00)
Residual plastic rotation (rad %)	No damper	0.45 (0.68)	0.08 (0.18)	0.00 (0.08)
	Passive	0.41 (0.59)	0.00 (0.00)	0.00 (0.00)
	LQR	0.39 (0.60)	0.00 (0.00)	0.00 (0.00)
	SMC	0.36 (0.59)	0.00 (0.00)	0.00 (0.00)
	DBB	0.42 (0.59)	0.00 (0.00)	0.00 (0.00)
	PAC	0.41 (0.59)	0.00 (0.00)	0.00 (0.00)

* Value in () denotes standard deviation of response

Table 9.9 Median and standard deviation values of DBF column maximum plastic rotation and residual plastic rotation, DBE level

		1st story	2nd story	3rd story
Maximum plastic rotation (rad %)	No damper	0.00 (0.19)*	0.00 (0.00)	0.00 (0.00)
	Passive	0.00 (0.05)	0.00 (0.00)	0.00 (0.00)
	LQR	0.00 (0.05)	0.00 (0.00)	0.00 (0.00)
	SMC	0.00 (0.04)	0.00 (0.00)	0.00 (0.00)
	DBB	0.00 (0.06)	0.00 (0.00)	0.00 (0.00)
	PAC	0.00 (0.06)	0.00 (0.00)	0.00 (0.00)
Residual plastic rotation (rad %)	No damper	0.00 (0.14)	0.00 (0.00)	0.00 (0.00)
	Passive	0.00 (0.04)	0.00 (0.00)	0.00 (0.00)
	LQR	0.00 (0.04)	0.00 (0.00)	0.00 (0.00)
	SMC	0.00 (0.03)	0.00 (0.00)	0.00 (0.00)
	DBB	0.00 (0.04)	0.00 (0.00)	0.00 (0.00)
	PAC	0.00 (0.04)	0.00 (0.00)	0.00 (0.00)

* Value in () denotes standard deviation of response

Table 9.10 Median and standard deviation values of DBF column maximum plastic rotation and residual plastic rotation, MCE level

		1st story	2nd story	3rd story
Maximum plastic rotation (rad %)	No damper	0.16 (0.58)*	0.00 (0.00)	0.00 (0.01)
	Passive	0.08 (0.40)	0.00 (0.00)	0.00 (0.00)
	LQR	0.06 (0.40)	0.00 (0.00)	0.00 (0.00)
	SMC	0.06 (0.38)	0.00 (0.00)	0.00 (0.00)
	DBB	0.07 (0.40)	0.00 (0.00)	0.00 (0.00)
	PAC	0.07 (0.40)	0.00 (0.00)	0.00 (0.00)
Residual plastic rotation (rad %)	No damper	0.14 (0.41)	0.00 (0.00)	0.00 (0.01)
	Passive	0.07 (0.35)	0.00 (0.00)	0.00 (0.00)
	LQR	0.06 (0.34)	0.00 (0.00)	0.00 (0.00)
	SMC	0.06 (0.34)	0.00 (0.00)	0.00 (0.00)
	DBB	0.07 (0.35)	0.00 (0.00)	0.00 (0.00)
	PAC	0.07 (0.35)	0.00 (0.00)	0.00 (0.00)

* Value in () denotes standard deviation of response

Table 9.11 Median and standard deviation values of maximum absolute velocity and acceleration, DBE level

		1st floor	2nd floor	3rd floor
Maximum absolute velocity (m/sec)	No damper	0.495 (0.224)*	0.524 (0.230)	0.792 (0.234)
	Passive	0.445 (0.233)	0.561 (0.231)	0.625 (0.230)
	LQR	0.444 (0.233)	0.546 (0.229)	0.629 (0.231)
	SMC	0.425 (0.231)	0.549 (0.230)	0.632 (0.231)
	DBB	0.441 (0.232)	0.562 (0.231)	0.635 (0.231)
	PAC	0.441 (0.232)	0.559 (0.230)	0.635 (0.230)
Maximum absolute acceleration (g)	No damper	0.611 (0.167)	0.548 (0.144)	0.660 (0.104)
	Passive	0.492 (0.089)	0.535 (0.071)	0.605 (0.054)
	LQR	0.493 (0.092)	0.499 (0.071)	0.605 (0.055)
	SMC	0.480 (0.091)	0.482 (0.063)	0.593 (0.056)
	DBB	0.484 (0.091)	0.516 (0.068)	0.606 (0.054)
	PAC	0.512 (0.091)	0.512 (0.071)	0.586 (0.057)

* Value in () denotes standard deviation of response

Table 9.12 Median and standard deviation values of maximum absolute velocity and acceleration, MCE level

		1st floor	2nd floor	3rd floor
Maximum absolute velocity (m/sec)	No damper	0.704 (0.335)*	0.695 (0.346)	1.004 (0.329)
	Passive	0.623 (0.354)	0.746 (0.355)	0.834 (0.359)
	LQR	0.618 (0.354)	0.731 (0.355)	0.866 (0.358)
	SMC	0.610 (0.349)	0.725 (0.349)	0.880 (0.352)
	DBB	0.619 (0.354)	0.750 (0.354)	0.845 (0.357)
	PAC	0.626 (0.353)	0.741 (0.354)	0.861 (0.356)
Maximum absolute acceleration (g)	No damper	0.849 (0.232)	0.750 (0.221)	0.845 (0.130)
	Passive	0.703 (0.140)	0.683 (0.097)	0.730 (0.092)
	LQR	0.705 (0.148)	0.660 (0.095)	0.729 (0.092)
	SMC	0.697 (0.146)	0.647 (0.101)	0.719 (0.099)
	DBB	0.700 (0.140)	0. 676 (0.096)	0.725 (0.092)
	PAC	0.716 (0.138)	0.682 (0.093)	0.703 (0.089)

* Value in () denotes a standard deviation of response

Table 9.13 Median and standard deviation values of maximum MR damper force

Controller	Maximum MR damper force (kN)			
	DBE		MCE	
	2^{nd} story	3^{rd} story	2^{nd} story	3^{rd} story
Passive	231.9 (6.4)*	241.5 (8.3)	248.4 (7.3)	260.2 (9.4)
LQR	219.2 (7.1)	231.6 (10.4)	239.9 (9.2)	258.7 (12.3)
SMC	220.0 (7.1)	225.9 (10.3)	239.1 (8.6)	250.6 (13.5)
DBB	219.4 (7.0)	235.0 (9.9)	238.9 (9.3)	257.8 (11.6)
PAC	219.4 (7.0)	237.0 (9.8)	238.7 (9.1)	259.3 (11.5)

* Value in () denotes a standard deviation of response

Table 9.14 RMS value for sensor noise (RMS_{noise})

Sensor	40dB		20dB		10dB	
	DBE	MCE	DBE	MCE	DBE	MCE
Displacement (m)	1.79e-4	2.82e-4	1.79e-3	2.82e-3	5.66e-3	8.91e-3
Velocity (m/sec)	7.71e-4	1.21e-3	7.71e-3	1.21e-2	2.44e-2	3.84e-2
Damper force (kN)	0.75	0.81	7.52	8.08	23.77	25.54

Table 9.15 MNS model parameters depicting various rise times of MR dampers

Rise time	MNS model parameters			
	α_0	α_1	β^+	β^-
T_r=0.05 sec	0.00	35.00	0.00	0.00
T_r=0.10 sec	0.00	16.00	0.00	0.00
T_r=0.27 sec	24.96	3.57	0.31	-0.30
T_r=0.50 sec	0.00	3.50	0.00	0.00
T_r=1.00 sec	0.00	1.75	0.00	0.00

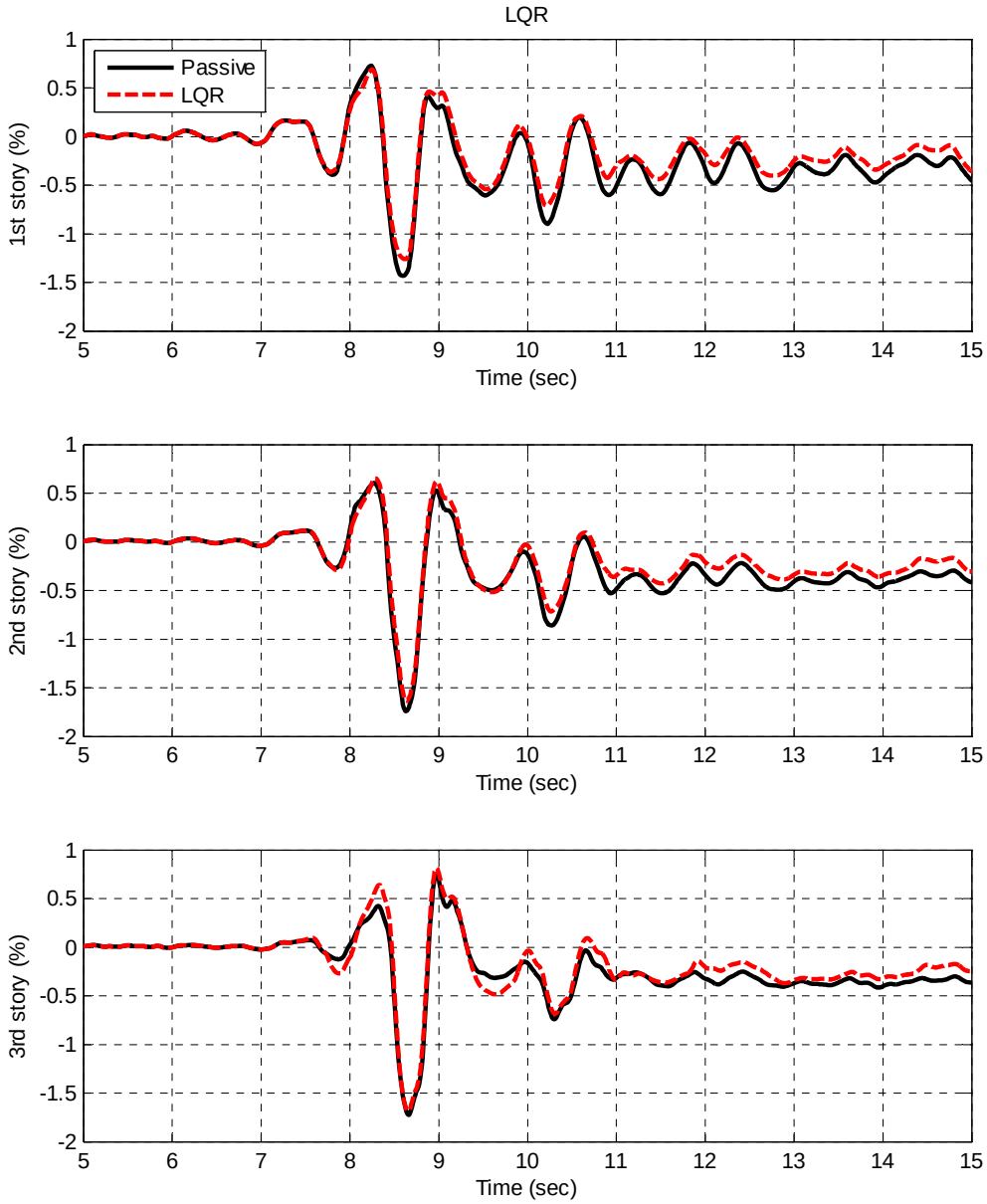

Figure 9.1 Comparison of story drifts between the passive control and the linear regulator (LQR) control under the 1999 Duzce ground motion, Turkey, DBE level

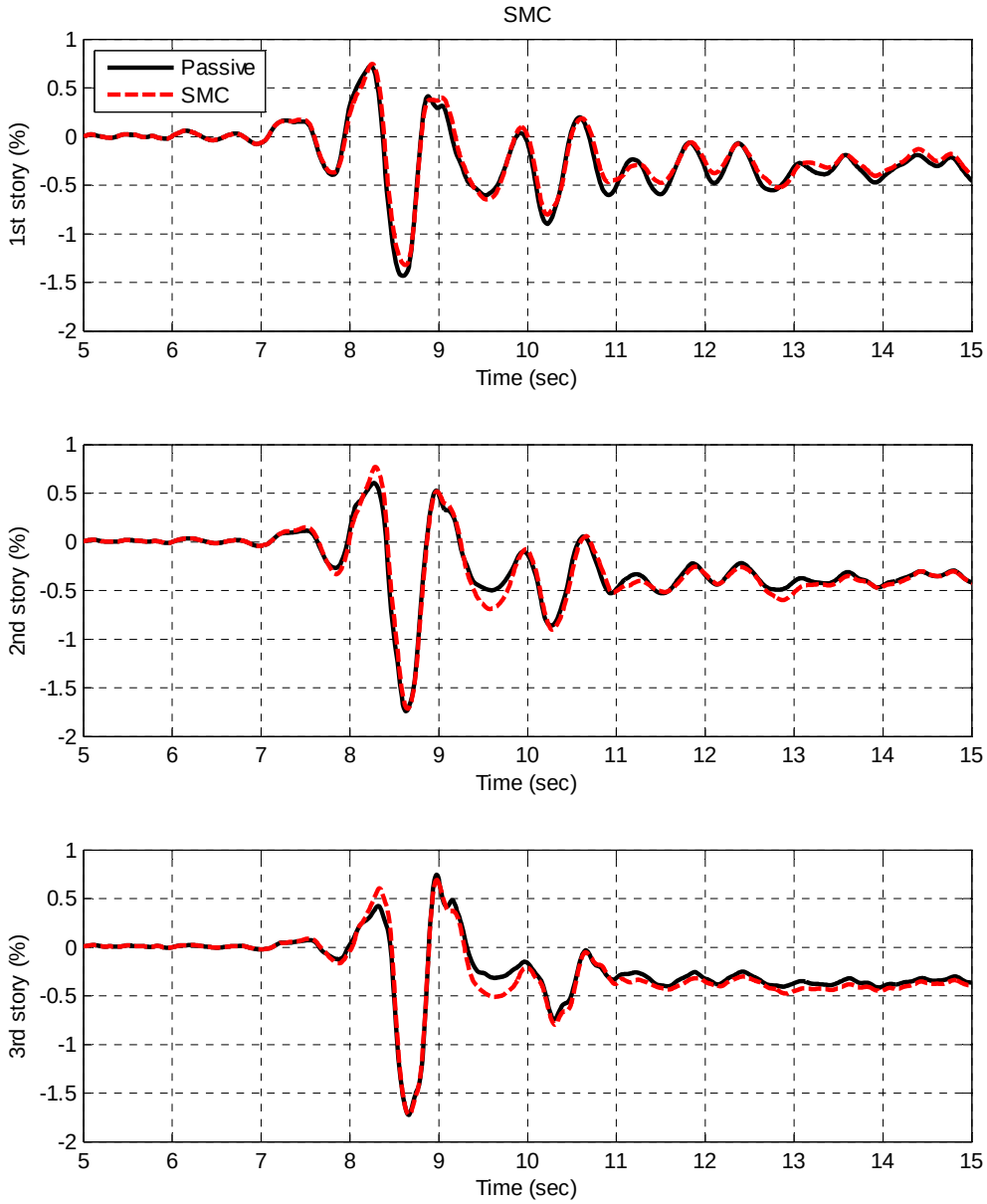

Figure 9.2 Comparison of story drifts between the passive control and the sliding mode control (SMC) under the 1999 Duzce ground motion, Turkey, DBE level

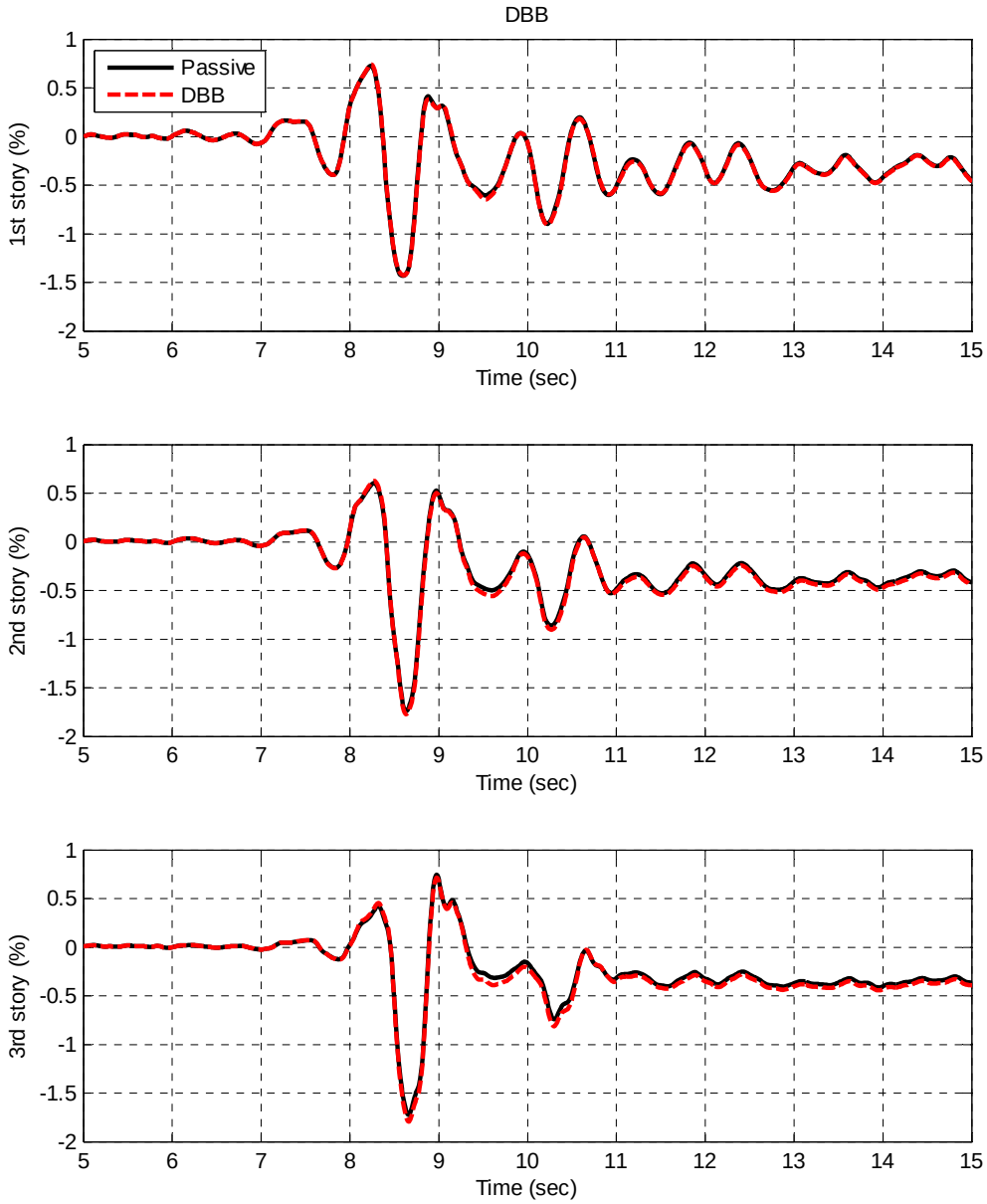

Figure 9.3 Comparison of story drifts between the passive control and the decentralized bang-bang control (DBB) under the 1999 Duzce ground motion, Turkey, DBE level

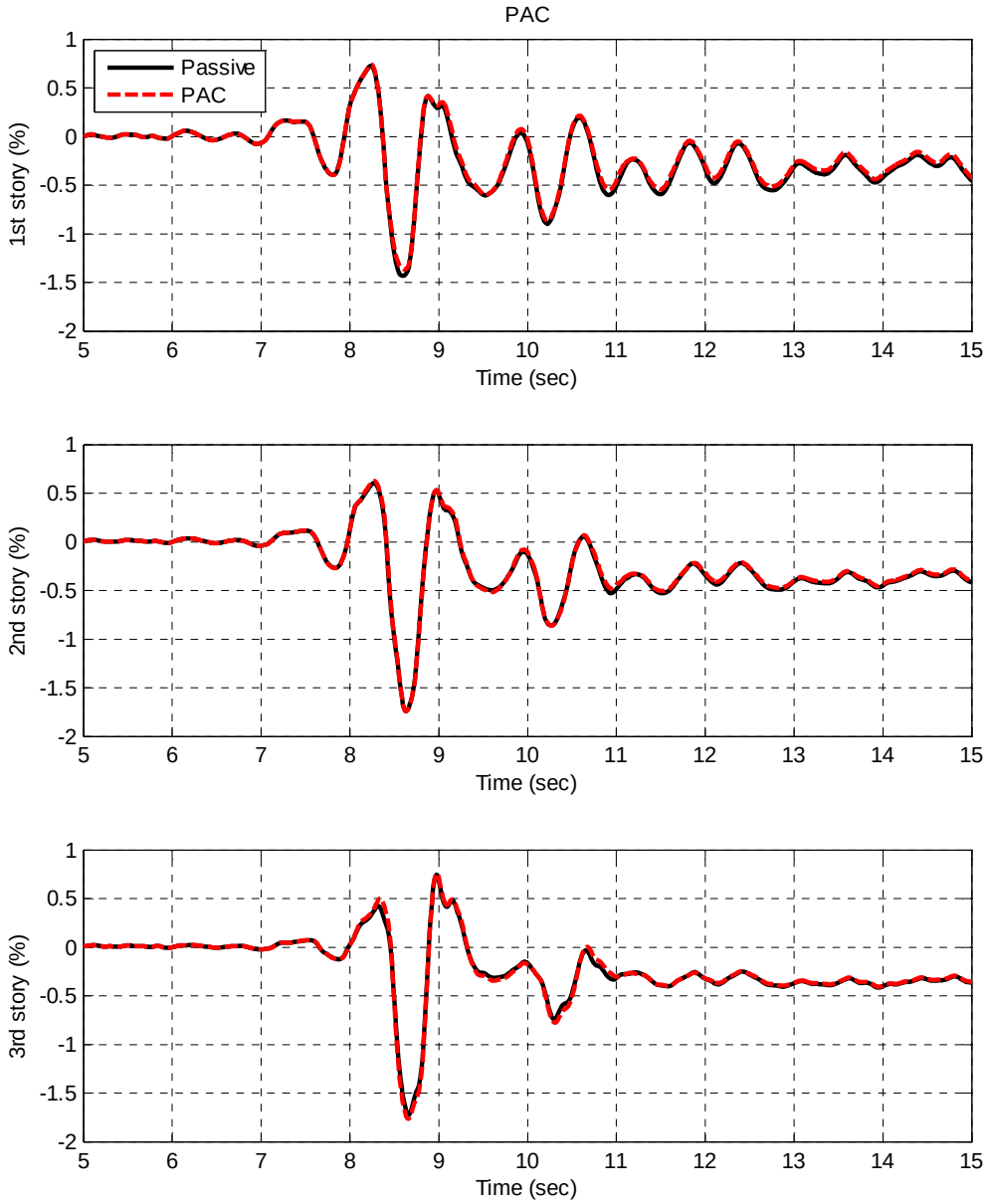

Figure 9.4 Comparison of story drifts between the passive control and the phase angle control (PAC) under the 1999 Duzce ground motion, Turkey, DBE level

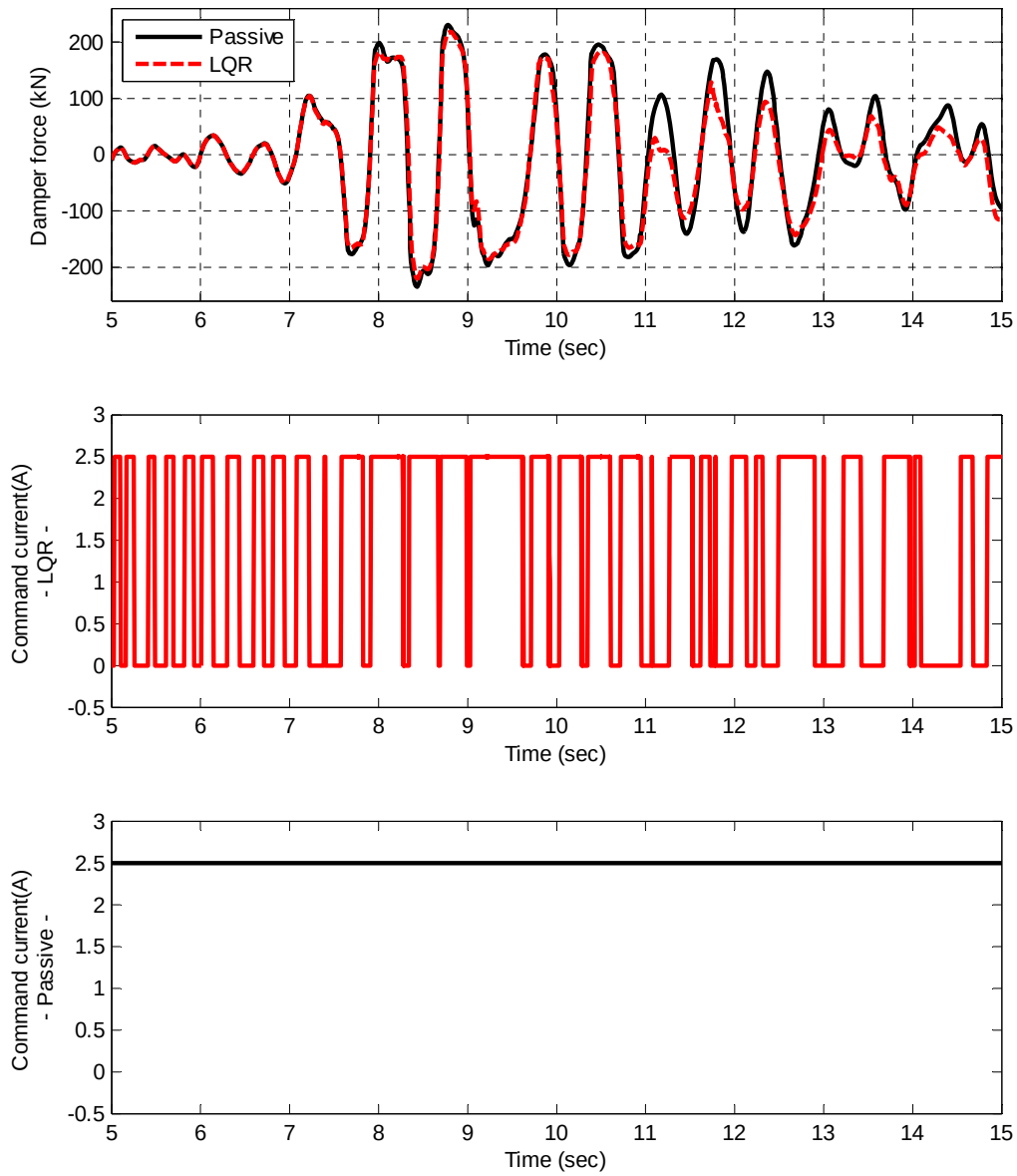

Figure 9.5 Comparison of damper force and command current (2nd story MR damper) between the passive control and the linear quadratic regulator (LQG) control under the 1999 Duzce ground motion, Turkey, DBE level

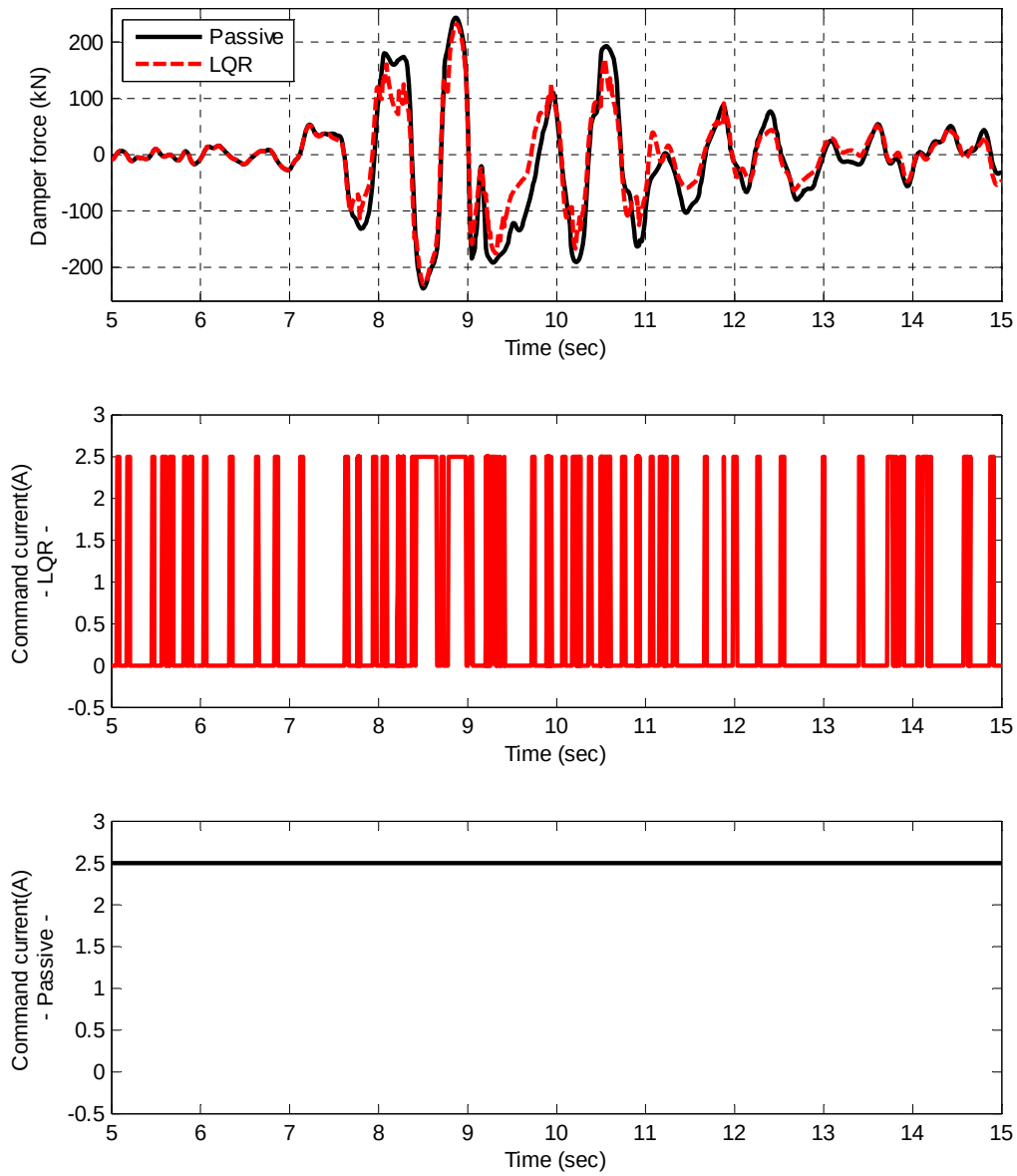

Figure 9.6 Comparison of damper force and command current (3rd story MR damper) between the passive control and the linear quadratic regulator (LQG) control under the 1999 Duzce ground motion, Turkey, DBE level

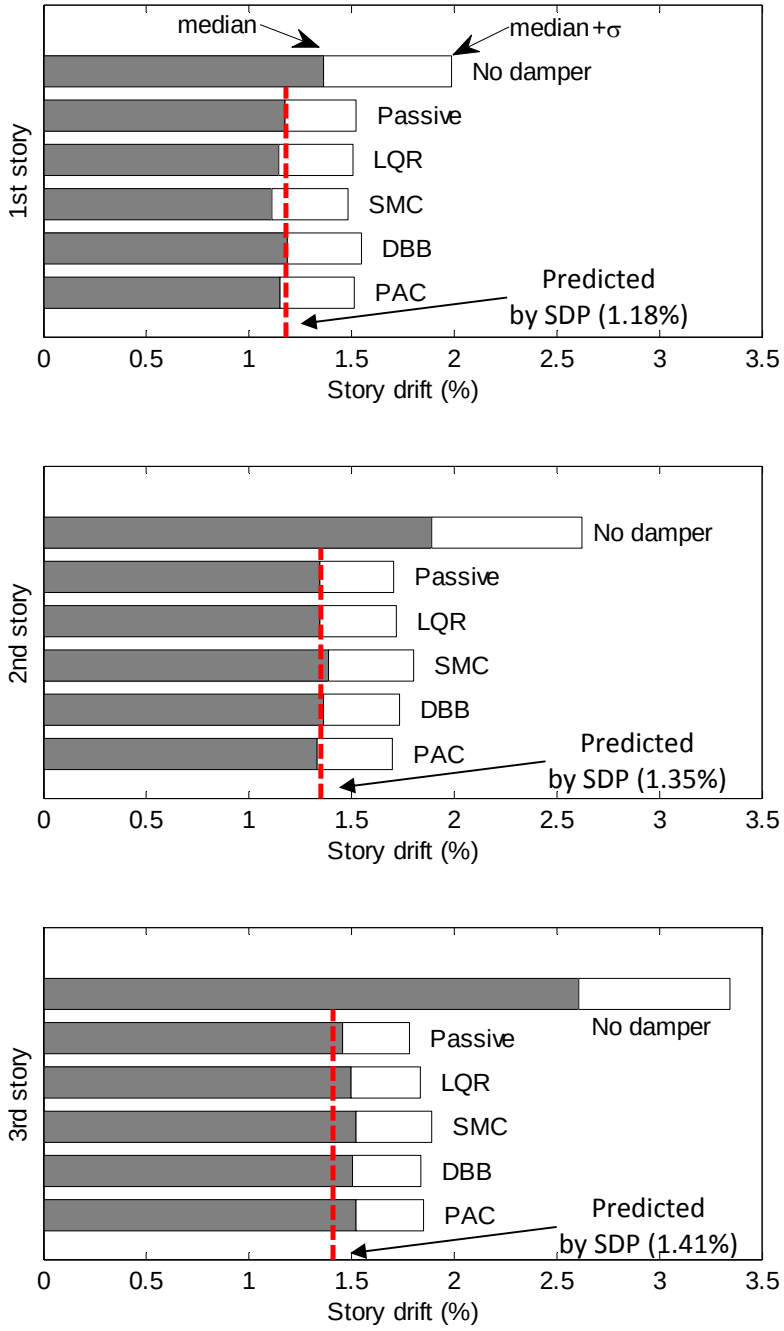

Figure 9.7 Comparison of maximum story drifts, DBE level

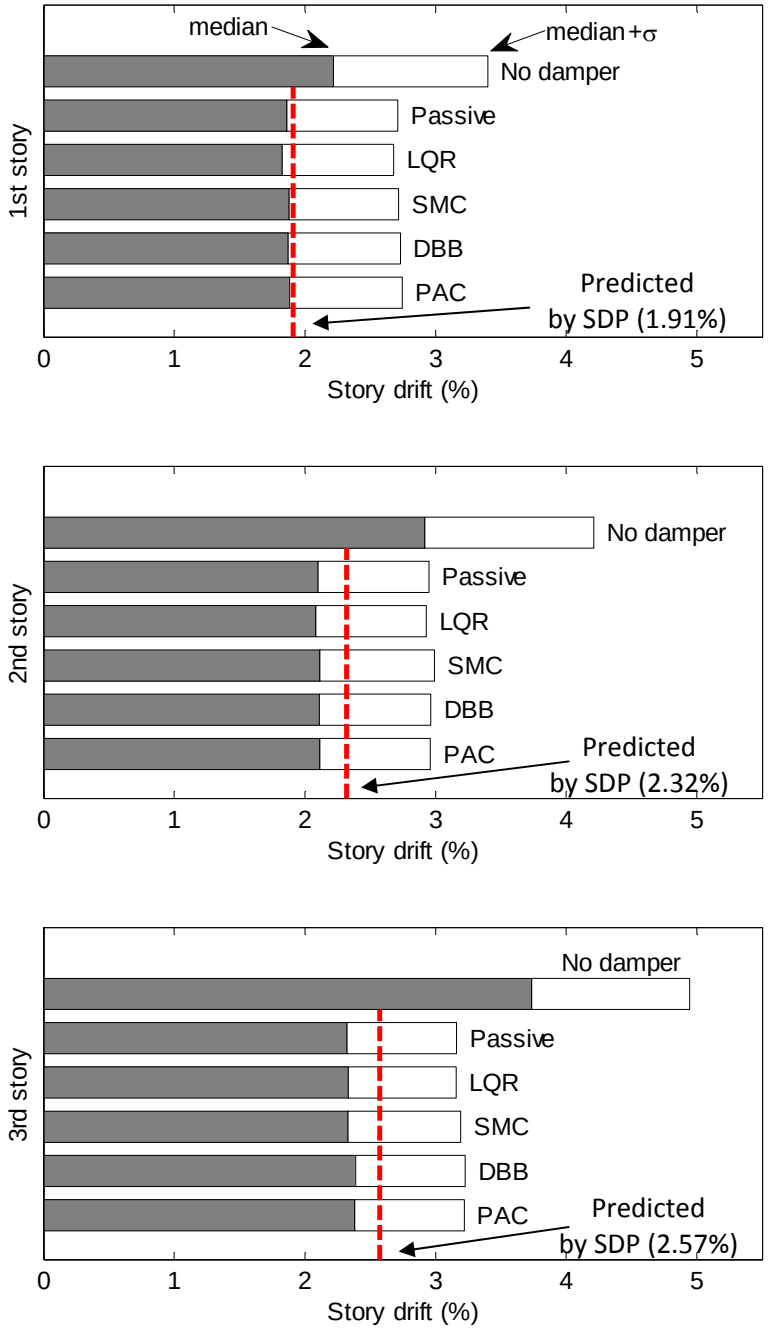

Figure 9.8 Comparison of maximum story drifts, MCE level

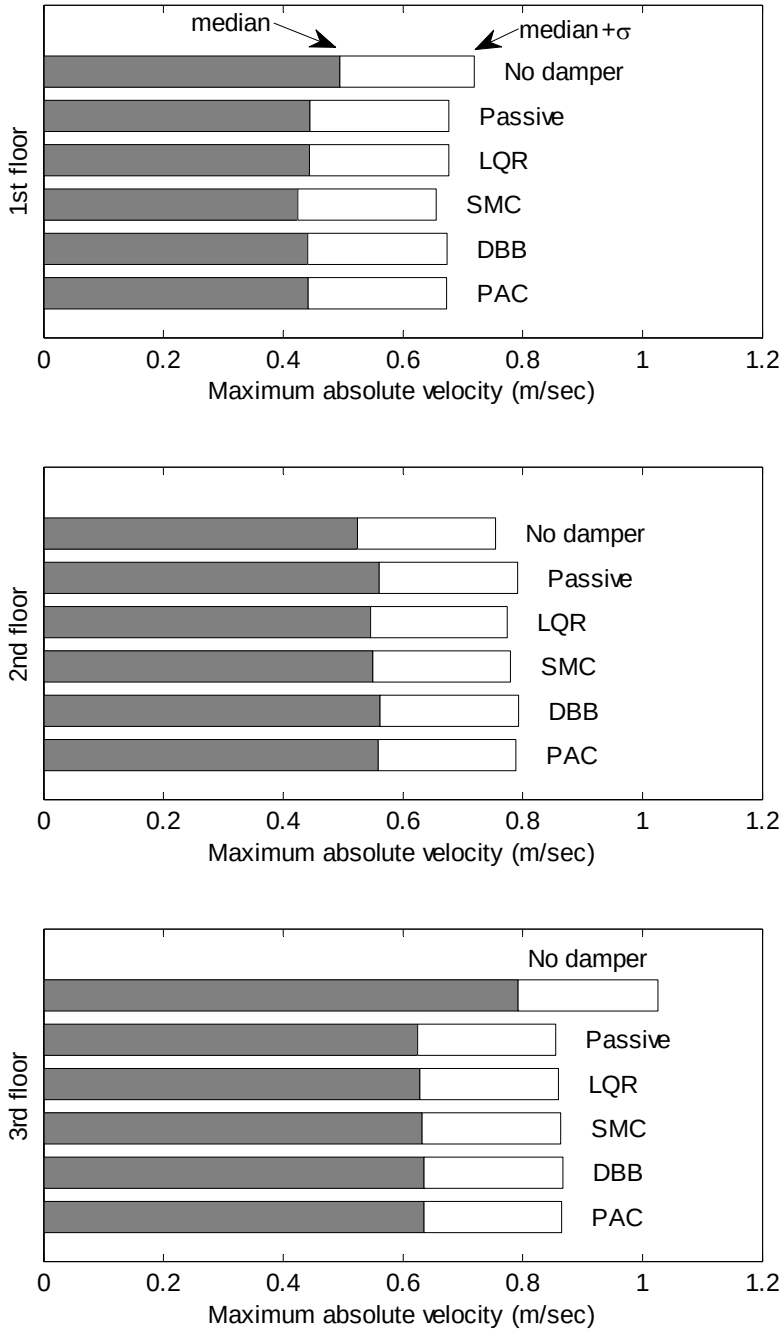

Figure 9.9 Comparison of maximum absolute velocities, DBE level

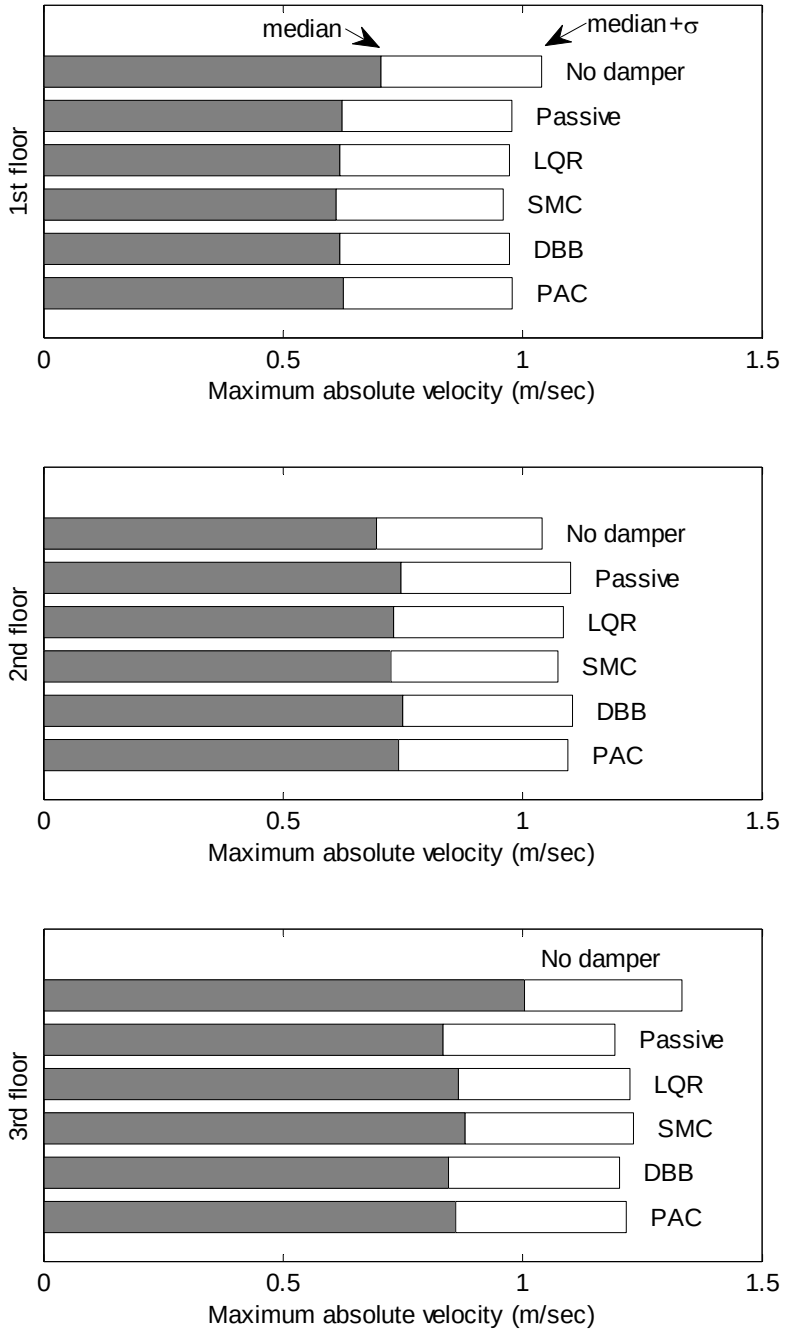

Figure 9.10 Comparison of maximum absolute velocities, MCE level

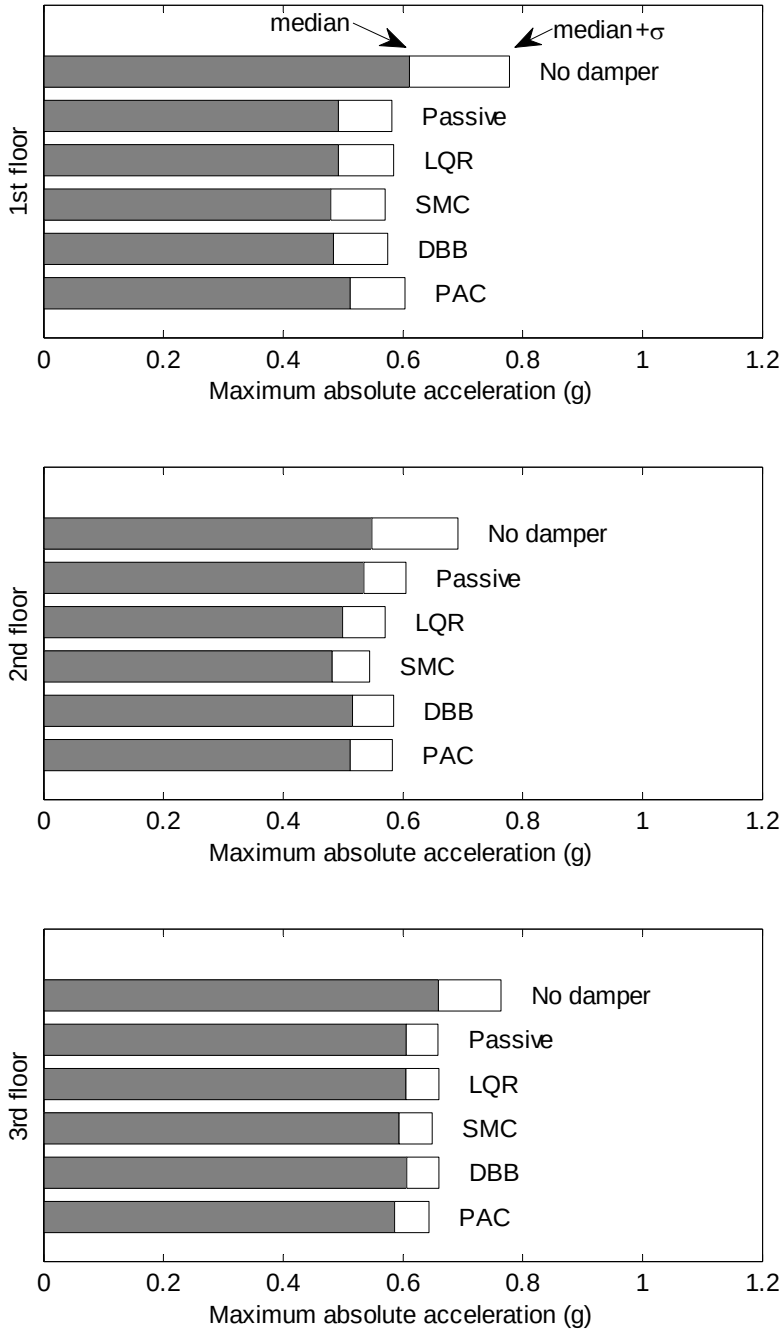

Figure 9.11 Comparison of maximum absolute accelerations, DBE level

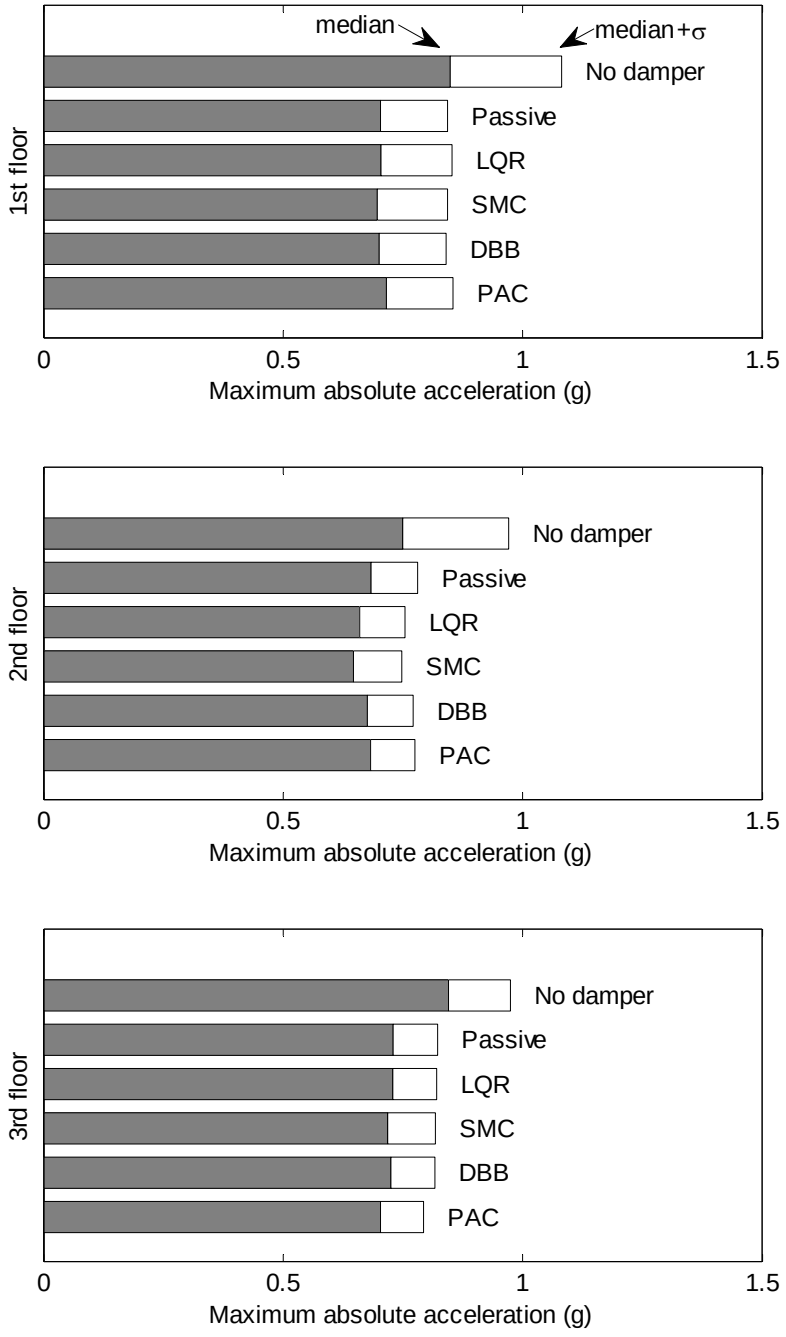

Figure 9.12 Comparison of maximum absolute accelerations, MCE level

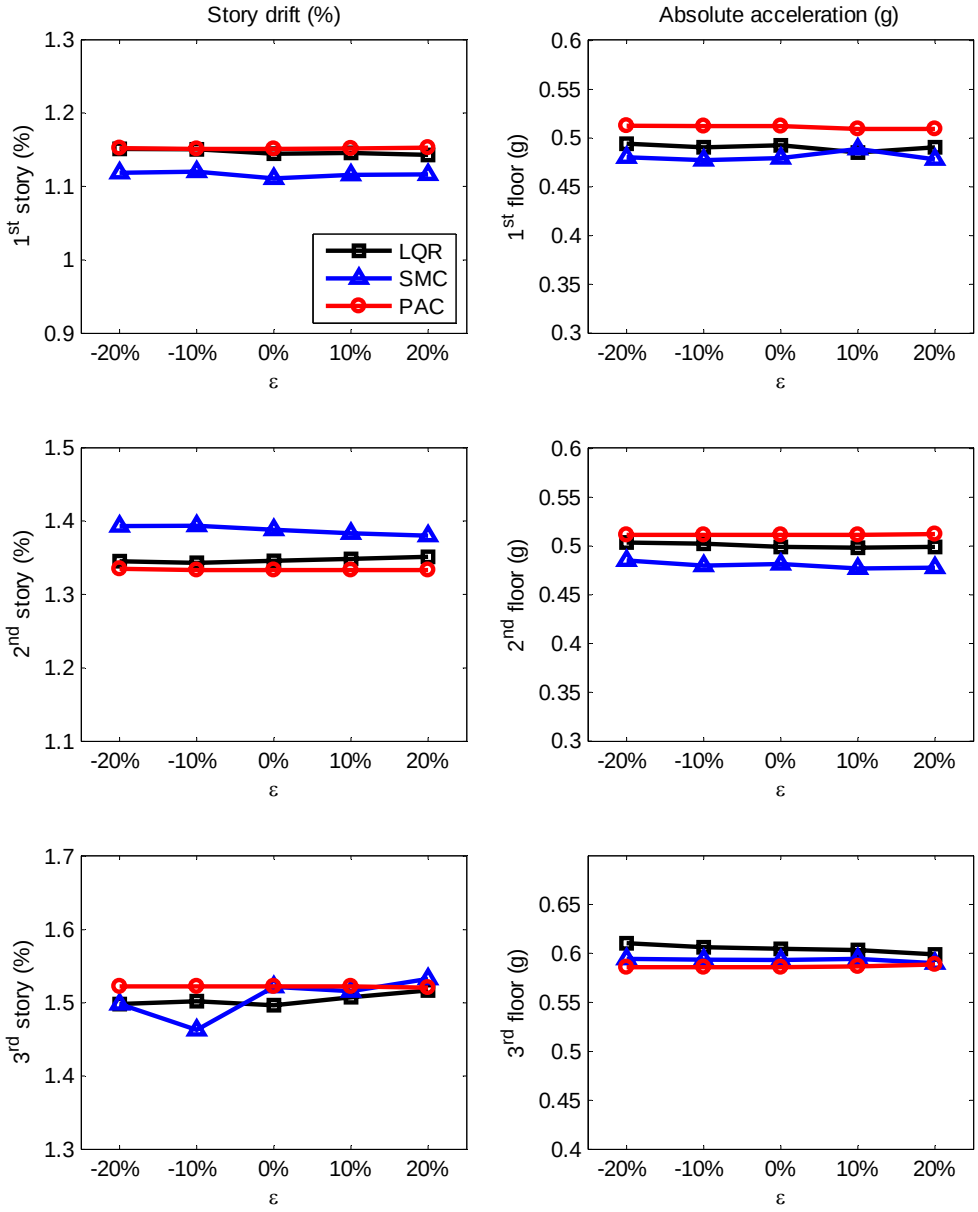

Figure 9.13 Effect of stiffness perturbation on the performance of semi-active controllers (median response, DBE level)

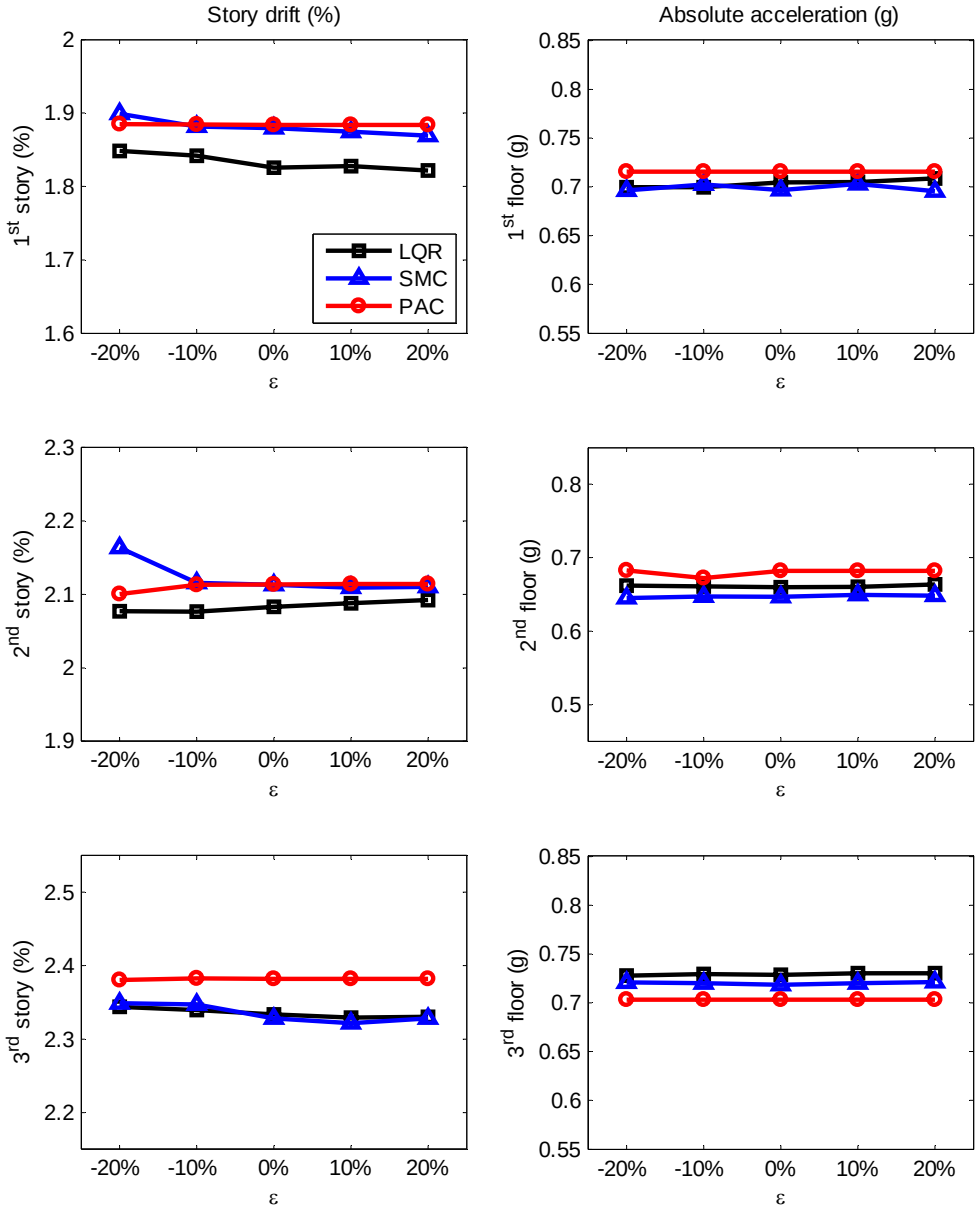

Figure 9.14 Effect of stiffness perturbation on the performance of semi-active controllers (median response, MCE level)

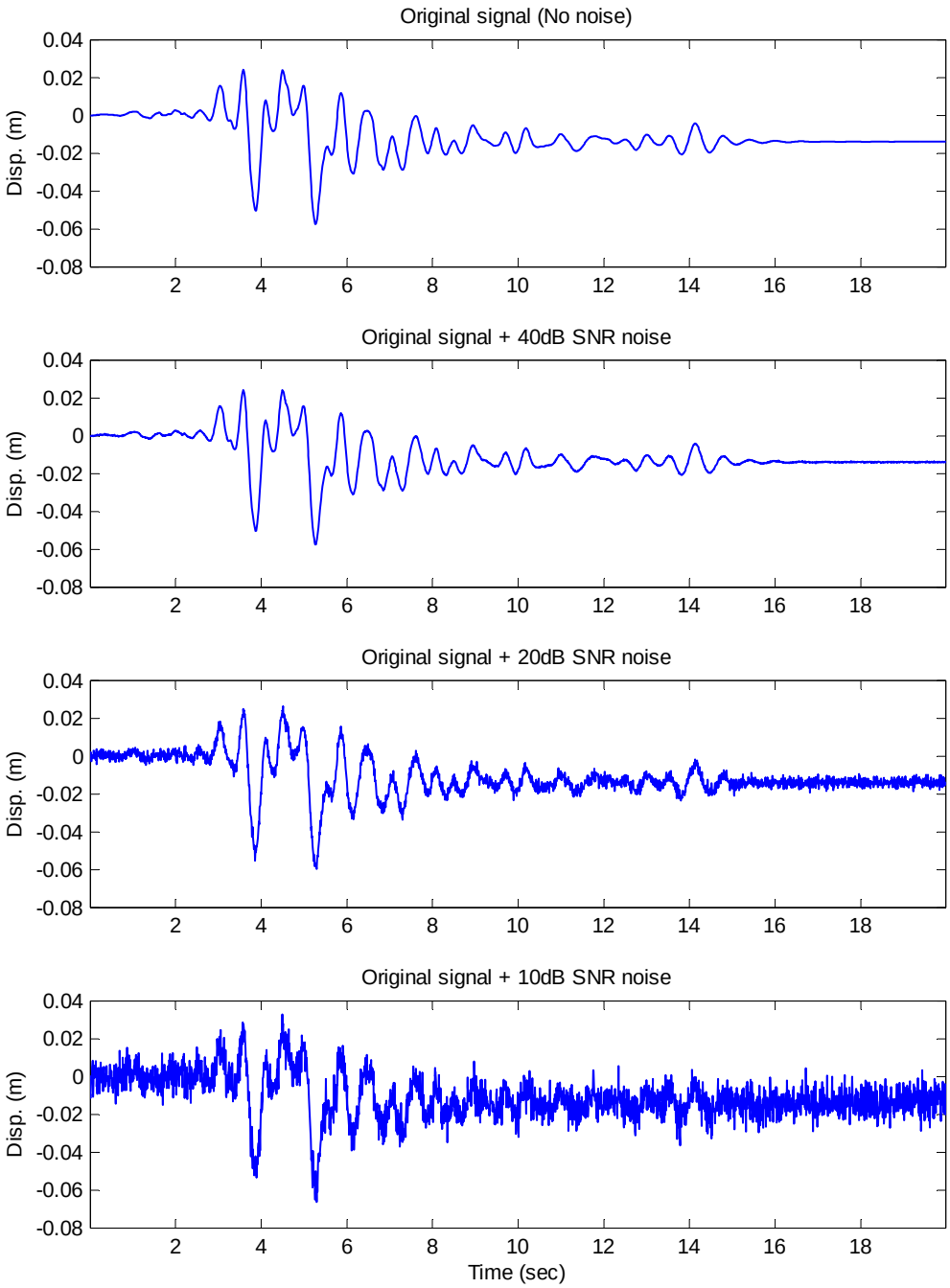

Figure 9.15 Corrupted signal by various noise levels

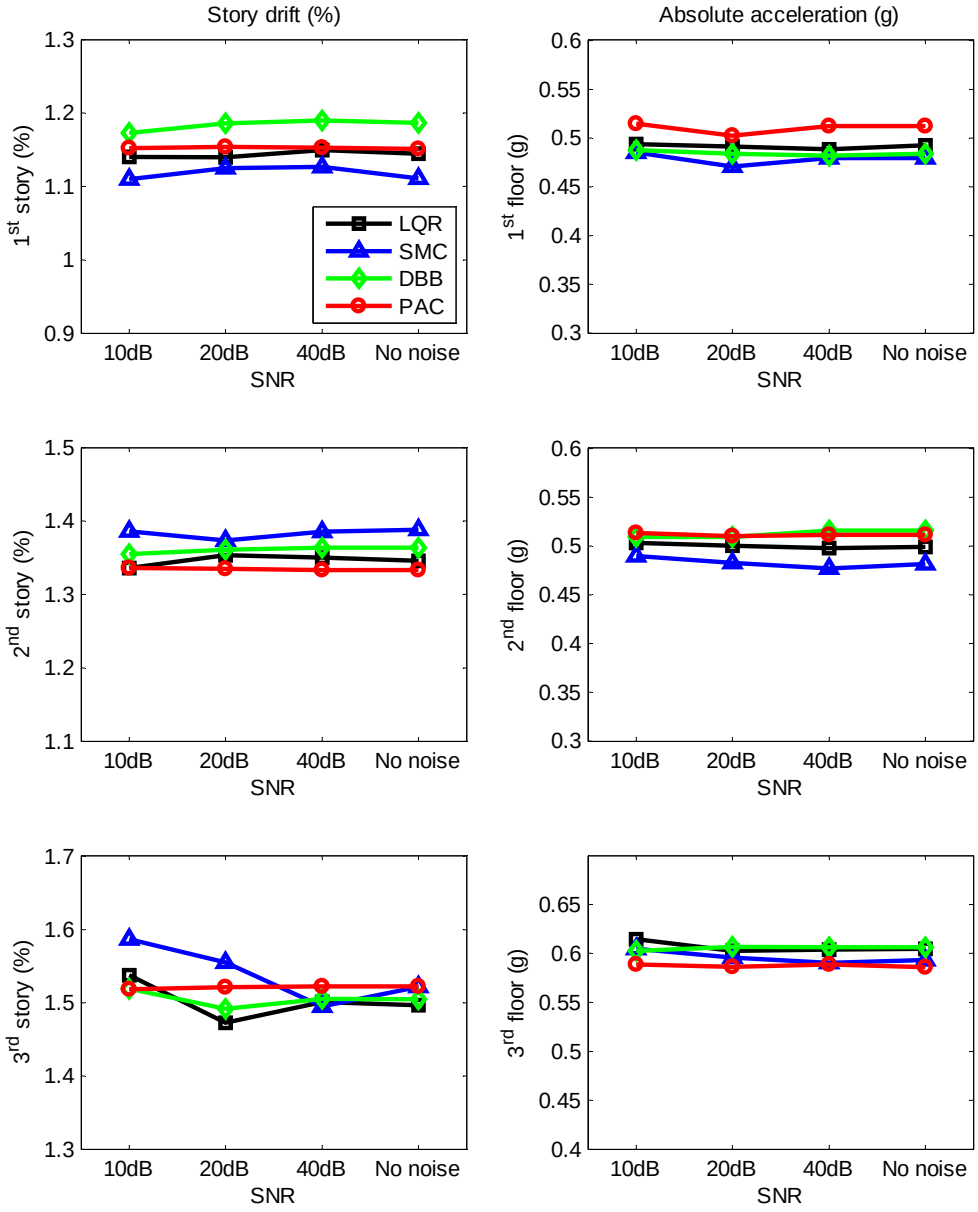

Figure 9.16 Effect of sensor noise level on the performance of semi-active controllers (median response, DBE level)

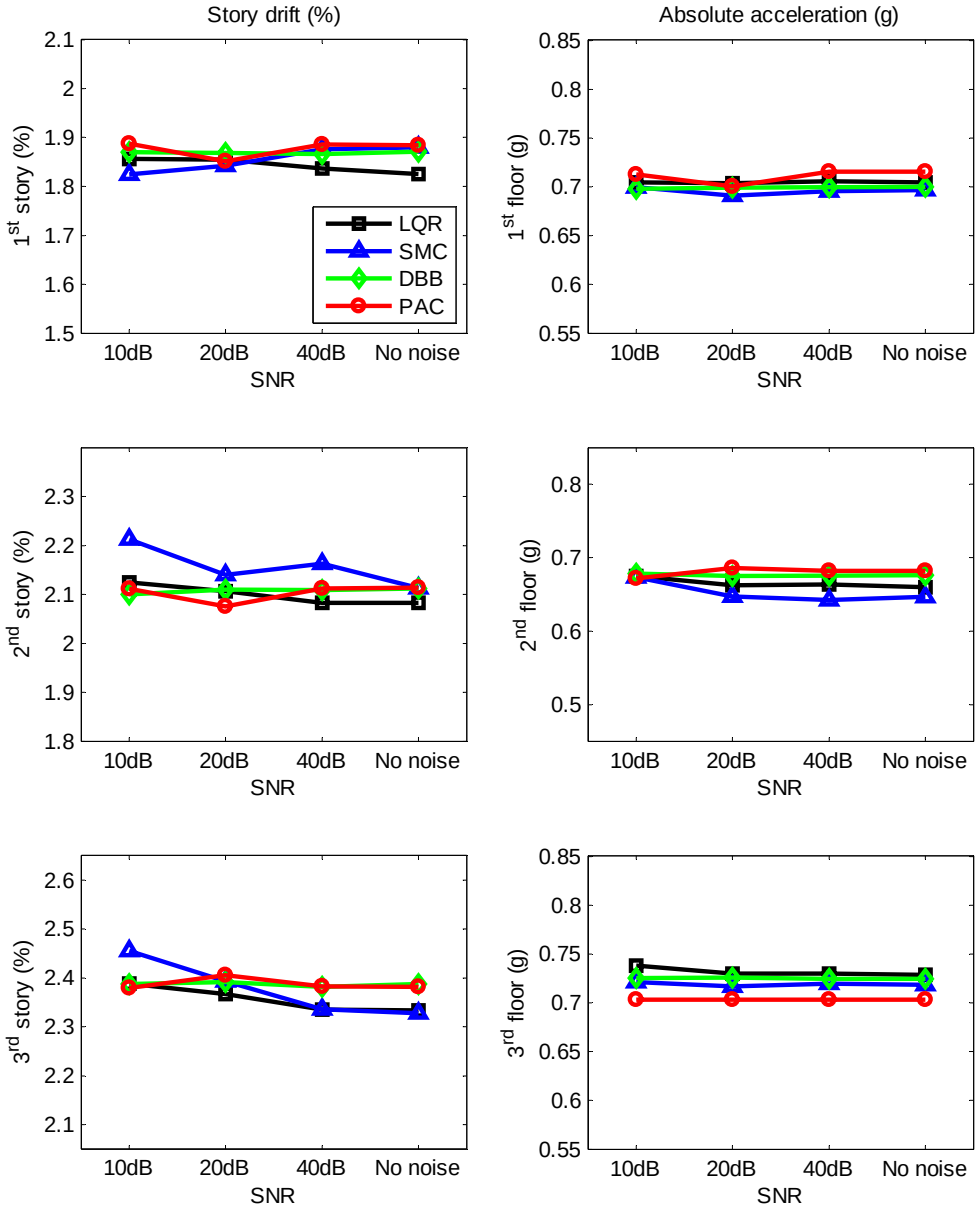

Figure 9.17 Effect of sensor noise level on the performance of semi-active controllers (median response, MCE level)

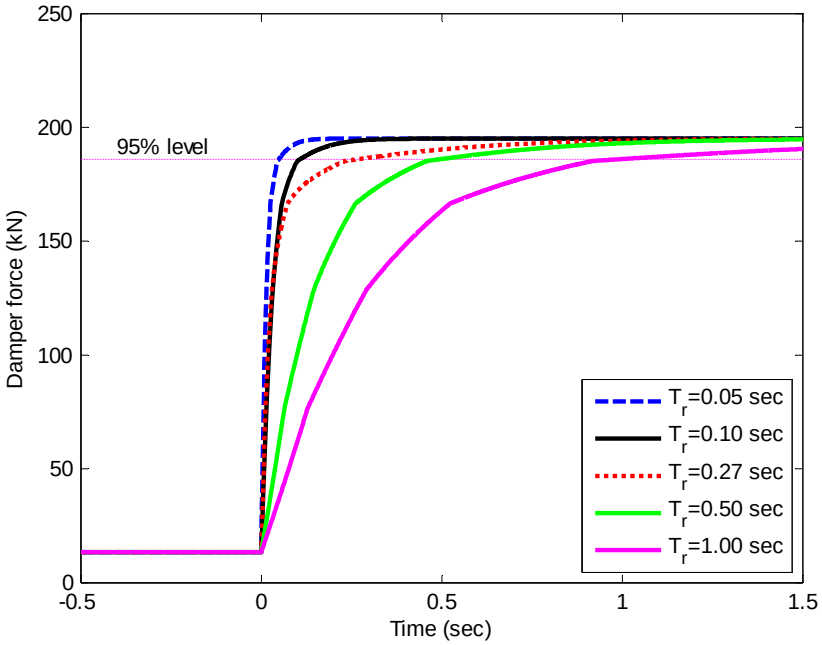

Figure 9.18 MR damper response with various rise times (T_r)

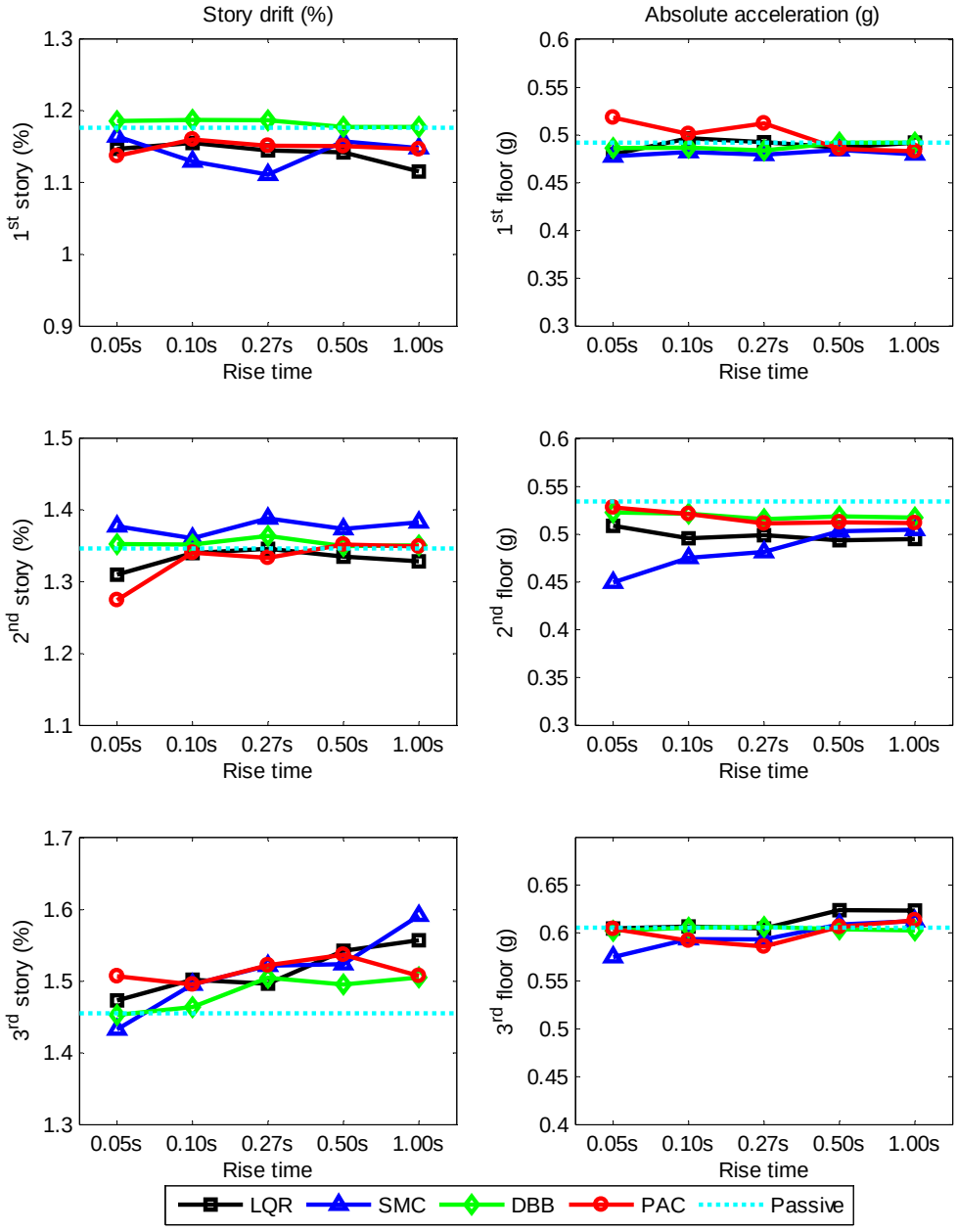

Figure 9.19 Effect of MR damper rise time on the performance of semi-active controllers (median response, DBE level)

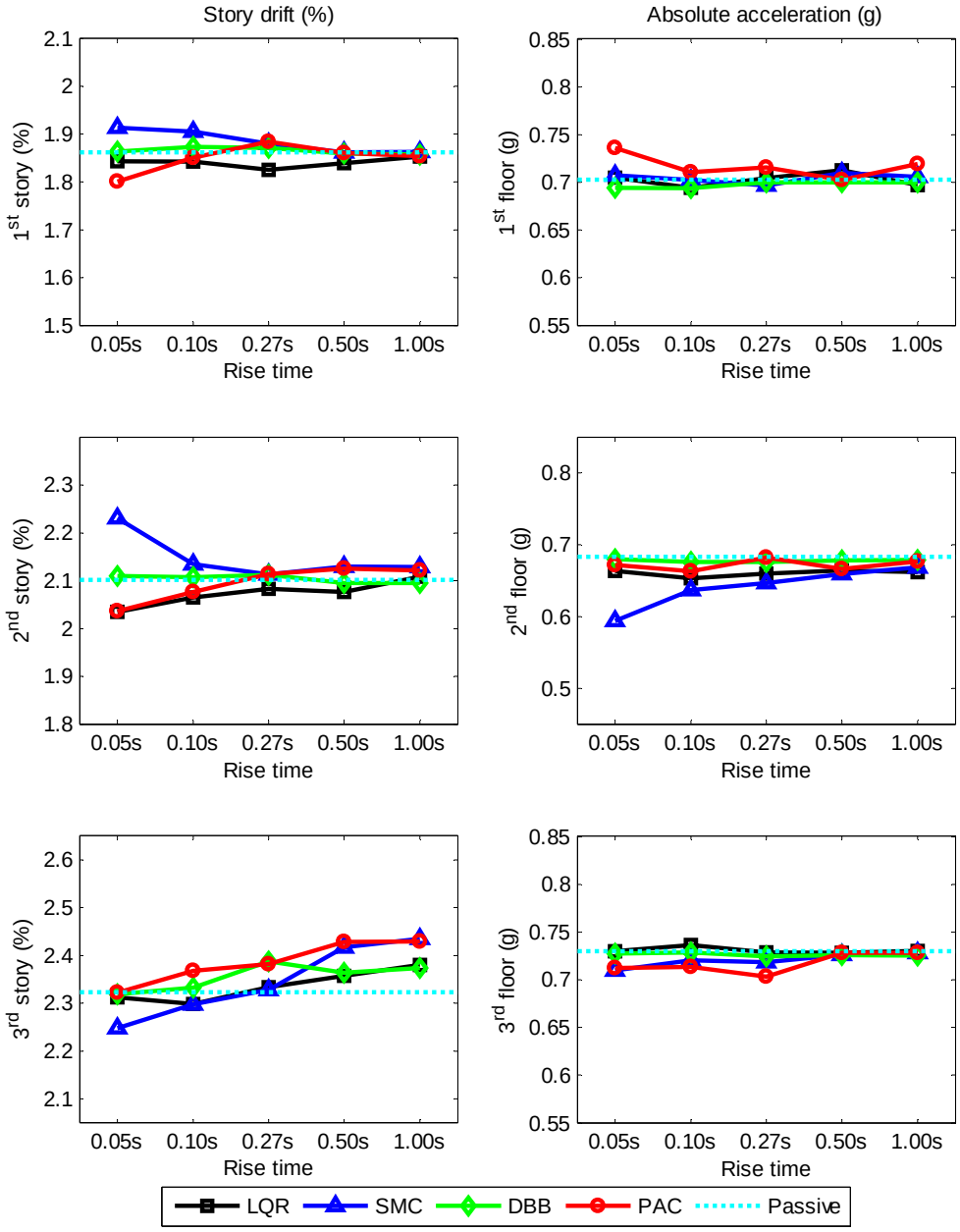

Figure 9.20 Effect of MR damper rise time on the performance of semi-active controllers (median response, MCE level)

Chapter 10

Assessment of Collapse Potential of Buildings with MR Dampers

10.1 General

In earthquake engineering, collapse implies that a structural system, or a part of it, is incapable of maintaining gravity load carrying capacity in the presence of seismic effects (Ibarra and Krawinkler 2005). When a building is subjected to large story drifts, it is vulnerable to dynamic instability due to P-Δ effects and deterioration in strength and stiffness of structural components, subsequently, resulting in collapse of the system. Protection against collapse has always been a major concern in the design of structures The recently developed FEMA P695 (ATC 2009) document provides a methodology for collapse assessment of structures.

While several studies have been conducted to assess the performance of supplemental damping systems and their effectiveness in mitigating the seismic hazard of structures under the DBE and MCE, the collapse resistance of buildings with MR dampers has not been investigated. The seismic collapse potential of structures with passive supplemental damping systems has been investigated by a few researchers using the incremental dynamic analysis (IDA) method (Solberg et al. 2007; Marshall and Charney 2010; Miyamoto et al. 2010). In this chapter, the collapse resistance capacity of the 3-story building structure with MR dampers investigated in Chapters 7 and 9 for seismic performance under the DBE and MCE is assessed for collapse based on the procedure given in FEMA P695. The nonlinear time history analyses used in the IDA

method are conducted using OpenSees. A phenomenological-based model developed by Ibarra and Krawinkler (2005) and modified by Lignos (2008) for modeling deterioration in beam plastic hinge regions is incorporated into OpenSees. IDA is performed on the building using five different controllers (one passive control case and the four semi-active controllers) presented in Chapter 9. Collapse fragility curves are obtained using the ensemble of 44 ground motions listed in Appendix 3. The collapse fragility curves for the various control cases are compared in order to assess the performance of the control strategies in mitigating structural collapse under extreme earthquake ground motions.

10.2 Deterioration Models

The P-Δ effect and the strength and stiffness deterioration of structural components are considered to be the major contributors to the collapse of a structural system under seismic loading. The P-Δ effect is well-understood and mathematical models have been formulated for use in linear and nonlinear structural analysis, while the modeling of strength and stiffness deterioration under seismic loading is an on-going research topic. For accurate evaluation of the collapse of a structure, it is necessary to construct a model that is capable of capturing the strength and stiffness deterioration of structural components under seismic loading. In this section, recently developed deterioration models are introduced. The models are used for the IDA presented later in this chapter.

10.2.1 Ibarra-Krawinkler Model

Ibarra and Krawinkler (2005) developed a hysteretic deterioration model to describe the moment and rotation behavior in the plastic hinge region of a steel or a concrete beam. The model is based on a backbone curve that defines a reference skeleton behavior of a non-deteriorated system. A set of rules are used to define the basic characteristics of the hysteretic behavior between the bounds defined by the backbone curve as well as deterioration in strength and stiffness with respect to the backbone curve.

The backbone curve is a reference force-deformation relationship that defines the bounds within which the hysteretic response of the component is confined. Thus, the backbone curve represents the maximum force capacity of element that can be sustained under cyclic loading. Figure 10.1 shows the shape of backbone curve by Ibarra and Krawinkler (2005). The quantities F and δ are generic force and deformation quantities, respectively. For flexural plastic hinge regions F and δ represent the moment and rotation angle, i.e., $F = M$ and $\delta = \theta$. In this model the emphasis is on the effective elastic stiffness K_e, the effective yield strength F_y, the effective strain hardening stiffness $K_s = \alpha_s K_e$, the capping point (point of maximum strength) defined by F_c and δ_c, the post-capping stiffness $K_c = \alpha_c K_e$, and the residual strength F_r. The ratio δ_c/δ_y is used as a reference value for the deformation capacity of the structural component that is being modeled. The Ibarra-Krawinkler model can be employed together with numerous basic linearized hysteretic models, e.g., the bilinear model, the peak-oriented model, or the pinching model.

The cyclic deterioration rule of the model is based on the hysteretic energy dissipated by the component under cyclic loading. In the model it is assumed that the component possesses a reference inherent hysteretic energy dissipation capacity, regardless of the loading history applied to the component.

The Ibarra-Krawinkler model is characterized by four different modes of deterioration: i) basic strength deterioration; ii) post-cap strength deterioration; iii) unloading stiffness deterioration; and iv) accelerated reloading stiffness deterioration. The detailed mathematical descriptions about these four modes of deterioration can be found in Ibarra and Krwawinkler (2005).

10.2.2 Modified Ibarra-Krawinkler Model

Lignos (2008) modified the Ibarra-Krawinkler model based on observations from data from several hundreds tests that had been conducted on steel and RC elements. Lignos modified the backbone curve and the cyclic deterioration modeling in the original Ibarra-Krawinkler model, where the new backbone curve proposed by Lignos is shown in Figure 10.2. In the modified model, a new branch is added to the original backbone curve that allows the simulation of complete loss of strength which can occur at large inelastic deformations, as observed, for example, when ductile tearing takes place in steel components. The backbone curve is also modified to be asymmetric in the positive and negative loading directions. The definitions of some parameters at the original model are also revised in the modified model to achieve a better description of the backbone curve. In Figure 10.2, δ_c is the cap deformation (deformation

associated with F_c for monotonic loading); F_y is the effective yield strength; δ_y is the effective yield deformation (=F_y/K_e); K_e is the effective elastic stiffness; F_r is the residual strength capacity; δ_r is the deformation at residual strength; δ_u is the ultimate deformation capacity; δ_p is the plastic deformation capacity associated with monotonic loading; δ_{pc} is the post-capping deformation capacity associated with monotonic loading; F_c/F_y is the post-yield strength ratio; F_{yp} is the predicted effective yield strength; F_{yn} is the nominal effective yield strength; κ is the residual strength ratio (=F_r/F_y); and F_c is the strength cap (maximum strength, incorporating average strain hardening). The strain hardening ratio α_s and the post-capping stiffness ratio α_c are defined as $\alpha_s = K_s/K_e = [(F_c/F_y)/\delta_p]/K_e$ and $\alpha_c = K_{pc}/K_e = (F_c/\delta_{pc})/K_e$, respectively.

The cyclic deterioration rule is also changed to enable different rates of cyclic deterioration in each loading direction to be considered which can be effectively applied to the behavior of composite sections, e.g., a steel beam with a composite concrete floor slab. The definition of the reference energy dissipation capacity E_t is also changed by using the parameter δ_p in the normalization of the reference energy dissipation capacity, i.e., $E_t = \Lambda\delta_p$, where Λ denotes the reference cumulative deformation capacity. Figure 10.3 shows the comparison of this modified model with experimental results for the moment-chord rotation of a steel beam-to-column moment connection tested by Ricles et al. (2004).

10.3 Modeling of the 3-Story Building Structure

The 3-story building structure described in Chapter 6 is used for the IDAs. The member sizes for the MRF and DBF are illustrated in Figure 7.2. An OpenSees model for the implementation of the IDA is provided in Figure 10.4. The model is similar to that used for assessing the SDP in Chapter 7 (see Section 7.2) and for assessing various controllers in Chapter 9, except for the inclusion of the deterioration element at the ends of the beams in the MRFs where plastic hinges are expected to occur..

Each beam of the MRF in the IDA model consists of three elements: two deterioration elements with zero length at the column faces based on the modified Ibarra-Krawinkler model; and one linear elastic element between the deterioration elements. The parameters for the deterioration element are summarized in Table 10.1, where M_y, θ_p and θ_{pc} denote the yield moment, plastic rotation capacity and the post-capping rotation capacity, respectively. The values of these parameters are based on Lignos and Krawinkler (2009) for the beam sections used in the structure.

To account for the P-Δ effect, a lean-on column is included as described in Chapter 7. Since the floor diaphragm is assumed to be rigid, the top node of the panel zone element in the MRF and the beam-column joint in the DBF are horizontally constrained together with the node of the lean-on column at each floor level, while the vertical and rotational dofs are released. The beams of the DBF are modeled using a linear elastic truss element because it was designed not to have a rotational stiffness at the beam-column joint and does not have any axial deformation due to the rigid diaphragm assumption.

The diagonal bracing in the DBF is modeled using a linear elastic truss element. Based on the demand-to-capacity ratio of the diagonal bracing designed in Chapter 6, the diagonal bracing remains linear elastic for MR damper forces up to 825kN. Therefore, there is a maximum allowable damper velocity that assures the linear elastic behavior of the brace. Using the post-yield curve of the MNS MR damper model with a current input of 2.5A, the damper velocity corresponding to a damper force of 825kN is calculated to be about 23m/sec. Assuming the damper velocity is equal to the pseudo-velocity of the damper, the damper displacement corresponding to the damper velocity of 23m/sec is obtained to be 3.1m based on the fundamental period of the building (T_1=0.85 sec), which corresponds to a story drift of 135% based on the story height of the building (2.286m). The structure will collapse before reaching the extreme story drift of 135%. Therefore, the modeling of the diagonal bracing using the linear elastic truss element appears to be reasonable.

As mentioned previously, the MR damper is assumed to be located between the top of the diagonal bracing and beam-column joint. Variable current MNS model is used for the nonlinear time history analysis. The parameters listed in Table 3.3 are used for the MNS model. The parameters provided in Chapter 4 for the dynamics of MR dampers associated with variable current (i.e., $\alpha_0 = 24.96$, $\alpha_1 = 3.57$, $\beta^+ = 0.31$, $\beta^- = -0.30$) are in simulating the semi-active behavior of the MR damper.

The structural model in Figure 10.4 has two major structural components that can lead to dynamic instability under extreme earthquake ground motions: (1) negative stiffness induced by the gravity loads (the P-Δ effect); and (2) deterioration elements in

the beams of the MRF. The columns of the MRF and DBF are assumed to have sufficient strength so that no deterioration in strength or stiffness of the columns is expected during the IDAs.

The large-scale MR dampers for this study have a stroke limit of ±279mm (=±11 inches). The story height of the 3-story building structure is 2.286m, implying that the dampers will reach their stroke limit at 12.2% story drift. Since large story drifts can be expected in a collapse simulation, the MR damper may bottom out with respect to the stroke limit under extreme earthquake ground motions. In this case, a gap or the hook element should be included in the model to account for the dynamic behavior associated with reaching the stroke limit, as suggested by Miyamoto et al. (2010). The MR dampers in this study are assumed to have a sufficient stroke limit to accommodate the large story drifts during a collapse simulation. To model the conditions when a damper reaches its stroke limit requires the use of experimental data to develop a damper model that includes all possible failure limit states (e.g., tension fracture of the damper piston rod). These types of experiments have not been conducted, and therefore this data does not exist. A future study of this topic is needed.

10.4 Ground Motions

The far-field ground motion record set provided in FEMA P695 was selected as ground motions for the IDA, and are listed in Appendix 3. These ground motions were selected from the PEER-NGA data base to permit evaluation of the record-to-record (RTR) variability of the structural response and to permit calculation of the median

collapse intensity. Among the 22 earthquakes, 14 are taken from the United States and 7 are from other countries. Event magnitudes range from M6.5 to M7.6, with an average magnitude of M7.0. Each earthquake has two horizontal components so that a total of 44 ground motions are used for the IDA.

FEMA P695 recommends to use the spectral acceleration at the fundamental period of a structure, S_{aT_1}, as the intensity measure (IM). The ground motions are scaled up (or down) based on the spectral acceleration at the fundamental period of the structure. The MR damper stiffness depends on the displacement amplitude. Hence, the effective fundamental period of the structure is dependent on the amplitude of the damper displacements, which is a function of the intensity of ground motion. In this study, the fundamental period of the structure without MR dampers is used to determine the spectral acceleration corresponding to the IM, rather than using the effective fundamental period with the dampers. The fundamental period without MR dampers is 0.94 sec as provided in Table 6.17, and the scaling of ground motions is performed based on the spectral acceleration at this period.

10.5 Controllers

The controllers employed in Chapter 9 are used here for the IDA, namely: i) passive control; ii) linear quadratic regulator (LQR); iii) sliding mode control (SMC); iv) decentralized bang-bang control(DBB); and v) phase angle control (PAC). The same parameters for each controller (i.e., the LQR gain and the sliding surface for SMC) as presented in Chapter 9 are applied to the IDAs. A constant current with I=2.5A is

supplied to the MR dampers for passive control, while either I=0.0A or 2.5A is used for the semi-active controllers.

10.6 Incremental Dynamic Analyses

The incremental dynamic analysis (IDA) curves are a set of plots that correlate a damage measure (DM) with the intensity measure (IM) that characterizes the applied scaled accelerograms (Vamvatsikos and Cornell 2002).The roof drift ratio of the building structure, θ_{roof}, is selected as the DM for this study. A ground motion is scaled up until dynamic instability occurs, where an IDA curve becomes a flat line, i.e., at collapse. In this study, it is assumed that collapse occurs by the time that θ_{roof} reaches 17%. A selected ground motion is gradually scaled up until θ_{roof} exceeds 17%. For the 44 ground motions in the ensemble, the IDA curves all became flat indicating collapse before θ_{roof} reached 17%. The median roof drift when the IDA curves become flat was approximately 14%.

Figures 10.5 through 10.8 show individual IDA curves as the various controllers are used. Each semi-active controller is compared with the passive control case and the case without MR dampers. The IDA curves in the figure are obtained for the 1999 Kocaeli earthquake (Duzce, 180 component). As can be observed in Figure 10.5, the roof drift of the building gradually increases with increasing spectral acceleration and collapse occurs at $S_{aT_1} = 1.66$ g and $S_{aT_1} = 2.25$ g for the building without MR dampers (no damper case) and with passive control, respectively. Apparently, the collapse potential of the building is reduced by using the MR dampers. When the semi-

active controllers are used, collapse of the building occurs at $S_{aT_1} = 2.31$ g, $S_{aT_1} = 2.19$ g, $S_{aT_1} = 2.23$ g, and $S_{aT_1} = 2.23$ g for the LQR, SMC, DBB, and PAC semi-active controllers, respectively (see Figures 10.5 through 10.8). Although the LQR controller shows a marginally higher collapse spectral acceleration than the passive control case, overall the collapse potential of the building with semi-active controllers is similar to that with passive control for this selected earthquake ground motion.

As observed in Chapter 9, the structure with MR dampers performs better than the building without dampers when the intensity of ground motion is around the DBE or MCE level. However, the situation may change when the intensity is large, depending on the characteristics of the ground motion and the structural properties. Figure 10.9 compares the time histories for roof and 1st story drifts for three different control cases (no damper, passive control, and LQR) when the building is subjected to the Gilroy array#3, 090 component from the 1989 Loma Prieta earthquake scaled to S_{aT_1}=2.0g. The no damper case has the smallest roof drift, compared to the remaining two cases with MR dampers. The roof drift for the passive control case gradually increases, displaying the potential for incipient collapse due to P-Δ effect and strength deterioration, while the LQR case is relatively stable and has a smaller roof drift than the passive control case.

The behavior of a nonlinear structure is path dependent and influenced by the input ground motion. The building reaches its peak roof drift in the negative direction at *t*=3.6 sec. At this time instant, the roof drift for the building with MR dampers is less than that without MR dampers due to the energy dissipation by the MR dampers. After

t=3.6 sec. the building displaces in the positive direction and reaches a local maximum roof drift at t=4.3 sec. During this transition from the negative maximum roof drift to the positive local maximum roof drift, the roof drift changes by about 12.4%, 13.4%, and 13.3% for the no damper, passive, and LQR cases, respectively. The roof drift for the no damper case at t=4.3 sec is about 3.5%, while that for the building with MR dampers is about 8.7% and 8.3% for the passive and LQR controllers, respectively. Since the negative maximum roof drift for the no damper case was larger in amplitude in the negative direction than the passive or LQR cases, the roof drift for the no damper case becomes the smallest one when the structure reaches the positive local maximum roof drift at t=4.3 sec.

Figure 10.10 shows the base shear and the 1st story drift relationships for the three different control strategies. The base shear is obtained from the sum of the story shear forces at the near the base of the MRF and DBF columns. When t=4.3 sec, the 1st story drift for the passive and LQR cases are 8.7% and 8.3%, where the onset of negative stiffness due to the P-Δ effect and strength deterioration of the MRF beams occurs, as shown in Figure 10.10. However, the 1st story drift for the no damper case is still far from the initiation of a negative stiffness (where at where t=4.3 sec the roof drift is 3.5%). After t=4.3 sec, the building undergoes small oscillations in the story drift without any significant reversal in the story drift. Thus, the maximum story drift for the no damper case is less than that for the cases with MR dampers under this ground motion with S_{aT_1} = 2.0g. This example illustrates that adding dampers to a building does not always result in reduced drift response.

As shown in Figure 10.10, the base shear capacity of the passive control case decreases with increasing story drift due to the P-Δ effect. The passive control case has a gradual increase in story drift, while the LQR controller has a stable response around the story drift of 10% (see Figure 10.9). After t=5.7 sec, the difference in drift between the passive and LQR cases is evident, which is consistent with the difference observed in the MR damper response as shown in Figures 10.11 and 10.12, where the MR damper responses for the 2nd story and the 3rd story MR dampers, respectively, are illustrated. Before t=5.7 sec, the MR damper forces for the LQR controller are almost the same as those for the passive controller. However, after t=5.7 sec, the command current for the 2nd story MR damper from the LQR controller becomes more frequently equal to zero, enough to reduce the MR damper force compared to that of the passive controller. In particular, the zero command current is mostly applied to the damper when the building moves toward its original undeformed shape (i.e., toward zero drift). In this situation, the reduced damper force makes the building less resistive to returning to its original position than the full damper force from the passive controller, which is beneficial to reduce the collapse potential. Therefore the LQR controller is better than passive control for this case.

Figures 10.13 ~ 10.18 show the IDA curves for the structure with various control strategies. These results are for the 44 ground motions. The collapse margin ratio (CMR) is defined by FEMA P695 (ATC 2009) as the ratio of the median value for the collapse spectral acceleration, $\hat{S}_{CT}$, to the spectral acceleration of the MCE, S_{MT}, at the fundamental period of the structural system:

$$\text{CMR} = \frac{\hat{S}_{CT}}{S_{MT}} \tag{10.1}$$

$\hat{S}_{CT}$ for each control case is calculated from the IDA curves and marked in Figures 10.13 ~ 10.18 along with the S_{MT}. Table 10.2 shows the CMR values for each control strategy. Since the purpose of this chapter is to evaluate the collapse capacity of a structure with MR dampers with various control strategies, the further adjustment of the CMR values based on the spectral shape factor (SSF) (ATC 2009) is not considered in this study. When the passive controller is used, the CMR value increases by about 26% compared to the no damper case, demonstrating the benefit of using MR dampers. The overall performance of semi-active controllers is very similar to that of the passive control case, except for the LQR controller. The LQR controller shows the highest CMR value, but the improvement over the passive control case is only 6.6%. However, the improvement in structural collapse performance involving the use of semi-active controllers seems to be more evident than the cases studied in Chapter 9 involving less intense DBE and MCE ground motions.

Figures 10.19 ~ 10.22 illustrate the median IDA curve, where the median IDA curves for the semi-active controllers are compared to those of the passive control and no damper cases. When the structure is without MR dampers, an almost linear relationship between roof drift and spectral acceleration S_{aT_1} occurs up to 5 % roof drift, followed by a softening behavior of the IDA curve. The IDA curve for the structure with passively controlled MR dampers has a smaller drift for the same S_{aT_1} than the case without MR dampers, demonstrating the improved performance of the structure by

employing MR dampers. For the passive control case, a significant softening of the IDA curve occurs at 8% roof drift, where the structure shows signs of incipient collapse beyond 8% drift.

The median IDA curves for semi-active controllers in Figures 10.19 through 10.22 show almost the same behavior as that for the passive control case, except for the LQR controller (see Figure 10.19). The IDA curve for the LQR controller is almost identical to that of passive control case up to about 9.5% roof drift. Then the IDA curve for the LQR controller exhibits larger S_{aT_1} values after 9.5% roof drift than the passive control case, resulting in a higher CMR value than the passive control case. The improvement in structural performance when using the LQR controller, as noted above, is about 6.6% compared to the passive control case.

10.7 Collapse Fragility Curves

A collapse fragility curve is the cumulative distribution function (CDF) which relates the intensity of ground motions to the probability of collapse, and is constructed utilizing the results of the IDAs (ATC 2009). For a prescribed level of spectral acceleration S_{aT_1} the number of cases, N_{SaT1}, where collapse occurs for a spectral acceleration equal to or less than this value of S_{aT_1} among the IDA curves for the various ground motions is counted. The probability of collapse then associated with this value of S_{aT_1} is N_{SaT1}/N_{tot}, where N_{tot} is the total number of IDA curves (i.e., ground motions) in the ensemble. The probability of collapse typically follows a lognormal distribution. A set of collapse data points can then be fitted using the lognormal

distribution to construct the collapse fragility curve. The fitted lognormal distribution is defined by two parameters, i.e., the median collapse spectral acceleration ($\hat{S}_{CT}$), and the standard deviation of the natural logarithm of the collapse spectral accelerations (ζ). The CDF with a lognormal distribution, $F(x)$, is mathematically expressed as

$$F(x) = \int_0^x \frac{1}{s\zeta\sqrt{2\pi}} \exp\left[-\frac{(\ln s - \lambda)^2}{2\zeta^2}\right] ds = \Phi\left(\frac{\ln x - \lambda}{\zeta}\right) \qquad (10.2)$$

where, Φ is the cumulative distribution function of the standard normal distribution and $\lambda = \ln \hat{S}_{CT}$. Figure 10.23 compares the collapse fragility curves for the passive control and the no damper cases. The fragility curve for the passive control case is located to the right of the fragility curve for the no damper case, which means the collapse potential of the structure with passive control is lower than that for the structure with no dampers. This result is also illustrated in Table 10.2 by a comparison of the CMR values. The collapse fragility curves for the semi-active control cases are similar to the passive control case, except for the LQR controller (see Figures 10.23 ~ 10.27, where the collapse fragility curves for various the semi-active control cases are compared to the passive control case). The collapse fragility curve for the building with the LQR controller is slightly to the right of that for the passive control case (Figure 10.24), indicating a lower probability of collapse compared to the passive control case, consistent with having a lower CMR value.

10.8 Collapse Mode

The collapse mode of the building structure studied in this chapter is characterized by the formation of plastic hinges in the beams and columns leading to a collapse mechanism. A soft story mechanism, where both ends of all columns at a particular story level develop plastic hinges, did not occur in any of the cases. The design methodology based on the strong-column-weak-beam appears to have helped avoid a soft story collapse mechanism.

Figure 10.28 shows the deformed shape of the building with passively controlled MR dampers at the time of maximum drift under the 1994 Northridge earthquake (Canyon country, 000 component), where the ground motion was scaled to a spectral acceleration of S_{aT_1}=2.25g. Collapse for this ground motion occurs when S_{aT_1}=2.27g. Both ends of each beam in the 1st through 3rd floor in the MRF and the ground level of the 1st story columns for both the MRF and CBF formed plastic hinges during the earthquake. Figure 10.29 shows the floor displacement of the building structure. The displacement of each floor gradually increased due to the P-Δ effect and the strength deterioration at the end of beams. After the end of the earthquake event, the roof displacement of the building is about 1.04m (15.1% roof drift). Figures 10.30 through 10.32 show the story shear and story drift relationship for the 1st, 2nd, and 3rd stories, respectively. The shear capacity of each story is observed to decrease with increasing story drift due to the P-Δ effect.

Figures 10.33 through 10.35 show beam end moment versus beam end rotation data from this simulation. As noted previously, the modified Ibarra-Krawinkler model is used to describe the flexural strength deterioration at the ends of beams. As is evident in

these figures, the flexural capacity of the beams deteriorates during the response, with a negative stiffness developing after the capping strength is reached. The beams all accumulate inelastic rotation, indicative of the onset of collapse of the structure.

10.9 Summary

In this chapter, the collapse potential of a building with MR dampers controlled by various control strategies was investigated. The 3-story building designed in Chapter 6 was used for the study. A brief review of the flexural strength and stiffness deterioration of a beam was made. Strength and stiffness deterioration along with the P-Δ effect is one of the major factors causing the dynamic instability of structures. Incremental dynamic analyses based on nonlinear time history earthquake simulation with OpenSees were conducted to obtain the statistical response and collapse margin ratios (CMRs) for the structure. Five different control strategies for the MR dampers were used, and the collapse potential for each case was compared. The passive control of MR dampers with a 2.5A constant current input improved the CMR value by about 26% compared to the structure without MR dampers. When the collapse potential of the structure with passive control is compared with that when semi-active controllers are used, no significant differences were observed except for the case when the LQR controller was used. The median IDA curves and the collapse fragility curves for the sliding mode control, the decentralized bang-bang control, and the phase angle control resulted in almost the same collapse potential as the passive control case, while the LQR controller provided a reduction in the collapse potential. The LQR controller

varied the MR damper forces adaptively during the response to the seismic excitation of the structure, resulting in better performance than the passive control case; the CMR is 6.6% greater for the structure with an LQR controller.

The LQR and SMC controllers require control gains to be specified. The effect of the control gains on the collapse potential needs to be investigated further. In addition, other semi-active controllers and various structural geometries (e.g. the height of the building) should be included in a study to derive a set of general conclusions on the collapse potential of structures with semi-active controllers under seismic loading. The median roof drift at collapse was approximately 14%. The damper stroke limit would result in the dampers "bottoming out" at about 12.2% story drift, before the median collapse roof drift is reached (assuming that the dampers have an unlimited stroke). The effect of a damper bottoming out on the collapse potential of structures with MR dampers needs to be investigated in future studies.

Table 10.1 Parameters for deterioration element for MRF beams

Beam size	Deterioration element parameters						
	K_e (kN-m/m)	M_y (kN-m)	α_s	θ_p (rad)	θ_{pc} (rad)	Λ	κ
W10X17	103531.2	116.28	0.002	0.062	0.207	1.244	0.01
W14X38	462519.7	382.54	0.002	0.043	0.171	1.084	0.01
W18X46	855748.0	563.94	0.002	0.033	0.186	1.104	0.01

Table 10.2 Collapse margin ratio (CMR) for 3-story building with various control strategies

	No damper	Passive	LQR	SMC	DBB	PAC
CMR	2.39	3.02	3.23	3.03	3.02	3.05

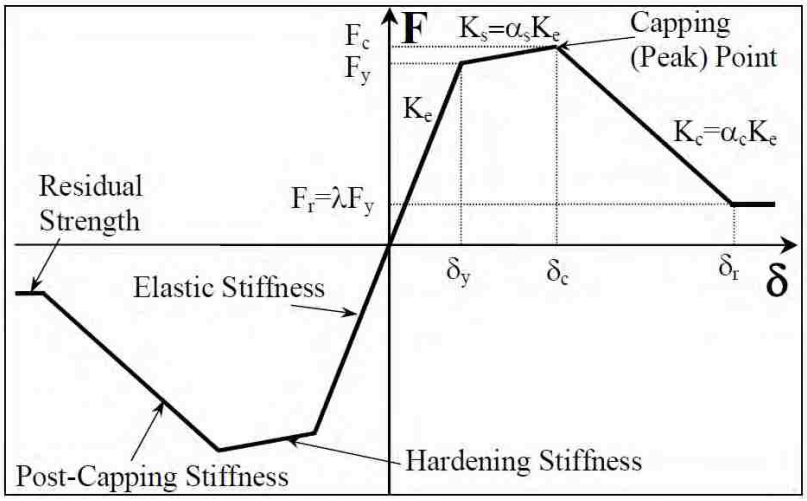

Figure 10.1 Backbone curve of Ibarra-Krawinkler model
(after Ibarra and Krawinkler 2005)

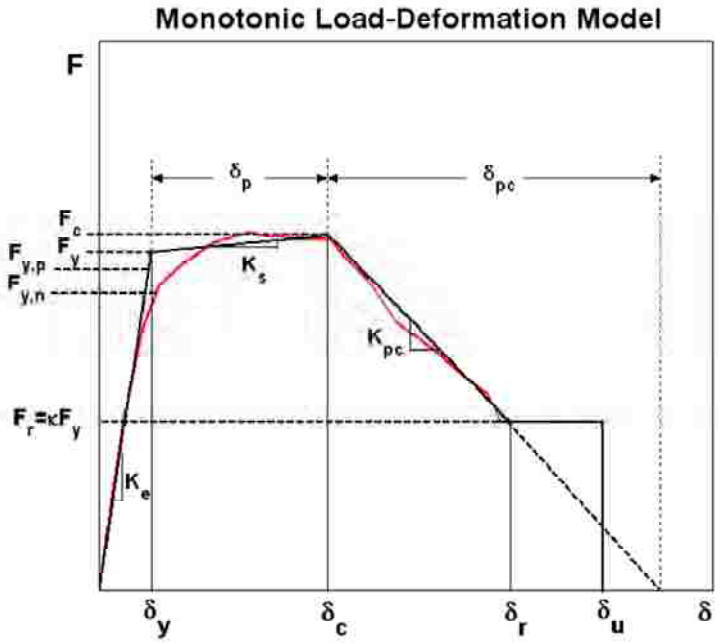

Figure 10.2 Modified backbone curve of Ibarra-Krawinkler model (after Lignos 2008)

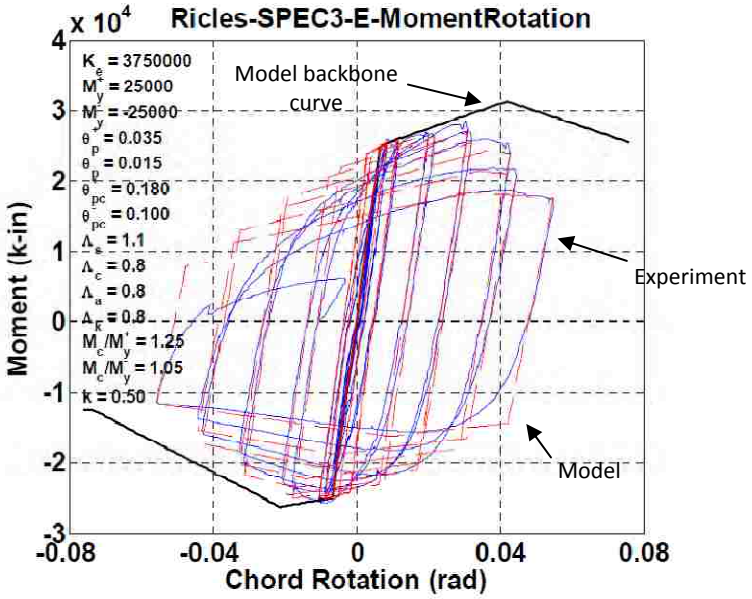

Figure 10.3 Comparison of the modified Ibarra-Krawinkler model with a test result (after Lignos 2008)

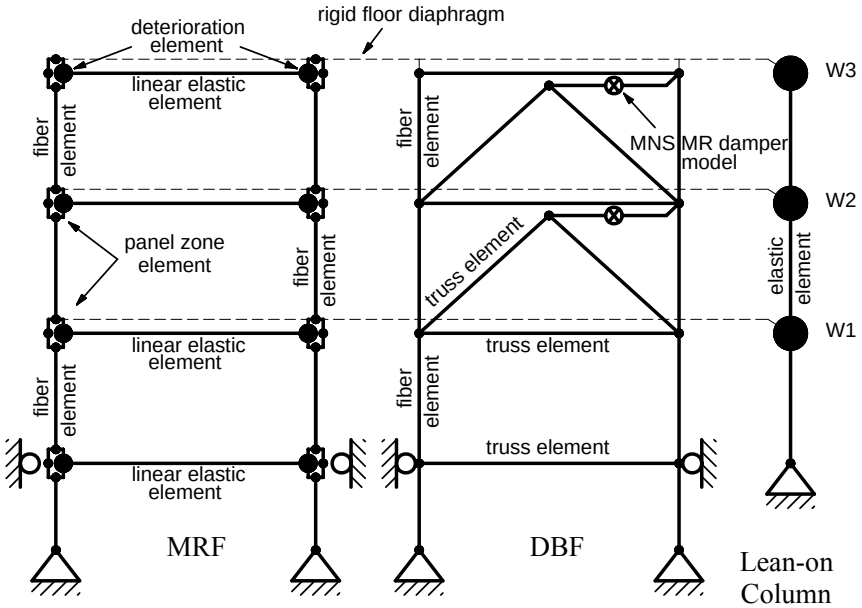

Figure 10.4 OpenSees model of the 3-story structure for the incremental dynamic analysis

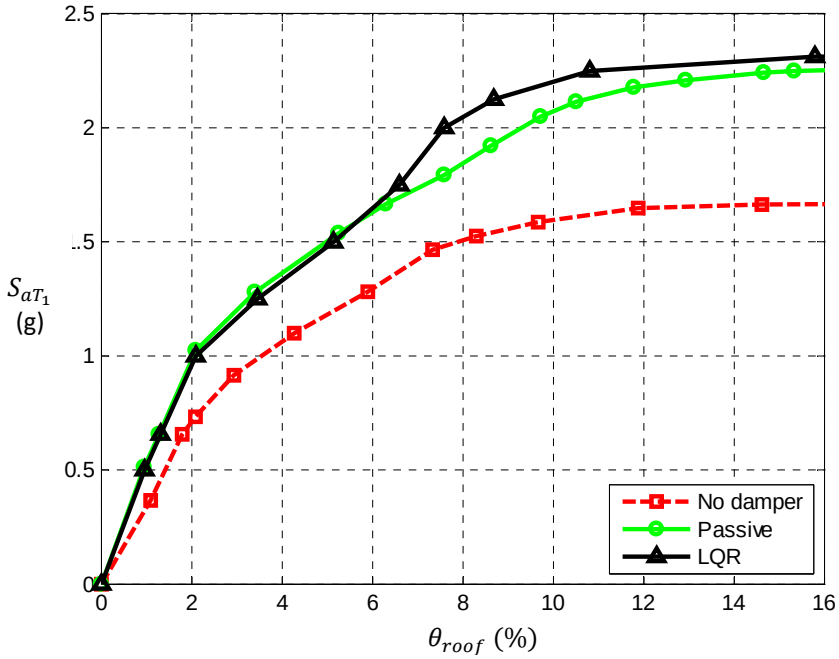

Figure 10.5 IDA curve for the 3-story building structure subjected to the 1999 Kocaeli earthquake (Duzce, 180 component) with different control strategies (No damper, Passive, and LQR)

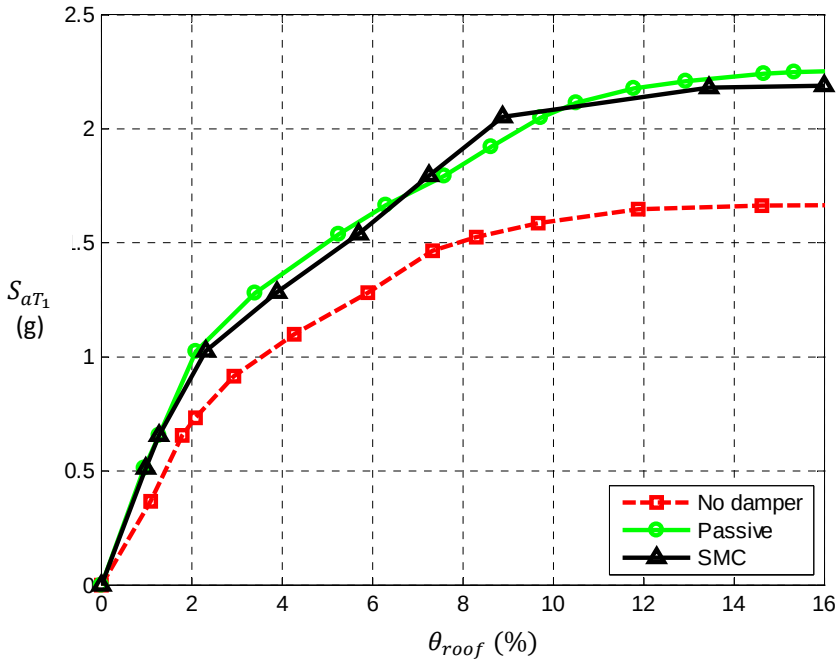

Figure 10.6 IDA curve for the 3-story building structure subjected to the 1999 Kocaeli earthquake (Duzce, 180 component) with different control strategies (No damper, Passive, and SMC)

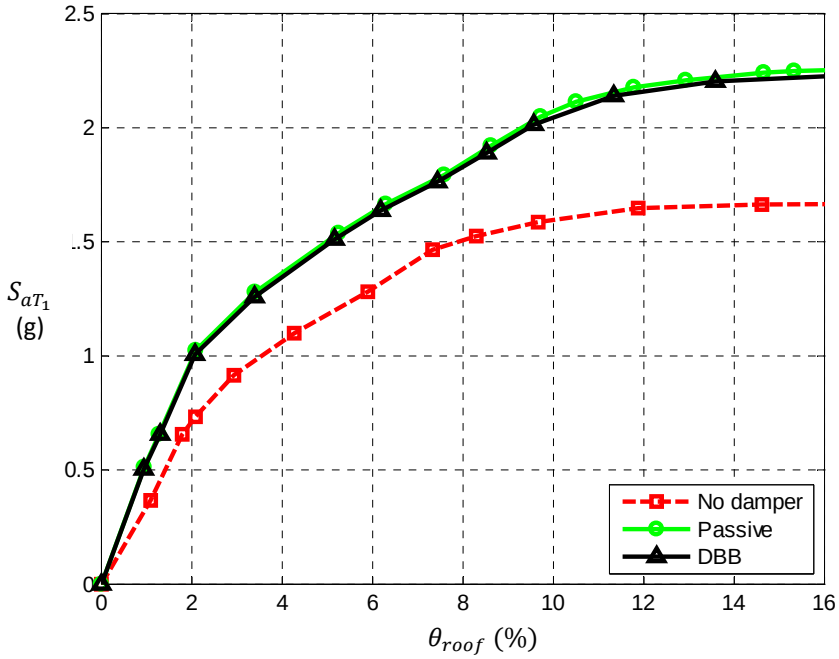

Figure 10.7 IDA curve for the 3-story building structure subjected to the 1999 Kocaeli earthquake (Duzce, 180 component) with different control strategies (No damper, Passive, and DBB)

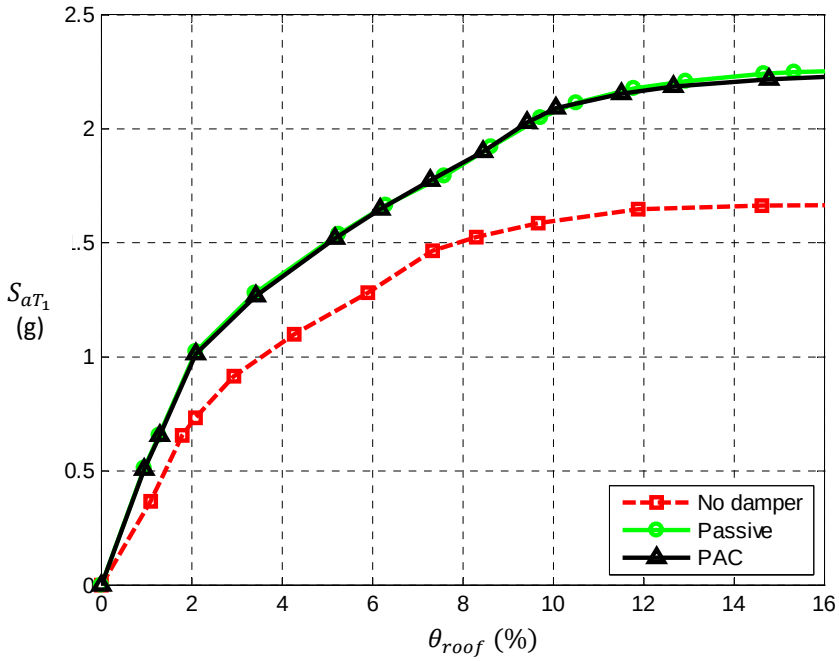

Figure 10.8 IDA curve for the 3-story building structure subjected to the 1999 Kocaeli earthquake (Duzce, 180 component) with different control strategies (No damper, Passive, and PAC)

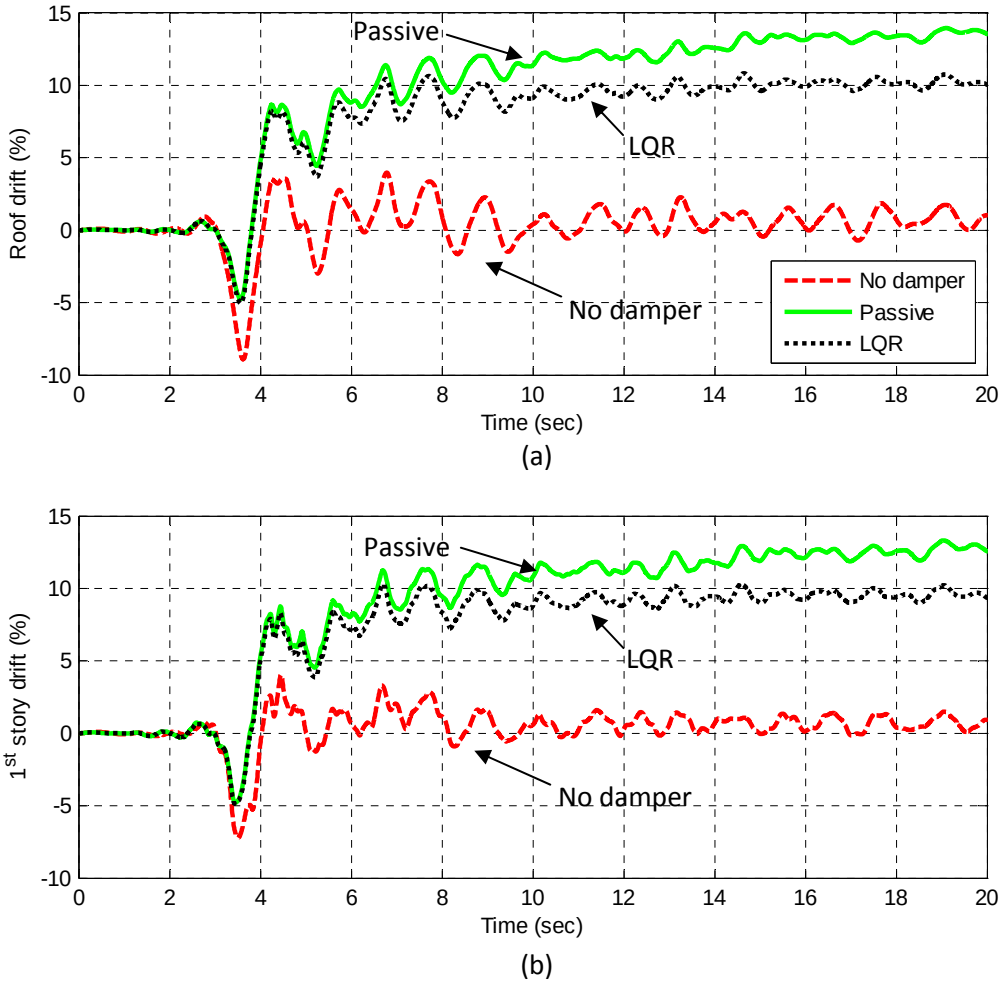

Figure 10.9 Time history of the drift of the building subjected to the 1989 Loma Prieta earthquake (Gilroy array #3, 090 component) with different control strategies ($S_{aT_1} = 2.0g$): (a) roof drift; (b) 1st story drift

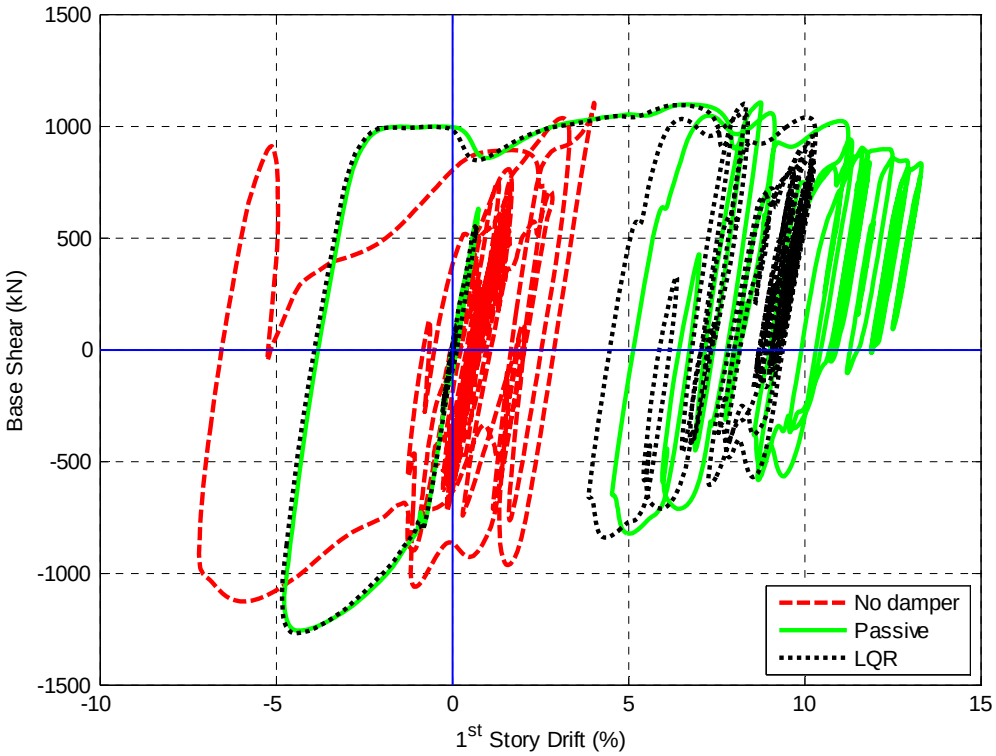

Figure 10.10 Base shear and 1st story drift relationship of the building subjected to the 1989 Loma Prieta earthquake (Gilroy array #3, 090 component) with different control strategies ($S_{aT_1} = 2.0$g)

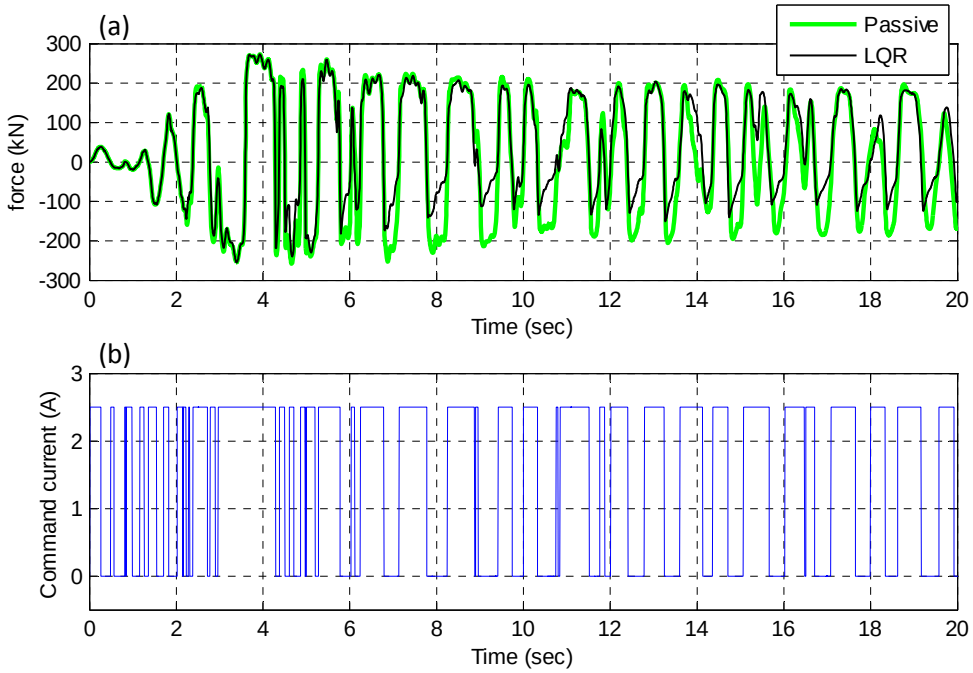

Figure 10.11 MR damper behavior in the 2nd story subjected to the 1989 Loma Prieta earthquake (Gilroy array #3, 090 component), $S_{aT_1} = 2.0$g: (a) comparison of damper force between passive and LQR controllers; (b) command current of LQR controller

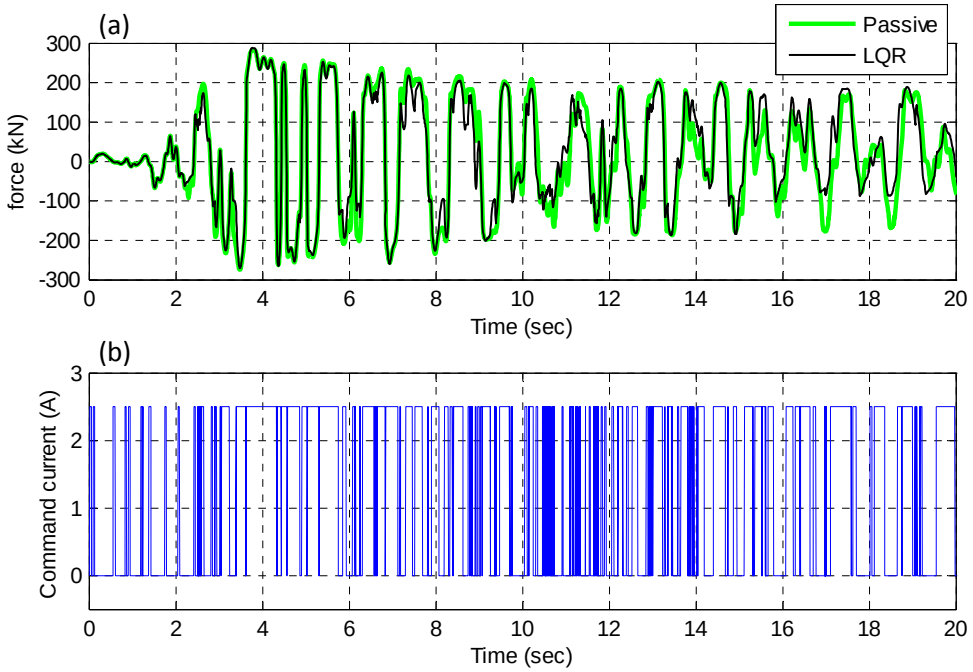

Figure 10.12 MR damper behavior in the 3rd story subjected to the 1989 Loma Prieta earthquake (Gilroy array #3, 090 component), $S_{aT_1} = 2.0$g: (a) comparison of damper force between passive and LQR controllers; (b) command current of LQR controller

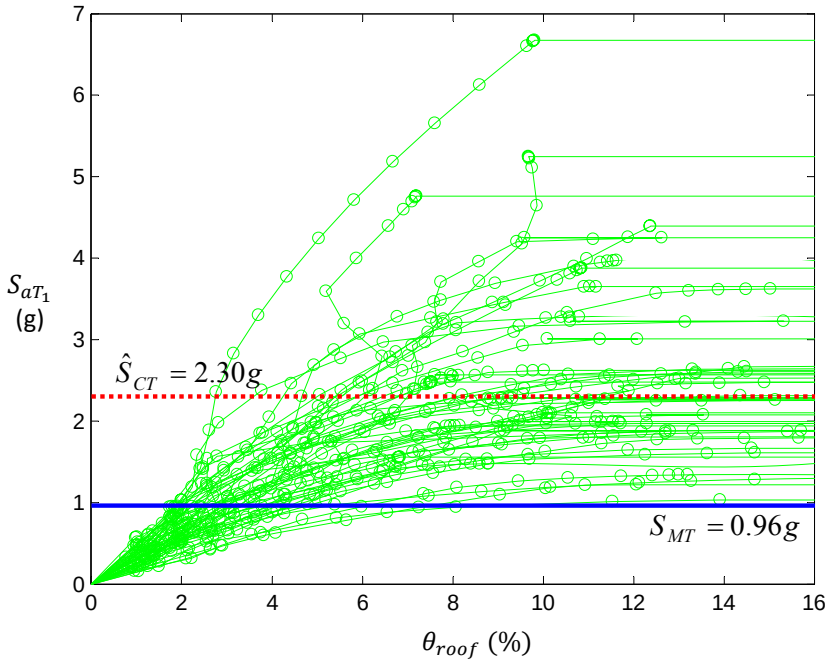

Figure 10.13 IDA curves: no damper case

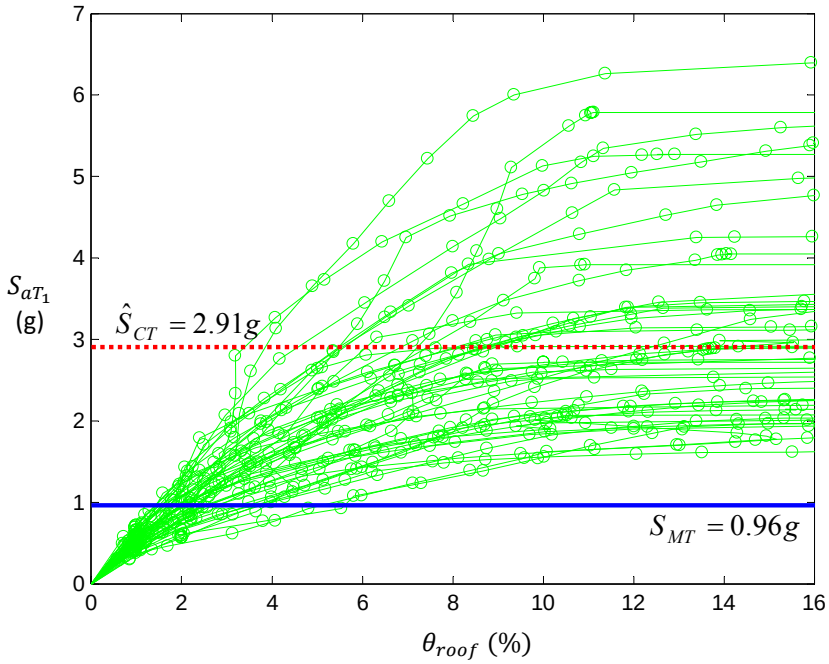

Figure 10.14 IDA curves: passive control

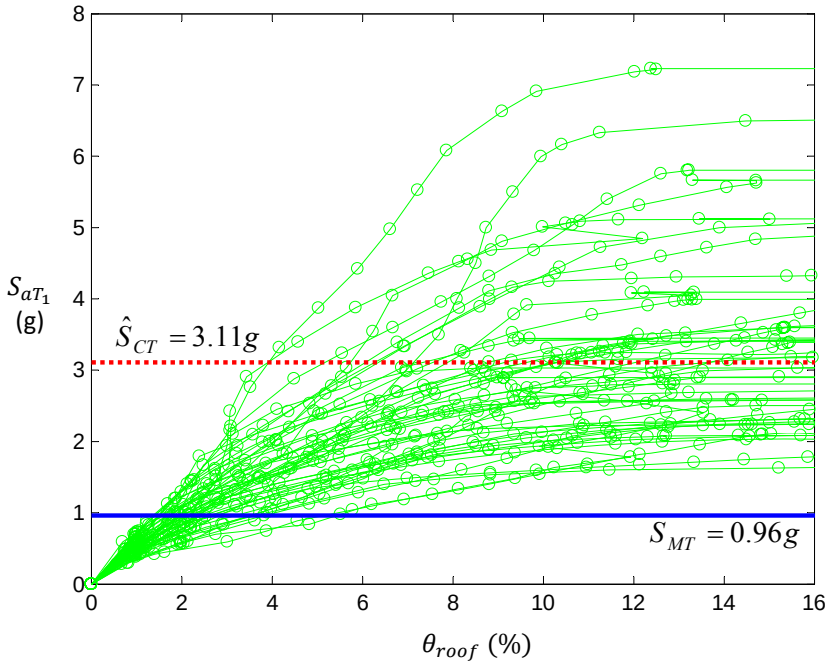

Figure 10.15 IDA curves: linear quadratic regulator (LQR) control

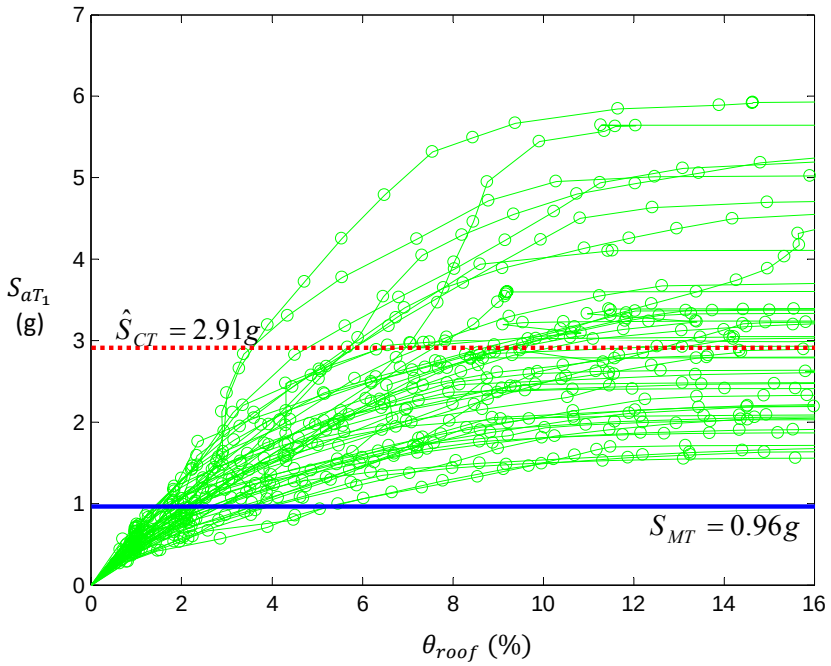

Figure 10.16 IDA curves: sliding mode control (SMC)

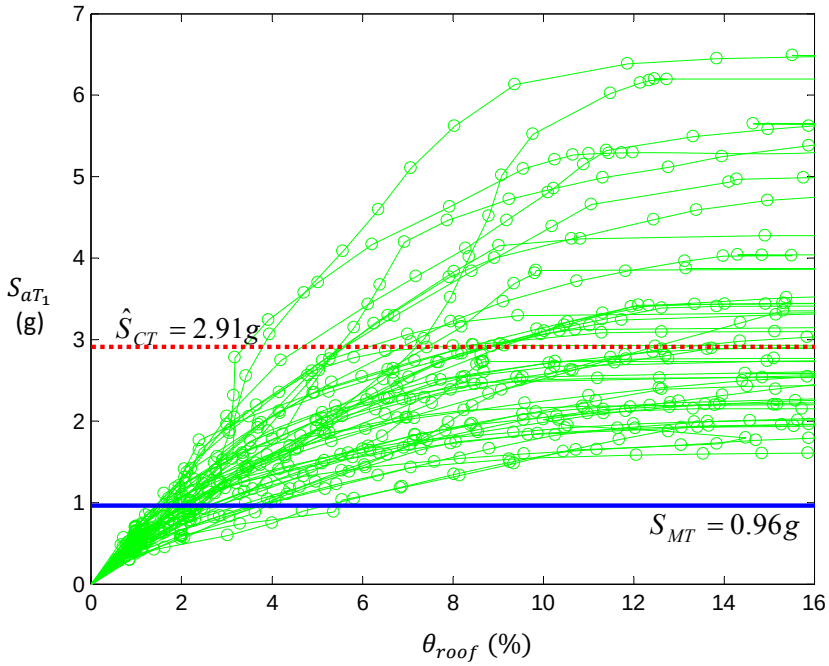

Figure 10.17 IDA curves: decentralized bang-bang (DBB) control

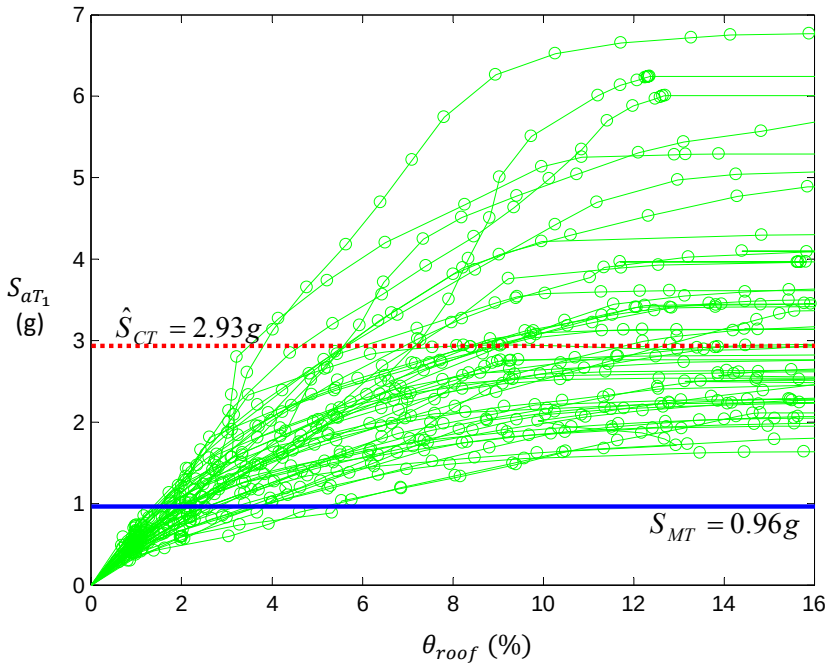

Figure 10.18 IDA curves: phase angle control (PAC)

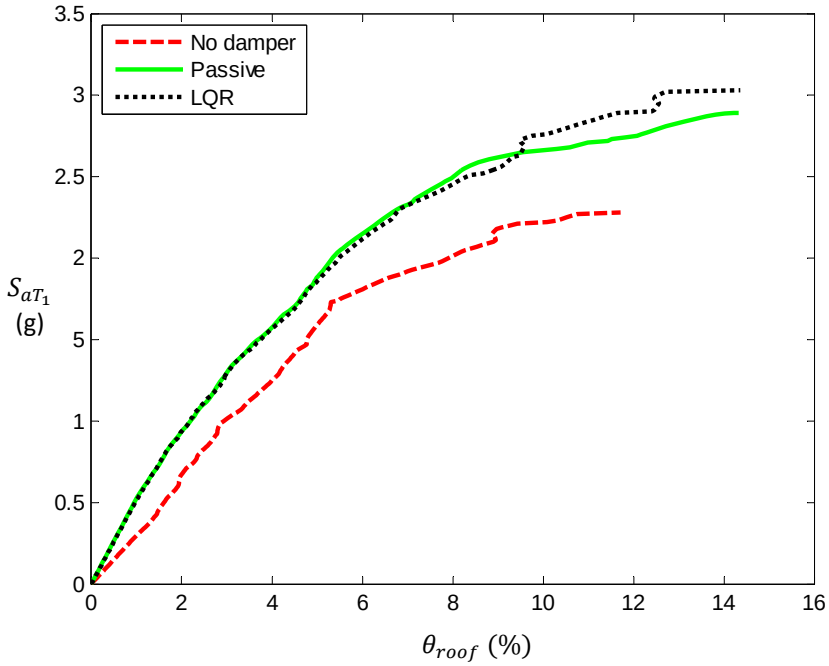

Figure 10.19 Median (50% fractile) IDA curve where the linear quadratic regulator (LQR) controller is compared with passive and no damper cases

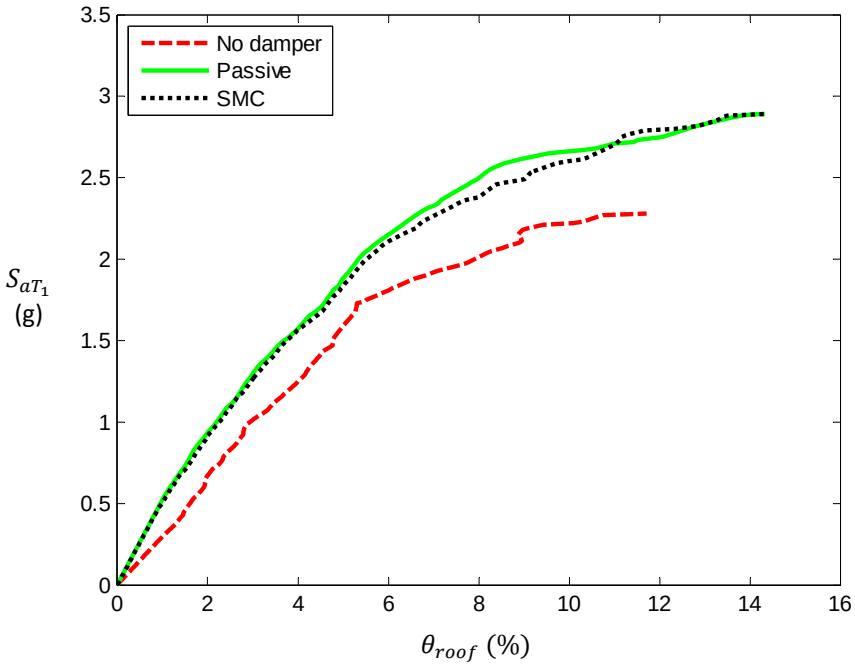

Figure 10.20 Median (50% fractile) IDA curve where the sliding mode controller (SMC) is compared with passive and no damper cases

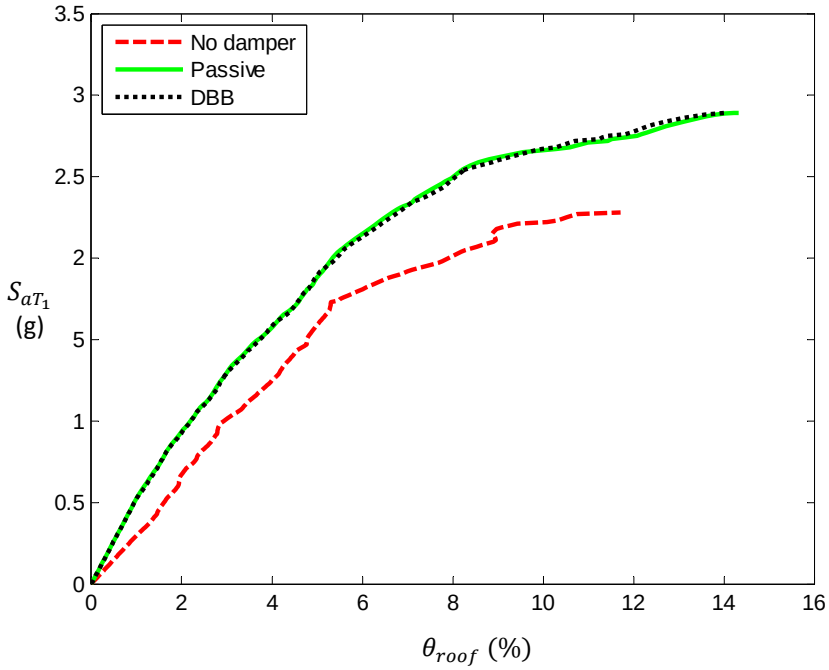

Figure 10.21 Median (50% fractile) IDA curve where the decentralized bang-bang (DBB) controller is compared with passive and no damper cases

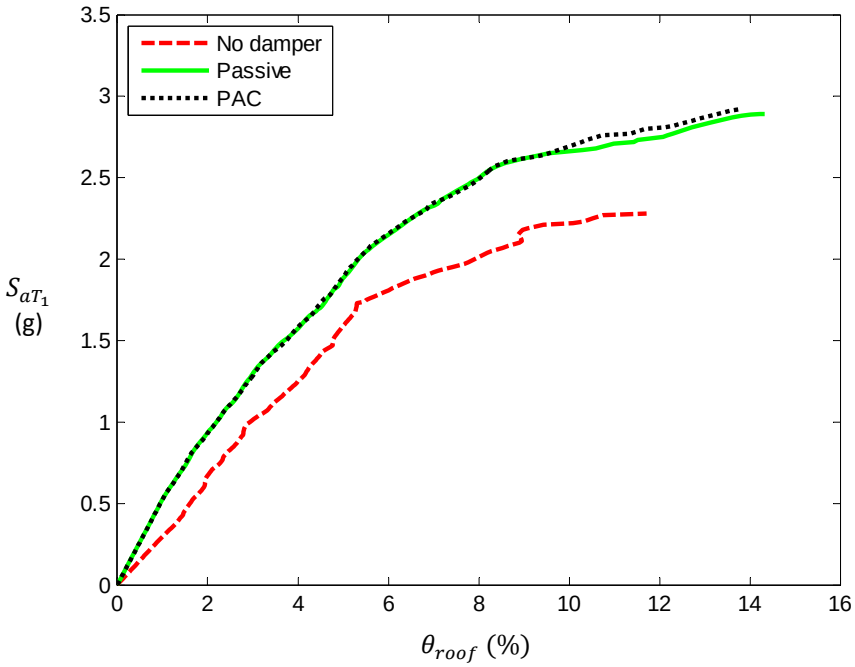

Figure 10.22 Median (50% fractile) IDA curve where the phase angle controller (PAC) is compared with passive and no damper cases

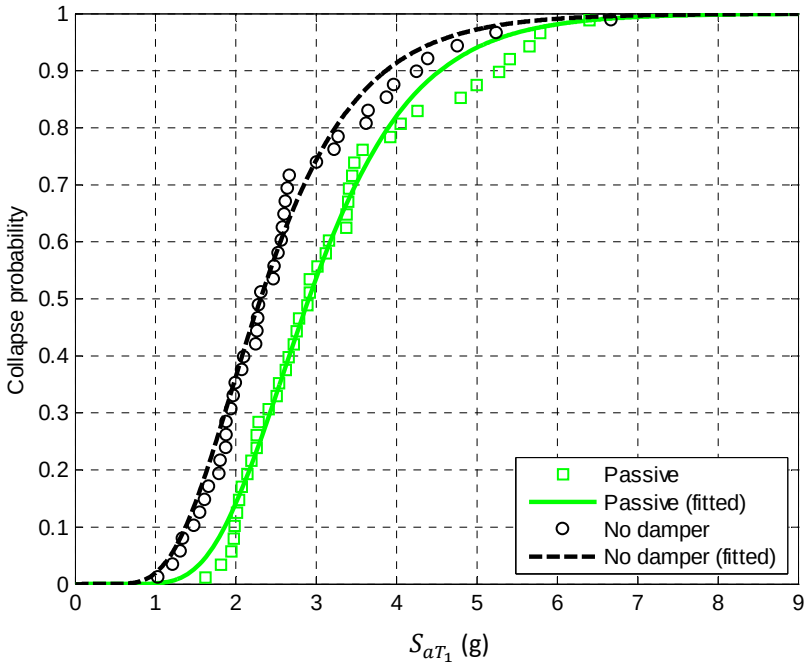

Figure 10.23 Collapse fragility curves where the no damper case is compared with the passive control case

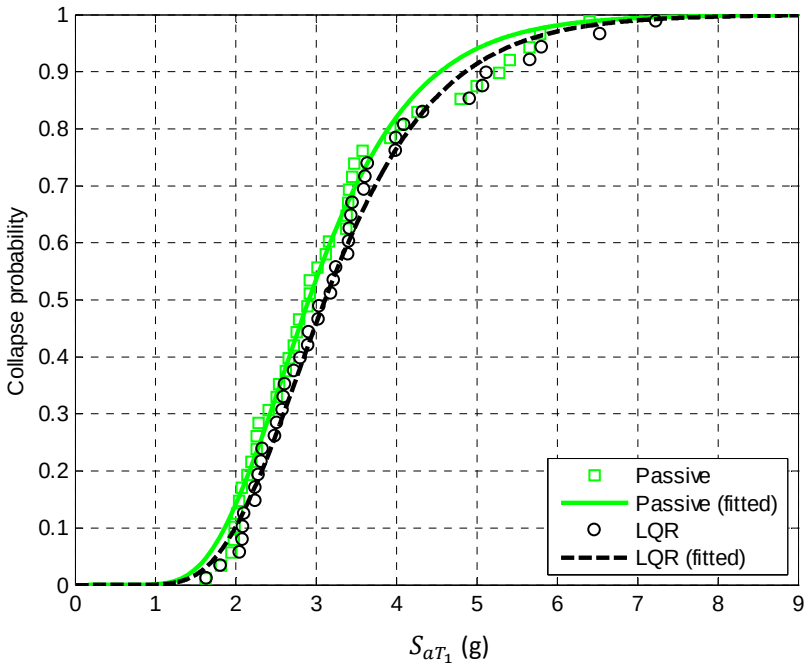

Figure 10.24 Collapse fragility curves where the linear quadratic regulator (LQR) controller is compared with the passive control case

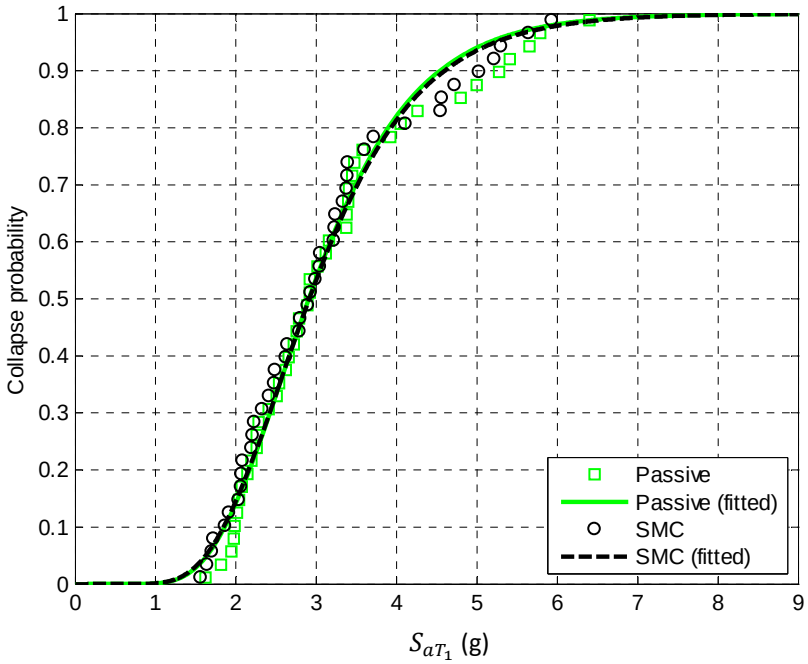

Figure 10.25 Collapse fragility curves where the sliding mode controller (SMC) is compared with the passive control case

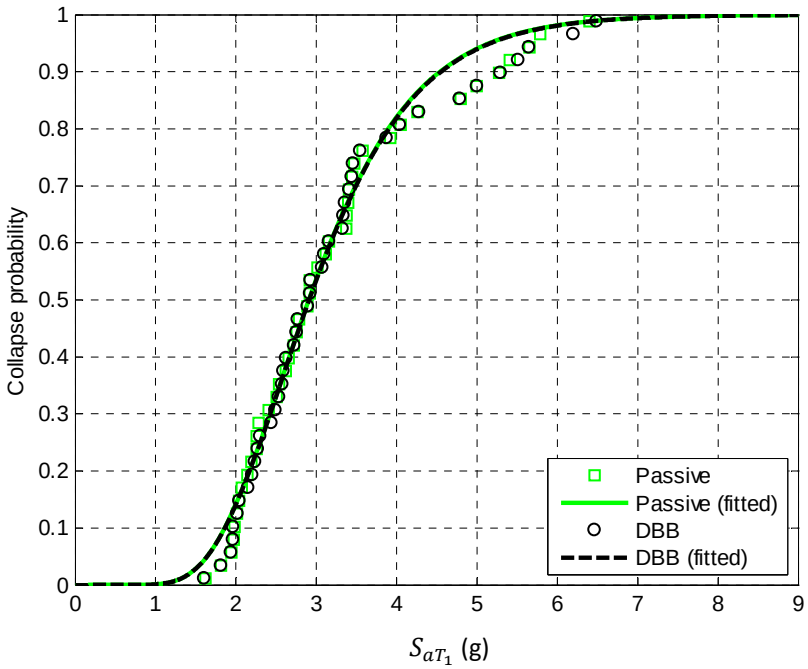

Figure 10.26 Collapse fragility curves where the decentralized bang-bang (DBB) controller is compared with the passive control case

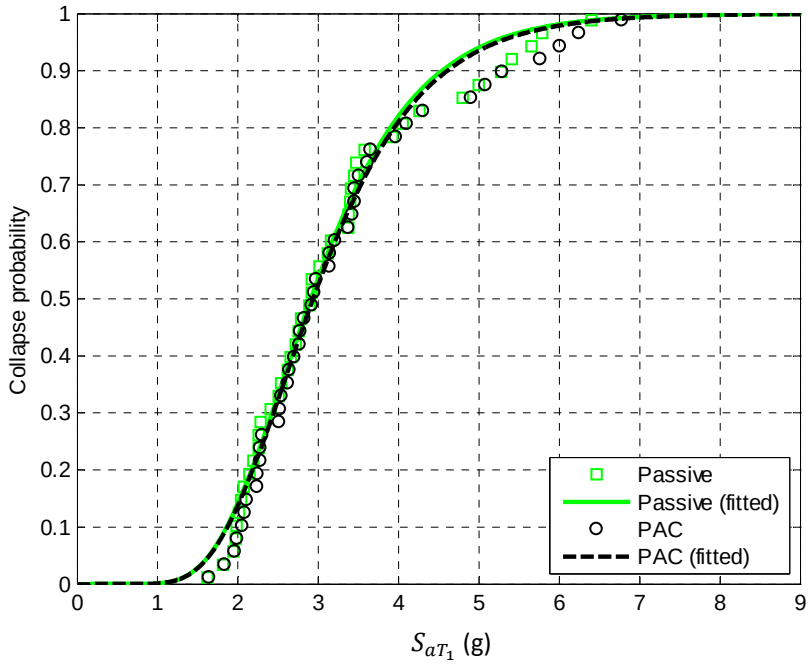

Figure 10.27 Collapse fragility curves where the phase angle control (PAC) is compared with the passive control case

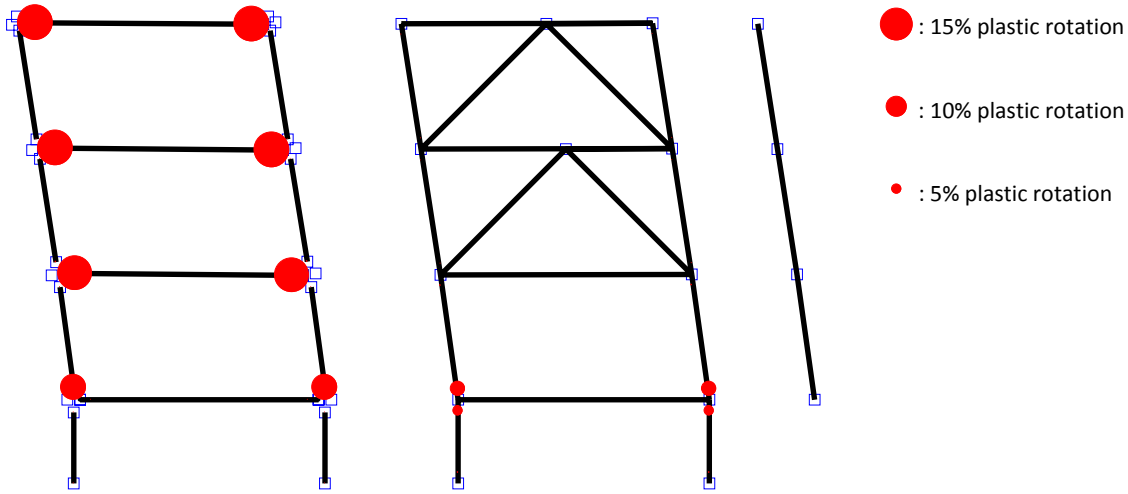

Figure 10.28 Deformed shape of the building structure at incipient collapse, where the solid circles represent the location of plastic hinges and their size denotes the magnitude of the plastic rotation; 1994 Northridge ground motion (Canyon country, 000 component) scaled to a spectral acceleration of S_{aT_1}=2.25g

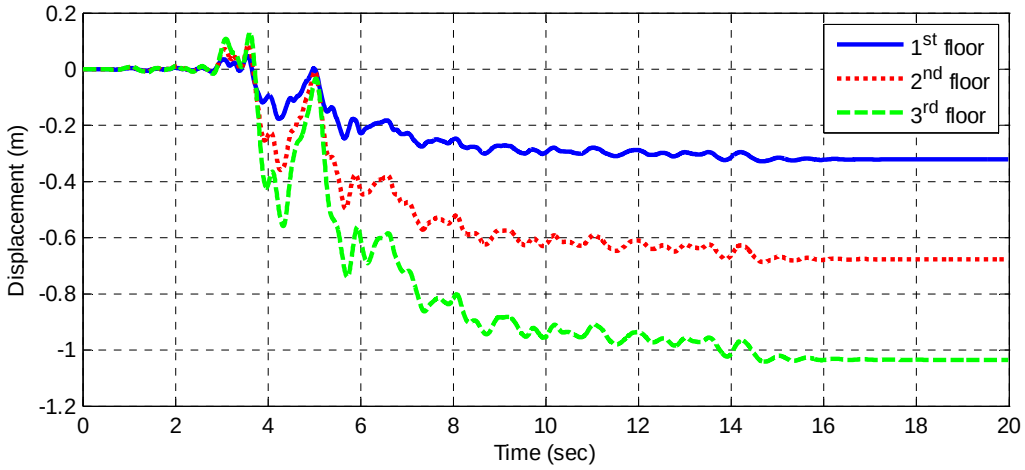

Figure 10.29 Floor displacement of the building structure; 1994 Northridge ground motion (Canyon country, 000 component) scaled to a spectral acceleration of S_{aT_1}=2.25g

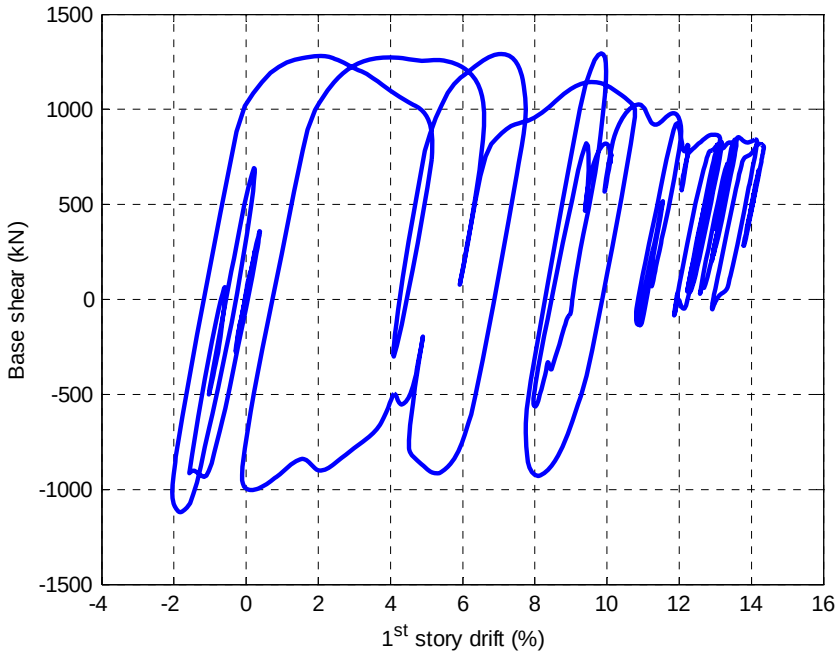

Figure 10.30 Base shear and 1st story drift relationship of the building structure; 1994 Northridge ground motion (Canyon country, 000 component) scaled to a spectral acceleration of S_{aT_1}=2.25g

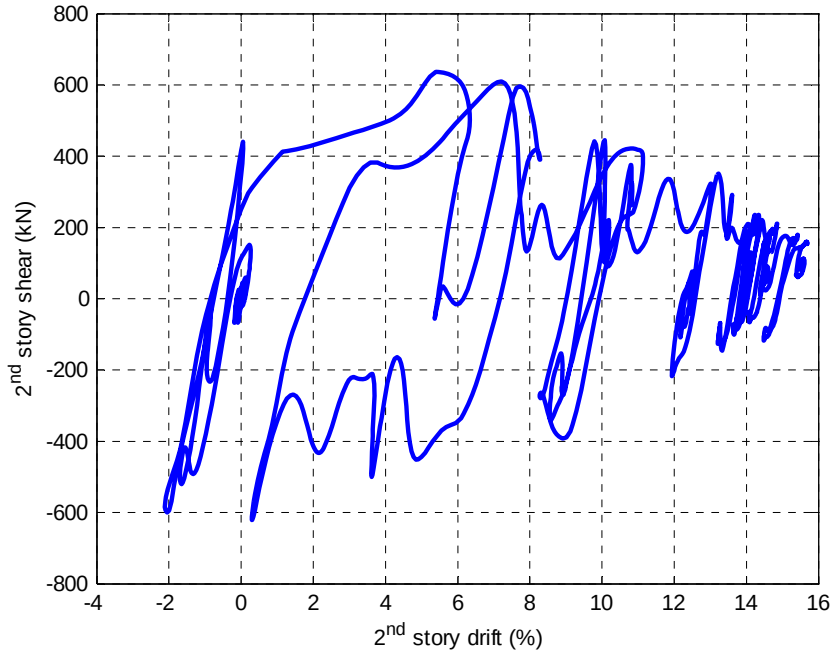

Figure 10.31 2nd story shear and 2nd story drift relationship of the building structure; 1994 Northridge ground motion (Canyon country, 000 component) scaled to a spectral acceleration of S_{aT_1}=2.25g

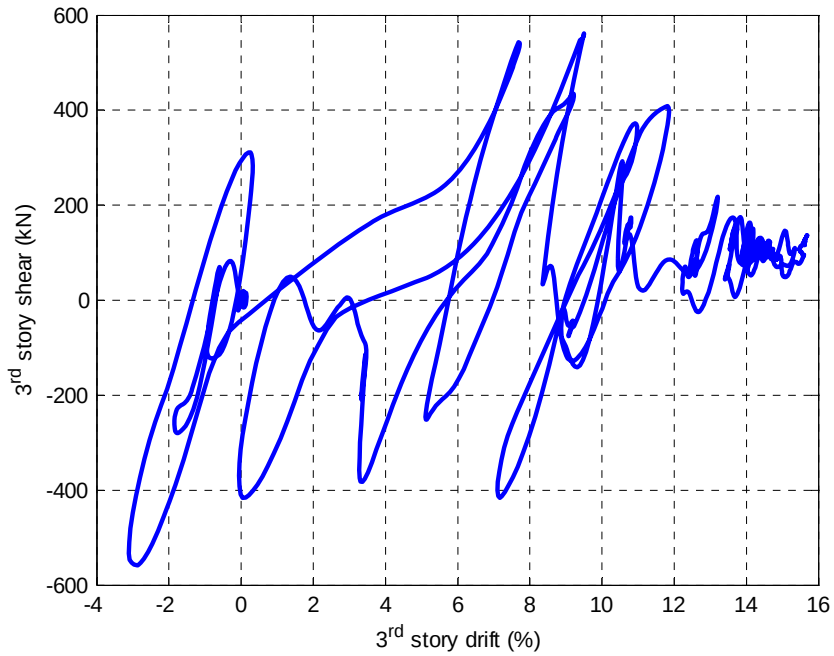

Figure 10.32 3rd story shear and 3rd story drift relationship of the building structure; 1994 Northridge ground motion (Canyon country, 000 component) scaled to a spectral acceleration of S_{aT_1}=2.25g

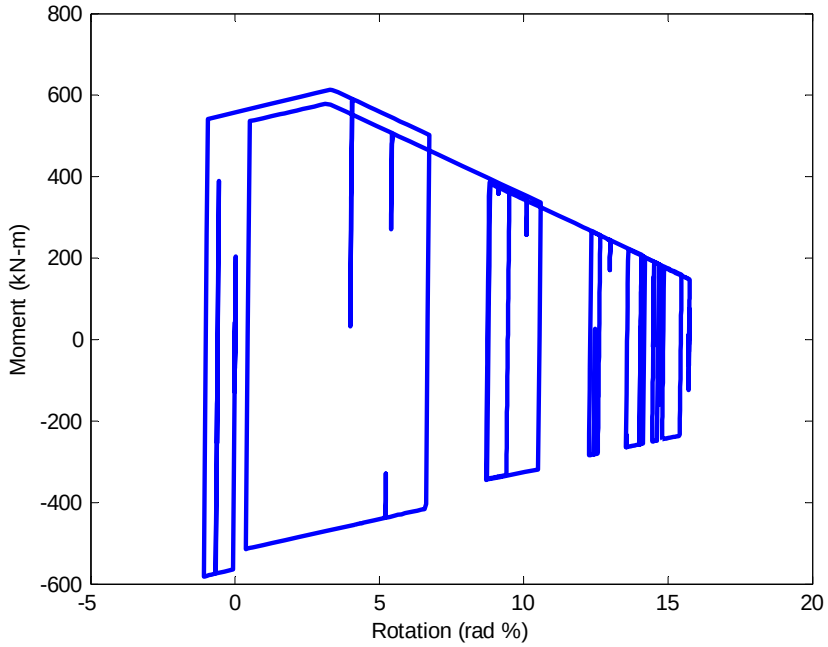

Figure 10.33 Moment versus beam end rotation relationship at the end of the 1st floor beam; 1994 Northridge ground motion (Canyon country, 000 component) scaled to a spectral acceleration of S_{aT_1}=2.25g

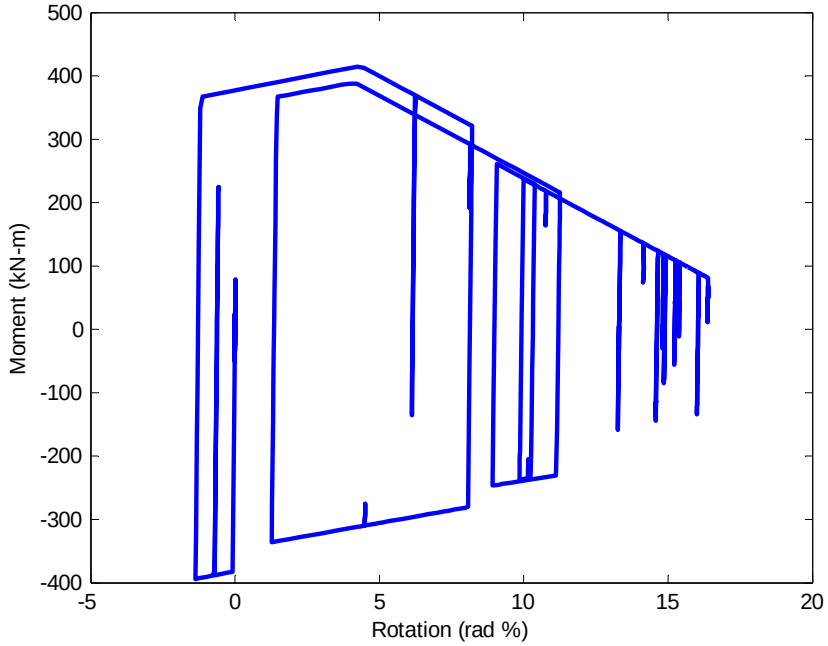

Figure 10.34 Moment versus beam end rotation relationship at the end of the 2nd floor beam; 1994 Northridge ground motion (Canyon country, 000 component) scaled to a spectral acceleration of S_{aT_1}=2.25g

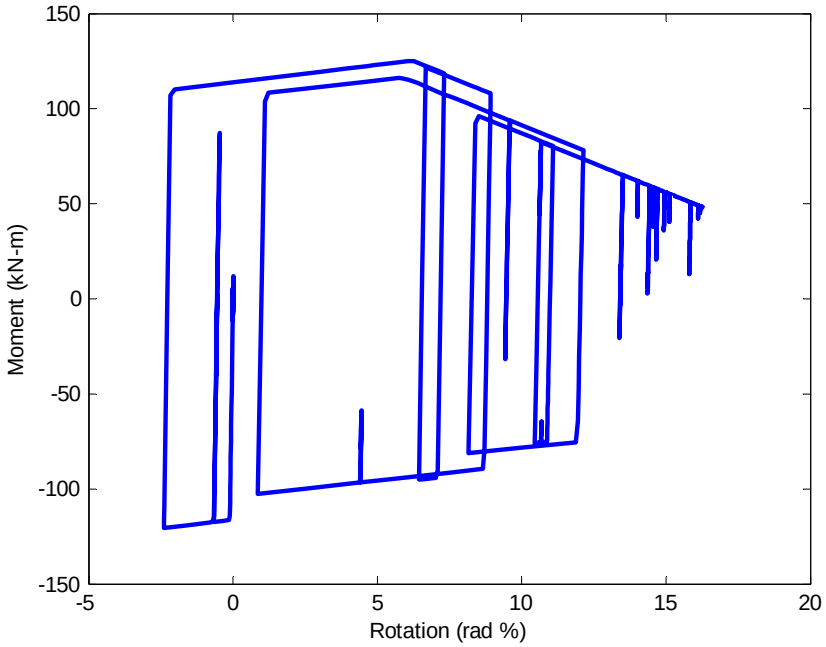

Figure 10.35 Moment versus beam end rotation relationship at the end of the 3rd floor beam; 1994 Northridge ground motion (Canyon country, 000 component) scaled to a spectral acceleration of S_{aT_1}=2.25g

Chapter 11

Real-Time Hybrid Simulation of Structures with MR Dampers

11.1 General

In this chapter, a set of real-time hybrid simulations are presented. The objectives of these simulations are: i) to experimentally assess the simplified design procedure (SDP) under realistic seismic demand from the design earthquake (i.e., DBE); ii) to experimentally evaluate structural control strategies for MR dampers under realistic seismic demands from the design earthquake; and iii) to experimentally investigate the collapse potential of structures under realistic seismic demands. The real-time hybrid simulations were performed on the structure designed using the SDP as presented in Chapter 6, and studied using numerical simulations as presented in Chapters 7 and 9. To experimentally assess the SDP and structural control strategies, five different ground motions are selected from the ensemble of ground motions listed in Appendix 3, and scaled to the DBE level. The various control strategies, including passive control and the semi-active controllers studied in Chapter 9, are included in the simulations. The assessment involved examining the statistics of the experimental response of the structure with the various controllers and comparing them with results from the SDP under the DBE ground motions. The behavior of the structure under an extreme ground motion is studied by conducting a series of real-time hybrid simulations for a selected ground motion, gradually increasing the intensity of the ground motion in

each subsequent simulation. Results from the real-time hybrid simulations are presented and discussed, and comparisons are made with numerical simulation results.

11.2 Real-Time Hybrid Simulation Concepts

Real-time hybrid simulation is an efficient test method for investigating the dynamic behavior of complex structures. It combines physical testing and numerical simulation to enable the entire structural system to be included in the simulation. Hybrid simulation divides a structural system into analytical and experimental substructures, as illustrated in Figure 11.1. During a real-time hybrid simulation, the coupling between the experimental and analytical substructures is achieved by maintaining compatibility and equilibrium at the interface between these substructures. The discretized equations of motion of the structure at time step *i* are expressed as

$$\mathbf{m}\ddot{\mathbf{x}}_i + \mathbf{c}\dot{\mathbf{x}}_i + (\mathbf{r}_i^{\mathrm{a}} + \mathbf{r}_i^{\mathrm{e}}) = \mathbf{F}_i \tag{11.1}$$

where **m** and **c** are the mass and viscous damping matrices of the structure, respectively. $\mathbf{r}^{\mathrm{a}}$ and $\mathbf{r}^{\mathrm{e}}$ are the restoring forces from the analytical and experimental substructures, respectively. **F** is the external load applied to the structure, and $\dot{\mathbf{x}}$ and $\ddot{\mathbf{x}}$ are the velocity and acceleration vectors associated with the degrees of freedom of the structure, respectively. The inertial and damping forces (the first two terms in the equations of motion, Equation (9.1) are calculated analytically. The displacement response of the structural system is calculated using an algorithm that integrates the equations of motion

in conjunction with restoring forces from the substructures (i.e., $\mathbf{r}^a$ and $\mathbf{r}^e$) that are developed under the imposed displacement response.

The analytical and experimental substructures, the integration algorithm, and the servo-hydraulic actuators and associated controllers combine together to form the frame work for a real-time hybrid simulation. The displacement response from the integration algorithm that is intended to be imposed on the experimental substructure at each time step is referred to as the *command displacement*. Real-time hybrid simulation poses several challenges, including the requirement that the integration algorithm should be efficient, stable, and accurate; the servo-hydraulic system must enable actuators to accurately and reliably impose command displacements onto the experimental substructure in real-time; the state determination process for the analytical substructures to compute the $\mathbf{r}^a$ restoring forces must be efficient, stable and accurate; and the communication between the integration algorithm, servo-hydraulic system controller, and analytical substructure needs to be synchronized and have minimal delay (Chen et al. 2009a). To successfully impose the command displacements on the experimental substructure in real time, it is necessary to have accurate actuator control to achieve the correct displacement amplitude and to avoid actuator delay.

Real-time hybrid simulations have been successfully conducted by Chen et al. (2009b) to investigate the dynamic behavior of structures with rate-dependent devices. When real-time hybrid simulation is utilized to evaluate the performance of a structure with MR dampers, the dampers may be modeled as experimental substructures while the remaining part of the structural system is modeled analytically (i.e., as the analytical

substructure). This is the hybrid simulation arrangement used for the simulations presented in this chapter. Compared to shaking table tests, this arrangement of the experimental and analytical substructures in a real-time hybrid simulation is economical, while the reliability of the simulation results is preserved when the analytical model of ths structure used for the analytical substructure is accurate. The added benefit of this experimental technique is that it enables a large number of ground motions to be applied to the structure, resulting in various levels of structural damage, without the need to repair the test specimens if the damage is confied to the analytical substructure.

11.3 Lehigh NEES RTMD Facility

The real-time hybrid simulations of this study were conducted at the Real-Time Multi-Directional (RTMD) earthquake simulation facility located in the ATLSS Engineering Research Center, at Lehigh University. The RTMD is part of the George E. Brown, Jr. Network for Earthquake Engineering Simulation (NEES). The Lehigh NEES RTMD facility specializes in real-time hybrid simulations in addition to conventional hybrid simulations of large-scale structural systems. The ATLSS laboratory includes a strong floor that measures 31.1m x 15.2 m in plan, and a multi-directional reaction wall up to 15.2 m in height.

11.3.1 RTMD Hydraulic System

The RTMD facility hydraulic system has five large capacity dynamic actuators, three with a 1700kN maximum force capacity and the remaining two with a 2300kN

maximum force capacity. Figure 11.2 shows the hydraulic power curve for the actuators. Each actuator is ported for three servo valves, where each servo-valve has a maximum flow capacity rate of 2,082lpm (550gpm) at a hydraulic supply pressure of 20.7MPa (3000psi). The hydraulic supply system consists of 5 pumps, each with a 450 lpm (118.9 gpm) capacity, and 16 piston accumulators, 190 liters (50.2 gallons) each, connected to 9 Nitrogen gas bottles, 1,325 liters (850.2 gallons) each. This configuration enables a typical earthquake to be simulated in real-time for a duration of 30 seconds with the supply pressure maintained between 20.7 to 24.1MPa, where the experimental substructure consists of a 4-story half-scale frame structure. For the real-time hybrid simulations performed in this study, the experimental substructure consists of two MR dampers and two 1,700 kN actuators (to be discussed in Section 11.5) with three servo valves mounted on each actuator.

11.3.2 RTMD IT System

Figure 11.3 shows the architecture of the RTMD IT system. It is an integrated system of various modules, designed to enable real-time hybrid simulation of large-scale structural systems. Each module of the RTMD IT system communicates through SCRAMNET, a proprietary shared memory bus based on fiber optic network technology. Within the RTMD IT system, the servo controller (RTMDctrl) communicates with all of the servo-valves, actuators, HSM control box and simulation computer (RTMDsim) with a sampling frequency of 1024Hz. The servo controller consists of a digital signal processor (DSP) real-time control card, which is housed in

the RTMDctrl. The real-time hybrid simulation is controlled and implemented by the RTMDxPC module. A MATLAB Simulink file on the RTMDsim computer is compiled and downloaded to RTMDxPC (which is an xPC workstation) which runs Mathwork's real-time Target PC software package. This system provides commands to and receives feedback from RTMDctrl in real time over SCRAMNet, which has a communication delay of less than 180 nsec between modules.

11.4 Integration Algorithm and Actuator Delay Compensation

In this study, the CR integration algorithm (Chen et al. 2009a) is used for the numerical integration of the equations of motion during the real-time hybrid simulation. In the CR integration algorithm the variation of displacement and velocity over a time step are defined as

$$\dot{\mathbf{x}}_{i+1} = \dot{\mathbf{x}}_i + \Delta t \boldsymbol{\alpha}_1 \ddot{\mathbf{x}}_i \tag{11.2}$$

$$\mathbf{x}_{i+1} = \mathbf{x}_i + \Delta t \dot{\mathbf{x}}_i + \Delta t^2 \boldsymbol{\alpha}_2 \ddot{\mathbf{x}}_i \tag{11.3}$$

where, $\mathbf{x}$ is the displacement vector of a structure, Δt is the integration time step, and $\boldsymbol{\alpha}_1$ and $\boldsymbol{\alpha}_2$ are integration parameter matrices obtained from the structural properties. The CR integration algorithm was developed using control theory (Chen and Ricles, 2008a) and is an explicit unconditionally stable algorithm for the structure with a softening behavior (Chen and Ricles 2008b). For the structure with a stiffening behavior, it is conditionally stable. The accuracy of the CR integration algorithm is 2nd order and the

same as the Newmark-β constant average acceleration method (Chen et al. 2009a). Figure 11.4 illustrates how the CR integration algorithm is incorporated into a real-time hybrid simulation.

As indicated in Figure 11.4, the command displacement for each actuator is imposed to the experimental substructure in *n* substeps, where the substeps have a time step size of δt=1/1024 sec. (i.e., the inverse of the sampling frequency of the servo-controller for the actuators). Since a hydraulic actuator has its own dynamic properties, there is a time delay between the input command displacement and the output measured displacement of the actuator. If this time delay is not compensated appropriately, the result of a real-time hybrid simulation is inaccurate and the system can be unstable if the delay is substantial. To minimize the actuator delay problem, the inverse compensation method developed by Chen and Ricles (2010) is used in this study. It is based on a simplified model of the servo-hydraulic system. By assuming at the end of substep *j* within the $(i+1)^{th}$ time step, (i.e., at time $t_{i+1}^{(j)}$), that the actuator has achieved the displacement $x_{i+1}^{d(j)}$, and with the actuator response shown in Figure 11.5, the delayed displacement response $x_{i+1}^{d(j+1)}$ at the end of the $(j+1)^{th}$ substep can be expressed as

$$x_{i+1}^{d(j+1)} = x_{i+1}^{d(j)} + \frac{1}{\alpha}\left(x_{i+1}^{c(j+1)} - x_{i+1}^{d(j)}\right) \tag{11.4}$$

where $x_{i+1}^{c(j+1)}$ is the interpolated command displacement from the ramp generator for the $(j+1)^{th}$ substep issued to the experimental substructure and α is the ratio of the duration t_d that it takes for the actuator to achieve the displacement $x_{i+1}^{c(j+1)}$ to the sampling interval of the servo-controller, δt. A value of $\alpha = 1.0$ is associated with no actuator delay. Applying the discrete z-transform to Equation (11.4), the discrete transfer function $G_d(z)$ relating the delayed actuator response $x_{i+1}^{d(j)}$ to the command displacement $x_{i+1}^{c(j+1)}$ is equal to

$$G_d(z) = \frac{X^d(z)}{X(z)} = \frac{z}{\alpha z - (\alpha - 1)} \tag{11.5}$$

where $X^d(z)$ and $X(z)$ are the discrete z-transforms of $x_{i+1}^{d(j)}$ and $x_{i+1}^{c(j+1)}$, respectively. The inverse compensation method requires tuning of the delay constant α in order to have the method effectively compensate for actuator delay. The method is based on a constant delay, although it is effective in compensating for delay in systems which develop a moderate amount of variable actuator delay during a simulation (Chen and Ricles 2009c). The delay constant α for the 1,700kN actuator connected to the MR damper in each test bed of the experimental substructure was identified as 20 (representing an actuator delay of 19/1024sec) and is the value used in the real-time hybrid simulations. The inverse compensation method modifies the command displacement to enable the targeted displacement $X(z)$ to be achieved by the actuator at

the end of each time step, and is based on inverting Equation (11.5). The discrete transfer function $G_c(z)$ associated with the actuator delay compensation is expressed as:

$$G_c(z) = \frac{X_p(z)}{X(z)} = \frac{\alpha z - (\alpha - 1)}{z} \tag{11.6}$$

In Equation (11.6) $X_p(z)$ is the modified interpolated command displacement sent to the servo-controller for the substep.

11.5 Real-Time Hybrid Simulation for Assessment of the SDP and Evaluation of Structural Control Strategies

A schematic of the real-time hybrid arrangement used for the simulations presented in this dissertation is shown in Figure 11.1. The total structure is divided into the two analytical and the experimental substructures as shown, where the dampers are placed in test setups to create the experimental substructure and the remaining part of the structural system is modeled analytically (i.e., as the analytical substructure). The restoring forces $\mathbf{r}^a$ and $\mathbf{r}^e$ from the two substructures are appropriately summed to enable the equations of motion to be numerically integrated for each time step, as illustrated in Figure 11.4.

11.5.1 HybridFEM as a Tool for Real-Time Hybrid Simulation

The finite element program HybridFEM (Karavasilis et al. 2009) is used to model the analytical substructure in the hybrid simulation. HybridFEM is developed

using the MATLAB/Simulink software (Mathworks 2009) and is compiled with Mathworks's Real-Time Workshop and placed on the RTMDxPC. Various structural elements and material modeling options are available in the HybridFEM element and material libraries to enable complex analytical substructures to be created. The element library currently includes linear and nonlinear elements such as a linear-elastic beam-column element, a nonlinear lumped plastic hinge element, a nonlinear fiber element, a nonlinear panel-zone element, a nonlinear strength deterioration element, and a nonlinear lean-on column to model the P-delta effect. Currently, the CR integration and the Rosenbroke-W (Lamarche et al. 2009) methods are implemented in HybridFEM.

Figure 11.6 shows the Simulink block diagram for the real-time hybrid simulation of the 3-story building structure with either passive or semi-active controllers. The 'Generate Element Restoring Forces' block represents the analytical substructure, and produces the element restoring forces of the analytical substructure. The 'MR dampers" block represents the experimental substructure, where communication with the RTMDctrl takes place via SCRAMNet to command the actuators to impose the calculated command displacements on the dampers, and to provide the measured experimental substructure restoring forces (from the MR dampers). The element restoring force vector is added to the measured MR damper forces from the 'MR dampers' block and fed into the 'Integrator' block where the time integration of the equations of motion is performed. The displacement and velocity from the 'Integrator' are supplied to the 'Generate Element Restoring Forces' block, the 'Controllers' block, and the 'MR dampers' block.

The 'Controllers' block contains the five different control strategies of Chapter 9, where each controller is activated by turning on a multiport switch within the block. The 'Controller' has three inputs: the displacement and velocity of the structure, and the measured damper force, which are used for determining the command currents for the MR dampers based on a selected control law. In Chapters 2 and 8, the semi-active control designs were described, where each required a feedback force from each damper along with the state vector **z** consisting of either displacement and velocity (LQR, SMC, and PAC), or just velocity $\dot{x}$ (DBB). For the real-time hybrid simulations, the feedback signal for displacement and velocity of the structure used for the control laws was based on the solution from the integration of the equations of motion. The effects of noise were excluded, since this issue was studied in Chapter 9, and found not to be significant on the performance of the controller. Hence, the two MR dampers are controlled by the displacement from the 'Integrator' and the command current from the 'Controllers' in the 'MR dampers' block. The inverse compensation algorithm and sub-blocks for communicating with the SCRAMNet are embedded into the 'MR dampers' block.

The sampling frequency of the RTMD IT system is 1024Hz. The 'Integrator', 'Controllers', and 'MR dampers' blocks are implemented with a time step of 1/1024sec. to enable the interpolated command displacement for each actuator to be imposed in n substeps of δt=1/1024sec over the duration associated with the time step size Δt via the ramp generator. The 'Generate Element Restoring Forces' block can be run at an integer multiple of 1/1024sec (e.g., m/1024sec where $m<n$) by inserting a rate transition block before and after the 'Generate Element Restoring Forces' block, since the analytical

substructure restoring force is not required to be made available until near the end of the time step, as shown in Figure 11.4. In summary, the response of the structure is updated every at the end of each time step, where the time step $\Delta t = n/1024$sec, and the displacements imposed onto the MR dampers by the actuators are controlled by the ramped (interpolated) displacement over n substeps. For the real-time hybrid simulations of this study values of $n=5$ and $m=4$ are used whereby the size of the time step Δt for the integration algorithm is 5/1024sec. Convergence studies were performed using numerical simulations (i.e., time history analysis) and trial hybrid simulations to ensure the value of Δt =5/1024 sec. resulted in an accurate solution from the integration algorithm.

11.5.2 Analytical Substructure

The analytical substructure model is similar to that used for assessing the SDP in Chapter 7 (see Section 7.2), except that displacement-based fiber and stress resultant beam-column elements were used for modeling of the beams and columns of the structure instead of the force-based fiber element. Figure 11.7 shows the analytical substructure for real-time hybrid simulation created using HybridFEM. The dampers of the experimental substructure are included in Figure 11.7 to illustrate the connectivity between the analytical and experimental substructures. The hybrid simulation included a total of 190 degrees of freedom, where nodal translational and rotation degrees of freedom exist in the model. The displacement-based fiber element has five sections along the element length and the cross-section is discretized into 18 fibers, including 12

fibers for the web and 3 fibers for each flange of the members. In order to make the state determination of the analytical substructure more efficient, since the plastic behavior occurs near the ends of the beams and columns of the MRF structure, the beams and columns are divided into three parts: one linear elastic element in the middle and one displacement-based fiber element at each end. The length of the displacement-based fiber element is taken as 10% of the member length. This procedure also results in a more accurate determination of the plastic rotations near the end of the element, since the displacement-based fiber element is based on a formulation that has a linear variation in curvature along its length.

11.5.3 Experimental Substructure

The test setup for each damper of the experimental substructure was the same as that used for the characterization tests that were presented in Chapter 3, and is shown in Figure 11.8. A photograph of the test setup showing both dampers is given in Figure 11.9. Each setup has one servo-hydraulic actuator with supports and roller bearings, a reaction frame, and a tie-down beam to secure the damper to the strong floor. In each test setup a 1,700kN actuator imposes the command displacement on the MR damper and the load cell between the damper and the actuator measures the damper force. The electric circuits and current drivers described in Chapter 3 are used to supply the command current to the dampers. The command current is 2.5A for the passive control and either 0.0A or 2.5A for the semi-active controllers.

11.5.4 Ground Motions

Five ground motions from Appendix 3 were selected for the real-time hybrid simulations and are listed in Table 11.1. The ground motions are scaled to the DBE level using the procedure described in Section 5.6. Figure 11.10 shows the response spectrum of the ground motions listed in Table 11.1 compared to the design (DBE) response spectrum. The response spectrum is for the full-scale structure. The median response spectrum of these ground motions matches well the DBE level response spectrum (IBC 2006) around the fundamental period of the 0.6-scale building structure with MR dampers, which was estimated to be 0.85 sec. (see Table 6.17). Since the structure is scaled down with a geometric scale factor of 0.6, the time axis for the ground motion is scaled by $\sqrt{0.6}$ to satisfy similitude laws (see Table 6.6).

11.6 Results of Real-Time Hybrid Simulations for Control Algorithm Assessment

Five different ground motions and five different control strategies are considered in the real-time hybrid simulations to evaluate the performance of the structural control strategies. A total of 25 real-time hybrid simulations therefore are conducted; Tables 11.2 through 11.6 summarize the results of the real-time hybrid simulations. Maximum story drift results appear in Table 11.2. When the Duzce ground motion is used, the LQR controller works better than the other controllers in reducing the maximum story drift, maximum plastic rotations in the members, maximum absolute velocity and maximum absolute accelerations in the lower stories and floors. The maximum story drift is about 12% less in the first story compared to the passive control case in Table

11.2. Moreover, the reduction in the absolute acceleration of the structure when the LQR controller is used is large; where a 17% reduction in the maximum acceleration is observed at the second floor compared to the passive control case (see Table 11.6). However, a more rational assessment of the control strategies is based on statistical response results for the various ground motions. The median of the maximum story drift and the standard deviation are provided at the bottom of each table. In Table 11.3 the median maximum first story drift for the passive control case is slightly larger than that for the semi-active controllers; however, the median maximum second and third story drifts are lower for the passive control case than for the semi-active controllers. Similar to the results given in Chapter 9, the median maximum story drifts for the various semi-active controllers do not have significant differences.

The maximum plastic rotations of the beams and columns in the MRF are summarized in Tables 11.3 and 11.4. The median maximum responses for the passive control case are similar to or lower than those for the semi-active controllers, which is also consistent with the results given in Chapter 9 (see Tables 9.5 and 9.7).

The maximum absolute velocity and maximum absolute acceleration are compared in Tables 11.5 and 11.6. These quantities are used to evaluate the non-structural component behavior and potential damage in the building. Similar to the story drift results, no significant differences between the results for the various controllers are observed in the median maximum absolute velocities. For the maximum absolute acceleration, the LQR controller has a slightly better performance than the passive control for all three floors. The median value of the maximum absolute acceleration at

the 3rd floor level, where the maximum acceleration is observed, is about 7.5% less than that for the passive control case. However, the maximum 3rd story drift for the LQR controller is increased by about 7.2 % compared to the passive control case (see Table 11.2), illustrating a trade-off between the maximum displacement and maximum absolute acceleration response.

Although only five ground motions are used for the real-time hybrid simulations, the statistical response of the simulations also shows that the performance of passive control is similar to that of semi-active controllers, which is consistent with the conclusions of Chapter 9 where the numerical study was conducted with 44 ground motions.

Table 11.7 summarizes the results from the SDP and the median maximum story drifts and median maximum damper forces from the real-time hybrid simulations. For the 1st and 2nd story drifts the SDP shows good agreement with the results of the real-time hybrid simulations. The 3rd story drift from the SDP is less than that of the real-time hybrid simulations (by 7.8%). As discussed in Chapter 7, the SDP results were slightly less than the damper force from the nonlinear time history analyses. Similar results are observed here where the damper forces from the SDP are less than those from the real-time hybrid simulations for the passive control case. In addition, the median maximum damper forces for the semi-active control cases are less than that for the passive control case from the real-time hybrid simulations. The results from the SDP are based on passive control of the MR damper. The median maximum damper forces in the 2nd and 3rd stories from the real-time hybrid simulations with passive control are

3.3% and 8.3% smaller, respectively, than the SDP results. Overall, reasonably good agreement between the SDP results and the real-time hybrid simulation results is observed (i.e., within about 8%), experimentally demonstrating the simplified analysis procedure in the SDP.

11.7 Validation of Real-Time Hybrid Simulations

11.7.1 Servo-Hydraulic Actuator Response

Since the real-time hybrid simulation combines the analytical substructure and the experimental substructure into one integrated structure, the restoring forces from the two substructures need to be acquired in real-time, and an effective actuator delay compensation method is required to accurately impose the command displacements on the experimental substructure, so that the experimental substructure restoring forces are synchronized with the analytical substructure restoring forces. In this study, the inverse compensation algorithm is applied to both 1,700kN actuators as mentioned previously. Figures 11.11 and 11.12 compare the time histories of actuator command displacements and actuator measured displacements for the 2nd and 3rd story dampers, where the results are for the simulation involving the 1992 Landers earthquake ground motion and the LQR controller. Figures 11.10 (b) and 11.11(b) provide a close-up near the time at the maximum response. A slight difference in the amplitude of the command and measured actuator displacements is evident, where the measured displacements are larger. The maximum error is 3.8% and 7.2% for the actuators attached to the 2nd and 3rd story dampers, respectively. Overall, the measured displacement follows the command

displacement very well. The synchronized subspace plots comparing the measured and command actuator displacements are given in Figures 11.13 and 11.14. Any deviation from a 45 degree line indicates a delay or lead in the actuator response. The results in Figures 11.13 and 11.14 show that no significant delay is observed. The overall comparison between the command and the measured displacements shows good agreement and the inverse compensation method for actuator delay appears to work well.

11.7.2 Comparison of Response

To validate the response of the 3-story building from the real-time hybrid simulations, numerical simulations were also conducted using OpenSees with the variable current MNS MR damper model and the results are compared with the results from the real-time hybrid simulations. The same types of elements as used in HybridFEM (Figure 11.7) were employed to model the beams, columns, diagonal braces, and panel zones of the structure in the numerical simulations. The time integration algorithm used in OpenSees is the Newmark-β method with constant average acceleration. The Newton-Raphson method was used to account for element nonlinearity and an iteration procedure was performed until the displacement error norm (the Eucilidean norm) was of 5×10^{-5} for each time step.

For the dampers in the OpenSees model, the variable current MNS model was used where the parameters for the 3rd story damper are the same as those identified in Chapter 3 (see Table 3.3). Although both dampers have the same configuration, the

dynamic behavior of each damper was slightly different; thus, new characterization test was conducted on the 2nd story MR damper using the procedure described in Chapter 3. Table 11.8 lists the MNS model parameters for the 2nd story MR damper. The 2nd and 3rd story MR damper models used the same parameters for the dynamics of electromagnetism (i.e., $\alpha_0 = 24.96, \alpha_1 = 3.57, \beta^+ = 0.31, \beta^- = -0.30$).

Figures 11.15 through 11.16 compare the story drift and MR damper responses from the real-time hybrid simulation (RTHS) and the numerical simulation with OpenSees. The global time step used in the numerical simulations is Δt=0.005 sec. The damper force for the MNS models are obtained by evaluating the numerical integration with this time step utilizing the procedure given in Appendix 2. Figure 11.15 compares the story drift response when the structure is passively controlled and subjected to the 1987 Superstition Hill ground motion. Figures 11.16 and 11.17 compare the MR damper response for the 2nd story and the 3rd story MR dampers, respectively. The damper force predicted by the MNS model matches the experimental damper force from the real-time hybrid simulation. Good agreement is observed between the story drifts from the real-time hybrid simulation and the numerical simulation. The damper force-displacement relationship and the damper force-velocity relationship from the MNS model also show good agreement with the real-time hybrid simulation results. For the damper force-displacement relationship, the damper displacements from the real-time hybrid simulation are slightly larger than the numerical simulation results. The damper displacement was measured by the internal displacement sensor in the actuator in the real-time hybrid simulation. However, this does not affect the overall response of real-

time hybrid simulation significantly because the damper force is mostly determined by the damper velocity which is zero at the peak displacement amplitude. A comparison for the semi-active controller cases is provided in Figures 11.18 through 11.29 for different earthquakes. For each case good agreement between the real-time hybrid simulation and the numerical simulation results is observed.

A statistical comparison is presented in Tables 11.9 and 11.10, where the median maximum story drift and the median maximum absolute acceleration are tabulated for the real-time hybrid simulations and the numerical simulations using OpenSees. Good agreement is observed between the real-time hybrid simulation results and the numerical simulation results in these tables as well as in Figures 11.18 through 11.29, validating the results of the real-time hybrid simulations.

11.8 Real-Time Hybrid Simulations under Extreme Earthquake Ground Motions

In Chapter 10, a study of collapse potential of the building was conducted using incremental dynamic analyses with OpenSees. This section presents a set of real-time hybrid simulations conducted to investigate the behavior of the building and to validate the incremental dynamic analysis procedure by incrementally increasing the intensity of the ground motions over a series of real-time hybrid simulations. In these real-time hybrid simulations, three different control strategies were studied: (1) passive controller; (2) the linear quadratic regulator (LQR); and (3) the phase angle controller (PAC). The sliding mode controller (SMC), the decentralized bang-bang (DBB)

controller, and the phase angle controller (PAC) had very similar performance to the passive control case in Chapter 10, and therefore only PAC is considered here.

11.8.1 Analytical Substructure

The analytical model is similar to that used for the numerical simulations assessing the collapse potential presented in Chapter 10 (see Section 10.3); an exception is the columns where the displacement-based fiber element in HybridFEM is used to model the columns of the MRF and the DBF instead of the force-based fiber element. Figure 11.30 shows the analytical substructure model for real-time hybrid simulation created using HybridFEM. The dampers of the experimental substructure are included in Figure 11.30 to illustrate the connectivity between the analytical and experimental substructures. The hybrid simulations included a total of 174 degrees of freedom. Nodal translational and rotation degrees of freedom were modeled in the model. The displacement-based fiber element has five sections along the element length and is discretized into 18 fibers, including 12 fibers for the web and 3 fibers for each flange of the members. The same parameters for the deterioration element at the end of beams in the MRF are used as listed in Table 10.1. In addition, the columns of the MRF are divided into three parts, with one linear elastic element in the middle and two displacement-based fiber elements at both ends. The length of the displacement-based fiber element is taken as 10% of the member length.

11.8.2 Experimental Substructure

The experimental setup describe in Section 11.5.3 was also used for the extreme ground motions. The command current was 2.5A for passive controller, and either 0.0A or 2.5A for the LQR and the PAC controllers.

11.8.3 Ground Motions

Only one ground motion was used in these real-time hybrid simulation. The 000 component of the Canyon Country from 1994 Northridge earthquake (Table 11.1) was used. Three different ground motion intensities are considered, including: 1.0 times the MCE level, 1.33 times the MCE level, and 2.0 times the MCE level. The basis for the maximum intensity being 2.0 times the MCE level is explained later. The spectral accelerations at the fundamental period of the 0.6-scale building without the MR dampers, T=0.94 sec. (see Table 6.17), for these intensity levels are S_{aT_1}=0.77g, S_{aT_1}=1.02g, and S_{aT_1}=1.54g, respectively, based on the scaling procedure discussed in Chapter 5.

11.9 Results of Real-Time Hybrid Simulation under Extreme Earthquake Ground Motions

Since three control cases (passive, LQR, and PAC) were used, so a total 9 real-time hybrid simulations were performed.

As mentioned in Chapter 10, the large-scale MR dampers of this study have a stroke limit of ±279mm, implying that the damper can be operated up to a story drift of about 12.2%. The dampers however were not operated to their full stroke in the real-

time hybrid simulations to avoid damaging them. Moreover, the two actuators in the test setup for the experimental substructure each have an operational velocity limit, as can be observed in Figure 11.2. With no force in the 1700kN actuator with 3 servo valves, the maximum velocity that can be achieved is 1.14m/sec . The maximum intensity of the ground motion is therefore limited to 2.0 times the MCE level to avoid exceeding the stroke limit of the dampers and the operational limits of the actuators in the test setup.

Figure 11.31 shows the results of the real-time hybrid simulations (RTHS) compared to the IDA curves obtained from the numerical simulations with OpenSees. The IDA curve from the numerical simulations shows the LQR controller has better performance than passive control and the PAC controller for the selected ground motion. This trend is also observed in the numerical simulations in Figure 11.31 as well as the results reported in Chapter 10 involving the ensemble of 44 ground motions. When the intensity is 2.0 times the MCE level, the structure with the LQR controller has a smaller drift than the other cases. At 1.33 times the MCE intensity level, the results from the real-time hybrid simulations are slightly different than the results from the numerical simulations for the LQR controller. However, an overall comparison shows that the hybrid simulation results match well the numerical simulations. Moreover, if HybridFEM is used for the numerical simulation, where the MR dampers are analytically modeled using the MNS model, the numerical simulation results exhibits better agreement with the real-time hybrid simulation results, as shown in Figure 11.32. The small difference between the real-time hybrid simulation and numerical simulation

results plotted in Figure 11.31 is attributed to the different integration algorithms used in the two simulations. As noted previously, the real-time hybrid simulations are conducted using HybridFEM in conjunction with the explicit CR integration algorithm. OpenSees was used conjunction with an implicit form of the Newmark-β method (constant average acceleration) along with Newton-Rahpson iteration. However, no significant differences in the predictions made by OpenSees and HybridFEM are observed, and the results are very consistent with those from the real-time hybrid simulations.

Figure 11.33 compares story drift time histories from a real-time hybrid simulation and an OpenSees numerical simulation for a ground motion intensity of 2.0 times the MCE, where the global time step of Δt=0.005 sec is used.. The results in Figure 11.33 are for the LQR controller. The maximum displacement of the 3rd floor is about 0.4m in both cases, which corresponds to a 6% roof drift (3rd floor displacement divided by the building height from the ground level). The floor displacement from OpenSees shows good agreement with that from the real-time hybrid simulation. Figures 11.34 and 11.35 compare the MR damper response in the 2nd and the 3rd floors, respectively. The maximum velocity demand for the 3rd story MR damper is almost 0.9 m/sec., which is much higher than that for the DBE level ground motion (where the maximum damper velocity was about 0.3 to 0.4m/sec). The damper forces from the MNS model are shown to match well the experimental damper forces under an extreme ground motion intensity.

Figures 11.31 through 11.35 validate the real-time hybrid simulation results under an extreme ground motion; the responses from the real-time hybrid simulations have good agreement with results from the numerical simulations. The MNS model is shown to predict well the MR damper response, even when under a high velocity demand, providing an accurate response prediction of structures with MR dampers under extreme earthquake ground motions.

11.10 Summary

Real-time hybrid simulation were conducted to assess the SDP and evaluate the structural control strategies under the DBE, and to investigate the behavior of a structure under an extreme ground motion. The real-time hybrid simulations were performed on the 3-story building with MR dampers designed using the SDP as presented in Chapter 6. The hybrid simulation results were compared with numerical simulation results. The numerical simulations were performed using OpenSees, using a different integration algorithm. The experimental substructure consisted of two large-scale MR dampers. The analytical substructure was composed of various nonlinear elements considering the shear and flexural deformations at the panel zone, along with the moment-axial force interaction in the beams and columns. The real-time hybrid simulations were conducted using HybridFEM.

The analytical results from the SDP show good agreement with the results of the real-time hybrid simulations with the dampers in passive control. The statistical experimental response from the structure with various semi-active controllers was also

similar to that with passive control, consistent with the finding from the numerical study presented in Chapter 9.

The real-time hybrid simulations conducted under the extreme ground motions showed good agreement with the IDA curves obtained from the numerical simulations. The MNS model is shown to accurately predict damper behavior under the DBE and MCE ground motions, as well as at higher levels of ground motion intensity where larger velocity demands are imposed on the dampers. These comparisons verify the accuracy of the MNS model and demonstrate its robustness.

Table 11.1 Ground motions for real-time hybrid simulation

ID	EQ name	Year	Station	Mag.	Comp.	DBE scale factor
1	Superstition Hills	1987	Poe Road (temp)	6.5	270	1.71
2	Duzce, Turkey	1999	Bolu	7.1	90	0.64
3	Landers	1992	Coolwater	7.3	LN	2.15
4	Imperial Valley	1979	El Centro Array #11	6.5	230	1.95
5	Northridge	1994	Canyon Country-WLC	6.7	000	1.16

Table 11.2 Real-time hybrid simulation result for maximum story drift (%), DBE ground motions

		Passive	LQR	SMC	DBB	PAC
Superstition Hills	1st story	1.10	1.11	1.11	1.14	1.10
	2nd story	1.13	1.20	1.14	1.14	1.17
	3rd story	1.26	1.50	1.30	1.32	1.44
Duzce, Turkey	1st story	1.37	1.22	1.32	1.36	1.30
	2nd story	1.70	1.66	1.69	1.71	1.68
	3rd story	1.75	1.81	1.75	1.79	1.80
Landers	1st story	0.99	0.91	0.96	0.97	0.90
	2nd story	1.11	1.13	1.13	1.12	1.09
	3rd story	1.31	1.34	1.33	1.34	1.35
Imperial Valley	1st story	1.57	1.53	1.59	1.58	1.57
	2nd story	1.63	1.70	1.70	1.67	1.72
	3rd story	1.76	1.88	1.84	1.82	1.91
Northridge	1st story	1.17	1.11	1.14	1.16	1.15
	2nd story	1.33	1.37	1.34	1.34	1.38
	3rd story	1.52	1.63	1.52	1.55	1.63
Median response	1st story	1.17	1.11	1.14	1.16	1.15
	2nd story	1.33	1.37	1.34	1.34	1.38
	3rd story	1.52	1.63	1.52	1.55	1.63
Standard deviation	1st story	0.23	0.23	0.24	0.23	0.25
	2nd story	0.27	0.26	0.28	0.28	0.28
	3rd story	0.24	0.22	0.25	0.24	0.23

Table 11.3 Real-time hybrid simulation result for MRF maximum beam plastic rotation (rad %), DBE ground motions

		Passive	LQR	SMC	DBB	PAC
Superstition Hills	1st floor	0.24	0.25	0.25	0.27	0.25
	2nd floor	0.10	0.22	0.12	0.11	0.18
	3rd floor	0.15	0.37	0.16	0.20	0.31
Duzce, Turkey	1st floor	0.59	0.48	0.56	0.58	0.53
	2nd floor	0.72	0.73	0.72	0.74	0.74
	3rd floor	0.55	0.63	0.54	0.59	0.61
Landers	1st floor	0.10	0.06	0.09	0.09	0.04
	2nd floor	0.15	0.18	0.18	0.17	0.16
	3rd floor	0.17	0.19	0.17	0.19	0.22
Imperial Valley	1st floor	0.77	0.76	0.81	0.79	0.80
	2nd floor	0.58	0.69	0.68	0.64	0.70
	3rd floor	0.65	0.78	0.74	0.71	0.84
Northridge	1st floor	0.31	0.27	0.29	0.30	0.31
	2nd floor	0.35	0.44	0.38	0.37	0.43
	3rd floor	0.34	0.48	0.34	0.38	0.49
Median response	1st floor	0.31	0.27	0.29	0.30	0.31
	2nd floor	0.35	0.44	0.38	0.37	0.43
	3rd floor	0.34	0.48	0.34	0.38	0.49
Standard deviation	1st floor	0.27	0.27	0.28	0.28	0.29
	2nd floor	0.27	0.26	0.28	0.28	0.27
	3rd floor	0.22	0.23	0.25	0.23	0.24

Table 11.4 Real-time hybrid simulation result for maximum plastic rotation of MRF at the 1st story column base (rad %), DBE ground motions

	Passive	LQR	SMC	DBB	PAC
Superstition Hills	0.04	0.04	0.04	0.05	0.04
Duzce, Turkey	0.16	0.06	0.13	0.15	0.11
Landers	0.02	0.02	0.02	0.02	0.02
Imperial Valley	0.34	0.28	0.35	0.34	0.33
Northridge	0.04	0.02	0.03	0.03	0.03
Median response	0.04	0.04	0.04	0.05	0.04
Standard deviation	0.14	0.11	0.14	0.14	0.13

Table 11.5 Maximum absolute velocity (m/sec) of structure from real-time hybrid simulations, DBE ground motions

		Passive	LQR	SMC	DBB	PAC
Superstition Hills	1st floor	0.401	0.432	0.404	0.402	0.410
	2nd floor	0.474	0.457	0.472	0.465	0.458
	3rd floor	0.595	0.654	0.605	0.604	0.619
Duzce, Turkey	1st floor	0.354	0.350	0.349	0.352	0.352
	2nd floor	0.471	0.442	0.456	0.465	0.459
	3rd floor	0.597	0.637	0.595	0.599	0.600
Landers	1st floor	0.404	0.393	0.400	0.401	0.399
	2nd floor	0.457	0.425	0.451	0.453	0.438
	3rd floor	0.520	0.523	0.516	0.516	0.504
Imperial Valley	1st floor	0.616	0.633	0.618	0.614	0.607
	2nd floor	0.602	0.630	0.616	0.608	0.625
	3rd floor	0.656	0.697	0.663	0.660	0.680
Northridge	1st floor	0.366	0.370	0.372	0.367	0.368
	2nd floor	0.399	0.403	0.396	0.395	0.405
	3rd floor	0.526	0.553	0.527	0.527	0.530
Median response	1st floor	0.401	0.393	0.400	0.401	0.399
	2nd floor	0.471	0.442	0.456	0.465	0.458
	3rd floor	0.595	0.637	0.595	0.599	0.600
Standard deviation	1st floor	0.107	0.115	0.108	0.107	0.103
	2nd floor	0.074	0.091	0.082	0.079	0.086
	3rd floor	0.056	0.073	0.060	0.060	0.071

Table 11.6 Maximum absolute acceleration (g) of structure from real-time hybrid simulations, DBE ground motions

		Passive	LQR	SMC	DBB	PAC
Superstition Hills	1st floor	0.509	0.543	0.521	0.515	0.537
	2nd floor	0.555	0.553	0.559	0.560	0.564
	3rd floor	0.703	0.698	0.696	0.702	0.638
Duzce, Turkey	1st floor	0.517	0.517	0.472	0.507	0.546
	2nd floor	0.605	0.515	0.568	0.592	0.589
	3rd floor	0.602	0.584	0.589	0.598	0.597
Landers	1st floor	0.356	0.356	0.354	0.345	0.363
	2nd floor	0.435	0.409	0.412	0.424	0.420
	3rd floor	0.628	0.584	0.619	0.630	0.581
Imperial Valley	1st floor	0.537	0.466	0.539	0.534	0.504
	2nd floor	0.616	0.613	0.623	0.615	0.609
	3rd floor	0.742	0.739	0.738	0.740	0.684
Northridge	1st floor	0.393	0.405	0.369	0.389	0.422
	2nd floor	0.459	0.427	0.446	0.452	0.446
	3rd floor	0.562	0.560	0.535	0.559	0.555
Median response	1st floor	0.509	0.466	0.472	0.507	0.504
	2nd floor	0.555	0.515	0.559	0.560	0.564
	3rd floor	0.628	0.584	0.619	0.630	0.597
Standard deviation	1st floor	0.082	0.077	0.085	0.085	0.079
	2nd floor	0.083	0.086	0.089	0.085	0.086
	3rd floor	0.074	0.080	0.082	0.074	0.051

Table 11.7 Comparison of response from SDP and median maximum response from real-time hybrid simulation

	Story	SDP	Real-time hybrid simulation				
			Passive	LQR	SMC	DBB	PAC
Maximum story drift (%)	1	1.18	1.17	1.11	1.14	1.16	1.15
	2	1.35	1.33	1.37	1.34	1.34	1.38
	3	1.41	1.52	1.63	1.52	1.55	1.63
Maximum damper force (kN)	1	-	-	-	-	-	-
	2	222.9	230.4	222.8	216.6	223.4	216.3
	3	233.6	254.7	226.6	251.2	250.7	242.2

Table 11.8 MNS model parameters for the 2nd story MR damper

Current I (Amps)	c (kN s/m)	k (kN/m)	Positive force post-yield curve				Negative force post yield curve				m_0 (kNs^2/m)
			a (kN)	b (kN s/m)	n	$\dot{x}_t^+$ (m/s)	a (kN)	b (kN s/m)	n	$\dot{x}_t^-$ (m/s)	
0.0	12,000	120,000	19.5	158.6	1.30	0.010	-19.5	-158.6	1.30	-0.010	1.50
0.5	11,500	118,000	41.2	162.5	0.81	0.010	-41.2	-162.5	0.81	-0.010	1.50
1.0	12,000	118,000	91.5	122.5	0.52	0.010	-96.0	-134.9	0.60	-0.010	1.60
1.5	12,000	118,000	95.0	195.5	0.61	0.010	-95.0	-195.5	0.61	-0.010	1.50
2.0	11,491	110,030	111.3	209.3	0.62	0.003	-115.7	-199.3	0.64	-0.003	1.05
2.5	11,500	115,000	126.6	213.9	0.63	0.010	-127.6	-216.7	0.68	-0.010	1.05

Table 11.9 Comparison of maximum story drift between real-time hybrid simulation and numerical simulation with OpenSees, DBE ground motions

		Maximum story drift (%)		
		1st story	2nd story	3rd story
Passive	RTHS	1.17	1.33	1.52
	OpenSees	1.18	1.36	1.48
LQR	RTHS	1.11	1.37	1.63
	OpenSees	1.16	1.40	1.53
SMC	RTHS	1.14	1.34	1.52
	OpenSees	1.15	1.37	1.49
DBB	RTHS	1.16	1.34	1.55
	OpenSees	1.15	1.38	1.51
PAC	RTHS	1.15	1.38	1.63
	OpenSees	1.13	1.37	1.52

Table 11.10 Comparison of median maximum absolute acceleration between real-time hybrid simulation and numerical simulation with OpenSees, DBE ground motions

		Maximum absolute acceleration (g)		
		1st floor	2nd floor	3rd floor
Passive	RTHS	0.509	0.555	0.628
	OpenSees	0.458	0.558	0.610
LQR	RTHS	0.466	0.515	0.584
	OpenSees	0.453	0.524	0.621
SMC	RTHS	0.472	0.559	0.619
	OpenSees	0.449	0.523	0.600
DBB	RTHS	0.507	0.560	0.630
	OpenSees	0.441	0.554	0.606
PAC	RTHS	0.504	0.564	0.597
	OpenSees	0.509	0.533	0.595

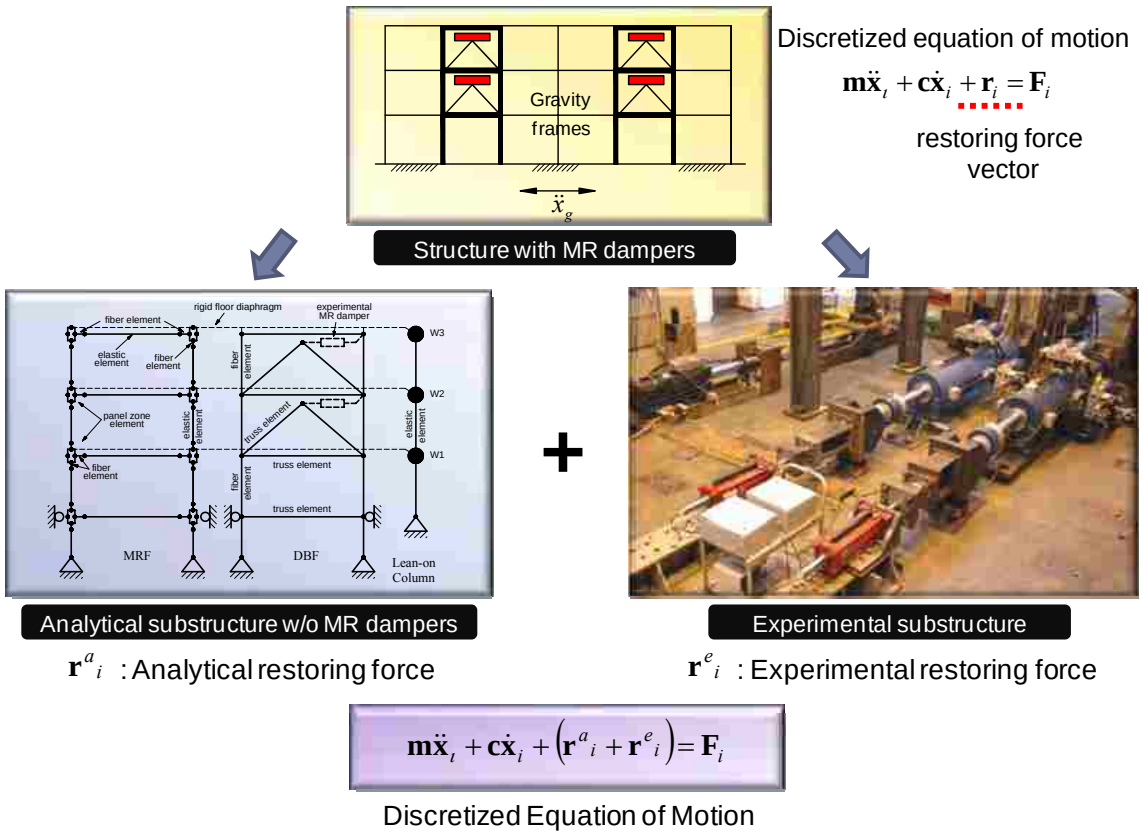

Figure 11.1 Schematic of real-time hybrid simulation for a structure with MR dampers

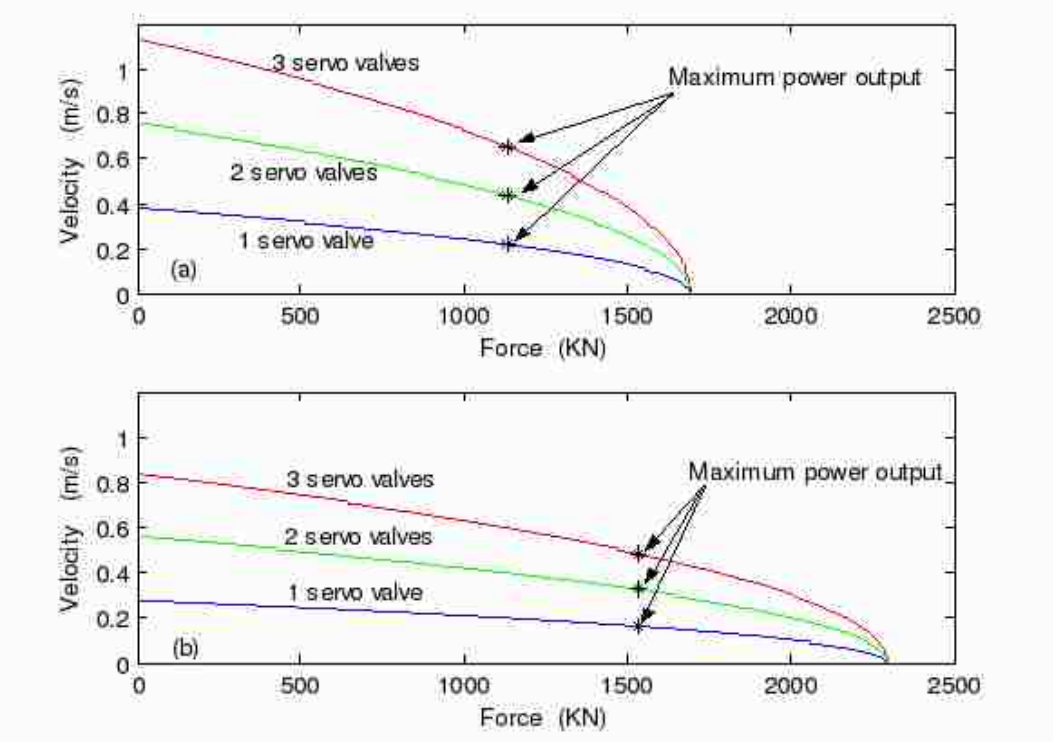

Figure 11.2 Hydraulic actuator power envelop for (a) a 1,700 kN actuator, and (b) 2,300 kN actuator with a 20.7 MPa supply pressure

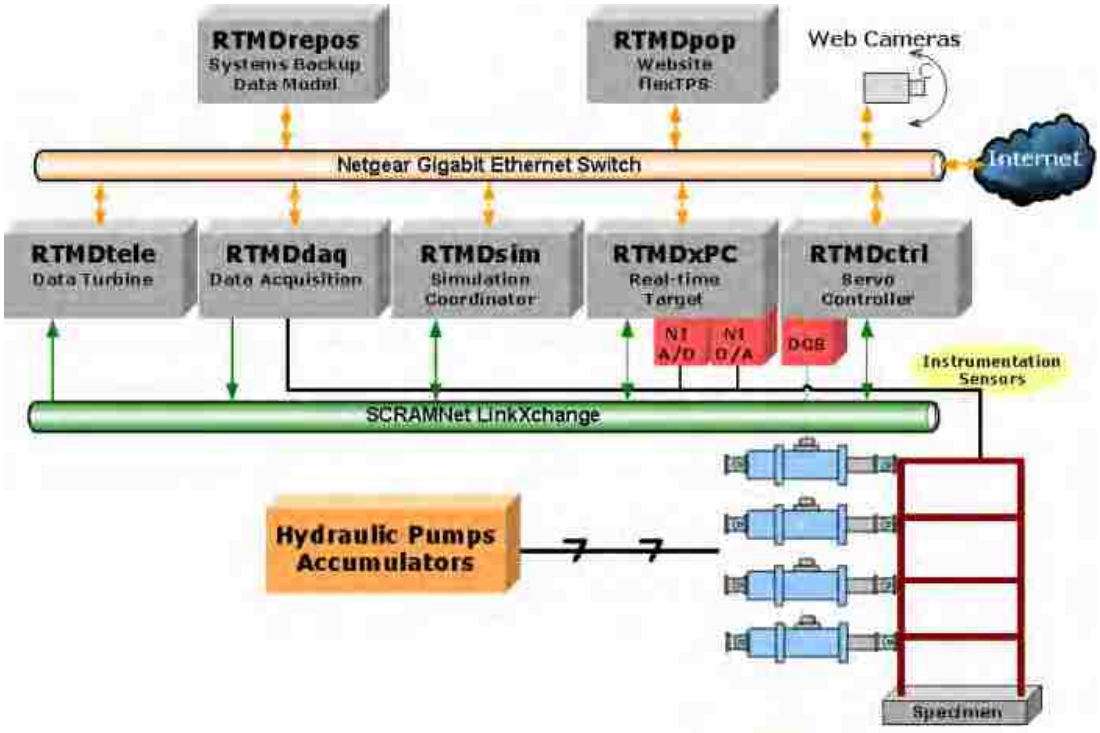

Figure 11.3 Architecture of Lehigh RTMD IT system

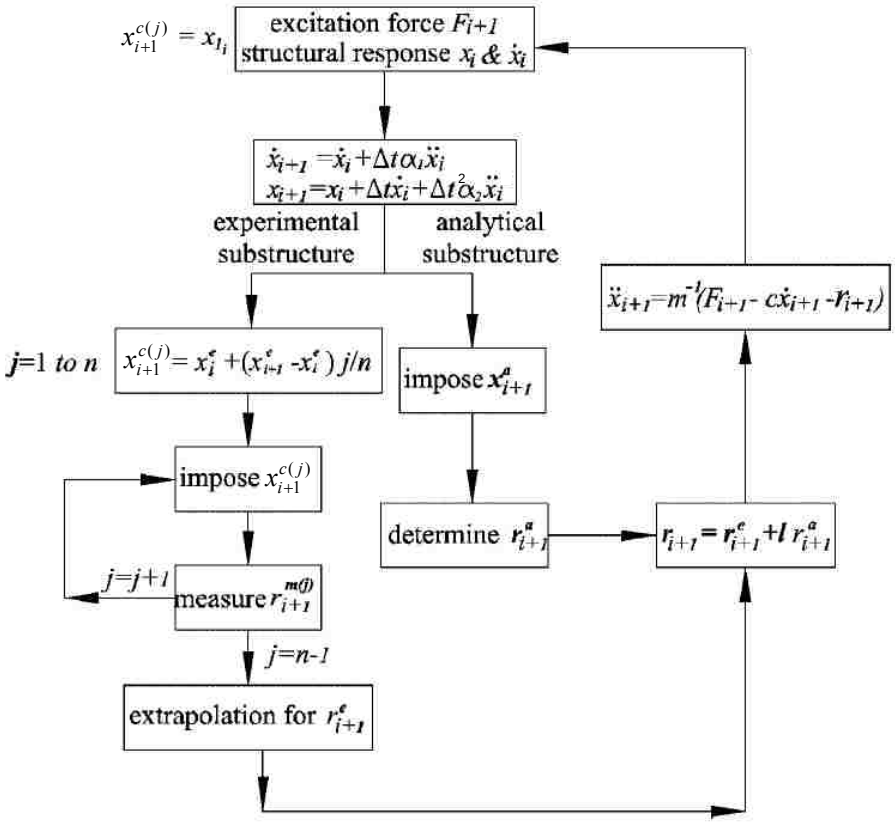

Figure 11.4 Implementation of CR integration algorithm for real-time hybrid simulation (after Chen et al. 2009a)

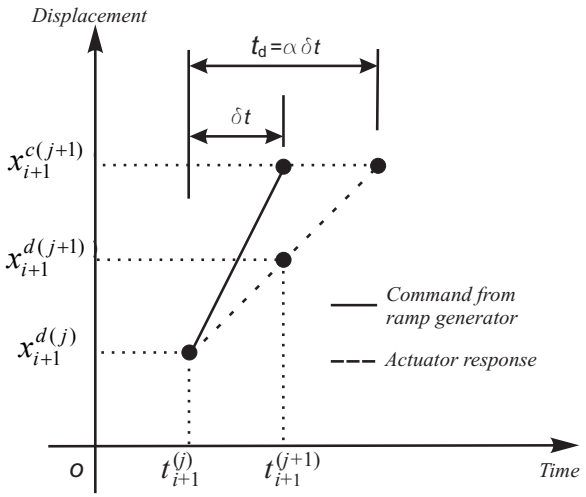

Figure 11.5 Conceptual actuator delay for inverse compensation (after Chen and Ricles 2009c)

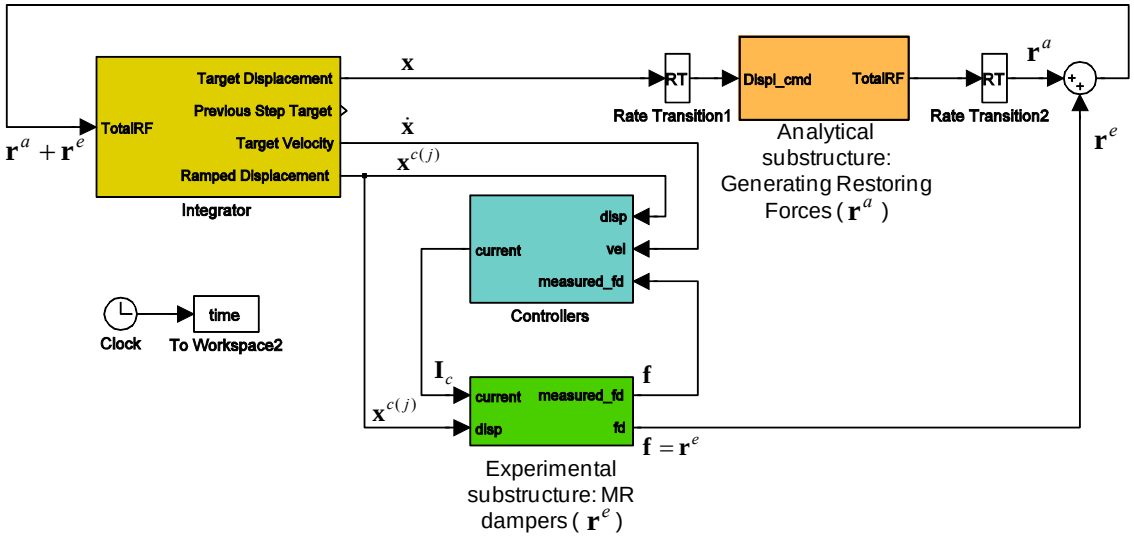

Figure 11.6 MATLAB Simulink blocks for HybridFEM

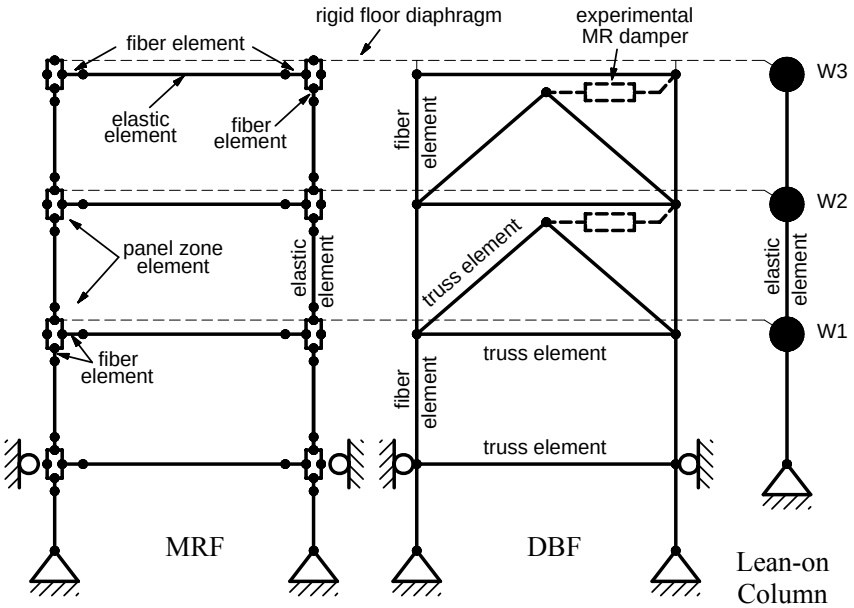

Figure 11.7 Analytical substructure model for the evaluation of structural control strategies (dampers of experimental substructure included for clarity)

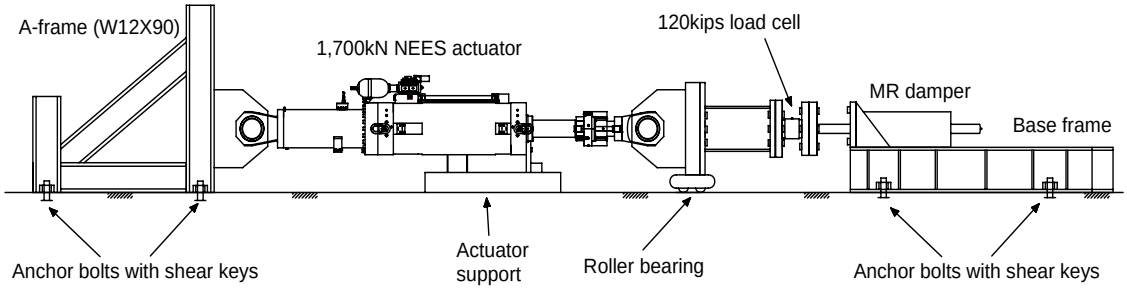

Figure 11.8 Schematic of test setup for each damper of the experimental substructure

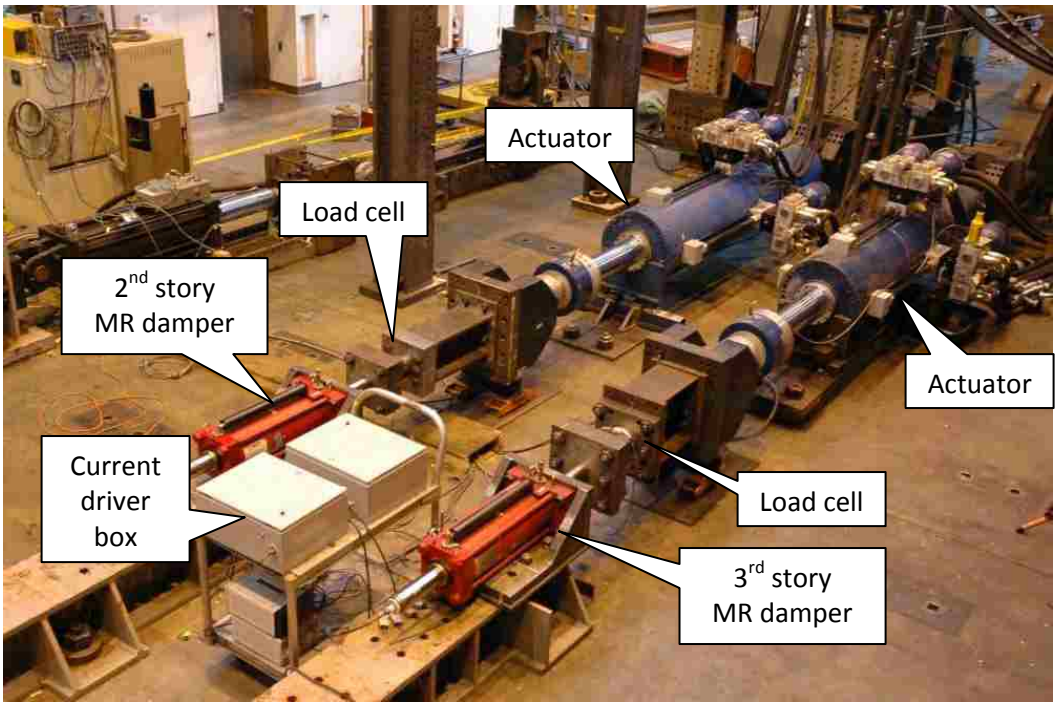

Figure 11.9 Experimental substructure with two MR dampers

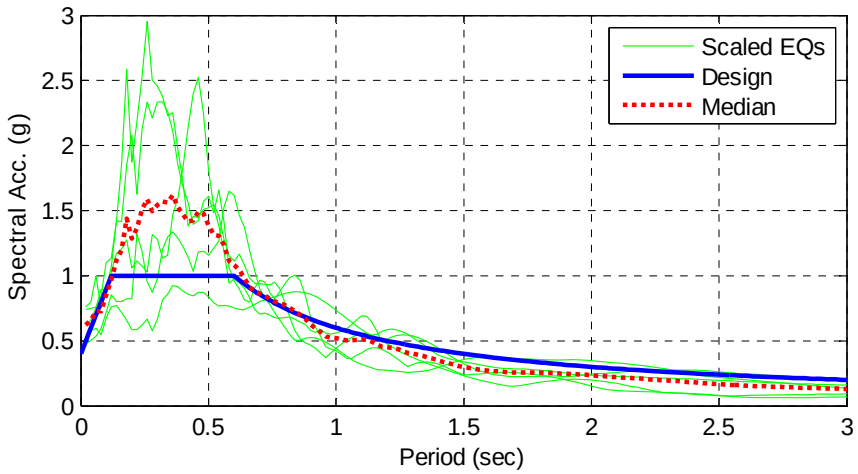

Figure 11.10 Response spectrum of ground motions scaled to DBE

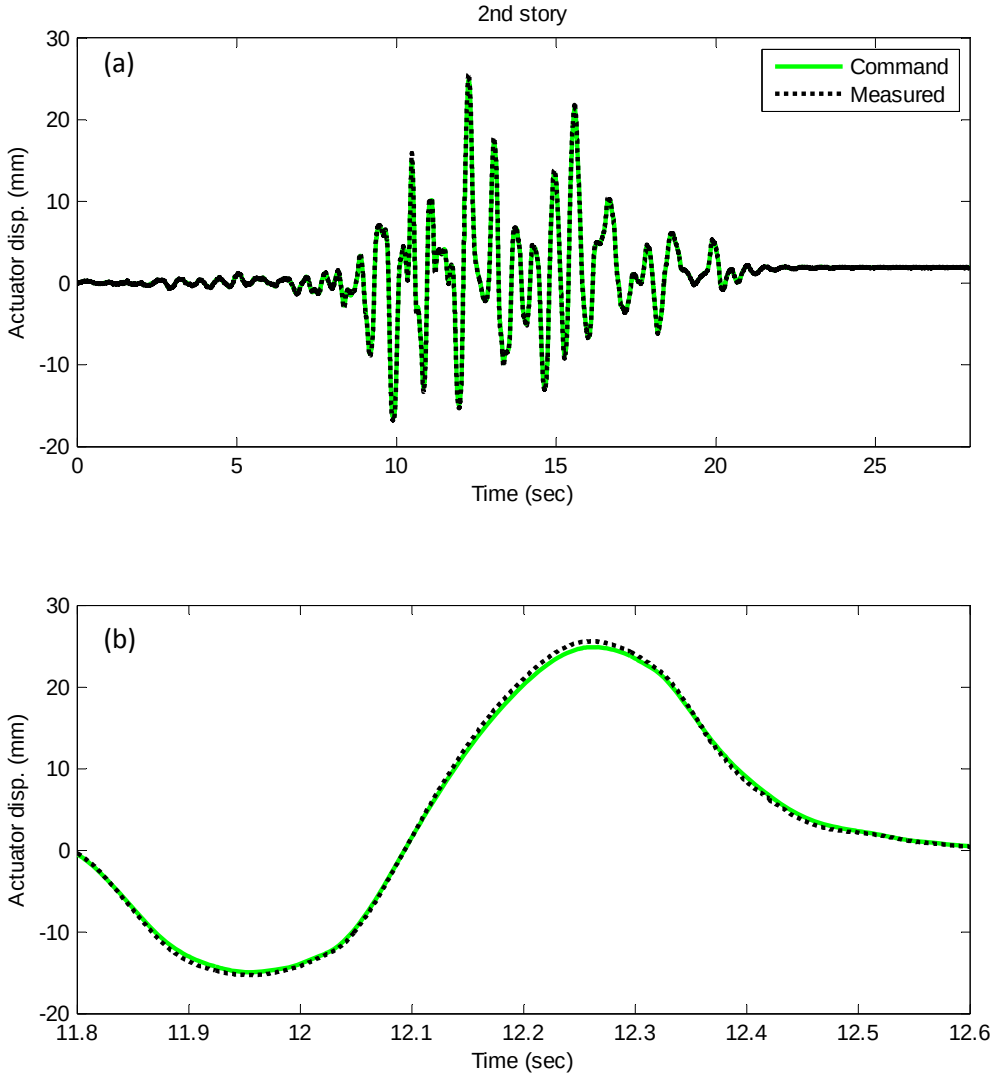

Figure 11.11 Comparison of command and measured actuator displacements for 2nd story MR damper where structure is subjected to Landers ground motion and damper is controlled by LQR controller: (a) overall comparison; (b) close-up near time of maximum displacement

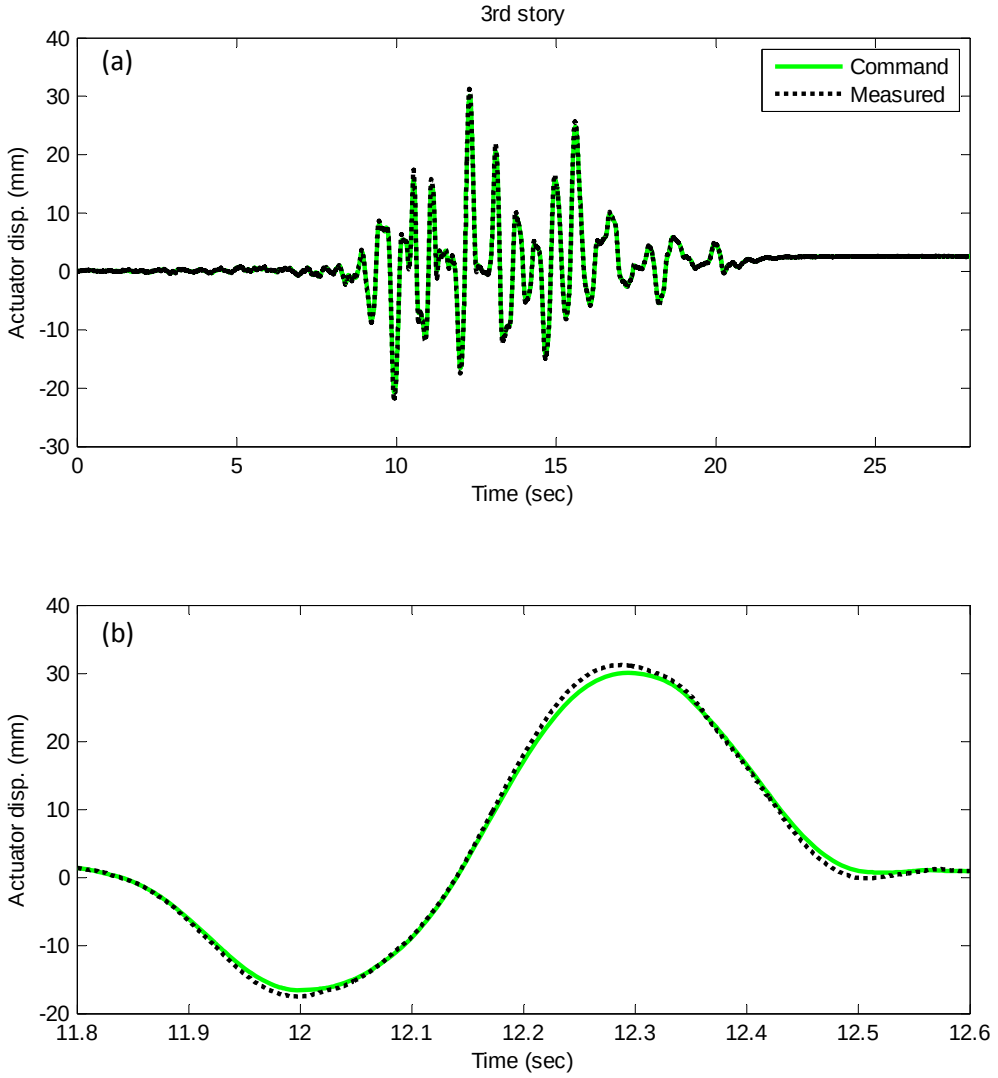

Figure 11.12 Comparison of command and measured actuator displacements for 3rd story MR damper where structure is subjected to Landers ground motion and damper is controlled by LQR controller: (a) overall comparison; (b) close-up near time of maximum displacement

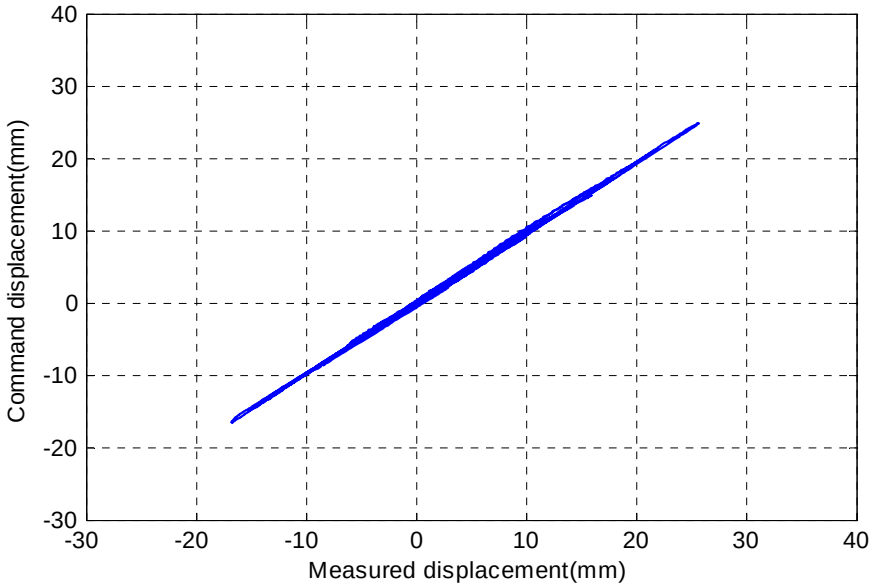

Figure 11.13 Synchronized subspace plot for 2nd story damper where structure is subjected to Landers ground motion and damper is controlled by LQR controller

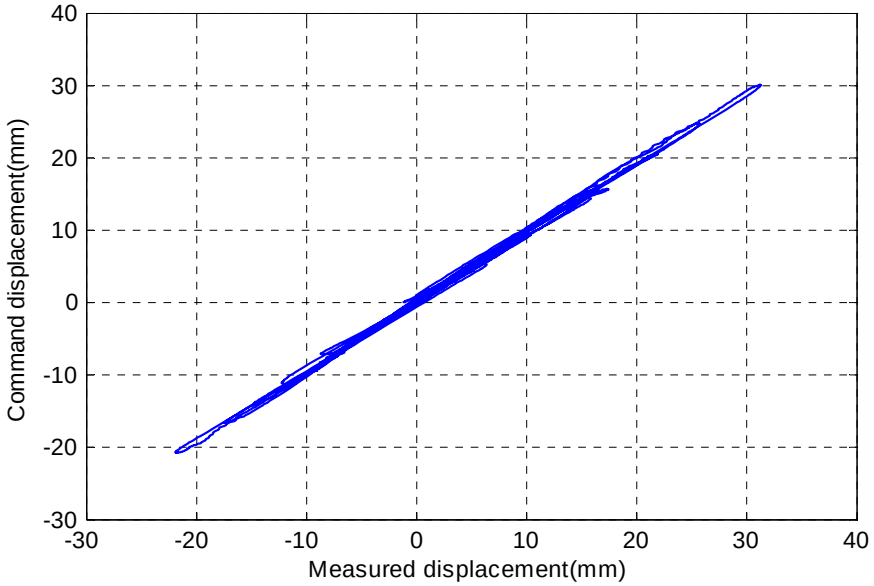

Figure 11.14 Synchronized subspace plot for 3rd story damper where structure is subjected to Landers ground motion and damper is controlled by LQR controller

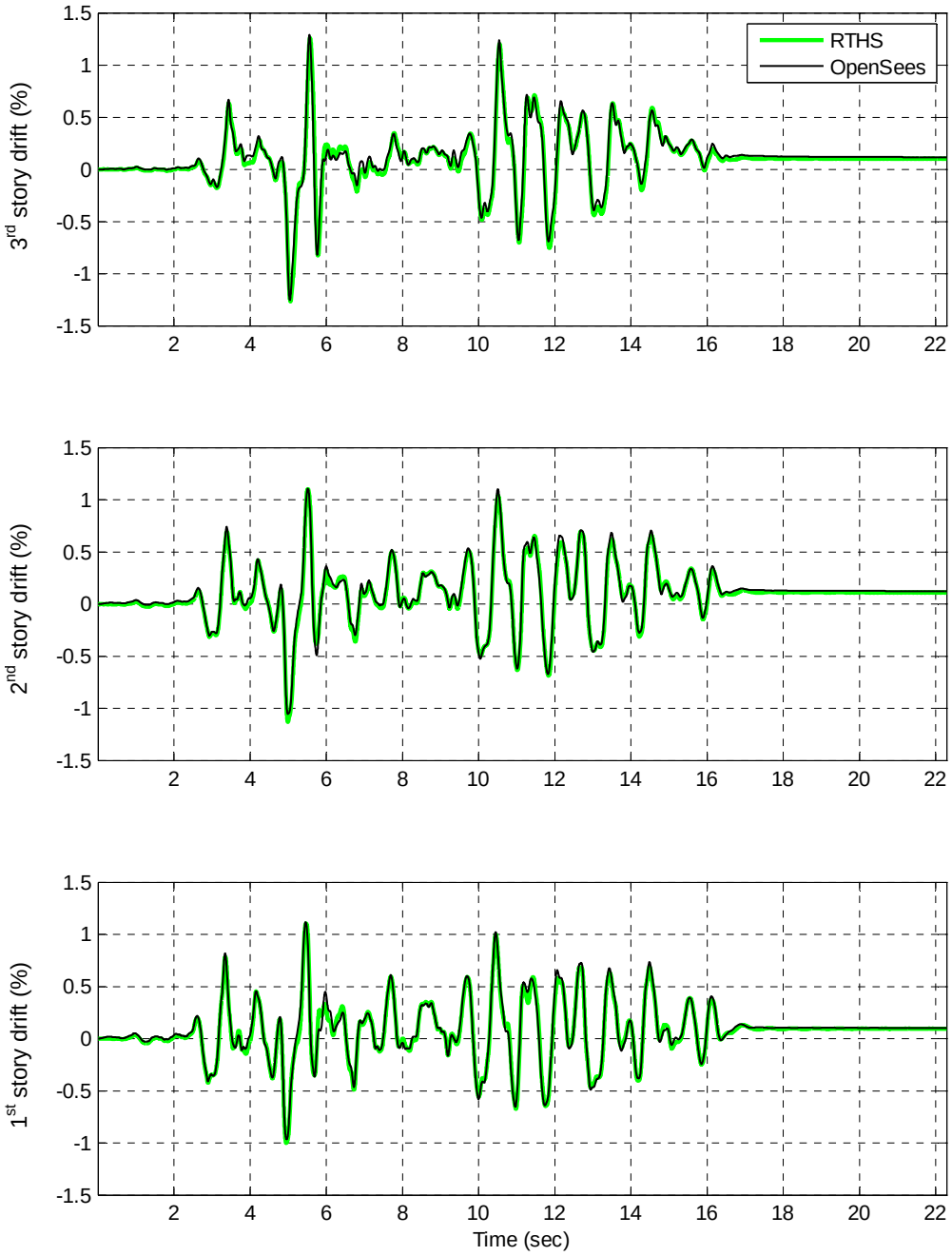

Figure 11.15 Comparison of story drifts between RTHS and OpenSees (Input EQ: Superstition Hill ground motion; Controller: passive)

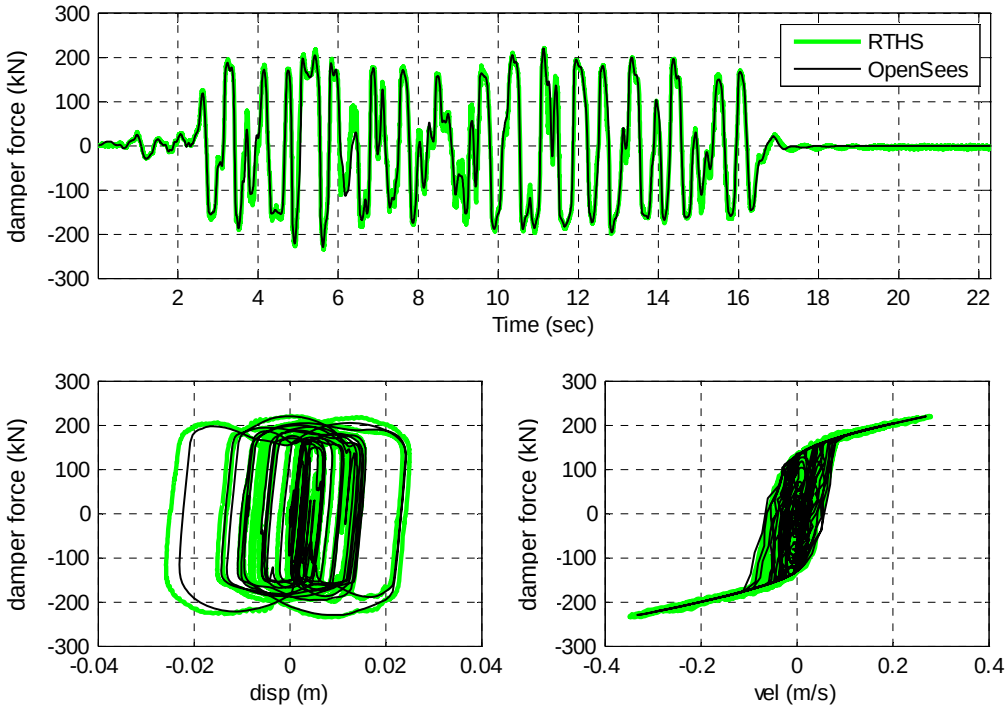

Figure 11.16 Comparison of the 2nd story MR damper response
(Input EQ: Superstition Hill ground motion; Controller: passive)

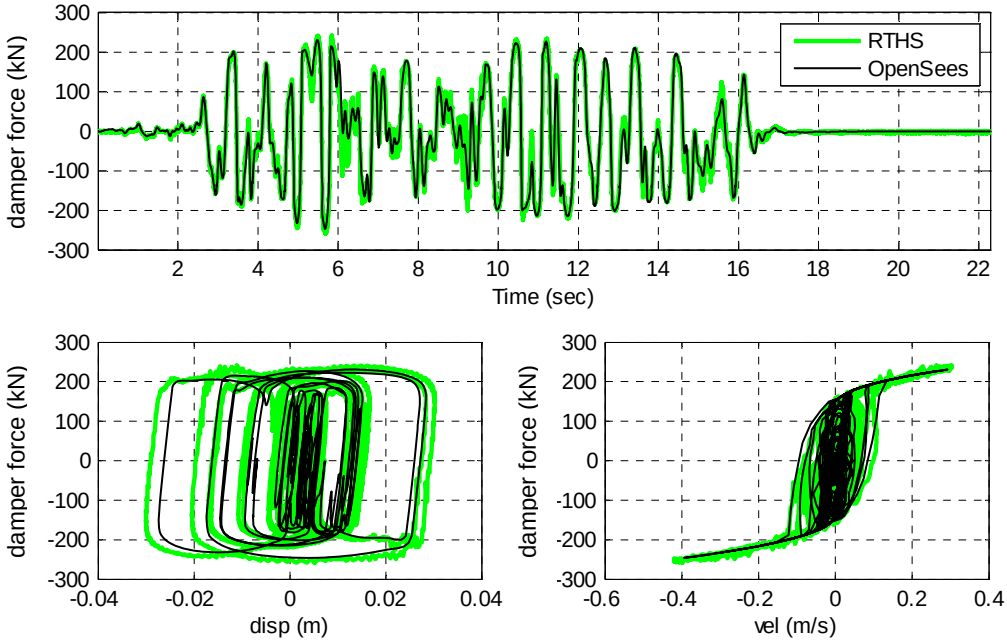

Figure 11.17 Comparison of the 3rd story MR damper response
(Input EQ: Superstition Hill ground motion; Controller: passive)

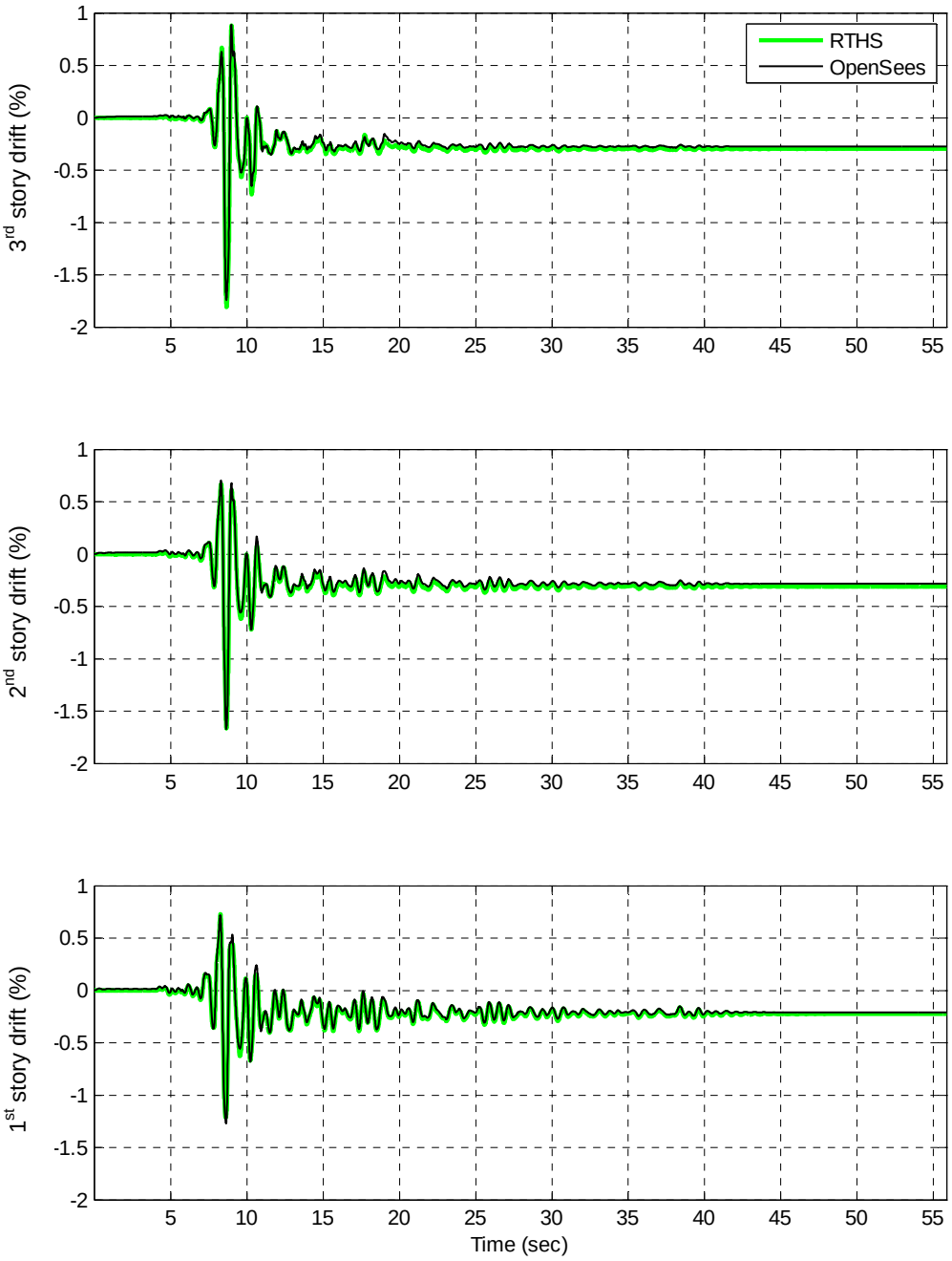

Figure 11.18 Comparison of story drifts between RTHS and OpenSees
(Input EQ: Duzce ground motion; Controller: LQR)

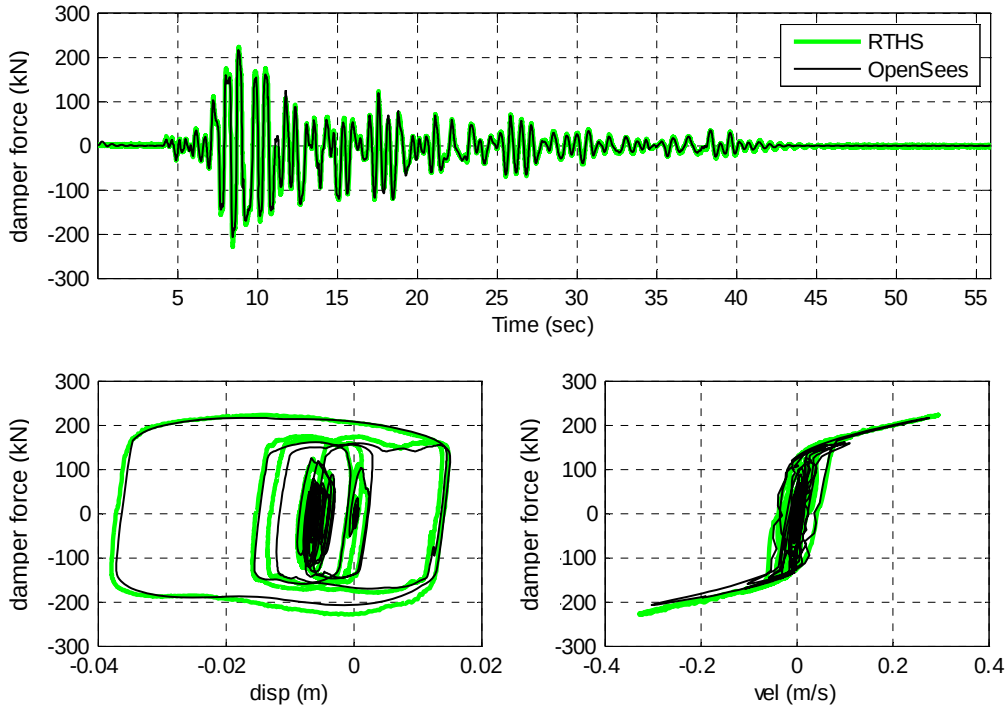

Figure 11.19 Comparison of the 2nd story MR damper response
(Input EQ: Duzce ground motion; Controller: LQR)

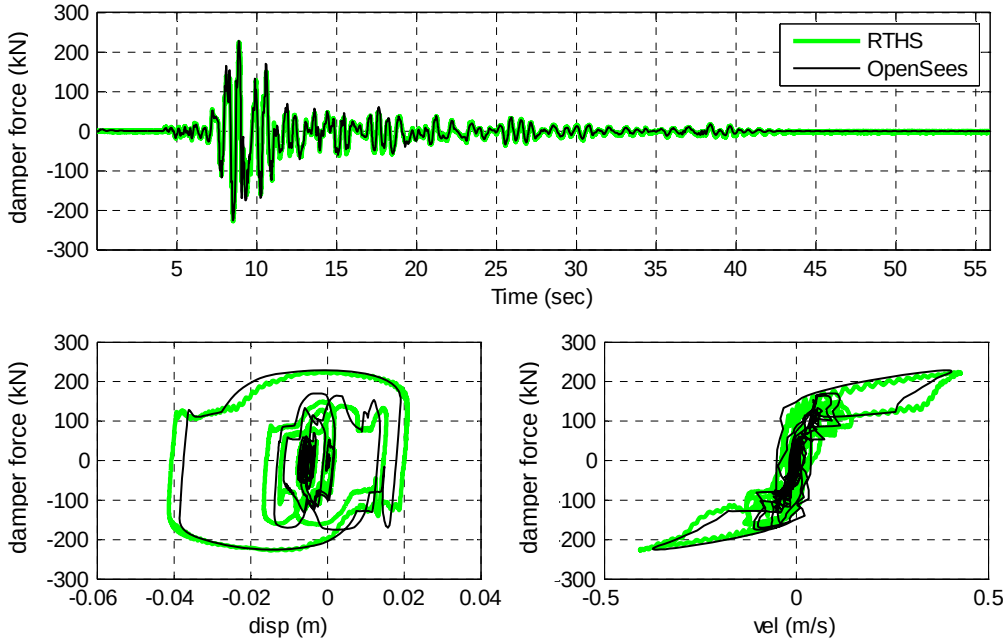

Figure 11.20 Comparison of the 3rd story MR damper response
(Input EQ: Duzce ground motion; Controller: LQR)

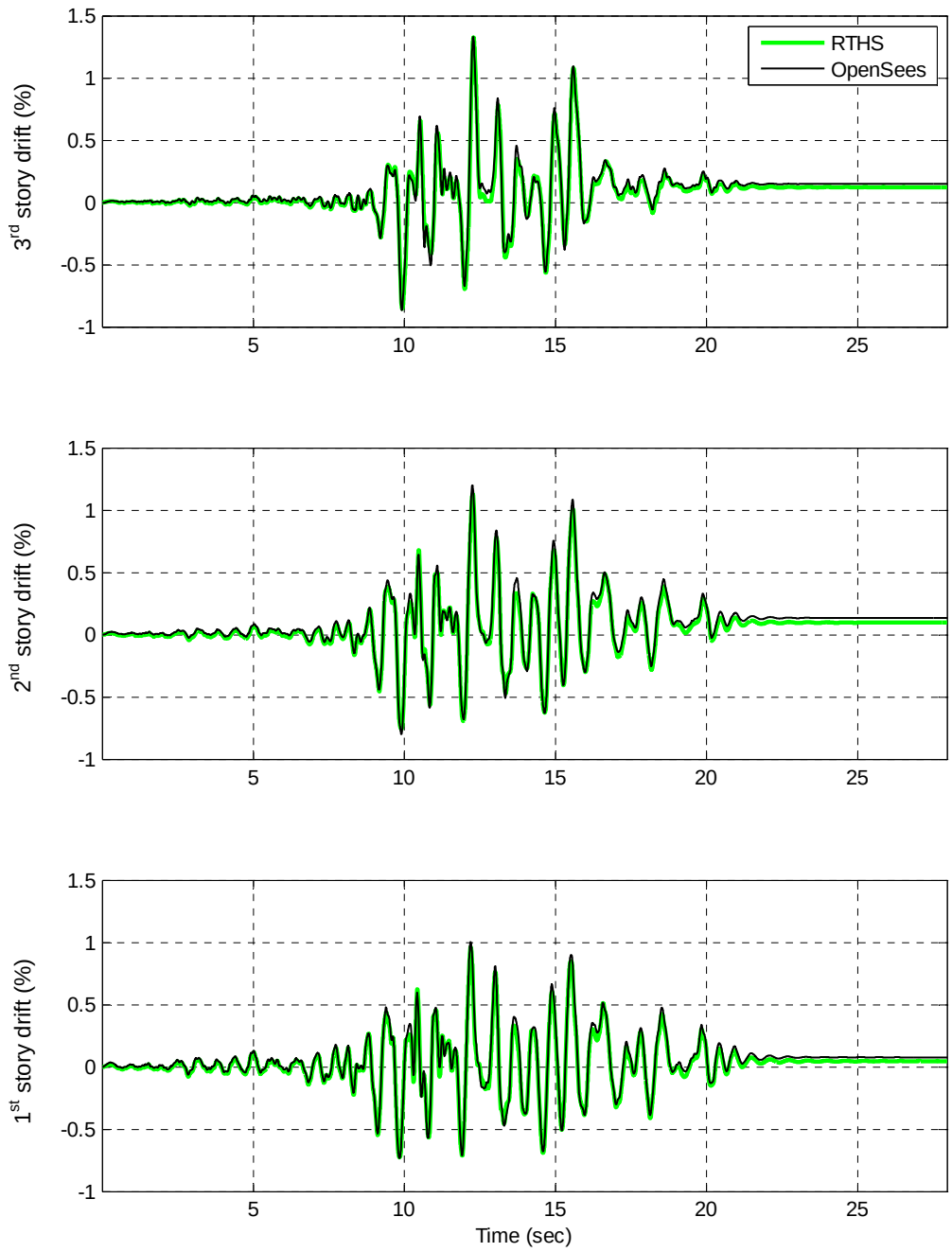

Figure 11.21 Comparison of story drifts between RTHS and OpenSees
(Input EQ: Landers ground motion; Controller: SMC)

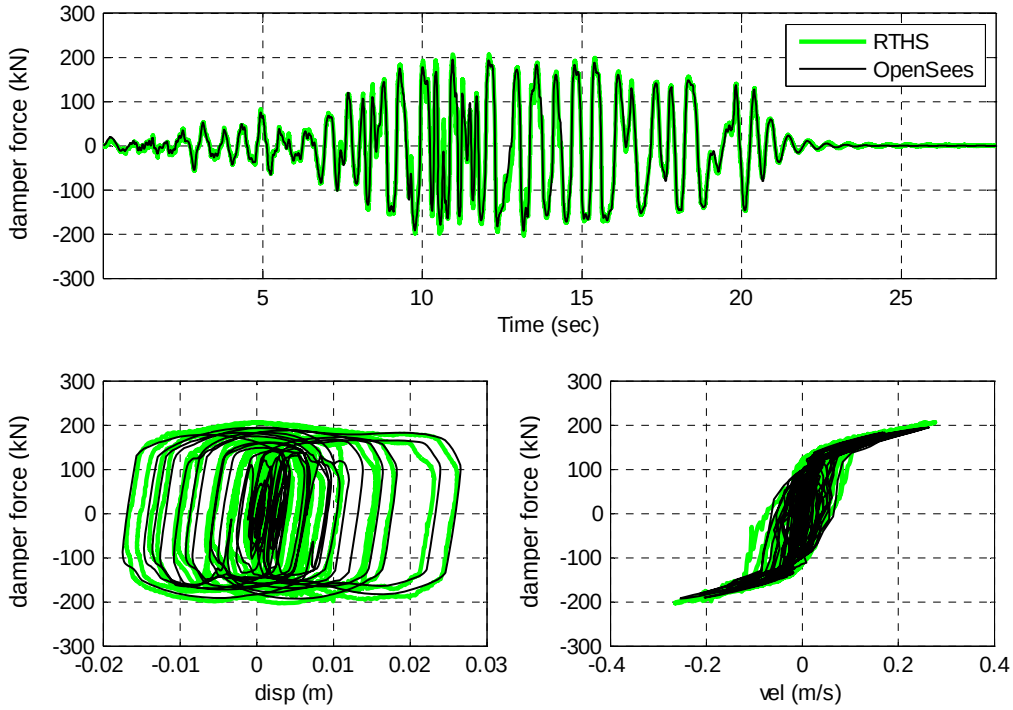

Figure 11.22 Comparison of the 2nd story MR damper response
(Input EQ: Landers ground motion; Controller: SMC)

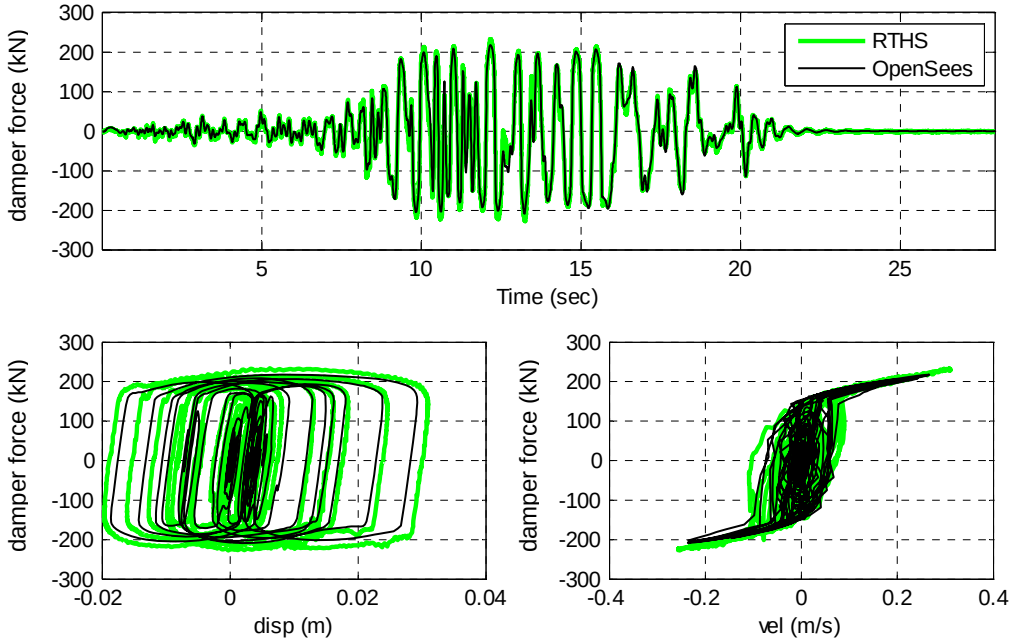

Figure 11.23 Comparison of the 3rd story MR damper response
(Input EQ: Landers ground motion; Controller: SMC)

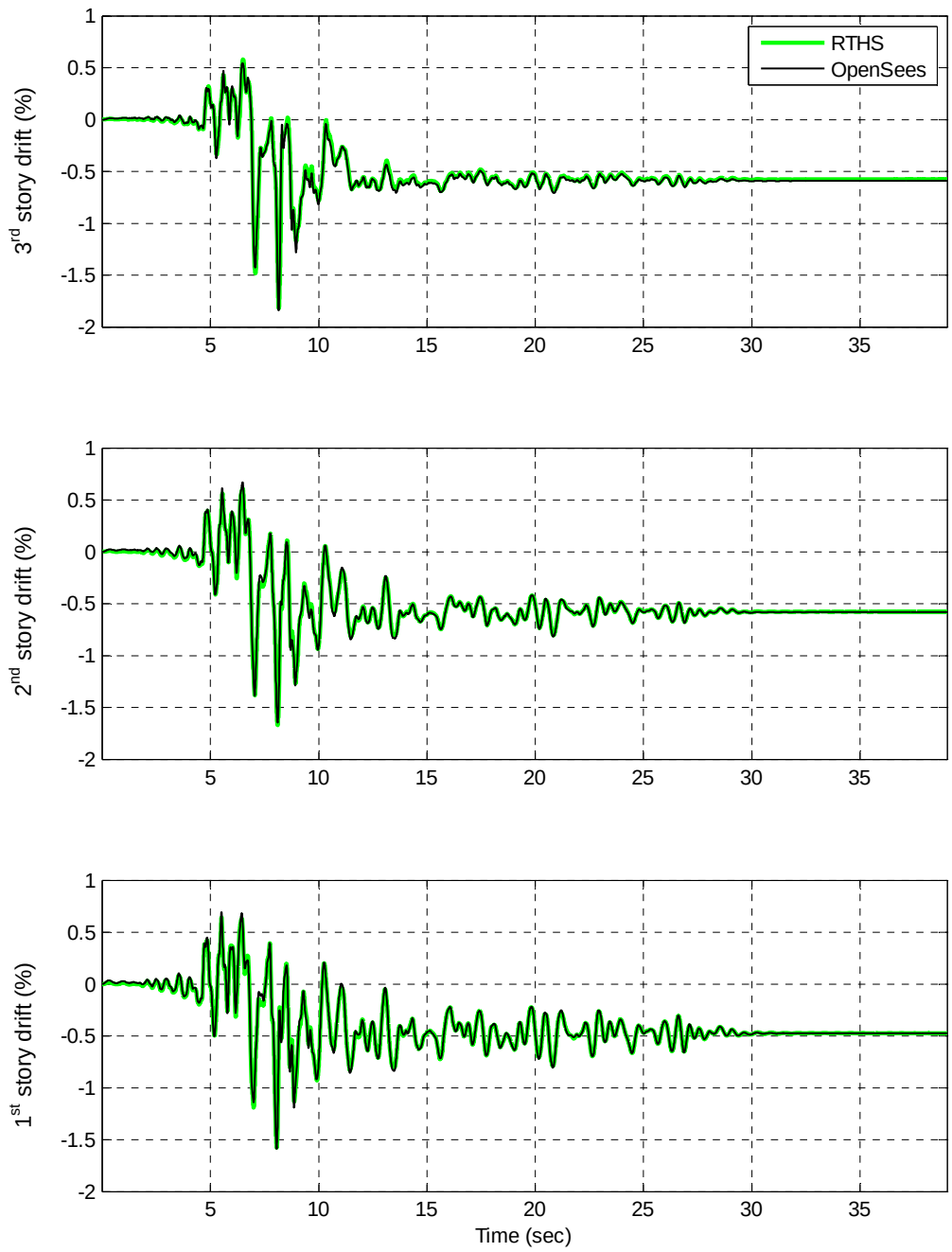

Figure 11.24 Comparison of story drifts between RTHS and OpenSees (Input EQ: Imperial Valley ground motion; Controller: DBB)

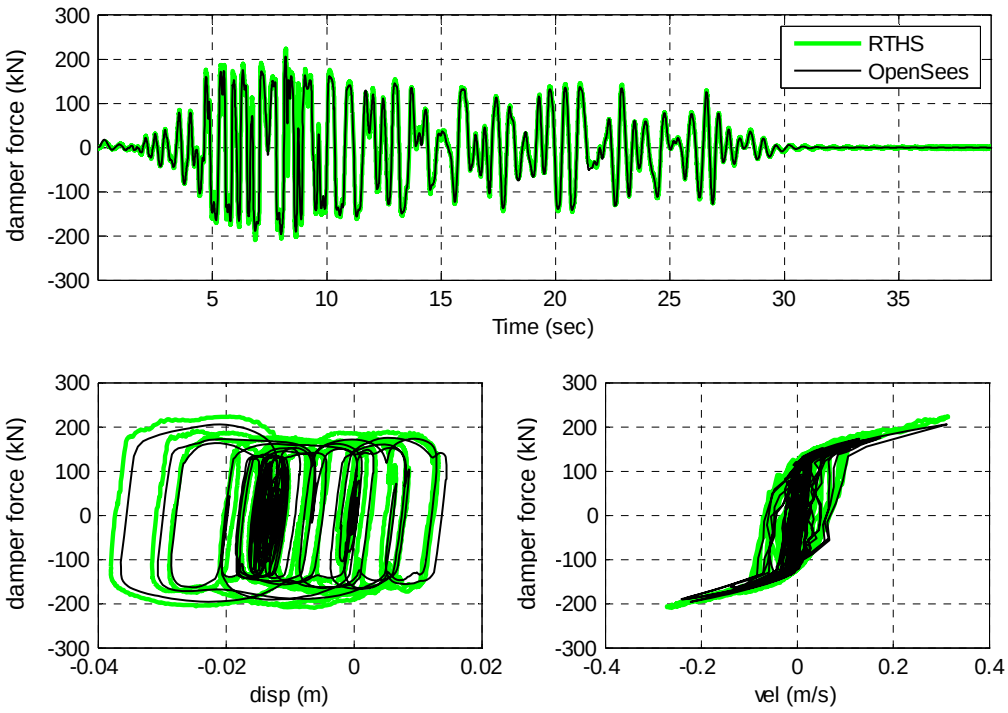

Figure 11.25 Comparison of the 2nd story MR damper response
(Input EQ: Imperial Valley ground motion; Controller: DBB)

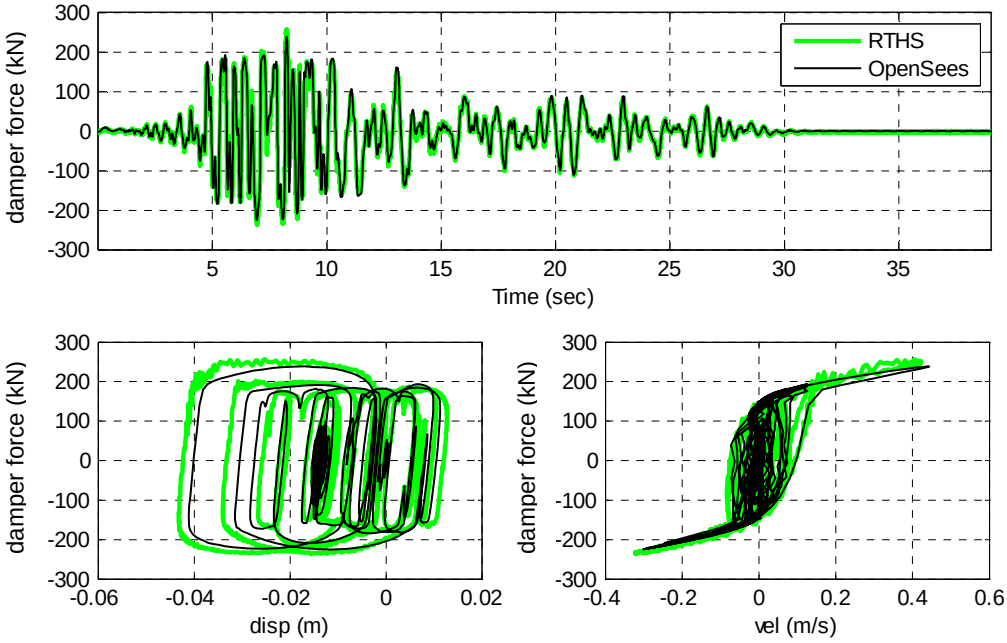

Figure 11.26 Comparison of the 3rd story MR damper response
(Input EQ: Imperial Valley ground motion; Controller: DBB)

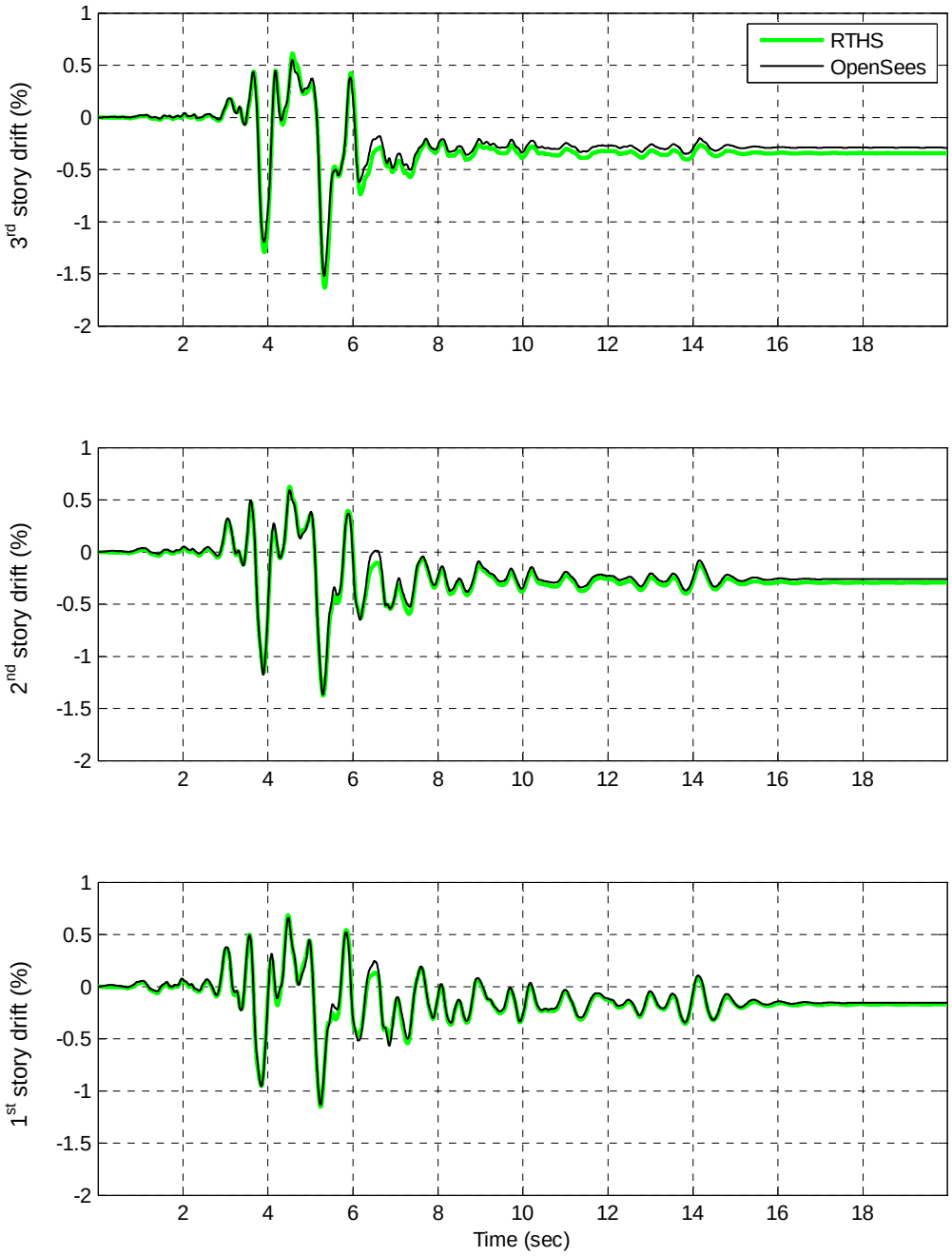

Figure 11.27 Comparison of story drifts between RTHS and OpenSees (Input EQ: Northridge ground motion; Controller: PAC)

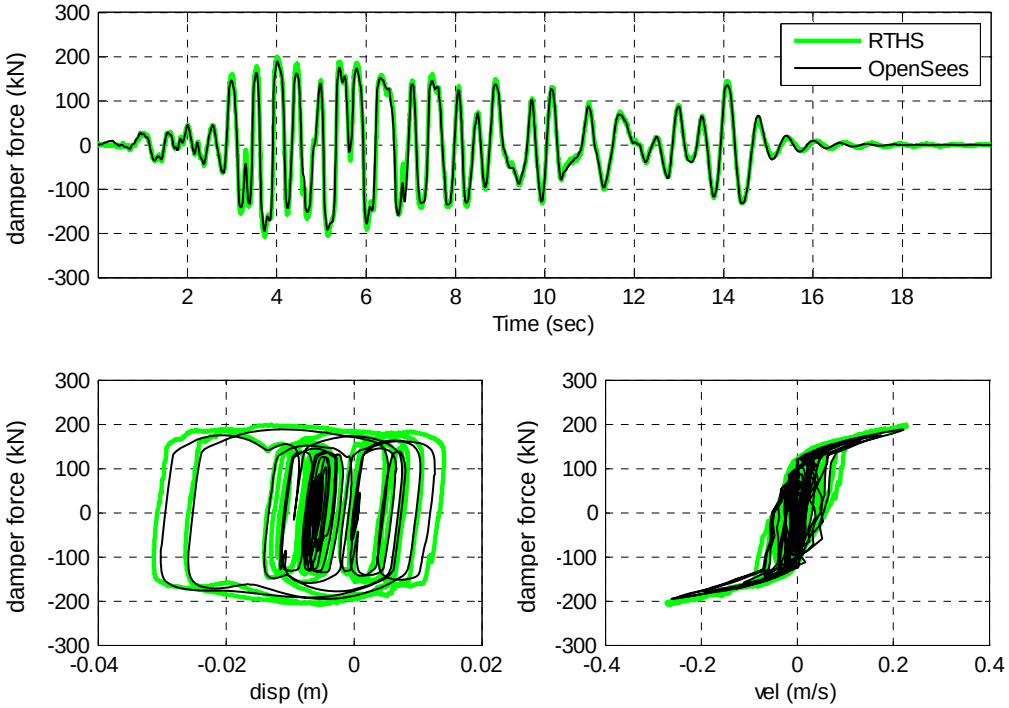

Figure 11.28 Comparison of the 2nd story MR damper response
(Input EQ: Northridge ground motion; Controller: PAC)

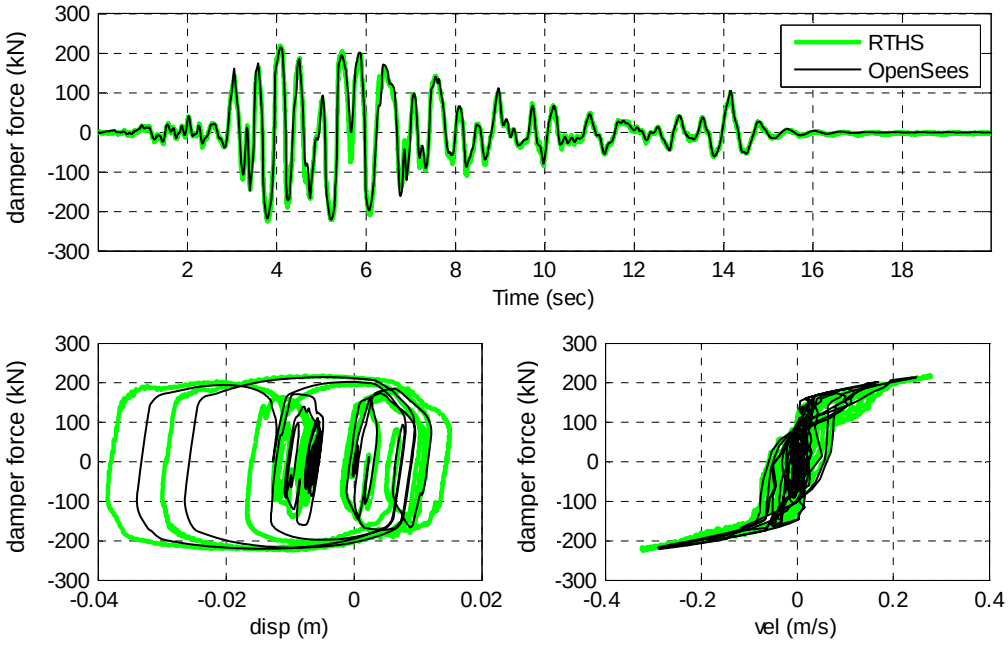

Figure 11.29 Comparison of the 3rd story MR damper response (Input EQ: Northridge ground motion; Controller: PAC)

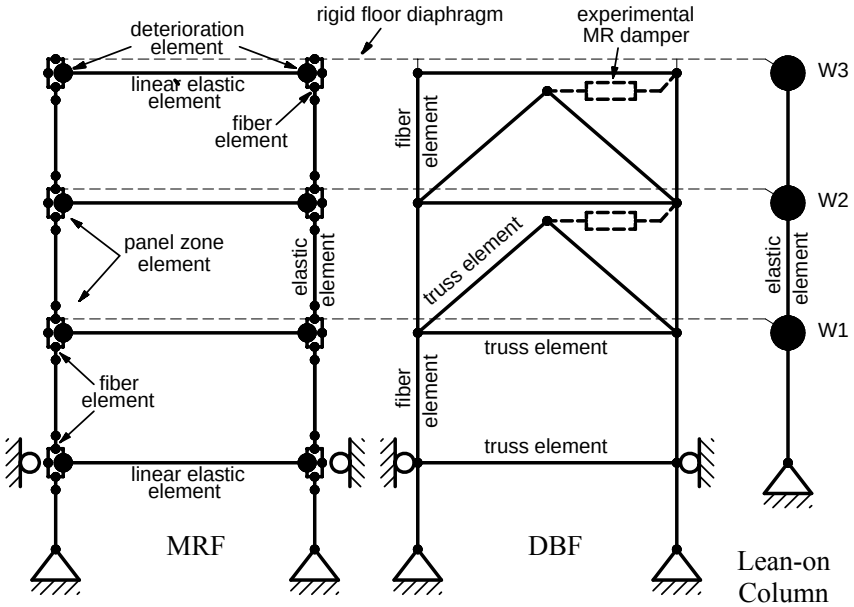

Figure 11.30 Modeling of the analytical substructure for real-time hybrid simulation with extreme ground motions (dampers of experimental substructure included for clarity)

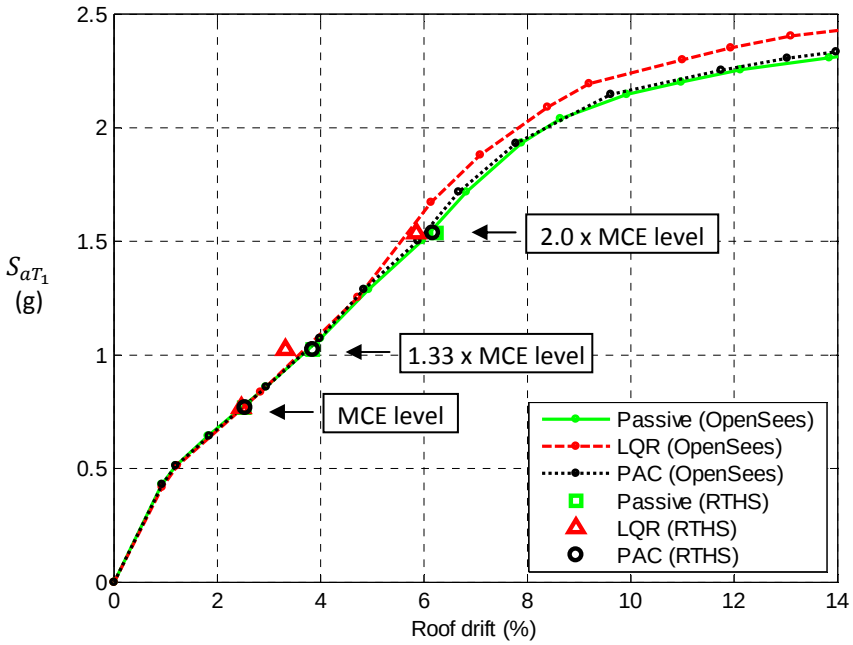

Figure 11.31 IDA curves from OpenSees and real-time hybrid simulations for the Northridge ground motion

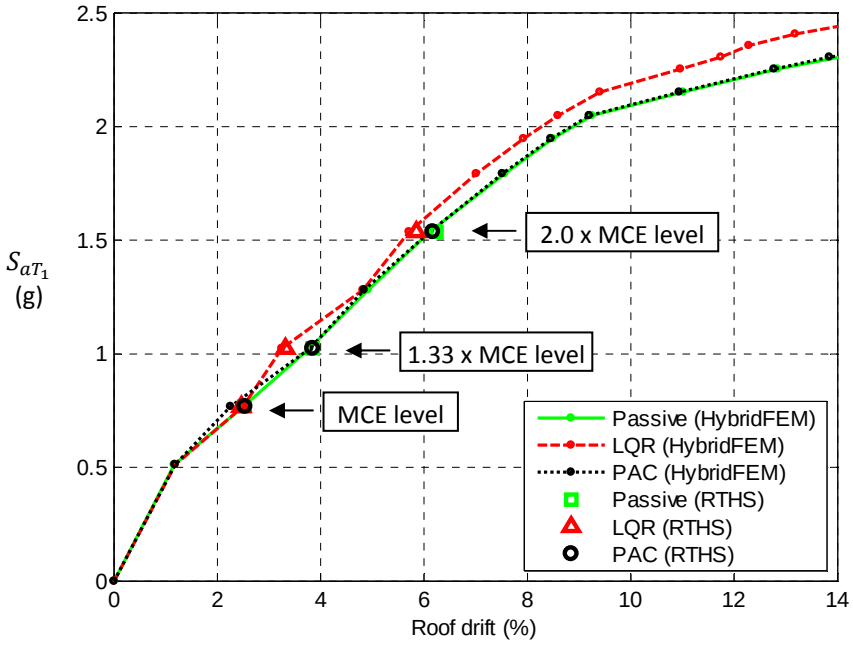

Figure 11.32 IDA curves from HybridFEM and real-time hybrid simulations for the Northridge ground motion

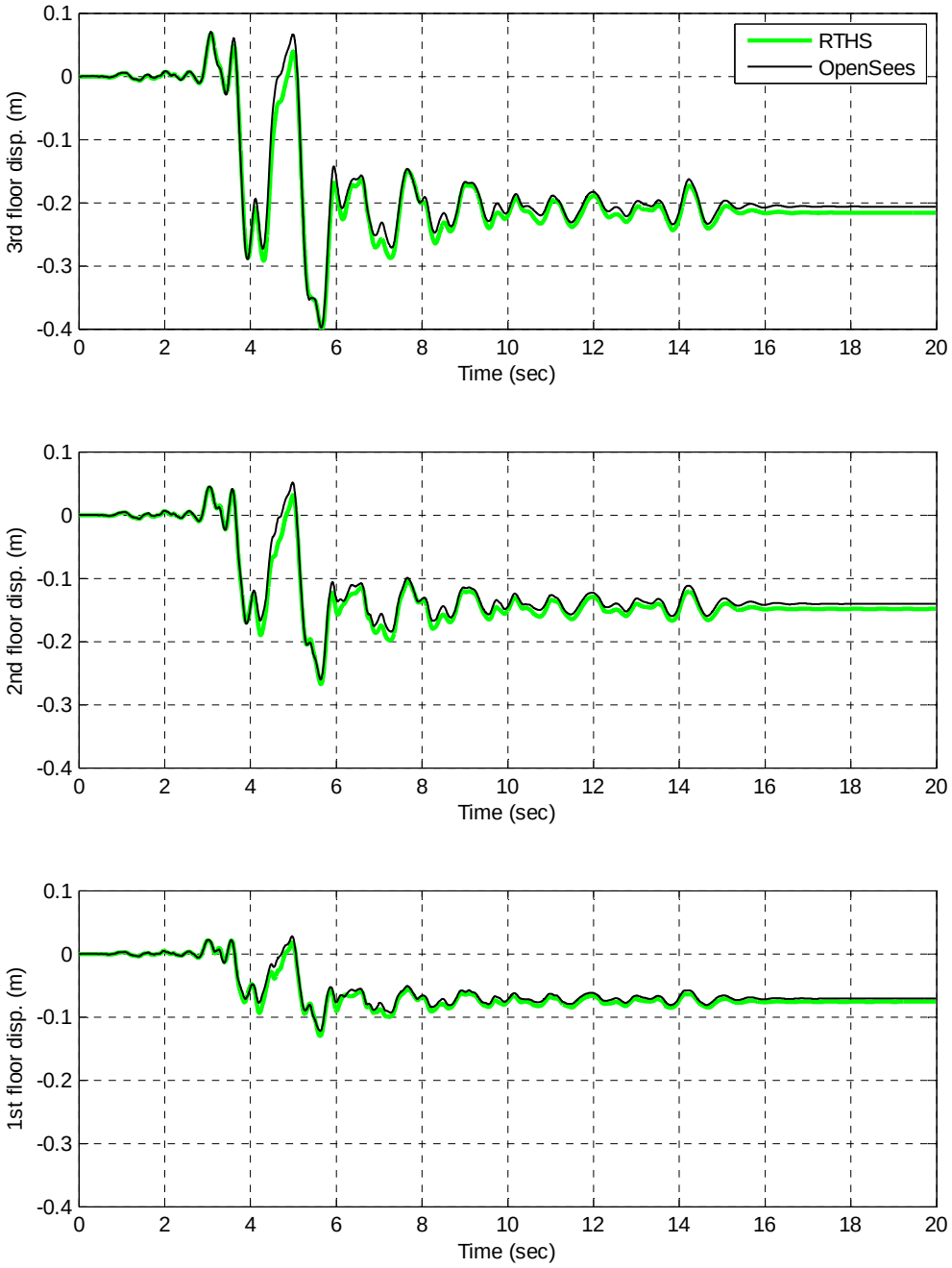

Figure 11.33 Floor displacements of the building with LQR controller subjected to the Northridge ground motion with two times the MCE level intensity (S_{aT_1}=1.54g)

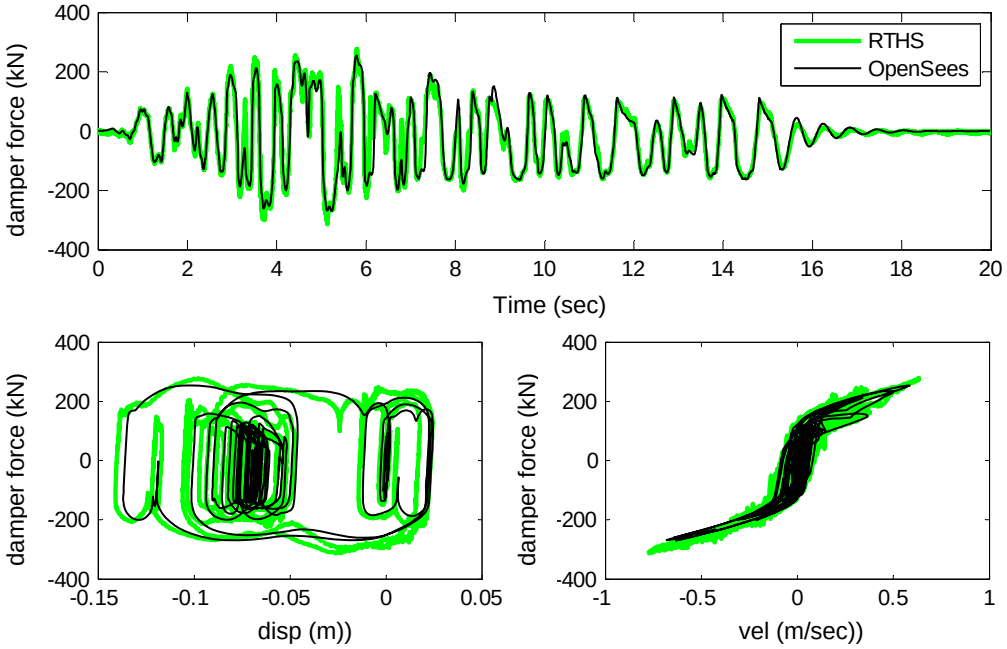

Figure 11.34 2nd story MR damper response of building structure with LQR controller subjected to the Northridge ground motion with two times the MCE level intensity (S_{aT_1}=1.54g)

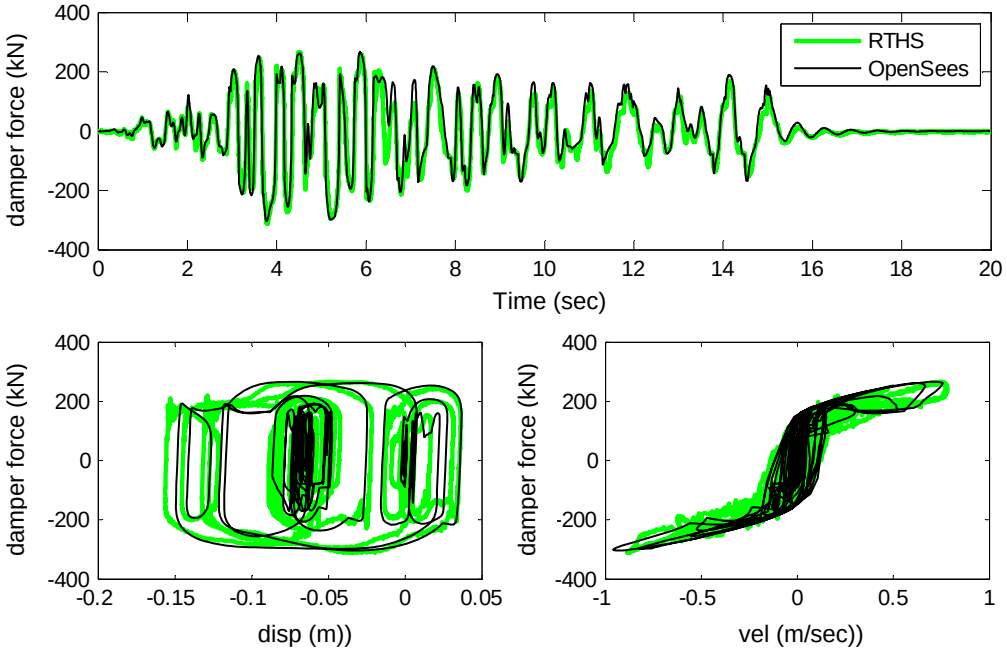

Figure 11.35 3rd story MR damper response of building structure with LQR controller subjected to the Northridge ground motion with two times the MCE level intensity (S_{aT_1}=1.54g)

Chapter 12

Summary, Conclusions, and Recommended Future Research

12.1 General

In this dissertation, the seismic hazard mitigation of buildings using magneto-rheological (MR) dampers was investigated. The study involved the identification and characterization of large-scale MR dampers, the development and assessment of a seismic performance-based design procedure, the performance evaluation of various MR damper structural control strategies under various seismic hazard levels, and the experimental validation of the performance based design procedure and numerical results by performing real-time hybrid simulations of a structure with MR dampers. The following is a more detailed summary of the research performed in this dissertation.

12.2 Summary

In Chapter 2, a review of the existing MR damper models and semi-active controllers were conducted. Existing MR damper models based on mechanical components and intelligent systems, respectively, were summarized and their performance is discussed. The mathematical details for some commonly used semi-active controllers for MR dampers were introduced. These controllers include: i) linear quadratic regulator (LQR); ii) sliding mode control (SMC); and iii) decentralized bang-bang (DBB) control.

Although various MR damper models have been developed, these models are based mostly on experimental data from tests performed on small-scale MR dampers. Only a few tests performed using large-scale MR dampers have been reported. The Bouc-Wen model and the hyperbolic tangent model have been employed by prior researchers to describe the behavior of large-scale MR dampers, and have been shown to predict reasonably well the nonlinear behavior of MR dampers. However, due to the complexity of these models that includes the nonlinear components of the model, the estimation of model parameters for these damper models is not easy. Moreover, it is difficult for these models to account for the non-Newtonian fluid behavior (i.e., shear thinning or thickening behavior) when a high velocity is imposed on the damper which can be prominent during a strong earthquake. To overcome these problems, a new MR damper model, called the Maxwell Nonlinear Slider (MNS) model, was developed and experimentally validated for passive (constant current input) and semi-active (variable current) applications in Chapter 3 and 4, respectively.

In Chapter 3, characterization tests conducted on a large-scale MR damper and the formulation for the MNS damper model are presented, separating the pre-yield and post-yield behavior that occurs in the MR damper. A procedure for identifying the model parameters was presented using the particle swarm optimization (PSO) algorithm. An appropriate initial guess for the model parameters was easily made since the MNS model independently describes the pre- and post-yield modes of the damper. The MNS model parameters were identified for current levels from 0.0A to 2.5A with a 0.5A incremental step. The damper forces from the MNS model were compared to the

experimental damper forces from the characterization tests involving random displacement input and a pre-defined earthquake response input with a constant current input for the MR damper, i.e., in passive mode.

In Chapter 4 the current driver used to provide variable current to the large-scale MR dampers was characterized by applying band limited Gaussian white noise command current to the driver. A second order transfer function correlating the command current with the output current from the current driver was provided. In order to account for the delayed response of the MR damper to a change in current, the eddy current effect was considered as well as the magnetization behavior of damper materials. The eddy current opposing the formation of a magnetic flux around the orifice of the damper causes the slow response of the MR damper to a change of current. An equation for a first order filter was derived based on electromagnetism theory, and a nonlinear equation correlating the current in the damper coil with an equivalent static current was proposed to accurately predict the damper behavior under variable current. The predicted damper behavior using the nonlinear equation was compared to the measured damper response during real-time hybrid simulations performed on a 3-story building structure.

In order to enable the use of MR dampers for the seismic hazard mitigation of structures, a methodology to predict the behavior of MR dampers and to evaluate their contribution to reduce the structural response to seismic load needs to be incorporated into a design procedure. In this dissertation, a performance-based design procedure is proposed for structures with MR dampers based on a quasi-static MR damper model.

This procedure is called the simplified design procedure (SDP) because it uses only iterative linear elastic-static analyses. A systematic analysis procedure was developed in Chapter 5 to calculate the response of an SDOF structure with diagonal bracing and an MR damper without performing a nonlinear time history analysis. The prediction was based on the Hershel-Bulkley quasi-static MR damper model. The loss factor and equivalent stiffness of the MR damper were calculated from the hysteretic response of the quasi-static MR damper model. The equivalent damping ratio of the structural system was shown to be dependent on the displacement amplitude. Examples of response prediction by the procedure were presented and compared to the results of nonlinear time history analysis using OpenSees with the MNS model.

Based on the work in Chapter 5, a simplified design procedure (SDP) for the performance-based design of structures with MR dampers was developed in Chapter 6. The SDP can be characterized into two major parts: i) estimation of the required MR damper capacity using a simple frictional model for the damper; ii) revision of design of the structure using a more sophisticated MR damper model. The simple frictional MR damper model can approximately provide a required force capacity of MR dampers, and designers can select MR dampers based on this information. Once the MR damper properties are determined, the Hershel-Bulkley quasi-static MR damper model enables a more accurate estimation of the response. A design example of a 3-story building structure utilizing the SDP with three different performance objectives was demonstrated. The moment resisting frame (MRF) of the building structure was designed to satisfy the current building code strength requirements. The drift

requirement was satisfied by adding a damped braced frame (DBF) with MR dampers. The performance objectives included limiting the maximum story drift of the structure to 1.5% and having the DBF remain elastic under the design basis earthquake (DBE), while under the maximum considered earthquake (MCE) the maximum story drift is limited to 3.0%. In Chapter 7 the SDP was validated by comparing the estimated response using the SDP with the statistical results of nonlinear time history analyses. An ensemble of 44 ground motions was used to generate the response statistics under the DBE and MCE in order to assess whether the performance objectives were met.

A newly developed semi-active controller, called the *Phase Angle Controller* (PAC), is introduced in Chapter 8. The PAC does not require any user defined control parameters. It is based on the concept of having the damper reduce the response of the structure by having the current set to a maximum current if an impulse response of the damper is out of phase with the free vibration response of the structure based on current displacement and velocity.

An evaluation of the performance of the four different semi-active controllers was performed in Chapter 9, including: i) LQR; ii) SMC; iii) DBB; and, iv) PAC. Nonlinear time history analyses were conducted with 44 ground motions scaled to the DBE and MCE levels, respectively, and statistical responses of the structure for each semi-active control case were compared to the passive control case (where the current is constant) and the case of the structure without dampers. The structure designed by the SDP presented in Chapter 6 was used for these numerical simulations. Issues of uncertainty related to incorrect structural properties and noise corruption of feedback

data are also studied in Chapter 9, as well as the effect of the response time of the MR damper force under variable current input.

In Chapter 10, incremental dynamic analyses (IDA) using OpenSees are used to assess the collapse potential of the 3-story building structure with MR dampers designed as presented in Chapter 6 and studied in Chapter 9 under the DBE and MCE. The statistical response from the IDA was used to determine the collapse margin ratios (CMRs) of the building structure. A brief review of a flexural strength and stiffness deterioration structural element based on the modified Ibarra-Krawinkler model was presented. Flexural strength and stiffness deterioration in plastic hinge is considered along with the P-Δ effect as the major factors leading to the dynamic instability of a structure during an earthquake. The four semi-active controllers for MR dampers, the passive control case, and the case of no dampers were used in the numerical simulations. The collapse resistance of the structure with these various control strategies was compared using the CMRs and the collapse fragility curves.

Chapter 11 describes real-time hybrid simulations that were performed to investigate the behavior of a structure with MR dampers under more realistic seismic demand. The various control strategies were systematically investigated, including the passive control and the four semi-active controllers. Two sets of real-time hybrid simulations were conducted. The first set was used to assess the various control strategies studied in Chapter 9 under the DBE and to assess the results from the SDP studied in Chapter 6. Five earthquake ground motions were selected and used in the real-time hybrid simulations. Statistical responses were obtained and the results of the

real-time hybrid simulations were compared to those of numerical simulations. The second set of real-time hybrid simulations was used to investigate the structural response under extreme ground motions that have a larger intensity level than the MCE, and which can lead to collapse of the structure. The second set of hybrid simulations used one ground motion with the intensity increased in each successive simulation in the set. The results were compared to IDA curves that were obtained numerically in Chapter 10. The hybrid simulation results for the structure and dampers were compared to the numerical simulation results from OpenSees to assess the MNS model as well as the real-time hybrid simulation concept over a range of earthquake intensities.

12.3 Conclusions

Based on the observations and findings in this dissertation, the following conclusions are drawn.

12.3.1 Characterization of MR Dampers

- Non-Newtonian fluid behavior, i.e., the shear thinning or shear thickening behavior of MR fluids, was observed in the characterizations tests, as well as the real-time hybrid simulations involving the large-scale MR dampers used in this study. When the input current into the MR damper is 2.5A, the damper shows shear thinning behavior, while it shows shear thickening behavior for 0.0A current input.
- It is difficult for the Bouc-Wen and the hyperbolic tangent models to account for the non-Newtonian fluid property, since the post-yield behavior of these models are

predominantly described by a linear dashpot. The MNS model based on the Hershel-Bulkley visco-plasticity element accurately captures the non-Newtonian MR fluid behavior..

- The damper force predicted by the MNS model shows exceptional agreement with the experimentally obtained damper force from tests involving constant and variable currents. These tests include the real-time hybrid simulations and tests with a predefined displacement input into the damper. The MNS model is shown to have a better prediction of actual MR damper behavior than the Bouc-Wen and hyperbolic tangent MR damper models.
- The MNS model shows good response prediction for the cases where high velocity demands are imposed on the damper under extreme ground motions. The predicted damper forces and story drifts from numerical simulations matched well with the experimental damper forces obtained from real-time hybrid simulations, demonstrating the robustness of the MNS model.
- The current driver manufactured by the Advanced Motion Controls exhibits a nonlinear response to the command current. The amplitude frequency response of the current driver varied according to the amplitude of the input command current, while the phase angle response was found not to be sensitive to the variation of input command current.

12.3.2 Simplified Design of Structures with MR Dampers

- The equivalent stiffness and loss factor of the MR damper were derived from a damper hysteretic loop based on the Hershel-Bulkley visco-plasticity model. A simplified linear analysis procedure for estimating the response of an SDOF system with an MR damper was developed based on this linearized model for dampers. Good agreement between the results of nonlinear time history analyses and the maximum response from the equivalent SDOF was observed.
- Using the 3-story building structure designed by the simplified design procedure (SDP), the procedure was validated by comparing the response of the structure from the SDP with the results of nonlinear time history analyses. The story drifts and maximum MR damper forces from the SDP showed good agreement with the median nonlinear time history analysis results. The response obtained from the nonlinear time history analyses showed that the performance objectives for the design of the building were met, confirming the accuracy of the SDP.
- Two different methods were provided in the SDP for conducting the linear elastic-static analysis; the equivalent lateral force (ELF) method and the response spectrum analysis (RSA) method. The responses calculated using the ELF are more conservative than those using the RSA for the 3-story building structure due to the fact that the total mass of the structure (instead of the first modal mass) is considered in calculating the base shear for the ELF.

12.3.3 Assessment of MR Damper Semi-Active Controllers

- The statistical responses from the nonlinear time history analyses of the 3-story structure with 44 ground motions scaled to the DBE and MCE levels indicate that that the performance of the structure with the dampers in passive control is statistically similar to the that of the structure with semi-active controlled dampers. No significant differences in the structural response between the cases involving passive control and semi-active controllers were observed.
- The stiffness matrix of the structure used in the design of the semi-active controllers was perturbed from -20% to 20 %, and the influence on the performance of semi-active controllers under DBE and MCE levels of ground motion was investigated. It was found that the effect of a perturbed stiffness on the performance of the semi-active controllers in controlling the structural response was not significant.
- The study to investigate the effect of noise corruption in the feedback data, band limited Gaussian white noise was added to the feedback signal, where the amplitude of noise was calculated based on a selected signal-to-noise ratio (SNR). The effect of noise on the performance of semi-active controllers under DBE and MCE levels of ground motion was found from numerical simulations not to be significant. Even when the SNR was low (i.e., the noise level was high), no significant change in the performance of the semi-active controllers was observed.
- The effect of the response time of the MR damper force on the performance of the semi-active controllers was numerically evaluated by adjusting the MNS model parameters related to the response time of the MR damper force. Some structural responses appeared to be affected by the response time when the SMC was used.

However, the overall performance of the semi-active controllers was not significantly affected by the response time, and in some cases improved performance was observed with a slower response time.

12.3.4 Collapse Potential of Structures with MR Dampers

- Except for the LQR controller, the performance of semi-active controllers was found to be similar to the passive control case with regards to the collapse resistance of the structure with MR dampers. In the case of the LQR controller, the MR damper forces were effectively controlled so that the collapse margin ratio (CMR) was improved compared to the passive control case. Although the improvement may not be significant (a 6.6% increase in the CMR compared to the passive control case), this result is clearly different than the results under the less intense DBE and MCE level ground motions where all of the semi-active controllers have similar performance to the passive control case.

12.3.5 Real-Time Hybrid Simulation of Structures with MR Dampers

- The results of real-time hybrid simulations show good agreement with the responses from the SDP, demonstrating again the accuracy of the SDP.
- Results obtained from the real-time hybrid simulations involving the use of 5 ground motions and various damper control strategies (both passive and semi-active) show good agreement with the structural response and damper forces obtained from the numerical simulations.

- The maximum ground motion intensity that was applied during the real-time hybrid simulations was 2.0 times the MCE level. The experimental results from the real-time hybrid simulations show good agreement with the numerically obtained incremental dynamic analysis (IDA) curves.
- The excellent agreement between the real-time hybrid simulations and the numerical simulations validate the method used for the real-time hybrid simulations, and demonstrate the accuracy of the MNS model under a range of ground motion intensities, ranging from the DBE to intensities larger than the MCE that lead to incipient collapse of the structure. In these real-time hybrid simulations, the performance of passive control was also found to similar to that of the semi-active controllers.

12. 4 Recommended Future Research

The MNS model of this dissertation does not consider the effect of temperature. A rise in the temperature of the dampers was observed during the real-time hybrid simulation. A reduction in the damper force with increasing temperature was observed. During an earthquake for which the duration of strong motion is less than one minute, the temperature rise and its effect on the damper force may not be significant. However, if the MR damper is subjected to long duration dynamic loadings, such as wind load, the temperature may increase significantly causing the MR damper force to be reduced significantly. The effect of temperature on the MR damper response needs to be further

studied, and MR damper models possibly refined to account for reduced damper force due to temperature rise.

The dynamics of an MR damper associated with variable current is affected by the eddy current and the nonlinear magnetization of damper materials. Although the nonlinear differential equation proposed in Chapter 4 works well for the semi-active controllers considered this dissertation, it is not general for a wide range of input current with various frequencies and amplitudes. A rigorous experimental study needs to be performed to enable the development of models that accurately account for the hysteretic magnetization of damper materials.

It is recommended that the SDP be used to design various structures with MR dampers to investigate the effect of building geometry (e.g., height, plan layout of lateral load resisting frames, mass distribution, and 3-D response) on the accuracy of design response prediction and the success of the SDP to achieve the design performance objectives. These studies should include different controller designs, where the effects of the parameters of the controller on the damper response and the structural performance are investigated.

The conclusion that passive control results in a similar performance compared to the semi-active controllers under DBE and MCE ground motions is based on linear elastic theory for the controller design. To draw more general conclusions it is necessary to consider semi-active controller designs based on nonlinear structural response. Moreover, the effect of the user-defined parameters of the semi-active controller needs to be further investigated. The performance of the semi-active

controllers can be affected by the values of the user-defined parameters. The effect of building geometry (e.g., height, plan layout of lateral load resisting frames, mass distribution, and 3-D response) on the performance of the controllers needs to be investigated.

Under extreme ground motions the performance of the LQR controller was statistically shown to be slightly better than passive control. Although the improvement was not very large, this result showed the feasibility of using semi-active controllers to enhance the collapse resistance capacity of a structure. It is recommended to further study the performance of semi-active controllers under extreme ground motions to assess their ability to improve structural response. These studies should include the effects of reaching the stroke limit of the dampers (when the dampers bottom out). The effect of building geometry should be included in these studies.

Real-time hybrid simulations need to be conducted involving experimental substructures comprised of frames with the dampers. The effects of noise in measured response used as feedback data and errors in structural properties used to design the controllers can be experimentally evaluated. These types of tests will be of value in assessing the accuracy of real-time hybrid simulations in predicting the response of actual structures where the simulations are performed involving experimental substructures comprised of only the dampers, which is a more economical simulation than that with experimental substructures comprised of frames and dampers. The measured response of the dampers in these simulations will be of value to further assess

damper models to predict damper response and capture any interaction effects between the dampers and the frame that occur.

References

AISC (2005) *Code of Standard Practice for Steel Buildings and Brdiges*, American Institute of Steel Construction, AISC 303-05.

AISC (2008) *Steel Construction Manual, 13th Edition*, American Institute of Steel Construction.

Alvarez, L. and Jimenez, R. (2003) "Semi-active control of civil structures using magnetorheological dampers" *Proceedings of the American Control Conference*, Denver, Colorado.

Applied Technology Council (ATC) (2009) "Quantification of building seismic performance factors" *FEMA P695, ATC-63 Project Report*, Redwood City, CA.

ASCE/SEI 7-05 (2006) *Minimum design loads for buildings and other structures* American Society of Civil Engineers.

Bani-Hani, K.A. and Sheban, M.A. (2006) "Semi-active neuro-control for base-isolation system using magnetorheological (MR) dampers." *Earthquake Engng. Struct. Dyn.*, 35, 1119-1144.

Bass, B. J. and Christenson, R. E. (2007) "System identification of a 200 kN, magneto-rheological fluid damper for structural control in large-scale smart structures." *Proc., American Control Conf.*, New York.

Carlson, J.D., Catanzarite, D.M. and St. Clair, K.A. (1995) "Commercial magneto-rheological fluid devices." *Proc. 5th Int. Conf. on ER Fluids, MR Fluids and Associated Tech.*, U. Sheffield, UK.

Carlson, J. D., and Spencer, B. F., Jr. (1996) ''Magneto-rheological fluid dampers for semi-active seismic control.'' *Proc., 3rd Int. Conf. on Motion and Vibration Control*, Vol. 3, Chiba, Japan, 35–40.

Carrion, J. E., and B. F. Spencer (2007) "Model-Based Strategies for Real-Time Hybrid Testing," *Newmark Structural Engineering Laboratory Report Series*, NSEL, University of Illinois, Report 006.

Chae, Y., Ricles, J.M., Sause, R., Dong, B., Chen, C., Christenson, R., Dyke, S., Agrawal, A., and Spencer, B.F. (2010) "Experimental studies on control strategies for steel frames with MR dampers for earthquake hazard reduction" *5th World Conference on Structural Control and Monitoring*, Tokyo, Japan.

Chang, K.C., Soong, T.T., Oh, S-T, and lai, M.L. (1992) "Effect of ambient temperature on viscoelastically damped structure" *ASCE Journal of Structural Engineering*, Vol. 117(8), pp.1955-1973.

Chen, C. (2007) "Development and numerical testing of hybrid effective force testing method," *Ph.D. Dissertation*, Department of Civil and Environmental Engineering, Lehigh University, Bethlehem, PA.

Chen, C. and Ricles, J.M. (2008a) "Development of direct integration algorithms for structural dynamics using discrete control theory," *ASCE Journal of Engineering Mechanics*, 134 (8), pp.676-683.

Chen, C. and Ricles, J.M. (2008b) "Stability analysis of direct integration algorithms applied to nonlinear structural dynamics" *ASCE Journal of Engineering Mechanics*, 134 (9), pp.703-711.

Chen, C. and Ricles, J.M. (2010) "Tracking error-based servo-hydraulic actuator adaptive compensation for real-time hybrid simulation," *J. Struct. Eng.*, 136(4).

Chen, C., Ricles, J.M., Marullo, T. M., and Mercan, O. (2009a) "Real-time hybrid testing using the unconditionally stable explicit CR integration algorithm" *Earthquake Engng. Struct. Dyn.*, 38, 23-44.

Chen, C., Ricles, J.M., Sause, R., Karavasilis, T., and Chae, Y. (2009b) "Design and experimental evaluation of steel MRF with magneto-rheological dampers for seismic hazard mitigation" *Sixth International Conference on Behavior of Steel Structures in Seismic Areas, STESSA 2009*, Philadelphia, PA, pp.767-773.

Chen, C., and Ricles, J.M (2009c) "Analysis of actuator delay compensation methods for real-time testing," *Journal of Engineering Structures*, 31(11), pp 2643-2655

Choi, K.M., Cho, S.W., Jung, H.J., and Lee, I.W. (2004) "Semi-active fuzzy control for seismic response reduction using magnetorheological dampers" *Earthquake Engng. Struct. Dyn.*, 33, pp.723-736.

Chopra, A.K. (2001) *Dynamics of Structures: Theory and Applications to Earthquake Engineering*, Prentice-Hall, NJ.

Christenson, R., Lin, Y.Z., Emmons, A. and Bass, B. (2008) "Large-scale experimental verification of semi-active control through real-time hybrid simulation." *J. Struct. Eng.*, ASCE, 134(4), 522-534.

Christopoulos, C. and Filiatrault, A. (2006) "Principles of supplemental damping and seismic isolation" *IUSS Press*, Milan, Italy.

Clough, R.W. and Penzien, J. (1993) *Dynamics of Structures*, Mc Graw Hill, New York.

Constantinou, M. C., Soong, T. T., and Dargush, G. F. (1998) *Passive energy dissipation systems for structural design and retrofit*, Monograph Series, MCEER, State Univ. of New York at Buffalo, Buffalo, N.Y.

Dyke, S.J., Spencer Jr., B.F., Sain, M.K. and Carlson, J.D. (1996) "Modeling and control of magneto-rheological dampers for seismic response reduction" *Smart Materials and Structures*, 5, 565-575.

Edwards, C. and Spurgeon, S.K. (1998) *Sliding Mode Control: Theory and Applications* Taylor and Francis.

Fan, C. P. (1998) "Seismic analysis, behavior, and retrofit of non-ductile reinforced concrete frame buildings with viscoelastic dampers." *Ph.D. dissertation*, Lehigh University, Bethlehem, Pa.

Fan, Y.C., Loh, Ch.H., Yang, J.N., and Lin, P.Y. (2008) "Experimental performance evaluation of an equipment isolation using MR dampers" *Earthquake Engng. Struct. Dyn.*, 38, pp.285-305.

Federal Emergency Management Agency (2000a) *Recommended Seismic Design Criteria for New Steel Moment-Frame Buildings*, Report No. FEMA-350, Washington, DC.

Federal Emergency Management Agency (2000b) *Prestandard and Commentary for the Seismic Rehabilitation of Buildings*, Report No. FEMA-356, Washington, DC.

Federal Emergency Management Agency (2006) *Next-generation performance-based seismic design guidelines*, FEMA-445, Washington, DC.

Gallent, S.I. (1993) *Neural network learning and expert system*, Cambridge, MA: MIT press

Gamota, D.R. and Filisko, F.E. (1991) "Dynamic mechanical studies of electrorheological materials: Moderate frequencies" *Journal of Rheology*, 35(3), pp.399-
425.

Gu, Z.Q. and Oyandiji, S.O. (2008) "Application of MR damper in structural control using ANFIS method" *Computers and Structures*, 86, pp.427-436.

Guo, A., Li, Z., Li, H. and Ou, J. (2009) "Experimental and analytical study on pounding reduction of base-isolated highway bridges using MR dampers" *Earthquake Engng. Struct. Dyn.*, 38, pp.1307-1333.

Han, Y.M., Nam, M.H., Han, S.S., Lee, H.G. and Choi, S.B. (2002) "Vibration control evaluation of a commercial vehicle featuring MR seat damper", *Journal of Intelligent Material Systems and Structures*, 13(9); 575-579.

Housner, G.W. et al (1997) "Structural control: past, present, and future" *ASCE Journal of Engineering Mechanics*, 123(9), pp.897-971.

Hudson, D. E. (1962) "Some problems in the application of spectrum techniques to strong motion earthquake analysis" Bull. Seismological Society of America, Vol. 52, No.2.

Ibarra, L.F. and Krawinkler, H. (2005) "Global collapse of frame structures under seismic excitations" *John A. Blume Earthquake Engineering Center*, Report No. 152.

International Code Council (2003). International Building Code, Falls Church, VA.

International Code Council (2006). International Building Code, Falls Church, VA.

Jansen, L.M. and Dyke, S.J. (2000) "Semi-active control strategies for MR dampers: comparison study" *J.Eng. Mech.*, ASCE, 126(8), 795-803.

Karamodin, A.K. and Kazemi, H.H. (2010) "Semi-active control of structures using neuro-predictive algorithm for MR dampers" *Struct. Control Health Monit.*, 17, pp.237-253.

Karavasilis, T.L., Ricles, J.M., Marullo, T., Chen, C. (2009) "HybridFEM. A program for nonlinear dynamic time history analysis and real-time hybrid simulation of structures" *ATLSS Report No. 09-08*, Lehigh University, Bethlehem, PA,.

Kennedy, J. and Eberhart, R. C. (1995) "Particle swarm optimization" *IEEE Int. Conf. on Neural. Networks (Perth)* **4** 1942–1949

Koo, J.H., Goncalves, F.D., and Ahmadian, M. (2006) "A comprehensive analysis of the response time of MR dampers" *Smart Mater. Struct.*, 15, pp.351-358.

Kwan, W. P. and Billington, S. L. (2003) "Influence of hysteretic Behavior on Equivalent Period and Damping of Structural Systems" *ASCE Journal of Structural Engineering*, 129(5), pp.576-585.

Lamarche, C.P., Bonelli, A., Bursi, O.S., and Tremblay, R. (2009) "A Rosenbrock-W method for real-time dynamic substructuring and pseudo-dynamic testing" *Earthquake Engineering and Structural Dynamics*, Vol. 38, pp1071-1092.

Lee, D. Y. and Wereley, N. M. (2000) “Analysis of electro- and magneto- rheological flow mode dampers using Herschel-Bulkley model” *Proc., SPIE’s 7th Annual Int. Symposium on Smart Structures and Materials* 244-255

Lee, K.-S., Fan, C.-P., Sause, R., and Ricles, J. (2005) “Simplified design procedure for frame buildings with viscoelastic and elastomeric structural dampers” *Earthquake Eng. Struct. Dyn.*, 34, 1271–1284.

Lee, K.-S., Ricles, J., and Sause, R. (2009) "Performance-based seismic design of steel MRFs with elastomeric dampers", *Journal of Structural Engineering*, Vol. 135, No. 5, pp.489-498.

Lignos, D. (2008) “Sidesway collapse of deteriorating structural systems under seismic excitations” *Ph.D Dissertation*, Stanford University, Stanford, CA.

Lignos, D., and Krawinkler, H. (2009) “Sidesway collapse of deteriorating structural systems under 17 Seismic Excitations,” *John A. Blume Earthquake Engineering Center Report No. TR 172*, Department of Civil Engineering, Stanford University.

Lin, P.Y., Roschke, P.N., and Loh, C.H. (2007) “Hybrid base-isolation with magnetorheological damper and fuzzy control” *Struct. Control Health Monit.*, 14, pp.384-405.

Lin, W.H. and Chopra, A.K. (2003) “Earthquake response of elastic single-degree-of-freedom systems with nonlinear viscoelastic dampers” *ASCE Journal of Engineering Mechanics*, 129(6), pp. 597-606.

Lu, K.C., Loh, C.H., Yang, J.N., and Lin, P.Y. (2008) “Decentralized sliding mode control of a building using MR dampers” *Smart Mater. Struct.* 17, doi:10.1088/0964-1726/17/5/055006.

Makris, N., Burton, S. A., Taylor, D. P. (1996) “Electrorheological damper with annular ducts for seismic protection applications” *Smart Materials and Structures*, 5 (1996), pp. 551-564.

Marshall, J.D. and Charney, F.A. (2010) “A hybrid passive control device for steel structures, I: Development and analysis”, *Journal of Constructional Steel Research*, 66, pp.1278-1286.

MATLAB (2009), MathWorks Inc., Natick, MA.

Miyamoto, H.K., Gilani, A.S.J., Ariyaratana, Ch., and Wada, A. (2010) “Probabilistic evaluation of seismic performance of steel moment framed buildings incorporating damper limit states” *ASCE Structures Congress*, Orlando, FL.

Moon, S.J., Bergman, L.A. and Voulgaris, P.G. (2002) "Sliding mode control of cable-stayed bridge subjected to seismic excitation." *J. Eng. Mech.*, ASCE, 129(1), 71-78.

Newmark, N.M. and Hall, W.J. (1973) "Seismic Design Criteria for Nuclear Reactor Facilities" *Report No. 46, Building Practices for Disaster Mitigation, National Bureau of Standards, U.S. Department of Commerce*, pp. 209-236.

Ogata, K. (1997) *Modern Control Engineering* Prentice Hall, New Jersey.

Ohtori, Y., Christenson, R. E., Spencer, Jr. B. F., and Dyke, S. J. (2004) "Benchmark control problems for seismically excited nonlinear buildings", *ASCE Journal of Engineering Mechanics* Vol. 130, No. 4, pp. 366–387.

OpenSees (2009) *Open System for Earthquake Engineering Simulation*, Pacific Earthquake Engineering Research Center, University of California, Berkeley, Available at http://opensees.berkeley.edu/

Ramirez, O.M., Constantinou, M.C., Gomez, J.D., and Whittaker, A.S. (2002) "Evaluation of simplified methods of analysis of yielding structures with damping systems" *Earthquake Spectra*, Vol. 18, No. 3, pp. 501-530.

Ribakov, Y. and Gluck, J. (2002) "Selective controlled base isolation system with magnetorheological dampers", *Earthquake Engineering and Structural Dynamics*, Vol 31., pp.1301-1324.

Ricles, J.M., Zhang, X., Lu, L.W., and Fisher, J. (2004). "Development of seismic guidelines for deep-column steel moment connections" *ATLSS Report No.* 04-13, Advanced Technology for Large Structural Systems.

Sahasrabudhe, S.S. and Nagarajaiah, S. (2005) "Semi-active control of sliding isolated bridges using MR dampers: an experimental and numerical study" *Earthquake Engng. Struct. Dyn.*, 34, pp.965-983.

Sause R., Hemingway, G.J. and Kasai, K. (1994) "Simplified seismic response analysis of viscoelastic-damped frame structures" *Proceedings of the 5th U.S. National Conference on Earthquake Engineering*, Vol. I, pp.839–848.

Schurter, K.C. and Roschke, P.N. (2000) "Fuzzy modeling of a magnetorheological damper using ANFIS" *Proc. 9th IEEE Int. Conf. on Fuzzy Systems* vol 1 (Piscataway, NJ: IEEE) pp.122–127.

Schurter, K.C. and Roschke, P.N. (2001) "Neuro-fuzzy control of structures using acceleration feedback", *Smart Materials and Structures*, 10, pp. 770-779.

Seo, C.Y., Lin, Y.C., Sause, R, and Ricles, J.M. (2009) "Development of analytical models for 0.6 scale self-centering MRF with beam web friction devices" *6th International Conference for Steel Structures in Seismic Area* (STESSA), Philadelphia.

Shiraishi, T., Morishita, S., and Gavin, H.P. (2004) "Estimation of equivalent permeability in magnetorheological fluid considering cluster formation of particles" *ASME Journal of Applied Mechanics*, 71, pp.201-207

Solberg, K., Bradley, B., Rodgers, G., Mander, J., Dhakal, R., and Chase, J. (2007) "Multi-level seismic performance assessment of a damage-protected beam-column joint with internal lead dampers" *New Zealand Society for Earthquake Engineering Annual Conference (NZSEE 07)*, Palmerston North, New Zealand.

Somerville P, Smith N, Punyamurthula S, and Sun J. (1997) "Development of ground motion time histories for phase 2 of the FEMA/SAC steel project" *Report No. SAC/BD-97/04*, SAC Joint Venture, Sacramento, CA.

Soneji, B.B. and Jangid, R.S. (2006) "Seismic control of cable-stayed bridge using semi-active hybrid system" *Bridge Structures*, 2(1), pp.45-60.

Soong, T.T. and Constantinou, M.C. (1994) *Passive and active structural vibration control in civil engineering* Springer Verlag Wien, New York.

Soong, T.T. and Dargush, G.F. (1997) *Passive energy dissipation systems in structural engineering* Wiley, West Sussex.

Soong, T.T. and Spencer Jr., B.F. (2002) "Supplemental energy dissipation: state-of-the art and state-of-the-practice" *Engineering Structures*, 24, pp.243-259.

Spencer, B.F., Dyke, S.J., Sain, M.K., and Carlson, J.D. (1997) "Phenomenological model for magnetorheological dampers" *ASCE Journal of Engineering Mechanics* 123, pp.230-238.

Spencer, B.F. and Nagarajaiah, S. (2003) "State of the art of structural control" *Journal of Structural Engineering*, 129, pp845-856.

Stelzer, G.J., Schulz, M.J., Kim, J. and Allegagn, J. (2003) "A Magnetorheological Semi-active Isolator to Reduce Noise and Vibration Transmissibility in Automobiles", *Journal of Intelligent Material Systems and Structures*, 14(2); 743-765.

Symans, M.D. and Constantinou, M.C. (1998) "Passive and fluid viscous damping systems for seismic energy dissipation" *ISET Journal of Earthquake Technology*, 35(4), pp.185-206.

Takesue, N., Furusho, J., and Kiyota, Y. (2004) “Fast response MR-fluid actuator” *JSME International Journal Series C,* 47, pp.783-791.

Utkin, V.I. (1992) *Sliding Modes in Control Optimization* Springer-Verlag, New York.

Vamvatsikos, D. and Cornell, C.A. (2002) “Incremental dynamic analysis” *Earthquake Engineering and Structural Dynamics*, 31, pp.491-514.

Wang, D.H. and Liao, W.H. (2005) “Modeling and control of magnetorheological fluid dampers using neural networks” *Smar Mater. Struct.* 14, 111-126.

Wang, X. and Gordaninejad, F. (2000) “Study of field-controllable, electro- and magneto- rheological fluid dampers in flow mode using Herschel-Bulkley theory” *Proc., SPIE’s 7th Annual Int. Symposium on Smart Structures and Materials* 232-243

Wilson, C.M.D. (2005) “Fuzzy control of magnetorheological dampers for vibration reduction of seismically excited structures” *Ph.D Dissertation*, Department of Civil and Environmental Engineering, The Florida State University, FL.

Xu, Y.L., Qu, W.L., and Ko, J.M. (2000) “Seismic response control of frame structures using magnetorheological/electrorheological dampers” *Earthquake Engng. Struct. Dyn.*, 29, pp.557-575.

Yang, G. (2001) “Large-scale magneto-rheological fluid damper for vibration mitigation: modeling, testing and control.” *Ph.D. Dissertation*, Dept of Civil Eng. and Geological Sciences, University of Notre Dame, Notre Dame, Indiana.

Yang, G., Spencer, B.F. Jr, Carlson, J.D., and Sain, M.K. (2002) “Large-scale MR fluid dampers: modeling and dynamic performance considerations” *Engineering Structures* 24, pp.309-323.

Yang, J.N., Wu, J.C., and Agrawal, A.K. (1995) “Sliding mode control for nonlinear and hysteretic structures” *J. Eng. Mech.*, ASCE, 121(12), 1330-1339.

Ye, M. and Wang, X. (2007) “Parameter estimation of the Bouc-Wen hysteresis model using particle swarm optimization” *Smart Material and Structures*, 16, pp.2341-2349.

Yi, F., Dyke, S.J., Caicedo, J.M., and Carlson, J.D. (2001) “Experimental verification of multiinput seismic control strategies for smart dampers” Journal of Engineering Mechanics, 127(11), pp.1152-1164.

Zhou, L., Chang, C.C. and Wang, L.X. (2003) “Adaptive fuzzy control for nonlinear building-magnetorheological damper system.” *J. Struct. Eng.*, ASCE, 129(7), 905-913.

Appendix 1

Determination of Coefficients of Maxwell Element

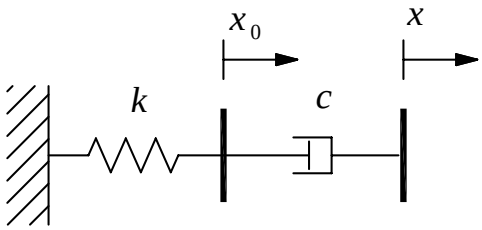

Figure A.1

The equilibrium equation of the Maxwell element shown in Figure A.1 is given by

$$kx_0 = c(\dot{x} - \dot{x}_0) \tag{A1.1}$$

Assuming the Maxwell element is subjected to a harmonic motion

$$x = u_0 \sin(\omega t) \tag{A1.2}$$

The time derivative of x is obtained as

$$\dot{x} = u_0 \omega \cos(\omega t) \tag{A1.3}$$

Since x is harmonic, x_0 is also a harmonic motion described as

$$x_0 = a\sin(\omega t) + b\cos(\omega t) \tag{A1.4}$$

where, a and b are constants that describes the amplitude of x_0 and the phase delay between x and x_0. The time derivative of x_0 is

$$\dot{x}_0 = a\omega\cos(\omega t) - b\omega\sin(\omega t) \tag{A1.5}$$

Substituting (A1.2) ~ (A1.5) into (A1.1) results in

$$(ka - c\omega b)\sin(\omega t) + (kb + c\omega a - u_0 c\omega)\cos(\omega t) = 0 \tag{A1.6}$$

Since the equation (A1.6) needs to be satisfied regardless at all instances of time t, the following equations are obtained

$$ka - c\omega b = 0 \tag{A1.7}$$

$$kb + c\omega a - u_0 c\omega = 0 \tag{A1.8}$$

Thus, a and b are determined by solving (A1.7) and (A1.8)

$$a = \frac{u_0\omega^2\lambda^2}{1+\omega^2\lambda^2} \qquad b = \frac{u_0\omega\lambda}{1+\omega^2\lambda^2} \tag{A1.9}$$

where, $\lambda = c/k$. The damper force of the MNS model during the pre-yield mode is obtained from the equilibrium equation (A1.1)

$$f = kx_0 = k\,a\sin(\omega t) + kb\cos(\omega t) \tag{A1.10}$$

When the damper velocity is a maximum, $\cos(\omega t) = 1$ from (A1.3); thereby, $\sin(\omega t) = 0$. Similarly, $\cos(\omega t) = 0$ and $\sin(\omega t) = 1$, when the damper velocity is zero. Therefore, f_0 and f_m in Figure 3.11 are determined as follows, by using (A1.10)

$$f_0 = ka \tag{A1.11}$$

$$f_m = kb \tag{A1.12}$$

Let $\rho = f_0/f_m$, then,

$$\rho = \frac{f_0}{f_m} = \frac{a}{b} = \omega\lambda \tag{A1.13}$$

Substituting (A1.13) into (A1.9)

$$a = \frac{u_0\rho^2}{1+\rho^2} \qquad b = \frac{u_0\rho}{1+\rho^2} \tag{A1.14}$$

The damper coefficient k and c are obtained as follows

$$k = \frac{f_0}{a} = f_0\frac{1+\rho^2}{u_0\rho^2} \tag{A1.15}$$

$$c = k\lambda = \frac{f_0}{\omega}\frac{1+\rho^2}{u_0\rho} \tag{A1.16}$$

By substituting $\rho = f_0/f_m$ into (A1.15) and (A1.16), the damper coefficients finally can be expressed as

$$c = \frac{1}{u_0\omega}\frac{f_0^2+f_m^2}{f_m}, \qquad k = \frac{1}{u_0}\frac{f_0^2+f_m^2}{f_0} \tag{A1.17}$$

Appendix 2

State Determination of MNS Model

A2.1 Formulation Based on the Newmark-β Direct Integration Algorithm

A2.1.1 Pre-yield Mode

The discretized equation of motion of MNS model during the pre-yield mode is written as

$$c\dot{z}_i + kz_i = ky_i \tag{A2.1}$$

The incremental form of (A2.1) is

$$c\Delta\dot{z}_i + k\Delta z_i = k\Delta y_i \tag{A2.2}$$

where, $\Delta\dot{z}_i = \dot{z}_{i+1} - \dot{z}_i$, $\Delta z_i = z_{i+1} - z_i$, and $\Delta y_i = y_{i+1} - y_i$. The incremental form of the Newmark-β direct integration algorithm is given as

$$\Delta\dot{z}_i = \frac{\gamma}{\beta\Delta t}\Delta z_i - \frac{\gamma}{\beta}\dot{z}_i + \Delta t\left(1 - \frac{\gamma}{2\beta}\right)\ddot{z}_i \tag{A2.3}$$

Using the constant average acceleration method (i.e., $\beta = 1/4, \gamma = 1/2$), Equation (A2.3) is rewritten as

$$\Delta\dot{z}_i = \frac{2}{\Delta t}\Delta z_i - 2\dot{z}_i \tag{A2.4}$$

Substituting Equation (A2.4) into Equation (A2.2) yields,

$$\Delta z_i = \frac{k\Delta y_i + 2c\dot{z}_i}{k + \frac{2c}{\Delta t}} \tag{A2.5}$$

Since $\dot{x} = \dot{y}$ during the pre-yield mode, Δy_i in Equation (A2.5) is obtained as

$$\Delta y_i = \Delta x_i = x_{i+1} - x_i \tag{A2.6}$$

where, x_{i+1} and x_i are known values. Therefore, the response at time t_{i+1} including values for the variables y and z as well as damper force f are determined using Δz_i from Equation (A2.5) and the known state of the MNS model at time t_i

$$z_{i+1} = z_i + \Delta z_i \tag{A2.7}$$

$$\dot{z}_{i+1} = \dot{z}_i + \Delta \dot{z}_i = \frac{2}{\Delta t}\Delta z_i - \dot{z}_i \tag{A2.8}$$

$$f_{i+1} = c\dot{z}_{i+1} = \frac{2c}{\Delta t}\Delta z_i - c\dot{z}_i \tag{A2.9}$$

With the given initial values, Equations (A2.7) ~ (A2.9) can be sequentially updated during the pre-yield mode. Once the mode changes from pre-yield to post-yield mode, these updated values are used as initial values for the state determination during the post-yield mode.

A2.1.2 Post-yield Mode

The variable y and z of the Maxwell element are continuously updated during the post-yield mode, and these updated values are used as initial conditions for the state determination of the pre-yield mode when the mode changes occurs from post-yield to pre-yield mode. The updating procedure for y and z is given below.

Equation (3.8) at time step t_i is expressed as

$$\dot{y}_i = \frac{\dot{f}_i}{k} + \frac{f_i}{c} \tag{A2.10}$$

The incremental form of Equation (A2.10) is

$$\Delta \dot{y}_i = \frac{\Delta \dot{f}_i}{k} + \frac{\Delta f_i}{c} \tag{A2.11}$$

where $\Delta f_i = f_{i+1} - f_i$ and $\Delta \dot{f}_i = \dot{f}_{i+1} - \dot{f}_i$. Since the damper is in the post-yield mode, f_i and f_{i+1} are given from Equation (3.4) or (3.5). $\dot{f}_i$ can be determined using the backward Euler scheme:

$$\dot{f}_i = \frac{f_i - f_{i-1}}{\Delta t} \tag{A2.12}$$

With the definition of $\dot{f}_i$, $\Delta \dot{f}_i$ is determined as

$$\Delta \dot{f}_i = \frac{f_{i+1} - 2f_i + f_{i-1}}{\Delta t} \tag{A2.13}$$

As the post-yield mode occurs after the pre-yield mode, the initial value of f_{i-1} can be obtained from the pre-yield mode response. Utilizing Equation (A2.4), Equation (A2.11) can be rewritten as

$$\frac{2}{\Delta t}\Delta y_i - 2\dot{y}_i = \frac{\Delta \dot{f}_i}{k} + \frac{\Delta f_i}{c} \tag{A2.14}$$

that is,

$$\Delta y_i = \frac{\Delta t}{2}\left(\frac{\Delta \dot{f}_i}{k} + \frac{\Delta f_i}{c} + 2\dot{y}_i\right) \tag{A2.15}$$

Knowing the state of the MNS model at time t_i, y_{i+1} is thus obtained as follows

$$y_{i+1} = y_i + \Delta y_i \tag{A2.16}$$

Finally, z_{i+1} is calculated by inserting Equation (A2.15) into Equation (A2.5), and then solving (A2.7).

A2.2 Formulation Based on the CR Direct Integration Algorithm

A2.2.1 Pre-yield Mode

The variation of displacement and velocity over the time step for the CR direct integration algorithm are defined as (Chen et al. 2009)

$$\dot{z}_{i+1} = \dot{z}_i + \Delta t \alpha_1 \ddot{z}_i \tag{A2.17}$$

$$z_{i+1} = z_i + \Delta t \dot{z}_i + \Delta t^2 \alpha_2 \ddot{z}_i \tag{A2.18}$$

The incremental form based on the CR direct integration algorithm is obtained by eliminating the acceleration term and combining Equations (A2.17) and (A2.18), where

$$\Delta \dot{z}_i = \dot{z}_{i+1} - \dot{z}_i = \frac{\alpha_1}{\alpha_2 \Delta t}(z_{i+1} - z_i - \Delta t \dot{z}_i) \tag{A2.19}$$

Since $\alpha_1 = \alpha_2$ in the CR direct integration algorithm, Equation (A2.19) can be rewritten as

$$\Delta \dot{z}_i = \frac{\Delta z_i}{\Delta t} - \dot{z}_i \tag{A2.20}$$

where, $\Delta z_i = z_{i+1} - z_i$. Substituting (A2.20) into (A2.2) yields,

$$\Delta z_i = \frac{k \Delta y_i + c \dot{z}_i}{k + \frac{c}{\Delta t}} \tag{A2.21}$$

where, Δy_i is obtained using (A2.6). Finally, the response at time t_{i+1} are determined using Δz_i from Equation (A2.21) and the known state information for z_i:

$$z_{i+1} = z_i + \Delta z_i \tag{A2.22}$$

$$\dot{z}_{i+1} = \dot{z}_i + \Delta \dot{z}_i = \frac{\Delta z_i}{\Delta t} \tag{A2.23}$$

$$f_{i+1} = c\dot{z}_{i+1} = \frac{c\Delta z_i}{\Delta t} \tag{A2.24}$$

A2.2.2 Post-yield Mode

The damper forces f_i and f_{i+1} in post-yield mode are obtained using Equation (3.4) or (3.5). Utilizing Equation (A2.20), Equation (A2.11) can be rewritten in terms of y instead of z

$$\frac{\Delta y_i}{\Delta t} - \dot{y}_i = \frac{\Delta \dot{f}_i}{k} + \frac{\Delta f_i}{c} \tag{A2.25}$$

where, $\Delta \dot{f}_i$ is defined by Equation (A2.13). By rearranging Equation (A2.25) with respect to Δy_i,

$$\Delta y_i = \Delta t \left(\frac{\Delta \dot{f}_i}{k} + \frac{\Delta f_i}{c} + \dot{y}_i \right) \tag{A2.26}$$

Thus, y_{i+1} is obtained as follows

$$y_{i+1} = y_i + \Delta y_i \tag{A2.27}$$

Δz_i is calculated by inserting Equation (A2.26) into (A2.21) and the damper force is determined using Equation (A2.24). The internal variables y and z of the Maxwell element are updated during the post-yield mode via Equations (A2.27) and (A2.22).

A2.3 Formulation Based on the Forward Euler Method

A2.3.1 Pre-yield Mode

Utilizing the forward Euler method, z_{i+1} is expressed as

$$z_{i+1} = z_i + \Delta t \dot{z}_i \tag{A2.28}$$

where, $\dot{z}_i$ is determined based on the MR damper force f_i

$$\dot{z}_i = \frac{f_i}{c} \tag{A2.29}$$

Since in pre-yield mode the velocities $\dot{y}_{i+1} = \dot{x}_{i+1}$, y_{i+1} is updated as

$$y_{i+1} = y_i + \Delta y_i = y_i + (x_{i+1} - x_i) \tag{A2.30}$$

where, x_{i+1} and x_i are known values. Therefore, the damper force at time t_{i+1} is obtained from the following equilibrium equation

$$f_{i+1} = k(y_{i+1} - z_{i+1}) \tag{A2.31}$$

A2.3.2 Post-yield Mode

During the post-yield mode, z_{i+1} can be updated using Equations (A2.28) and (A2.29), where f_i is obtained from Equation (3.4) or (3.5). y_{i+1} is updated using the forward Euler method as

$$y_{i+1} = y_i + \Delta t \dot{y}_i \tag{A2.32}$$

where, $\dot{y}_i$ is obtained from Equation (A2.10). $\dot{f}_i$ in Equation (A2.10) can be calculated by using either the backward Euler scheme as given by Equation (A2.12) or the forward Euler scheme.

Appendix 3 Ground Motions

Table A3.1 Far-field ground motions recommended for nonlinear time history analysis of structures (ATC 2009)

ID	Name	Year	M	Station	Component (file name)		Recorded Motion	
					Horz. 1	Horz.2	PGA (g)	PGV (cm/s)
1	Northridge	1994	6.7	Beverly Hills – Mulhol	MUL009	MUL279	0.52	63
2	Northridge	1994	6.7	Canyon Country – WLC	LOS000	LOS270	0.48	45
3	Duzce, Turkey	1999	7.1	Bolu	BOL000	BOL090	0.82	62
4	Hector Mine	1999	7.1	Hector	HEC000	HEC090	0.34	42
5	Imperial Valley	1979	6.5	Delta	H-DLT262	H-DLT352	0.35	33
6	Imperial Valley	1979	6.5	El Centro Array #11	H-E11140	H-E11230	0.38	42
7	Kobe, Japan	1995	6.9	Nishi-Akashi	NIS000	NIS090	0.51	37
8	Kobe, Japan	1995	6.9	Shin-Osaka	SHI000	SHI090	0.24	38
9	Kocaeli, Turkey	1999	7.5	Duzce	DZC180	DZC270	0.36	59
10	Kocaeli, Turkey	1999	7.5	Arcelik	ARC000	ARC090	0.32	40
11	Landers	1992	7.3	Yermo Fire Station	YER270	YER360	0.24	52
12	Landers	1992	7.3	Coolwater	CLW-LN	CLW-RT	0.42	42
13	Loma Prieta	1989	6.9	Capitola	CAP000	CAP090	0.53	35
14	Loma Prieta	1989	6.9	Gilroy Array #3	G03000	G03090	0.56	45
15	Manjil, Iran	1990	7.4	Abbar	ABBAR--L	ABBAR--T	0.51	54
16	Superstition Hills	1987	6.5	El Centro Imp. Co.	B-ICC000	B-ICC090	0.36	46
17	Superstition Hills	1987	6.5	Poe road (temp)	B-POE270	B-POE360	0.45	36
18	Cape Mendocino	1992	7.0	Rio Dell Overpass	RIO270	RIO360	0.55	44
19	Chi-Chi, Taiwan	1999	7.6	CHY101	CHY101-E	CHY101-N	0.44	115
20	Chi-Chi, Taiwan	1999	7.6	TCU045	TCU045-E	TCU045-N	0.51	39
21	San Fernando	1971	6.6	LA – Hollywood Stor	PEL090	PEL180	0.21	19
22	Friuli, Italy	1976	6.5	Tolmezzo	A-TMZ000	A-TMZ270	0.35	31

Vita

Yunbyeong Chae was born on December 15, 1976 in Boryeong, Korea. He received his Bachelor of Science degree in Civil Engineering in February 1999 and his Master of Science degree in Structural Engineering in February 2001 from Seoul National University, Seoul, Korea. The title of his master thesis is “Two dimensional analysis method for the dynamics of piled multi-block systems”. Upon the graduation, he worked as a structural engineer in Chungsuk Engineering, Seoul, Korea, where he was involved in various structural design projects. His major responsibility was focused on the seismic design of structures. In 2004, he moved to GS Engineering and Construction, Seoul, Korea to further develop his career in the area of construction, where he provided a great deal of technical support for bridge construction until he entered Lehigh University. He began to pursue his Ph.D in Structural Engineering at Lehigh University in 2006.